



UNIVERSITÀ
DEGLI STUDI
DI PADOVA

Head Office: **Università degli Studi di Padova**

Department

Department of Chemical Sciences

Ph.D. COURSE IN: **Molecular Sciences**

CURRICULUM: **Chemical Sciences**

SERIES: XXXV

Novel molecularly designed strategies for Artificial Photosynthesis

Coordinator: Prof. Leonard J. Prins

Supervisor: Prof. Andrea Sartorel

Ph.D. student: Ruggero Bonetto

1222 · 2022
800
A N N I



UNIVERSITÀ
DEGLI STUDI
DI PADOVA



Ph.D. Course in Molecular Sciences, Curriculum Chemical Sciences

University of Padova – Department of Chemical Sciences

Novel molecularly designed strategies for Artificial Photosynthesis

Ruggero Bonetto

Supervisor: Prof. Andrea Sartorel

Coordinator: Prof. Leonard J. Prins

ὅτε δὲ ἔκρινεν αὐτὸν ὅστις ἐστὶ δηλῶσαι, ἔρωτας ἐνεθουσίασε

θεοῖς καὶ αὐγὴν ἦν εἶχεν ἐν στέρνοις πλείονα ταῖς τούτων ἐχαρίσατο διανοίαις,

ἵνα πρῶτον μὲν ζητεῖν θελήσωσιν, εἶτα ἐπιθυμήσωσιν εὐρεῖν, εἶτα καὶ κατορθῶσαι δυναθῶσι.

Questa Tesi è dedicata alla mia famiglia, a Luana e al mio Supervisore.



Index

Preface	1
Context: climate change and the energy issue	1
Artificial photosynthesis	3
Thesis outline	5
SECTION 1.	
Molecular catalysis of the electrochemical reduction of carbon dioxide by iron Schiff base complexes	7
1. Introduction	8
1.1 CO ₂ valorization	8
1.2 Electrochemical catalysis	11
1.3 Catalyst benchmarking criteria	16
1.4.1 Cyclic voltammetry – Catalytic Tafel plots	18
1.4.2 Cyclic voltammograms hampered by side-phenomena – Foot of the wave analysis	26
1.4.3 Cyclic voltammetry of complicated catalytic systems	32
1.5 Simulation of electrochemical experiments	34
1.6 Constant potential electrolysis (CPE)	35
1.7 Spectroelectrochemistry (SEC)	37
1.8 CO ₂ reduction by iron complexes	38
1.8.1 CO ₂ reduction by Fe porphyrins	42
1.8.2 CO ₂ Reduction by Iron Porphyrins to Methane	46
1.8.3 CO ₂ Reduction by Iron Porphyrins to Formate	47
1.8.4 Non-heme Iron Mononuclear Complexes	49
1.9 Role of the ligand on the catalytic activity	52
1.9.1 Inner coordination sphere	52
1.9.2 Structure-activity relationships	54
1.9.3 Redox activity of the ligand and catalyst stability	62

1.10	Photocatalysis	64
1.10.1	Photosensitizers	64
1.10.2	Sacrificial electron donors	69
1.10.3	Two-component systems	71
1.11	Chapter 2 and 3 Rationale	73
Appendix 1		74
Appendix 1.1	– Computational simulation of electrochemical experiments	74
Appendix 1.2	– Electrochemical study of iron porphyrin catalyst	74
Appendix 1.3	– Synthetic procedure of 5,10,15,20-Tetraphenylporphin (TPP)	75
Appendix 1.4	– Synthesis of chlorido(5,10,15,20-Tetraphenyl-21H,23H-porphinato)iron(III) (Fe(TPP)Cl)	77
2.	Electrochemical Conversion of CO₂ to CO by Fe^I Salophen complexes	78
2.1	Rationale	78
2.2	Synthesis of the Salophen ligand and of its iron complexes, Fe(Salophen)Cl and Fe₂(Salophen)₂(μ–O)	79
2.3	Characterization of the complexes	81
2.4	Electrochemical properties of the complexes	83
2.4.1	Electrochemical Characterization of Fe(Salophen)Cl	83
2.4.2	Electrochemical Characterization of Fe₂(Salophen)₂(μ–O)	85
2.4.3	Interconversion of mononuclear and dinuclear species	88
2.5	Electrochemical behavior of Salophen Fe complexes in the presence of carbon dioxide	92
2.6	Electrochemistry in the presence of Phenol	99
2.6.1	Fe^I reactivity towards phenol	100
2.6.2	Catalytic CO₂ reduction in the presence of phenol	101
2.7	Preparative scale CO₂-to-CO electrochemical reduction	105

2.8 Homogeneous vs heterogeneous electrocatalytic routes and benchmarking	110
2.9 Electrochemical characterization of the Salophen ligand in acetonitrile	117
2.10 Higher nuclearity compounds as products of ligand-based electrochemistry	121
2.11 Experimental section	129
2.11.1 Materials and methods	129
2.11.2 Electrochemical setup	129
2.11.2.1 Cyclic voltammetry (CV)	129
2.11.2.2 Constant potential electrolysis (CPE)	131
2.11.2.3 Infrared spectroelectrochemistry (SEC-IR)	132
2.11.2.4 UV/Vis spectroelectrochemistry (SEC-UV/Vis)	133
2.11.3 Electron Paramagnetic Resonance (EPR) spectroscopy	134
2.11.4 Synthetic procedures	135
2.11.4.1 Synthetic procedure of Salophen ligand	135
2.11.4.2 Synthetic procedures of Fe(Salophen)Cl	136
Appendix 2	139
Appendix 2.1 – Fe ₂ (Salophen) ₂ (μ–O) characterization in dichloromethane	139
Appendix 2.2 – Binding of phenol to Fe(Salophen)Cl and Fe ₂ (Salophen) ₂ (μ–O)	140
Appendix 2.3 – Competitive binding of chloride and phenol	143
Appendix 2.4 – Foot-of-the-wave-analysis	147
3. Fe ^I intermediates bearing N ₂ O ₂ Schiff base ligands: study of the effects of ligand electronic properties and of the proton donor on reactivity with CO ₂	149
3.1 Rationale	149
3.2 Synthesis and characterization of the complexes	150

3.3	Reactivity of Fe ^I towards carbon dioxide	159
3.4	Effect of Proton Donors and Electrolysis	162
3.5	Fe(Salen) as catalyst for the electrochemical CO ₂ -to-CO reduction	166
3.6	Catalyst decomposition	167
3.7	Conclusions	174
3.8	Experimental section	176
3.8.1	Synthesis of the Schiff base ligands	176
3.8.1.1	N,N'-ethylene-bis(acetylacetonimine) (Acacen)	176
3.8.1.2	N,N'-ethylene-bis(benzoylacetonimine) (Beacen)	178
3.8.1.3	N,N'-ethylene-(acetylacetonimine)(salicylideneimine) (Acacsalen)	180
3.8.1.4	N,N'-ethylene-bis(acetylacetonimine) (Salen)	182
3.8.2	Synthesis of the Iron complexes	184
3.8.2.1	N,N'-ethylene-bis(acetylacetoniminato)chloroiron(III), Fe(Acacen)Cl	184
3.8.2.2	N,N'-ethylene-bis(benzoylacetoniminato)chloroiron(III), Fe(Beacen)Cl	185
3.8.2.3	N,N'-ethylene-(acetylacetoniminato)(salicylideneimine), Fe(Acacsalen)Cl	186
3.8.2.4	N,N'-ethylene-bis(acetylacetoniminato)chloroiron(III), Fe(Salen)Cl	187
3.8.3	Electrochemical methods	188
3.8.3.1	Cyclic voltammetry	188
3.8.3.2	Constant potential electrolysis	189
3.8.3.3	UV/Visible absorption spectroelectrochemistry	190
3.8.3.4	Electrolysis gaseous product quantification	191

SECTION 2.

Hybrid photoactive catalytic materials for photoelectrochemical water oxidation to O ₂	194
4 Dye-catalyst dyads as constituents of Photoelectrochemical Cells	195
4.1 Introduction	195
4.1.2 Semiconductors	197
4.1.3 Dyes	198
4.1.4 Water Oxidation Catalysts (WOC)	202
4.1.5 Dye-catalyst dyads	205
4.1.6 From molecular to nanostructured WOC: the case of cobalt oxide	212
4.1.7 Use of photoactive dye-WOC dyads in operational systems	215
4.1.7.1 Efficiency parameters of photoelectrochemical cells	215
5. Polyquinoid dye-cobalt oxide hybrids: novel rare metal-free dyads for photoelectrochemical Water Oxidation	220
5.1 Rationale	220
5.2 Synthesis and characterization of the hybrid particles	221
5.3 Photocatalytic experiments	228
5.4 Photophysical studies on the hybrid particles	232
5.5 KuQ3P_n@Co₃O₄^{heptOH} on <i>meso</i>-SnO₂: hybrid dyads for photoelectrochemical water oxidation	233
5.6 Faradaic efficiency for the Oxygen Evolution Reaction	242
5.7 Photoelectrochemical response under monochromatic illumination	244
5.8 Comparison with SnO₂/KuQ/Co₃O₄^{heptOH} photoanodes	246
5.9 Role of dye-electrode interactions – Anchor-free KuQ on SnO₂	250
5.10 Further insights and future perspectives	253

5.11	Experimental section	257
5.11.1	Materials and methods	257
5.11.2	Electrolyte solutions preparation	257
5.11.3	FTO/SnO₂ electrodes preparation	258
5.11.4	Photoanodes preparation	259
5.11.4.1	Hybrid-based photoanodes	259
5.11.4.2	Dye-sensitized FTO/SnO₂ electrodes preparation	260
5.11.5	Photocatalysis	262
5.11.6	Photoelectrochemical experiments	264
5.11.7	Determination of the Faradaic efficiency for O₂ evolution	265
5.11.8	Incident photon-to-current conversion efficiency (IPCE) determination	270

SECTION 3.	
Emerging (photo)electrochemical strategies for organic reactivity	275
6. Emerging (photo)electrochemical strategies for organic reactivity	276
6.1 Electrochemical carboxylation of α,β-unsaturated ketones	276
6.1.1 Contribution to the work	278
6.2 Photoelectrochemical C–H activation by SnO₂ electrodes dye-sensitized with Quinacridone	280
6.2.1 Introduction	280
6.2.2 Quinacridone-sensitized SnO₂ photoanodes	281
6.2.3 Contribution to the work	284
6.2.4 Further developments	286
6.3 Experimental Section	289
6.3.1 Electrochemical carboxylation of α,β-unsaturated ketones	289
6.3.2 Photoelectrochemical C–H activation by SnO₂ electrodes dye-sensitized with Quinacridone	292
* **	
7. Bibliography	297
Ringraziamenti – Acknowledgements	311

Preface

Context: climate change and the energy issue

Over the last century, our Planet has undergone a major climate change pathway, that evidence has linked to anthropic activity. Anthropogenic emissions of carbon dioxide, a greenhouse gas, have been proven responsible for the steady increase in CO₂ concentration into the Earth's atmosphere (420 ppm at the end of 2022), and are correlated with an overall global temperature increase (+1.2 °C since 1850–1900). CO₂ emissions are indeed foreseen to cause, mainly by the greenhouse effect and water bodies acidification, a major climate change of which we are beginning to experience the effects.

The main cause for the ever-increasing CO₂ emissions lies in energy production by combustion of fossil fuels (namely petroleum, coal, and natural gas). In fact, as per the latest reports, fossil fuels are still the most widely used sources of energy on the global scale, accounting for 80% of the total energy consumption. This implies severe consequences in terms of unbalanced carbon emissions with respect to the natural carbon capture ability of the environment. Furthermore, fossil fuel combustion is highly impacting on air quality, being associated with emissions of gaseous polluting agents (nitrogen oxides, carbon monoxide, uncombusted fuels) and particulate matter (PM), which compromise health with acute and chronic effects. Finally, processes for extracting fossil fuels are most often irreversibly impacting on delicate ecosystems with lingering and widespread consequences.

Global energy demand has been increasing consistently with the development of industrial civilisation. Since 1990, global energy consumption has increased from 8500 Mtoe (million tonnes of oil equivalent, 1 toe = 11.63 Wh) to over 14000 Mtoe in 2022, with a prominent contribution of developing countries in Asia. To supply the global energy demand, driven by world-scale development, the only long-term sustainable choice is the transition towards an energy supply based on sustainable sources. Currently, great effort is being devoted to substituting fossil

fuels for sustainably provided electricity, carbon-neutral fuels from CO₂, and on H₂ as a clean chemical energy vector. Together, these strategies are aimed at the so-called Energy Transition.

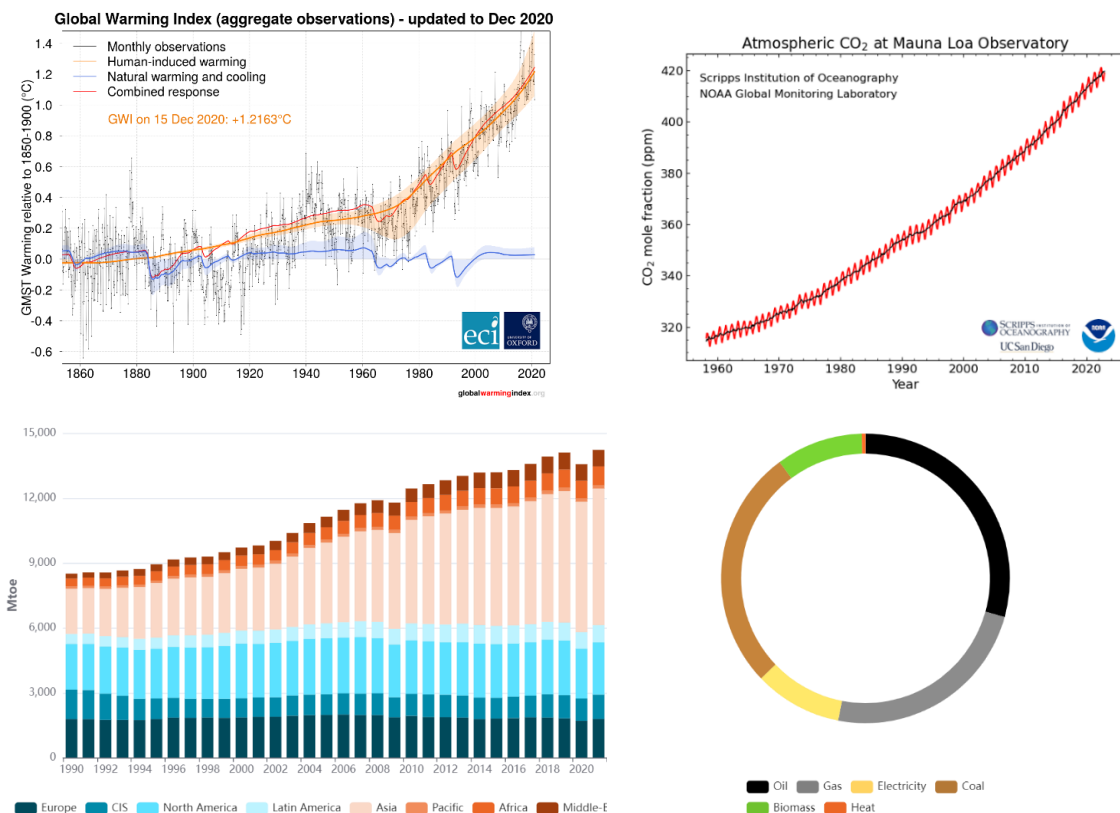


Figure A. Top left: plot of Global Warming Index as a function of time, data reported from <https://www.globalwarmingindex.org/>. Top right: atmospheric CO₂ concentration as a function of time, registered at Mauna Loa Observatory, data reported from <https://gml.noaa.gov/ccgg/trends/>. Bottom left: energy consumption as a function of time (1990-2021). Different colours indicate different geographical regions. Data reported from <https://yearbook.enerdata.net/total-energy/world-consumption-statistics.html>. Bottom right: graph of the different energy sources globally used (referred to 2021).

Scientific research should address these issues with competence, providing solutions both on the environmental and energetic fronts. In particular, Chemistry is involved with great potential and equally prominent responsibilities in:

- i) CO₂ emissions and pollution monitoring and remediation;
- ii) CO₂ valorization and recycling;
- iii) transition towards a sustainable energy-based civilisation.

These interconnected tasks encompass different specialized fields of chemical sciences, thus involving the chemist's community as a whole. Part of the thought arsenal to face the challenge is constituted by the 12 principles of Green Chemistry, which have been guiding the rise of a more sustainable approach to the chemical industry. Regardless, these should be integrated and encased in a larger context.

Another, complementary, key responsibility of scientists lies in knowledge dissemination and sensitization towards these themes, not only exposing the issues, but especially the possible solutions and their long-term viability.

The research work detailed in this Thesis is intended as a contribution to this greater endeavour, especially to highlight the importance of fine chemical design in conjunction with inspiration from the rich and powerful chemistry observed in Nature.

Artificial photosynthesis

Activation of small molecules – *i.e.*, naturally abundant, chemically simple substrates with low molecular weight – has potential benefits for synthetic and energy-oriented strategies. Two of the most targeted molecules are water and carbon dioxide: they represent the richest source of carbon and hydrogen in nature. However, they are the oxidative chain end of organic compounds, a thermodynamic sink that makes them unexploitable *per se*. Their activation and subsequent conversion to useful chemicals therefore calls for reduction processes to be performed.

Sustainably achieving hydrogen evolution from water and carbon dioxide reduction would provide access to carbon-neutral fuels compatible both with

current technologies and with the increasing energy demand, by maintaining a lighter environmental footprint.

Artificial photosynthetic systems aim at performing solar light-driven redox reactions through similar strategies exploited in natural photosynthesis, exploiting the most abundant natural energy source. A chromophore unit (photosensitizer) harvests light and generates a charge separation which in turn may trigger the target redox reaction in the presence of a suitable catalyst. This modular approach, which allows for optimization of each component of the system, has been directed towards water splitting into its elemental constituents (in particular generating H₂ as a fuel and commodity chemical), and also to carbon dioxide reductive activation. Viable strategies that have been explored may exploit a photovoltaic unit, which generates an electromotive force upon light absorption; electrochemically active systems are therefore devoted to separately perform the target redox reactions. Photoelectrochemical cells, on the other hand, incorporate photosensitizers and active redox centres in compact devices (photoelectrodes) to directly trigger reactions in the presence of a light source. Finally, a newly emerging trend targets colloidal photocatalytically active nanoparticles, either in suspension or immobilized.

In this context, ground-breaking research has been recently published, a testimony of the promising colloidal photocatalytic approach^{1,2}. Specifically, “frame box” transparent photoreactors containing layers have been reported by Domen and co-workers, who constructed a 100 m² array of photoreactors based on nanostructured aluminium-doped strontium titanate layers. These water splitting devices reached a conversion efficiency of solar light into H₂ of 0.76%, at the same time proving safe, scalable and durable. The same photoreactor architecture has been applied by Mi and co-workers, who reported nanostructured photocatalyst indium gallium nitride (InGaN/GaN), loaded with Rh/Cr₂O₃/Co₃O₄ reaching an outstanding 9.2% solar-to-hydrogen conversion efficiency from photocatalytic water splitting.

These recent findings are the testimony to the future of artificial photosynthesis as a strategy for integrating effective, bio-inspired approaches into active solutions to the energy-related and climatic issues.

Thesis outline

The present Thesis work is the *compte rendu* of the research carried out during my Doctorate in the Molecular Sciences Doctoral School at the University of Padova. The research themes are related to the NEXuS project (Nanochemistry for Energy and Health), granted to the Department of Chemical Sciences of the University of Padova. Given the nature of the research topics explored, the Thesis will be organized in three sections, namely:

1. Molecular catalysis of the electrochemical reduction of carbon dioxide by iron Schiff base complexes.
2. Hybrid photoactive catalytic materials for photoelectrochemical water oxidation to O₂.
3. Emerging (photo)electrochemical strategies for organic reactivity.

The research has been targeted towards the relevant topics described below, especially valorisation of CO₂ in terms of its conversion into fuels and chemical feedstock and its use in organic reactivity for fine chemistry. On a parallel front, novel systems exploiting solar light for relevant oxidative chemistry have been studied. These themes have been interpreted under different facets during my research, following a *fil rouge* binding together the rational design of molecules and their catalytic properties, with particular focus dedicated to the mechanistic description of the systems.

The work has been a collaborative effort, and the invaluable contribution of other researchers involved in the original work has been credited throughout the Thesis. A relevant portion of the material reported has been published in scientific journals during the Doctorate period. The publications are mentioned at the beginning of each competent Section.

SECTION 1.

Molecular catalysis of the electrochemical reduction of carbon dioxide by iron Schiff base complexes

Disclaimer:

This section contains material previously published in scientific journals, in the form of articles of which I was an author. Reproduction of the of graphic material from the publications in the present Thesis was authorized by the Editors.

*
**

“Electrochemical Conversion of CO₂ to CO by a Competent Fe^I Intermediate Bearing a Schiff Base Ligand” Bonetto, R.; Altieri, R.; Tagliapietra, M.; Barbon, A.; Bonchio, M.; Robert, M.; Sartorel, A. *ChemSusChem* **2020**, 13(16), 4111–4120.

Copyright Wiley 2020.

“Carbon Dioxide Reduction Mediated by Iron Catalysts: Mechanism and Intermediates That Guide Selectivity” Bonetto, R.; Crisanti, F.; Sartorel, A. *ACS Omega* **2020**, 5(34), 21309–21319.

Copyright 2020 American Chemical Society.

“Fe^I intermediates in N₂O₂ schiff base complexes: Effect of electronic character of the ligand and of the proton donor on the reactivity with carbon dioxide” Bonetto, R.; Civettini, D.; Crisanti, F.; Sartorel, A. *Energies* **2021**, 14(18), 5723.

1. Introduction

1.1 CO₂ valorization

Carbon dioxide is being currently regarded as an abundant carbon feedstock. Furthermore, utilization of CO₂ as reagent in chemical processes is considered a viable strategy to mitigate its environmentally impacting emissions. For these reasons, research aimed at upgrading CO₂ exploitation at the industrial level has sprung several approaches over the last decades. Relevant applications involve the cycloaddition of CO₂ to epoxides to generate polycarbonates or cyclic carbonates.³ More challenging transformations are the fixation of carbon dioxide into organic molecules, to obtain carboxyl derivatives.⁴ A third major route of CO₂ utilization is its conversion into fuels or commodity chemicals, to meet an economy based on carbon-neutral chemical energy income.⁵

To date, no electrochemical processes that involve reduction or fixation of CO₂ are industrialized. Carbon dioxide is characterized by a high stability, acting as a thermodynamic sink in all oxidative transformations of organic molecules. Indeed, its fixation into organic scaffolds or its conversion into fuels involves reduction at the carbon site. The thermodynamic barrier associated with CO₂ one-electron reduction is formalized by a standard reduction potential of -1.97 V vs SHE (Standard Hydrogen Electrode) in N,N-dimethylformamide (DMF). Formation of the radical anion requires population of antibonding orbitals in the CO₂ molecule upon reduction, and a geometry variation from linear to bent, thus justifying the very negative value of the standard potential and the high kinetic barriers for the process (Eq. 1).



When CO₂ activation is directed towards fuel or commodity chemicals synthesis, the processes consist in multi-electron reductions often involving an equal number of proton transfers. The presence of proton transfers renders the thermodynamics of CO₂ reduction less demanding, resulting in less negative values of E^0 (Table

1). Depending on the medium chosen, the proton source may be introduced as an external component, usually a weak acid, or be the reaction solvent, as in aqueous systems. While employing water as a solvent is appealing in the scope of working according to the principles of Green Chemistry, systems are often limited by the low solubility of CO₂ in water (*circa* 0.04 M). Organic solvents as acetonitrile (ACN) and N,N-dimethylformamide (DMF) are more frequently employed, given the high solubility of CO₂ (0.28 M and 0.23 M in ACN and DMF, respectively). Focusing on the possible reaction mechanisms, CO₂ reduction necessarily occurs in a multi-step reaction scheme. These reactions, consisting of proton-coupled electron transfer (PCET) events, accompany C–O bond cleavage and possible contextual C–H bond formation. Therefore, CO₂ reduction is usually mechanistically complex.⁶

The practical approaches to CO₂ reduction are the electrochemical and the photochemical strategies, both detailed below.⁷ From an introductory standpoint, it is useful to focus on CO₂ electrochemical reduction. In such a context, the electrons required to reduce carbon dioxide originate from an electrode surface contacting an electrolyte solution. The kinetic barrier associated with CO₂ reduction is quantified as an overpotential term (η), the additional voltage required to drive the reaction at a specified rate on the electrode material considered. Different electrode materials display a range of electroactivity towards CO₂ reduction, with metals being generally more active than cheaper carbon-based materials. However, direct reduction of carbon dioxide on electrode surfaces tends to suffer from a low selectivity resulting in a variegated mixture of gaseous and liquid products, together with a significant contribution from the hydrogen evolution reaction (HER).⁸ This latter is the most frequently encountered side-process, stemming from the necessity of employing proton sources as either the solvent or an additive. For these reasons, a fine control over the reaction mechanism to drive selective CO₂ reduction while operating at low overpotential is a highly valuable feature to be targeted. Such requirements call for the use of catalysis as the most powerful instrument to promote CO₂ reduction to functional devices.

Semi-reaction	E ⁰ / V vs SHE
$CO_2 + 2H^+ + 2e^- \rightarrow HCOOH$	-0.25
$CO_2 + H_2O + 2e^- \rightarrow HCOO^- + OH^-$	-1.08
$CO_2 + H_2O + 2e^- \rightarrow CO + 2OH^-$	-0.11
$CO_2 + 2e^- + 2H^+ \rightarrow CO + H_2O$	-0.93
$CO_2 + 4e^- + 4H^+ \rightarrow CH_2O + H_2O$	-0.07
$CO_2 + 3H_2O + 4e^- \rightarrow CH_2O + 4OH^-$	-0.90
$CO_2 + 6H^+ + 6e^- \rightarrow CH_3OH + H_2O$	+0.02
$CO_2 + 5H_2O + 6e^- \rightarrow CH_3OH + 6OH^-$	-0.81
$CO_2 + 8H^+ + 8e^- \rightarrow CH_4 + 2H_2O$	+0.17
$CO_2 + 6H_2O + 8e^- \rightarrow CH_4 + 8OH^-$	-0.66
$2CO_2 + 2H^+ + 2e^- \rightarrow H_2C_2O_4$	-0.50
$2CO_2 + 2e^- \rightarrow C_2O_4^{2-}$	-0.59
$2CO_2 + 12H^+ + 12e^- \rightarrow CH_2CH_2 + 4H_2O$	+0.06
$2CO_2 + 12H^+ + 12e^- \rightarrow CH_3CH_3OH + 3H_2O$	+0.08

Semi-reaction	Solvent	E ⁰ / V vs NHE
$CO_2 + 2e^- + 2H^+ \rightarrow CO + H_2O$	CH_3CN	-0.65, -0.75
	DMF	-1.36
	$DMF + 2 M H_2O$	-0.69
	$DMF + HBF_4$	-0.26
$CO_2 + 8e^- + 8H^+ \rightarrow CH_4 + 2H_2O$	CH_3CN	-0.48
	DMF	-1.11

Table 1. Carbon dioxide semi-reactions in aqueous (top) and organic (bottom) media, with the associated standard potentials values. Data taken from ⁹.

1.2 Electrochemical catalysis

Over the course of the last decades, intense efforts have been dedicated to the development of electrochemistry, highlighting its paramount role in the investigation of chemical processes. Indeed, electrochemistry provides an arsenal of tools for studying and performing chemical reactions, allowing to gain meaningful insights in their mechanism but also to operate preparative-scale experiments under finely controlled conditions. Given the key need for efficient catalytic systems to sustainably drive redox processes, the field of electrocatalysis naturally developed in conjunction with emerging topics such as battery research, analyte sensing and detection, pollution abatement, biomass upgrade, and fuel synthesis.

In the present thesis, the distinction formulated by Jean-Michel Savéant and collaborators between electrocatalysis and molecular catalysis of electrochemical reactions will be adopted¹⁰. The former implies an active role of the electrode surface in chemically mediating a target reaction, while the second relies on molecular catalysts to mediate electron transfer between an inert electrode and the reactants. The latter approach, schematically represented in Figure 1, has been followed throughout the work described herein.

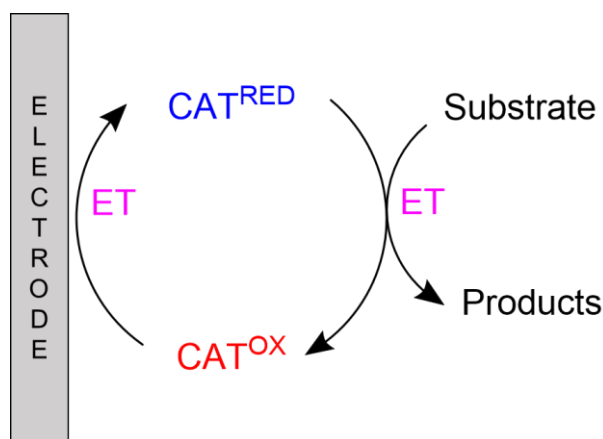


Figure 1. Schematic representation of the action mechanism of molecular catalysis for electrochemical reactions.

The need for a catalyst to drive a redox reaction lies in the inertness of the substrate towards chemical transformations. This feature is quantified in terms of overpotential, representing the required contribution that hampers the reaction from occurring at its standard potential value in the chosen conditions. The foremost role of the catalyst is therefore acting as a mediator of electron transfer (ET) from the electrode surface to the reactants, lowering the overpotential with respect to the direct use of the electrode material. Key requirements for a molecular catalyst to be employed in electrochemical reactions are the ability to easily access multiple reactive oxidation states and to interact with the substrate and with intermediates deriving from the subsequent steps of the catalytic cycle.^{11,12}

Specifically, molecular catalysts can be introduced in the electrolyte solution interfacing with the electrode or immobilized on its surface in the form of mono- or multilayers (*vide infra*).

The main advantages of homogeneous strategies for targeting a catalytic transformation are listed in comparison to heterogeneous systems:

- i) Mechanistic investigation is generally accessible and allows for an easier study and a more detailed understanding of the key steps of the catalytic cycle.
- ii) Optimization of catalyst performance through structure design, based on the aforementioned analyses is within the reaches of molecular synthetic protocols.
- iii) Good reproducibility of experimental results is generally attainable.
- iv) Benchmarking criteria are more easily established and allow a clear-cut comparison between different systems.

Nonetheless, homogeneous molecular catalysis suffers from the need of recycling the catalyst through separation from reactants and products. This issue can be somewhat overcome while keeping the above positive features of a molecular catalyst by transitioning to molecular immobilized catalysis. In this regime, the molecular catalyst is transferred to a functional surface, possibly after a minor

synthetic modification of its structure to satisfy such requirement. Immobilization can rely on coordination, covalent or non-covalent bonding interactions, often in combination with each other (Figure 2)^{13–24}. Such operation is however conducted under the assumption that the mechanistic features studied in homogeneous systems will apply to the immobilized ones, *i.e.* that immobilization is innocent towards the reaction mechanism and performance. When these strategies are directed towards electrochemical systems, it is straightforward to consider the working electrode, by definition, as the functional surface in an electrochemical cell. Several examples of electrolyzers and photoelectrochemical cells for carbon dioxide reduction featuring molecular catalysts immobilized on the surface of otherwise inert electrodes have indeed been recently reported^{25–29}.

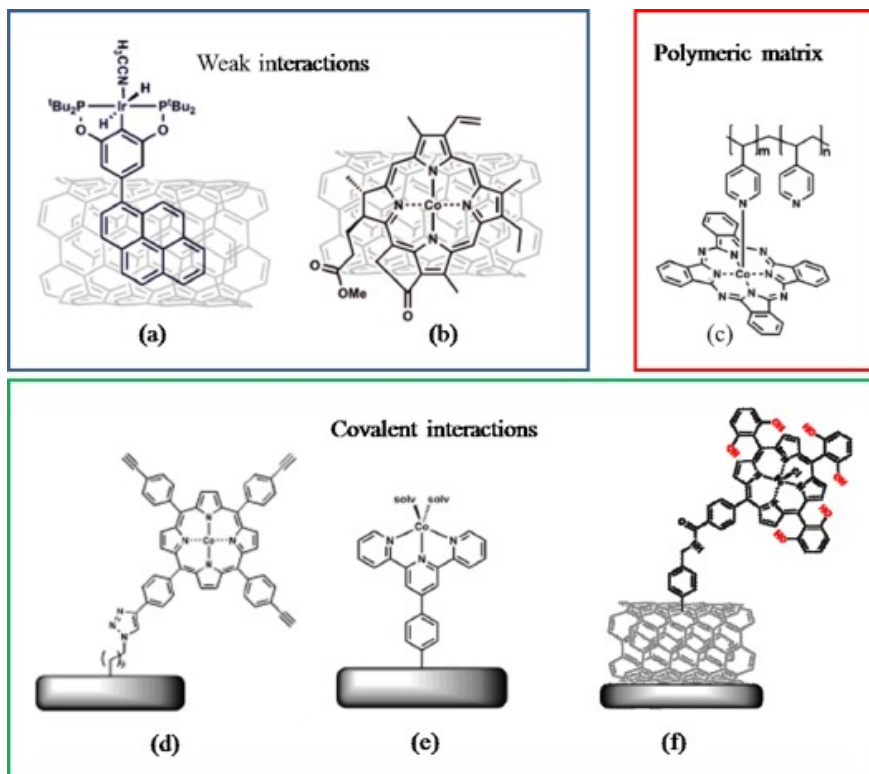


Figure 2. Examples of immobilization strategies of molecular catalysts on functional electrode surfaces. Figure reproduced with permission from ²⁴. Copyright 2017 Elsevier.

Despite the application-oriented nature of immobilized molecular catalysts in functional devices, and considering the nature of the work discussed in this Thesis, particular attention will be devoted to homogeneous systems. In these, the catalyst is present in solution and can reach the electrode surface by means of mass transport. The description of an electrocatalytic system depends on the physical and mathematical instruments necessary to define the experimental techniques chosen to perform such a study. In fact, electrochemical systems are theoretically described in terms of spatial composition profiles of the chemical species involved, as a function of the distance from the electrode surface, of its geometry and of the active modes of mass transport. The spatial region of interaction between the electrode and the catalyst is regardless confined in close vicinity to the electrode surface and is denoted as diffusion layer. In the presence of a substrate able to react with the active form of the catalyst generated at the electrode, a chemical reaction will accompany the Faradaic process at the level of the catalyst. Thus, homogeneous chemical transformations will occur in a region now denoted reaction-diffusion layer. The term refers to the spatial region in which electrochemical (interfacial) and chemical (solution) processes induce compositional changes of the solution with respect to the bulk (Figure 3). Catalyst and reactants access to the electrode and products release are the mass transport steps to be taken into account when formalizing a treatment of such systems, along with the homogeneous chemical reactions involved.³⁰⁻³⁵

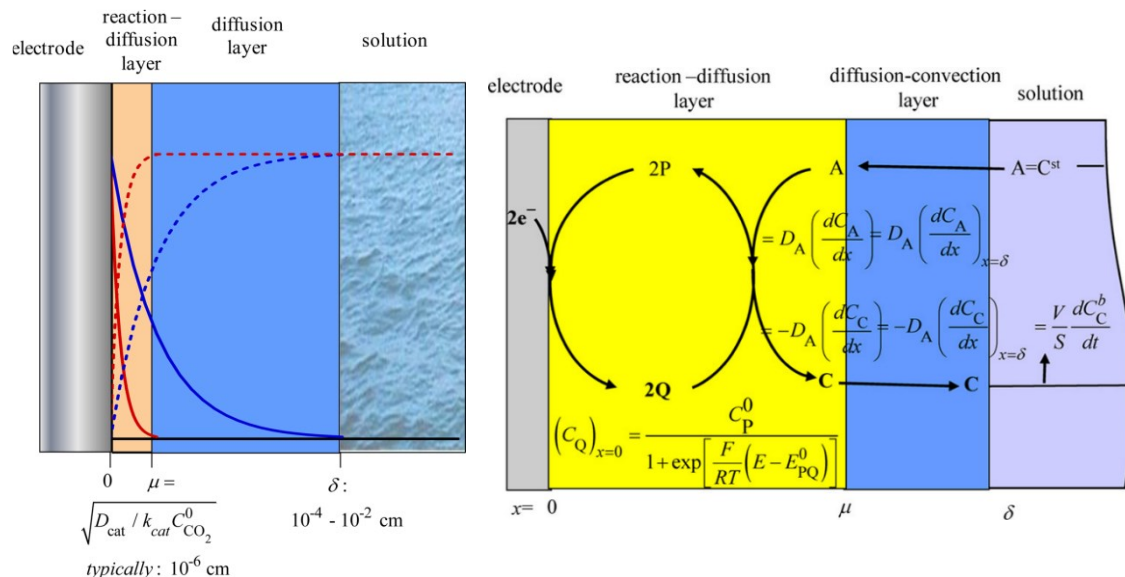


Figure 3. Left: schematic representation of the structure of the interphase between an electrode and a solution in the occurrence of an electrochemical reaction. Figure reproduced from with permission from ³⁵. Copyright 2015 American Chemical Society. Right: relevant mass transport and chemical reactions occurring in the different regions of the interphase, with respective equations. Figure reproduced with permission from ³³. Copyright 2012 American Chemical Society.

The brief introduction to the principles of electrochemical catalysis in homogeneous conditions is intended to highlight the intrinsically complicated nature of these processes. Regardless, electrochemistry provides a paramount advantage, since the tools used to drive electrochemical reactions allow to track them *in operando* by monitoring the temporal evolution of informative variables (current, potential, charge). Therefore, instrumental techniques carry the potential for extracting mechanistic information and benchmarking parameters *while* performing reactions.

1.3 Catalyst benchmarking criteria

The properties required to characterize any catalyst in terms of performance (catalyst benchmarking) are:

i) Turnover Frequency (TOF), defined by Eq. 2 as the ratio between the derivative of the evolved molar amount of target product (n_p) with respect to time (t) (*i.e.*, the reaction rate) and the molar amount of *catalytically active sites* n_{cat} .

$$TOF = \frac{dn_p(t)/dt}{n_{cat}} \quad (\text{Eq. 2})$$

These latter, in the case of a molecular electrocatalyst, correspond to the number of catalyst molecules at the interphase with the electrode surface, *i.e.*, the active catalyst molecules (*vide infra*).

ii) Turnover number, operatively defined as the ratio between the molar amount of a product and the molar amount of (active) catalyst, according to Eq. 3:

$$TON \approx \frac{n_p(t)}{n_{cat}} \quad (\text{Eq. 3})$$

Eq. 3 is linear in the regime of stable catalytic activity, *i.e.* of constant TOF, and usually levels to a *plateau* when the system suffers from processes determining its activity to diminish over reaction time. A useful parameter to be introduced is TON_{lim} , the maximum value of TON achievable before system deactivation.

iii) Chemical selectivity (CS), defined as the ratio between the molar amount of target products and the total molar amount of products, Eq. 4:

$$CS = \frac{n_p}{\sum_i n_i} \quad (\text{Eq. 4})$$

iv) In the field of electrocatalysis, a further key benchmarking parameter is the Faradaic efficiency (FE), or Faradaic yield (FY). This is defined by Eq. 5 as:

$$FE = \frac{n_e n_p}{[Q_{tot}/F]} \quad (\text{Eq. 5})$$

where Q_{tot} the total charge passed through the system, n_e is the number of electrons involved in the target reaction and F the Faraday constant (96485 Cmol⁻¹). The equation can be intended as the overall conversion of the charge passing through the system into the target product of the reaction. Values lower than the theoretical maximum are indicative of side-reactions that can lead also to abatement of chemical selectivity (such as the HER as parasite reaction towards CO₂ reduction) and/or to decomposition of the catalyst. In fact, Faradaic efficiency may be regarded as the *electrochemical* selectivity of the desired Faradaic reaction, with respect to the overall processes occurring in the system.

v) Overpotential (η), already defined as the difference between the potential applied to a working electrode to drive the catalytic reaction and the standard potential associated to the conversion of the substrate into the target product. As will be elucidated in Paragraph 1.4.1, molecular catalysts are characterized by well-defined relationships between their TOF and η . For this reason, meaningful catalyst benchmarking relies on considering *both* parameters. An oftentimes useful convention consists in providing the η value at the standard potential of the active form of the catalyst (E^0_{cat}), or at the specific potential applied in single experiments.

vi) Onset potential (E_{onset}). The elusive concept of onset potential for a catalytic reaction is hereafter introduced. Indeed, several definitions have been formulated for E_{onset} , two operatively useful being:

- a) The potential at which the current deviates from its baseline value *due to the insurgence of an electrocatalytic reaction*.³⁶
- b) The more positive (for cathodic processes) potential at which the targeted electrocatalytic reaction product is observable.^{36,37}

The onset potential is usually determined for benchmarking purposes, to provide the minimum overpotential value at which the catalyst is active. E_{onset} as per

criterion a) is easily obtained from voltammetric experiments. However, its definition is arbitrary, given that the increase of catalytic current can be erratic and depending on many parameters, including the operator choice. In the literature, a used internal convention substitutes E_{onset} for the overpotential at which a current density of 10 mAcm^{-2} is attained for rotating disk electrode voltammetry (RDV) experiments (at given scan rates and rotation speeds) as benchmarking parameter. Convention b) is supposed to afford a more reproducible determination of the minimum overpotential at which an electrocatalyst may be practically employed. However, determining trace products at the very foot of the catalytic wave can be experimentally demanding, requiring special techniques as on-line electrochemical mass spectrometry (OLEMS).³⁷

At any degree at which the discussion is to be sustained, it should be remarked that the use of E_{onset} as a benchmarking parameter for molecular catalysts has been heavily discouraged, given the lack of a formal derivation and a mechanistic significance of the onset of catalytic waves. Instead, the use of catalytic Tafel plots (*vide infra*) is to be preferred.³⁸

1.4.1 Cyclic voltammetry – Catalytic Tafel plots

The most widely used technique to characterize and evaluate electrocatalytic properties of molecular compounds is cyclic voltammetry, a non-destructive transient method operating under diffusion constraints. A detailed description of the technique and of its theoretical foundations is beyond the scope of the present thesis and may be found in specialized books. However, elucidating the principles of cyclic voltammetry applied to molecular catalysis of electrochemical reactions is beneficial for the subsequent discussion. In this context, the most important parameters used in the present Chapter are hereafter summarized in Table 2 for the sake of clarity^{11,12,39}.

In the presence of a catalytic reaction, the current response associated with the catalyst transitions from a usually reversible or quasi-reversible one-electron

redox couple to an irreversible, multi-electron wave. This is the resulting effect of turnover occurring in the diffusion-reaction layer when the active form of the catalyst is generated at the electrode. From the shape of the wave and the potential and current associated with it, it is possible to derive thermodynamic and kinetic information about the catalyst, specifically its operational overpotential and the rate constant for the catalytic process (k_{cat}). Systematic experimental studies of a catalyst can be performed by acting on substrate and catalyst concentration and scan rate, this latter defining the time domain of the voltammetric experiment.

Parameter	Definition	Dimensions
R	Gas constant	$8.314 \text{ JK}^{-1}\text{mol}^{-1}$
F	Faraday constant	96485 Cmol^{-1}
C^0	Analytical concentration of a species	molcm^{-3}
ν	Scan rate of a voltammetric experiment	Vs^{-1}
i	Current	A
i_{pl}	Plateau current of purely kinetic catalytic wave	A
i_{p}^0	Peak current in the absence of catalysis	A
A	Electrode area	cm^2
D	Diffusion coefficient of a species	cm^2s^{-1}
E	Potential	V
E^0	Standard potential	V
η	Overpotential	V
k_{cat}	Rate constant for the catalytic process	s^{-1}
γ	Excess factor	
λ	Kinetic parameter	
TOF	Turnover Frequency	s^{-1}
TOF_{max}	Maximum Turnover Frequency	s^{-1}
TOF_0	Turnover Frequency at $\eta = 0$	s^{-1}

Table 2. Summary of key parameters used in relevant equations in Chapter 1.4.

Theoretical treatment of the voltammetric response in electrocatalytic systems has been elaborated by Savéant and co-workers for simple catalytic mechanisms, involving one-electron transformations of the substrate (S) to generate a product (P) in one step (Eq. 6a-b)^{32,39,40}:



The mechanistic picture indicated by Eq. 6a and Eq. 6b is usually indicated as EC', where E and C stand for an electrochemical and a chemical step, respectively. Incidentally, the mechanism and its theoretical description provided herein refer to cathodic processes. This has resulted in the formal description of the possible shapes of catalytic waves, of the causes underlying the response, and of the quantitative kinetic and thermodynamic parameters obtainable in each case. The collective representation of the catalytic waves has been proposed in terms of a zone diagram, defined as a function of two parameters:

i) the kinetic parameter λ (Eq. 7),

$$\lambda = \left(\frac{RT}{F}\right) \left(\frac{k_{cat} C_{cat}^0}{v}\right) \quad (\text{Eq. 7})$$

ii) the excess factor γ , *i.e.* the ratio between the initial concentration of the substrate and of the catalyst (Eq. 8).

$$\gamma = C_S^0 / C_{cat}^0 \quad (\text{Eq. 8})$$

By acting on the two parameters, *i.e.* by modifying the scan rate v and the concentrations, it is possible to navigate the diagram, transitioning from one regime to the other. Each zone represents a family of catalytic curves that would deserve an individual discussion, as could be found in detailed publications. It should be noted *en passant* that, albeit escaping a readily available mathematical description, the experimental reconstruction of zone diagrams was achieved by

Dempsey and co-workers for the hydrogen evolution reaction catalyzed by a Co complex, involving an overall two-electron transformation with formation of hydride intermediates.

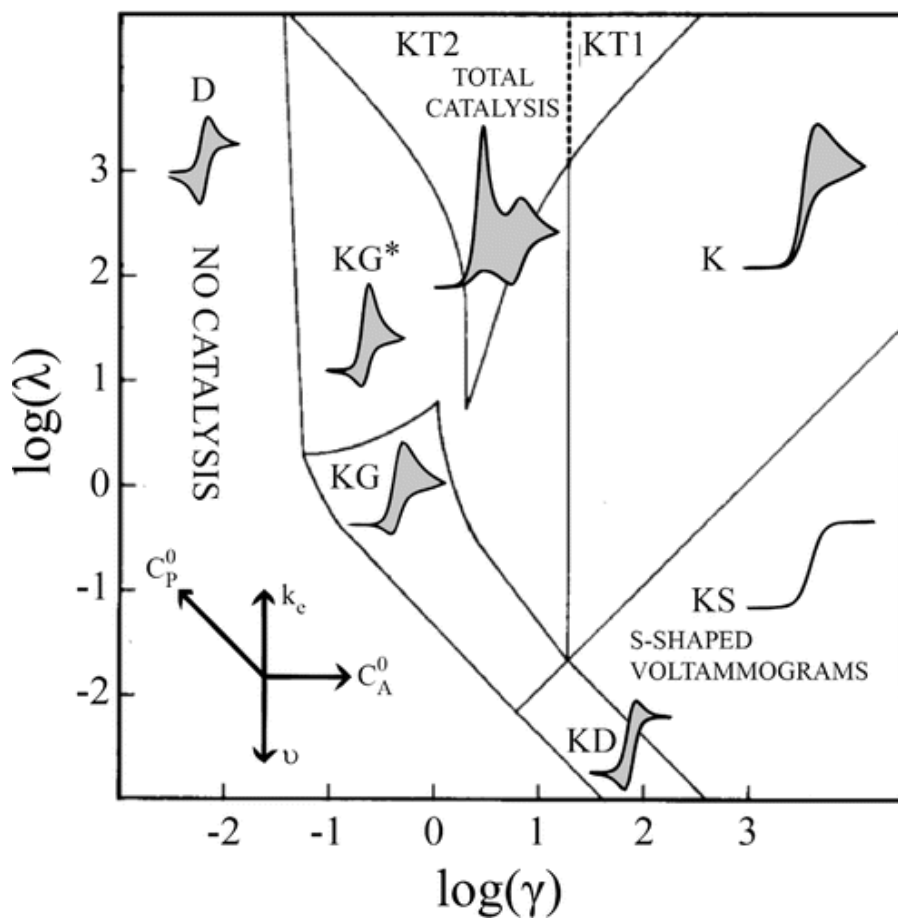


Figure 4. Kinetic zone diagram with simulated CV waveforms for the catalytic mechanism described by Eq. 6a and Eq. 6b. Figure adapted with permission from ⁴⁰. Copyright 1984 Elsevier. Simulated CV waveforms were added by Dempsey and co-workers, from ¹². The figure was reproduced with permission, Copyright 2014 American Chemical Society.

When the reaction occurs unhampered by mass transport of the reactants into the reaction-diffusion layer, a scan rate-independent sigmoidal wave is obtained. Such waves, pertaining to the pure kinetic conditions regime, can be exactly described by Eq. 9:

$$i = \frac{FAC_{cat}^0 \sqrt{D_{cat}} \sqrt{2k_{cat}C_S^0}}{1 + \exp\left[\frac{F}{RT}(E - E_{cat}^0)\right]} \quad (\text{Eq. 9})$$

Where A is the electrode area, D_{cat} the diffusion coefficient of the catalyst and E the applied potential; the other variables have been defined above. A *plateau* current is attained for potentials more negative than E_{cat}^0 . From the *plateau* current value (i_{pl}), k_{cat} is directly obtainable, Eq. 10:

$$i_{pl} = FAC_{cat}^0 \sqrt{D_{cat}} \sqrt{2k_{cat}C_S^0} \quad (\text{Eq. 10})$$

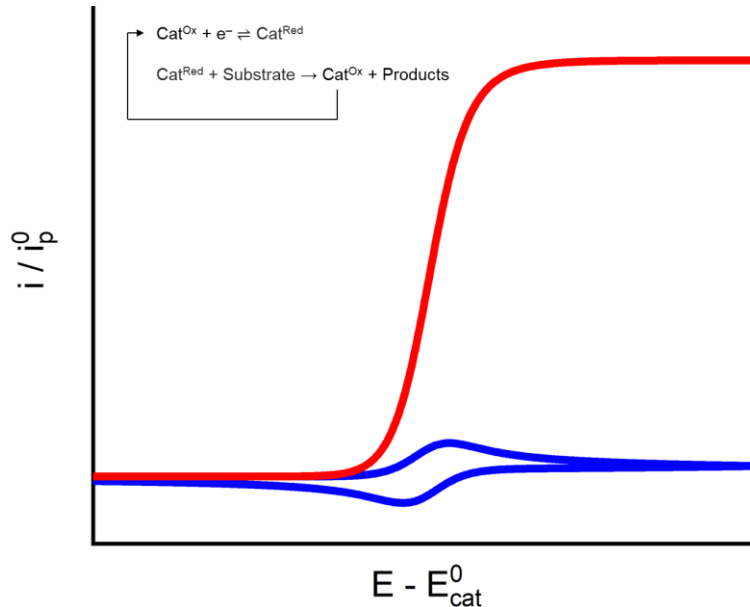


Figure 5. Simulated CV traces for a catalyst in the absence of catalysis (the reversible couple is observed, blue trace) and for a pure kinetic catalytic regime (red trace).

To simplify data treatment and avoid independently determining the electrochemical area of the electrode and D_{cat} , Eq. 11 can be divided by the Randles-Sevcik equation, valid for the peak current of the catalyst reversible couple in the absence of substrate (i_p^0).

$$i_p^0 = 0.446C_{cat}^0FA\sqrt{D_{cat}}\sqrt{Fv/RT} \quad (\text{Eq. 11})$$

Alternatively, the voltammogram can be linearized by plotting i/i_p^0 as a function of the potential-dependent function, $1 / \{1 + \exp[F / RT(E - E_{cat}^0)]\}$. From the slope of the straight line, the same kinetic information is obtainable.

Savéant and co-workers have derived a key relationship between an intrinsic property of the catalyst (TOF) and the applied potential E , Eq. 12:

$$TOF = \frac{2k_{cat}C_S^0}{1 + \exp\left[\frac{F}{RT}(E - E_{cat}^0)\right]} = \frac{2k_{cat}C_S^0}{1 + \exp\left[\frac{F}{RT}(E_{S/P}^0 - E_{cat}^0 - \eta)\right]} \quad (\text{Eq. 12})$$

It can be immediately recognized that the TOF- η relation shows the same functional dependency on the applied potential as the pure kinetic catalytic voltammogram. Therefore, it is possible to directly extract benchmarking parameters from the voltammetric response in the case of the scan-rate independent, S-shaped catalytic waves.

The TOF- η relationship can be formulated to explicitly indicate a Tafel-like dependency as Eq. 13:

$$\log(TOF) = \log(2k_{cat}C_S^0) - \frac{F}{RT\ln(10)}(E_{S/P}^0 - E_{cat}^0) - \frac{F}{RT\ln(10)}\eta \quad (\text{Eq. 13})$$

Eq. 13 provides the complete description of a catalyst's TOF as a function of the overpotential, in turn controllable by the operator. It should be remarked that the formulated expression of TOF is valid regardless from electrode or cell geometry, indeed allowing to work with easily determined quantities and avoiding estimating

the number of active catalyst molecules in the reaction-diffusion layer. The two key parameters that may be found in a catalytic Tafel plot are TOF_0 and TOF_{max} . The former represents the intrinsic catalytic activity of a catalyst, *i.e.*, the TOF at zero overpotential (Eq. 14):

$$\log(TOF_0) = \log(2k_{cat}C_S^0) - \frac{F}{RT\ln(10)}(E_{S/P}^0 - E_{cat}^0) \quad (\text{Eq. 14})$$

TOF_{max} may be directly obtained by knowing k_{cat} and the specific mechanism analyzed. For the mechanism sketched in Equations 6a and 6b, it is derived as per Eq. 15:

$$TOF_{max} = 2k_{cat}C_S^0 \quad (\text{Eq. 15})$$

Therefore, Eq. 12 may be reformulated as:

$$TOF = \frac{TOF_{max}}{1 + \exp\left[\frac{F}{RT}(E_{S/P}^0 - E_{cat}^0 - \eta)\right]} \quad (\text{Eq. 16})$$

Incidentally, Eq. 16 represents a mechanism-independent TOF- η relationship.

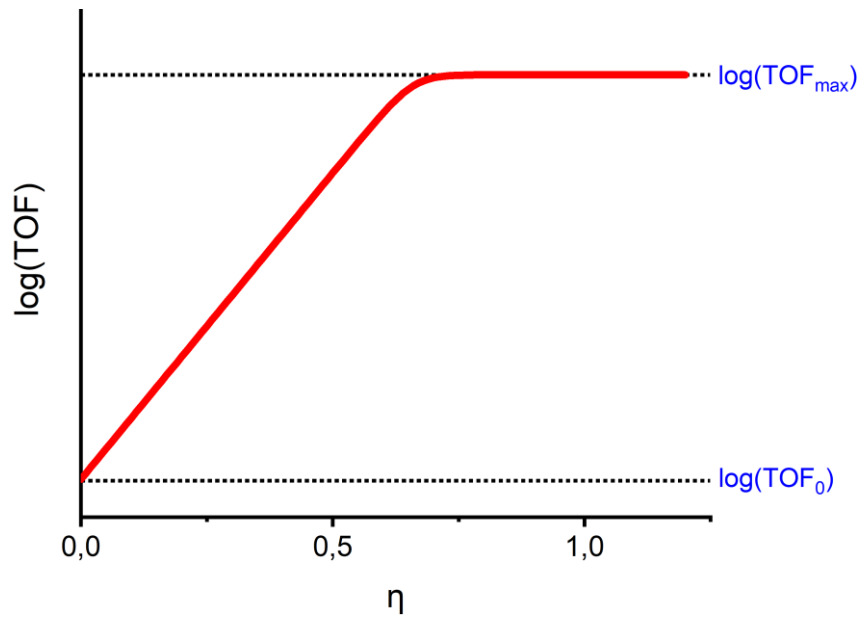


Figure 6. Example of a catalytic Tafel plot, constructed following Eq. 13.

The function provided has been derived under the assumption that the kinetics of electron transfer between the electrode and the catalyst are fast. It may be adapted to account for slower kinetics of electron transfer (Eq. 17), by considering the value of the electron transfer standard rate constant (k_e^{cat})⁴¹.

$$\frac{1}{TOF} = \frac{\exp[-(F/RT)\eta]}{TOF_0} + \frac{2\sqrt{2D_{cat}} \exp\left[-\frac{(F/RT)\eta}{2}\right]}{k_e^{\text{cat}}} + \frac{\exp[-(F/RT)(E_{S/P}^0 - E_{cat}^0)]}{TOF_0} \quad (\text{Eq. 17})$$

Additionally, as mentioned in the case of zone diagrams, extension of this treatise to multi-electron, multi-substrate transformations is more demanding.⁴² It has however been proven by Costentin and Savéant that it is possible to extend the approach also to catalytic reactions of the latter kind.⁴³ For a catalytic process consisting of a combination of two electrochemical events and two homogeneous

chemical steps (each characterized by a kinetic constant k) with more than one substrate, a general representation of the valid expression of TOF is Eq. 18:

$$TOF = \frac{f(k_1, k_2, C_j^0)}{1 + \exp \left[1 - \exp \left[\frac{F}{RT} (E - E_{cat}^0) \right] \right]} \quad (\text{Eq. 18})$$

This treatment is pertaining to common schemes of molecular catalysis of CO_2 or proton reduction, involving multiple intermediates.

The so-called catalytic Tafel plots represent the most powerful instrument to describe and benchmark molecular electrocatalysts. The key parameters obtainable from a catalytic Tafel plot are TOF_0 , the TOF value at zero overpotential, and TOF_{max} , the maximum TOF achievable by a catalytic system deprived of side-effects. In the scope of catalyst optimization, catalytic Tafel plots clearly demonstrate how to envision competitive new catalysts displaying high TOF values at low overpotentials.

1.4.2 Cyclic voltammograms hampered by side-phenomena – Foot of the wave analysis

Experimental voltammograms associated to catalytic processes often display peak-shaped waves, instead of the ideal S-shaped ones. These can be ascribed to the influence of side-phenomena, such as:³³

- i) Consumption of the substrate at the interphase with the electrode, needing replenishing *via* substrate diffusion.
- ii) Inhibition by the products of the reaction, such as gas bubbles shielding the electrode surface from the electrolytic solution.
- iii) Catalyst decomposition to inert species, or catalyst poisoning by the products (e.g., irreversible binding of CO to metal complexes).

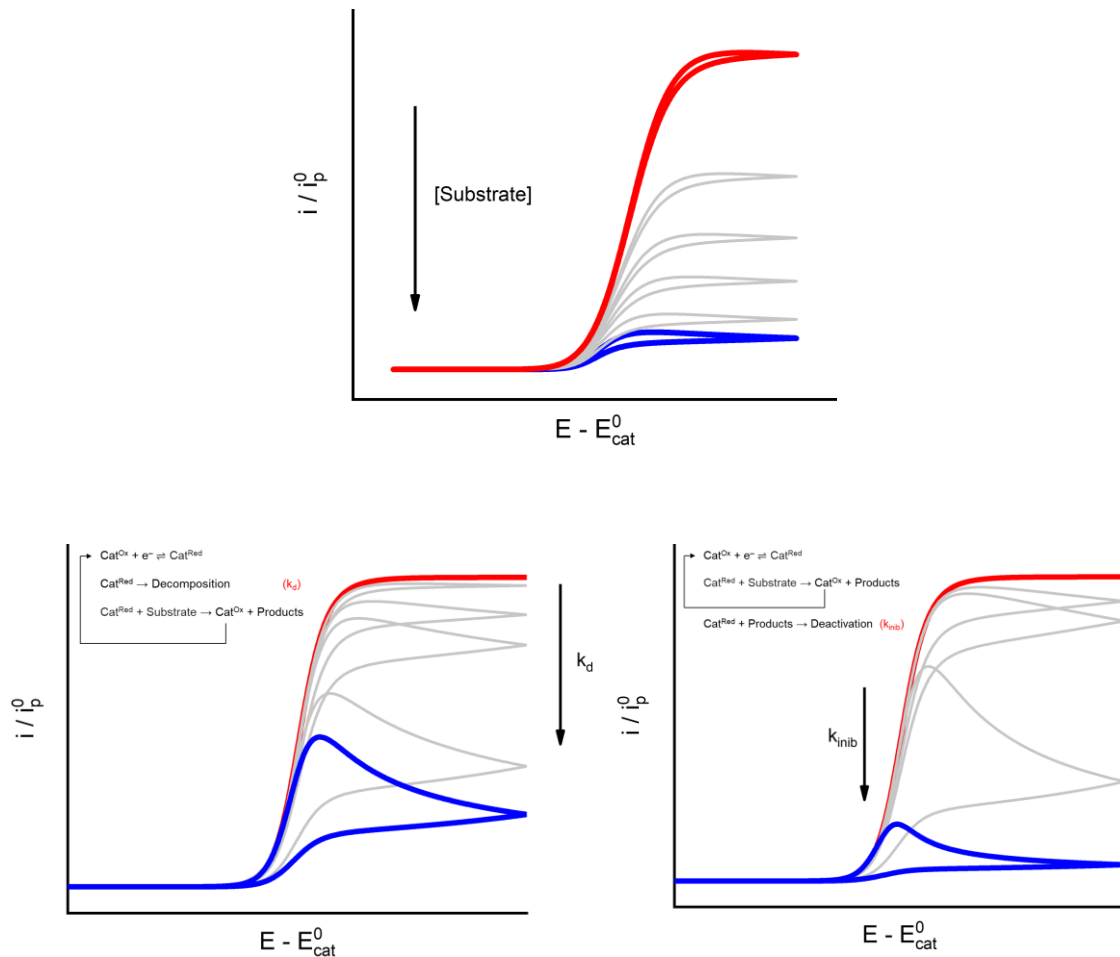


Figure 7. Simulated CV traces for a catalytic EC' mechanism as a function of decreasing substrate concentration (top), of increasing catalyst decomposition rate constant (bottom left), and of increasing rate constant for inhibition by product.

Of these, only substrate consumption was originally considered in Savéant's treatise, (corresponding to the K zone in the diagram)⁴⁰, formulated for a one-electron, one-chemical step mechanism not including catalyst decomposition or electrode fouling. These other effects have been formally treated in later works.^{44,45} For the three possible causes, the observation of a peak-shaped catalytic wave can be physically interpreted as the system not being able to sustain the expected catalytic current as the entity of the side phenomena increases with catalysis at higher η values.

The most immediate strategy to analyze K-type voltammograms is acting on the kinetic parameter, and therefore on the scan rate. By raising v , catalytic turnover and all the associated chemical processes are contrasted by the fast timescale of the voltammetric experiment. When the extent to which the catalytic process modifies the composition of the reaction-diffusion layer is decreased, also the influence of side-phenomena is less severe. As a result, by considering substrate consumption, raising the scan rate could in principle result in a transition from the K zone to the pure kinetic conditions, as evident in Figure 8. In fact, the Faradaic charge passing through the system per unit time is lower when the scan rate of the CV is brought to higher values. Such statement may be more easily visualized by considering the CV traces in which the current is normalized by the scan rate: catalytic waves registered at higher scan rates display *lower* normalized current (Figure 8). Similar considerations are valid for inhibition by the products or catalyst self-deactivation. However, experimental systems do not often reach a proper S-shaped wave, but rather approach a scan rate-independent response not displaying a definite *plateau*. As an example, Figure 8 reports the CV traces relative to Fe tetraphenylporphyrin Fe(TPP), a state-of-the-art molecular catalyst for CO₂-to-CO reduction in DMF (*vide infra*), at increasing scan rate values.

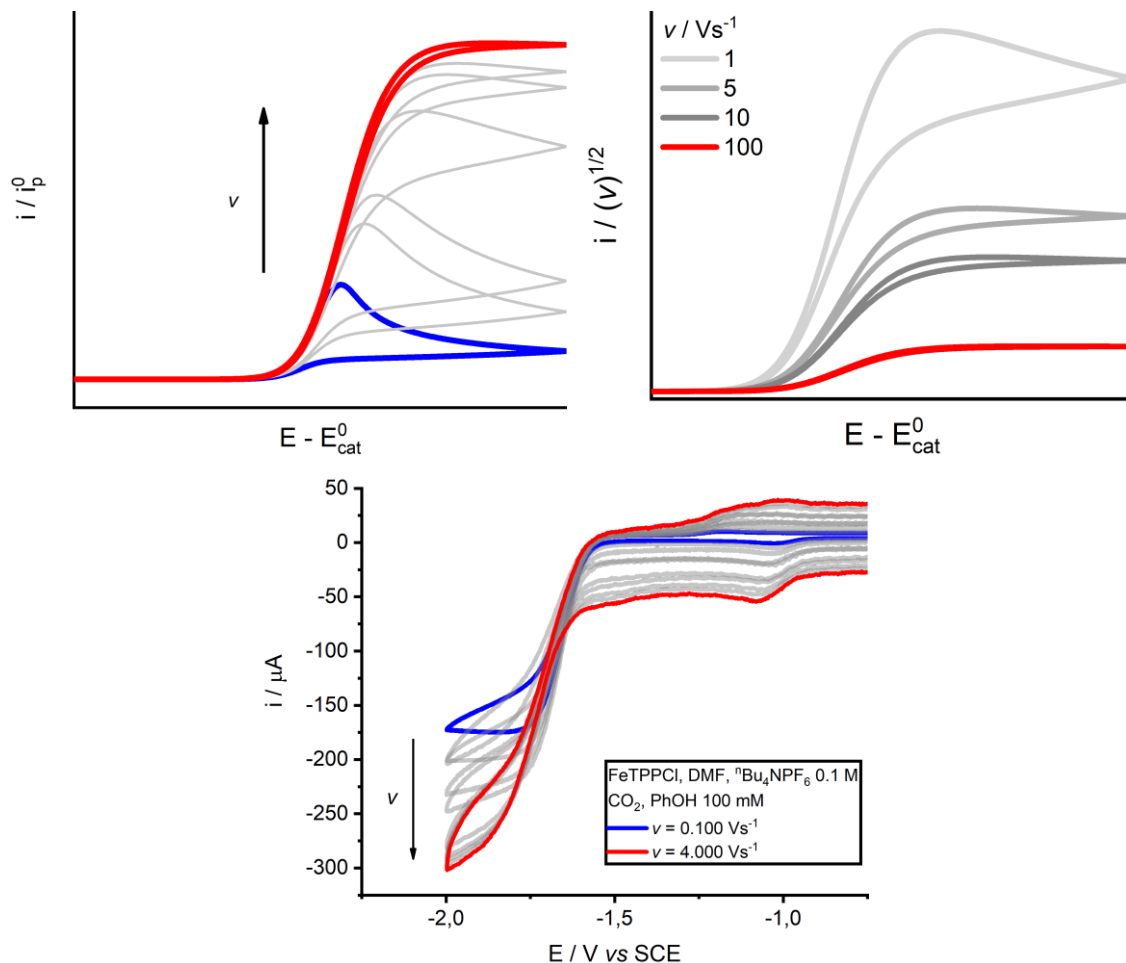


Figure 8. Top right: simulated CV traces for an EC' catalytic mechanism in the presence of substrate consumption, as a function of increasing scan rate. Top left: simulated CV traces for the same system, reported against the normalized current. Bottom: experimental CV traces relative to 1 mM Fe(TPP) in DMF, in the presence of 0.1 M phenol and 0.1 M tetrabutylammonium hexafluorophosphate.

It is also possible to act on the excess factor. Indeed, by decreasing γ , it would be possible in principle to transition from the K zone to the KT2 regime, labeled as “total catalysis conditions”. Voltammograms of the KT2 family arise when fast catalysis completely exhausts the substrate in the reaction-diffusion layer and are the only other immediately treatable curves.⁴⁶ The waveforms display a peak-shaped irreversible feature, corresponding to a catalytic wave rapidly decaying as the substrate is completely depleted, followed by the reversible couple of the

catalyst. The irreversible peak potential can be expressed through an explicit function, described by Eq. 19:

$$E_{cat}^p = E_{1/2}^{cat} - 0.409 \frac{RT}{F} + \frac{RT}{2F} \ln \left[\frac{RT k_{cat} (C_{cat}^0)^2}{C_S^0 v} \right] \quad (\text{Eq. 19})$$

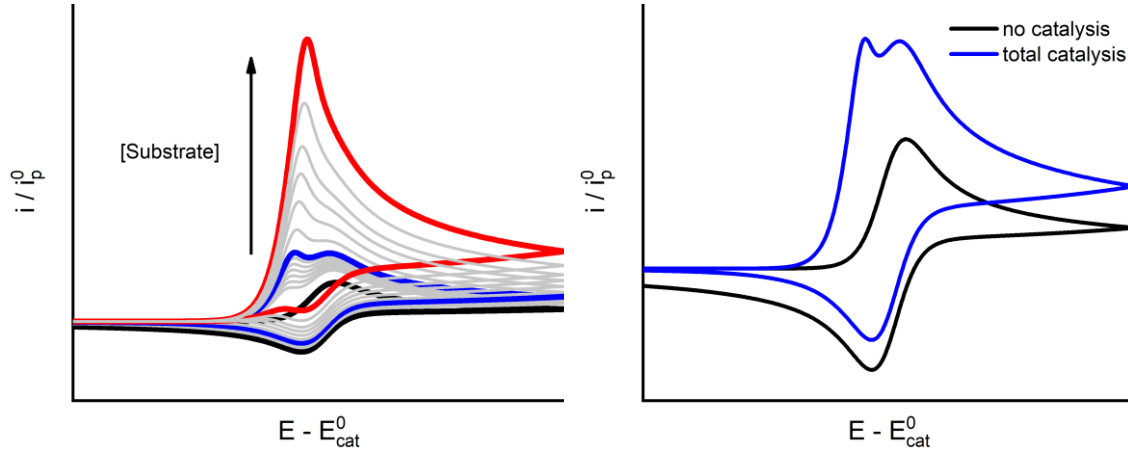


Figure 9. Left: simulated CV traces for an EC' mechanism as a function of substrate concentration to highlight the transition from the KT2 to the K regime. Right: simulated CV traces for the same EC' mechanism, in the absence of catalysis (black trace) and for the total catalysis (KT2) regime.

Therefore, k_{cat} may be directly obtained from the position of the catalytic peak. However, cases whereupon a transition to the total catalysis waveform is achievable are not common.

A method often employed in the literature to analyze K-type waves consists in treating the peak-shaped catalytic wave as a pure kinetic trace, approximating its peak current value (i_{cat}^0) to the limiting i_{pl} observed in the former case (Eq. 20).^{11,47,48}

$$\frac{i_p^{cat}}{i_p^0} \approx 2.24 \sqrt{\frac{\frac{RT}{F} 2k_{cat} C_S^0}{Fv}} \quad (\text{Eq. 20})$$

This rather drastic assumption has been demonstrated to result in an underestimation of k_{cat} and TOF values.¹¹

A more sophisticated approach involves recording catalytic voltammograms upon systematically varying the excess factor γ , and subsequently computing families of working curves to obtain λ , exemplified by Eq. 21:^{46,49}

$$\frac{i_p^{\text{cat}}}{i_p^0} = f[\log(\lambda)]_\gamma \quad (\text{Eq. 21})$$

Albeit accurate and substantiated by a vast set of experimental data, this strategy is experimentally and computationally demanding. Furthermore, it has been restricted to one-electron catalytic reactions, such as alkyl halide activation by Cu^I complexes.^{46,49}

Nonetheless, as may be appreciated from Figure 7, when deviation from the expected pure kinetic regime is not too severe, the foot of the peak-shaped catalytic waves overlaps with the initial trait of the S-shaped pure kinetic CV trace. Indeed, kinetic information is retained in the catalytic voltammograms and can be extracted by interrogating the experimental response in the potential range not strongly affected by side phenomena. This represents the core of the foot-of-the-wave-analysis (FOWA), presented by Costentin *et al.* in 2012.³³ Attempting the linearization procedure valid for Eq. 9 results in a function retaining a linear trend for values of $1 / \{1 + \exp[F / RT(E - E_{\text{cat}}^0)]\}$ close to zero, and deviating from linearity as the severity of the side phenomena impacts on the voltammogram (Figure 10). Nonetheless, the slope of the initial linear trait of the current function can be used to ultimately derive the TOF of the catalytic process, purged of the effect of side-processes. Furthermore, the FOWA approach was theoretically studied and validated also for 2-electron transformations such as CO₂-to-CO reduction. FOWA has indeed been recognized as the most versatile and affordable strategy to obtain kinetic information from peak-shaped catalytic waves.

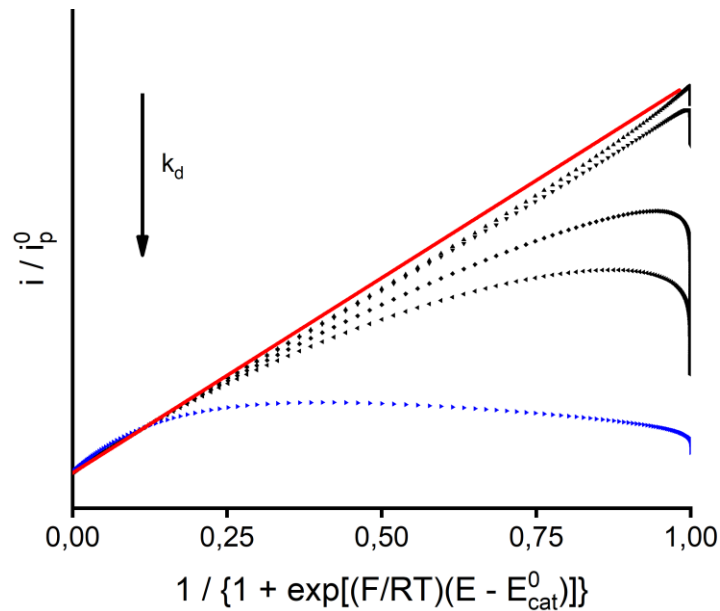


Figure 10. Foot-of-the-wave-analysis plot, relative to the simulated CV traces in Figure 7 (bottom left).

Regarding experimental data treatment to perform the FOWA, the best procedure would involve minimizing the effect of side-phenomena by increasing the scan rate. Indeed, FOWA allows to safely treat data referred to scan rate-independent, non-sigmoidal catalytic waves (*vide supra*).

1.4.3 Cyclic voltammetry of complicated catalytic systems

The last remarks about cyclic voltammetry as a diagnostic tool in catalysis regard the study of systems characterized by complicated reaction mechanisms. Indeed, cyclic voltammograms can provide evidence of intermediates accumulating in the reaction-diffusion layer that are detectable on the return scan, such as inert metal carbonyls from which CO is slowly released. Other common cases involve an irreversible reaction of the catalyst with the substrate producing an intermediate that requires further activation at the electrode to achieve turnover: when some low valent metal complexes react with CO₂, metal-CO₂ adducts can form that must be further reduced to generate CO₂ reduction products.

Further information derivable from CV measurements involves catalysts undergoing decomposition in operational conditions. Detecting transformations of a molecular catalyst to either inactive or active heterogeneous species relies on the occurrence of such phenomena on the timescale of the electrochemical experiment. Despite qualitative, the evidence can be extremely powerful in discriminating between a real homogeneous regime and a system in which the molecular species acts as a precursor of a heterogeneous catalyst on the electrode surface. Examples of such indicative features are pre-waves found at overpotentials lower than the catalytic onset, attributable to catalyst adsorption; curve crossing (*i.e.*, crossing of the forward and return scans in a CV), possibly due to electrode modification (Figure 11); stripping peaks on the return scan, associated with desorption of adsorbed material. Indeed, ascertaining the nature of these observations is crucial in determining the molecular nature of catalysis.^{50,51}

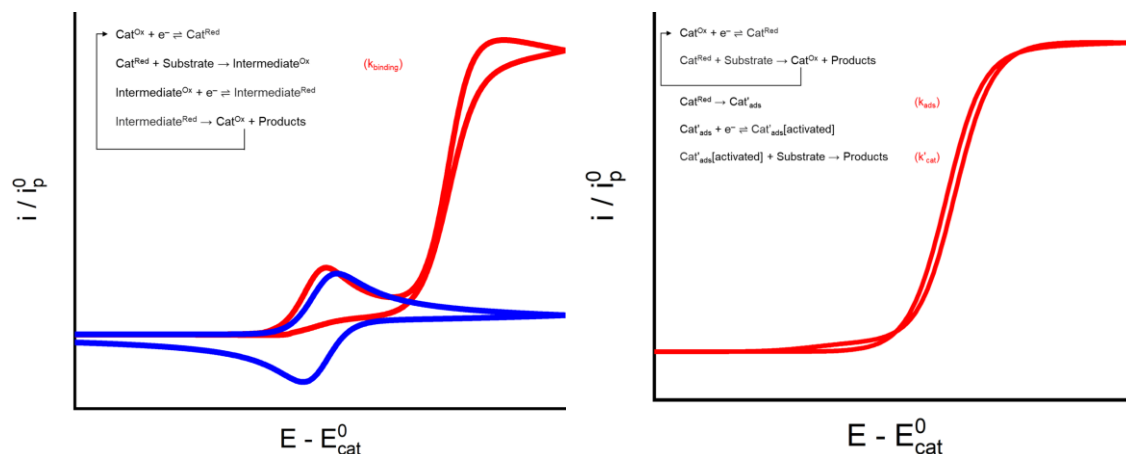


Figure 11. Left: simulated CV traces of a catalyst in the absence (blue trace) and in the presence (red trace) of a substrate with which an intermediate requiring further reduction to trigger catalysis. Right: simulated CV trace of a catalyst undergoing modification to a catalytically active adsorbed species, producing curve crossing.

For the analysis of any complex electrochemical system by means of cyclic voltammetry, the paramount systematic study involves performing experiments by varying the scan rate and the explored potential range. Additionally, it is possible to act on the temperature, when thermostated cells are available: formation of intermediates generally responds to variations in temperature, thus producing measurable differences in the voltammetric profile. Lastly, key studies involve “rinse tests”, used to ascertain whether the electrochemical reactions lead to formation of catalytically active deposits on the working electrode. These studies consist in examining the electrochemical response of the working electrode in the absence of the catalyst *after* employing it in its presence. However, in many cases the outcome of “rinse tests” in CV studies is not sufficiently informative if not integrated by surface analysis of the electrode after catalysis. By definition, this latter approach is more easily accessed when working in preparative-scale conditions (*vide infra*).^{50,52–55}

1.5 Simulation of electrochemical experiments

Software packages for simulating the outcome of electrochemical experiments, especially cyclic voltammetry, have been used for a long time. Their power consists in allowing to produce digital traces to be compared to experimental data or to fit these latter.^{56,57} The ultimate purpose of simulating cyclic voltammograms lies in the interpretation of complex electrochemical mechanisms or in aiding kinetic and thermodynamic data determination (*vide supra*). While detailed descriptions of the methodologies for building a simulation software are available in the literature, commercially available optimized packages are nowadays employed. The use of simulations, however, is not to be intended as a substitute for careful and exhaustive experimental work. Faithful matching of simulated to experimental data must be pursued especially when basic parameters, *i.e.*, scan rate, concentrations, *etc.* are varied over a wide range of accessible values. For these reasons, simulation must be undertaken with great care and not relied upon

a priori. Throughout the present manuscript, the use of simulations has been restricted and has mainly been applied for illustrative purposes.

1.6 Constant potential electrolysis (CPE)

Preparative scale electrocatalytic reactions are conducted in chronoamperometric conditions, *i.e.*, by applying a constant potential at the working electrode to produce the active form of the catalyst. Experiments are run under forced convection regime, by either rotating the working electrode or stirring the electrolytic solution. The outcome of the electrocatalytic reactions can be determined by detecting the amount of products generated during electrolysis. Detection of reaction products is performed by chromatography (in the liquid and gas phase), NMR, and/or dedicated probes such as Clark sensors for H₂ or O₂, or optical probes for O₂ evolution. Depending on the methods chosen, reaction products can be detected by on-line monitoring or by *ex situ* sampling of the electrolytic cell. Incidentally, to increase the electrolysis current, thus achieving a faster passage of charge, higher surface area working electrodes are usually employed than in CV experiments.

Additionally, precious information may be obtained from the current-time profile (*i.e.*, the hydrodynamic chronoamperogram). When the catalytic system is stable, thus operating in constant TOF regime, a constant electrolysis current is expected. From this, k_{cat} (and therefore TOF) derivation is straightforward, determined at the electrolysis potential $E_{electrolysis}$ by means of Eq. 22:^{32,58}

$$i = \frac{FA\sqrt{2k_{cat}C_S^0C_{cat}^0}}{1 + \exp\left[\frac{F}{RT}(E_{electrolysis} - E_{cat}^0)\right]} \quad (\text{Eq. 22})$$

A $\log(TOF)$ value obtained *via* Eq. 22 at a specific electrolysis potential should correspond to a single point on the catalytic Tafel plot curve. It is useful to compare this value to the one deriving from quantification of the reaction products (Eq. 2). For an ideal catalytic system (*i.e.*, not undergoing any deactivation), the

three TOF values obtained, namely from kinetic analysis of CV traces, from analysis of the current trace of electrolysis, and from the amount of products obtained from such bulk reaction, should be equal.

Given the extent of the reaction in bulk electrolysis, the current trace can easily undergo perturbation by side-phenomena. Indeed, electrode surface modifications or catalyst irreversible transformations can impact on the current trace and be detected. Specifically, catalyst deactivation may be recognized from a current decrease over electrolysis time. Catalyst transformation to an active deposit can instead result in an induction period followed by an increase in the electrolysis current, corresponding to the intervention of a more active catalytic species generated *in situ*. Interpretation of the current profiles should also be supported by “rinse tests”, by analyzing the electrode with surface techniques, and by mapping the chemical selectivity as a function of electrolysis time to provide a more complete description of the catalytic system.^{59,60}

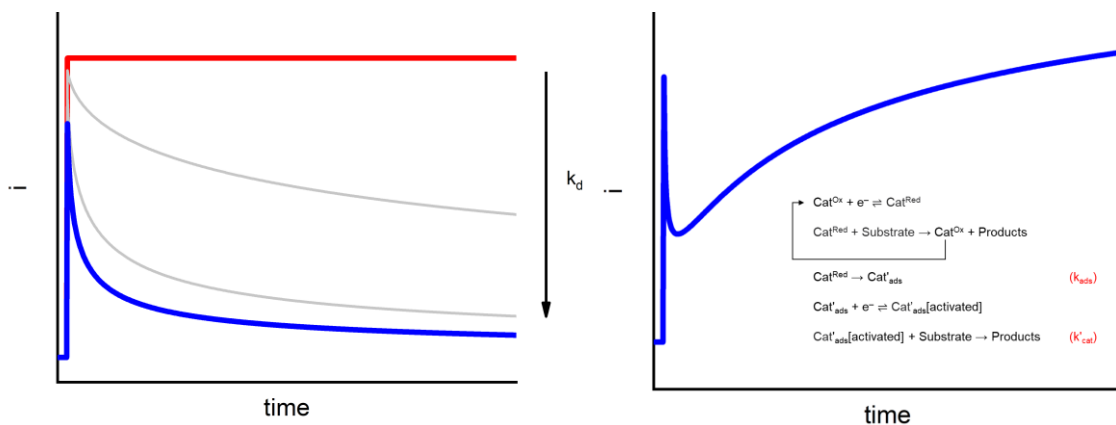


Figure 12. Left: simulated chronoamperograms of a catalyst involved in an EC' catalytic mechanism in the absence (red trace) and in the presence (blue trace) of catalyst deactivation processes. Right: simulated chronoamperometry of a catalyst undergoing modification to a catalytically active adsorbed species.

1.7 Spectroelectrochemistry (SEC)

Spectroelectrochemical methods involve the combination of spectroscopic and electrochemical techniques.^{11,61–68} Their nature allows to generate a reactive species at an electrode and contextually monitor the evolution of the spectral features of the electrolytic solution during the electrochemical transformations. The analysis may be performed *ex situ*, by operating a redox transformation in a coulometric cell and then transferring the analyte solution to an appropriate spectroscopic cell. Alternatively, SEC may be conducted *in situ*, in specialized cells that allow to drive the electrochemical reactions at the surface of a transparent electrode, constituted by a metal gauze (or mesh) or a transparent conductive oxide slide. Other sophisticated SEC cells allow to employ optical analysis in reflectance mode, thus avoiding the need for a transparent electrode. In all cases, the cell volume is minute, thus enabling complete electrolysis of the analyte contained in the thin layer in a short time (minute time scale). Usually, the spectral ranges explored are the UV-visible (UV/Vis) and the infrared (IR), although X-ray absorption (XAS) and electron paramagnetic resonance (EPR) may be employed. IR-SEC is particularly relevant in the field of CO₂ reduction catalysis, given the possibility to detect key intermediates such as metal-CO₂ and metal carbonyl intermediates (*vide infra*). It should be remarked, however, that the instrumental requirements of a SEC experiment may substantially differ from the conditions used in bulk electrolysis, mainly due to the choice of the transparent working electrode material. A common case involves the use of platinum gauzes, where H₂ evolution can interfere with the analysis in case of reductive conditions in the presence of proton donors. Therefore, if no true *operando* measurement is possible, the competence of intermediates identified by SEC should always be ascertained by independent experimental and/or computational analyses.

1.8 CO₂ reduction by iron complexes

In the field of homogeneous molecular catalysis for CO₂ reduction, research has been intensively focused on redox-active coordination complexes of transition metals. Seminal works have been directed towards the use of second and third row transition metals, while recently considerable efforts have been devoted to first row transition metals^{69,70}, with manganese^{14,71–76}, iron^{77–79}, cobalt^{69,80}, nickel^{81–84}, and copper^{85,86} being the preferred choice in the design and optimization of catalysts. Furthermore, previously unexplored chromium complexes have been recently reported as catalysts for CO₂ reduction, thus enriching the literature scenario.

A paramount role in the development of molecular catalysts for CO₂ reduction has been covered by iron complexes. Iron is the most abundant transition metal on Earth and its coordination chemistry is vast and may be bent to match several catalyst design requirements. Furthermore, the redox chemistry of iron in its coordination compounds is rich and allows for accessing several formal oxidation states and their peculiar reactivity.

Nature itself has developed iron-based enzymatic active sites which can evolve carbon monoxide from CO₂. The most notorious example is CO dehydrogenase (CODH) enzymes, found in *Carboxydotherrmus hydrogenoformans* and *Moorella Thermoacetica* microorganisms, whose catalytic activity relies on the presence of a polynuclear metallic cluster in which a [NiFe] CO₂ binding and activation site is coupled with an iron-sulfur cluster.^{87–90}

The enzyme was studied in electrochemical CO₂-to-CO reduction in aqueous phosphate buffer (pH 6.3), with methyl viologen acting as redox mediator. Incidentally, the use of single electron transfer redox mediators is often required when transferring redox enzymes to electrochemical systems, due to the slow interfacial electron transfer kinetics between the working electrode and redox-active proteins. Albeit the elaborate nature of the electrocatalytic system, CODH could be driven to catalyze CO₂ reduction to CO with quantitative Faradaic efficiency at almost null overpotential, reaching TOF of 700 h⁻¹. Later reports

demonstrated the possibility of using carbon electrodes modified with CODH in mediator-free conditions for reversible CO_2 reduction and CO oxidation, albeit without a dedicated focus on preparative electrocatalysis. Finally, White *et al.* reported the use of CODH for photocatalytic CO_2 -to-CO reduction in the presence of CdSe/CdS nanorods photosensitizers and an organic redox mediator.

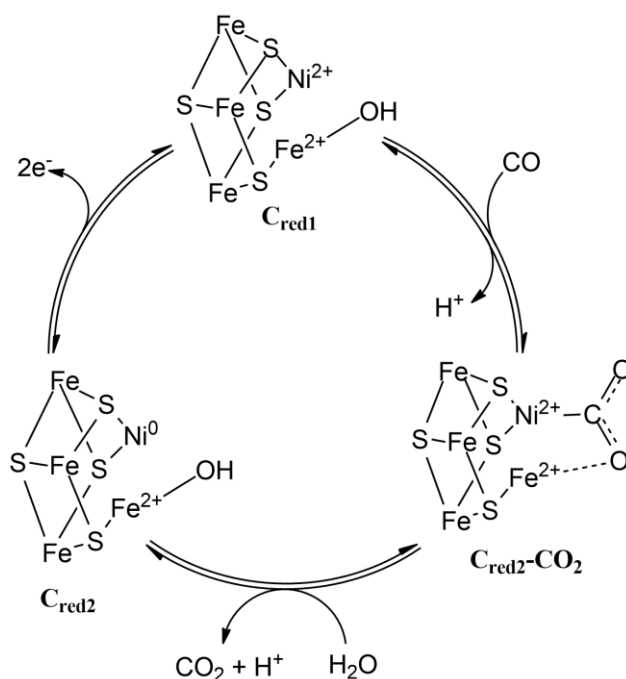


Figure 13. Catalytic cycle of the active site of CODH, involved in reversible conversion of CO_2 and CO. Figure reproduced with permission from ⁹⁰. Copyright 2003 American Chemical Society.

Most of the Fe-based catalysts for CO_2 reduction are mononuclear complexes, with iron porphyrins standing as the current benchmark of reactivity (Figure 14). This family of catalysts is highly selective for CO_2 -to-CO reduction, with Faradaic efficiency generally close to unity and reaching TOF_{max} values up to 10^6 s^{-1} at overpotentials as low as 220 mV (*vide infra*)⁹¹. Incidentally, albeit less active and stable, heme-type Fe complexes based on the corrole coordination motif (a close

relative of the porphyrin ring) have also been studied as catalysts for the electro- and photocatalytic reduction of CO₂ to CO.⁹²

During the last decade, several examples of non-heme iron complexes as competent catalysts for the electrochemical reduction of CO₂ have flourished, considerably enriching the literature scenario. The main products of Fe-catalyzed CO₂ reduction are the result of a 2-electron transformation, CO and HCOOH. Incidentally, higher reduction products are most often unattainable in electrochemical conditions, due to intrinsic constraints related to the experimental conditions, while it has been notably achieved in photocatalytic systems.

A notable family of Fe catalysts feature polydentate nitrogen based ligands, such as the N₅-macrocyclic 2,13-dimethyl-3,6,9,12,18-pentaazabicyclo-[12.3.1]octadeca-1(18),2,12,14,16-pentaene⁹³, the 2,2':6',2'':6'',2'''-quaterpyridine (qpy)^{58,94-97}, the N₆ ligand 2-4:6-8-bis(3,3,4,4-tetramethyldihydropyrrolo)-10-15-(2,2'-biquinazolino)-[15]-1,3,5,8,10,14-hexaene-1,3,7,9,11,14-N₆ (Mabiq)⁹⁸, and 6-(1,1-bis(pyridin-2-yl)ethyl)-2,2'-bipyridine (bpyPY2Me)⁹⁹. Secondly, examples that exploit 2-hydroxybenzene pendants on 1,10-phenanthroline or of 2,2'-bipyridine scaffolds thus producing a N₂O₂ coordination motif, 2,9-bis(2-hydroxyphenyl)-1,10-phenanthroline (H₂dophen)¹⁰⁰ and 6,6-di(3,5-di-tert-butyl-2-hydroxybenzene)-2,2'-bipyridine (t^{bu}dhbpy)¹⁰¹, have been reported to catalyze the reduction of CO₂ to a mixture of products, formate being the main one. Finally, Berben and co-workers published works related to iron polynuclear clusters able to reduce carbon dioxide to formic acid with high Faradaic efficiency.¹⁰²⁻¹⁰⁴

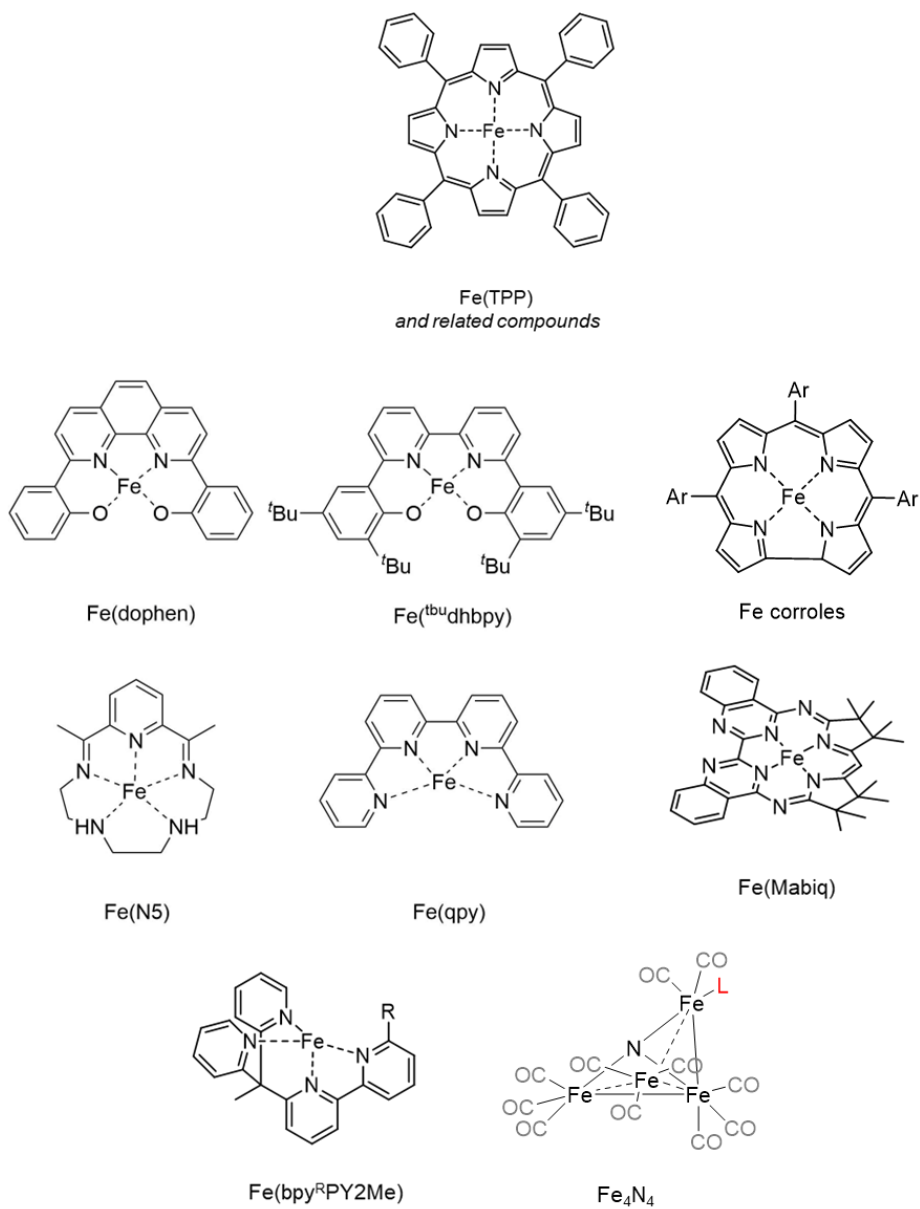


Figure 14. Chemical structures of relevant iron complexes acting as molecular catalysts for CO₂ electrochemical reduction.

1.8.1 CO₂ reduction by Fe porphyrins

To provide a competent discussion of the role of the catalyst in CO₂ reduction, a description of the most relevant aspects of the catalytic cycles in which the complexes are involved is in order. Among mononuclear iron complexes, Fe porphyrins have been the most investigated class of catalysts for CO₂ reduction.^{13,91,105–111} Such catalysts display high reactivity and selectivity toward CO and represent the forerunner category from both the application and the mechanistic knowledge standpoints. The reaction mechanism of this category shares several features with other iron mononuclear catalysts. Indeed, a key requirement of any catalyst is the ability of binding and activating CO₂ at the level of a formally low-valent metal center (usually Fe^I or Fe⁰). In the case of Fe porphyrins, four stable redox states are accessible: Fe^{III}, Fe^{II}, Fe^I, and Fe⁰, the latter being the active species for the catalytic process.

Subsequent reactions of the CO₂ coordinated iron complex eventually lead to the release of the product. In most of the cases, the reactivity of such intermediates is directed either toward the formation of an Fe–CO adduct, upon breaking of a C–O bond assisted by protons, or toward the formation of a formate-type adduct, upon protonation at the carbon site. These two routes ultimately lead to the production of CO and formic acid, respectively. The selectivity of the process depends on the nature of the η¹-C Fe–CO₂ intermediates, as can be understood by examining the issue from an organometallic standpoint. In such adducts, the Fe–carbon bond is characterized by a significant electron density donation from the d orbitals of the metal center to the π* orbitals of CO₂.¹¹²

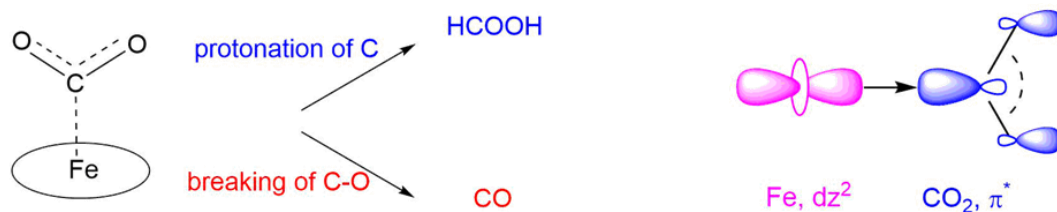


Figure 15. Left: representation of an $\eta^1\text{-C Fe-CO}_2$ adduct, and its evolution toward the production of formic acid (through protonation of carbon) or to carbon monoxide (upon cleavage of a C-O bond). Right: General scheme representing electron donation from d_{z^2} of Fe to π^* of CO_2 .

An illustrative example of reactivity of such intermediates is given by the reaction between CO_2 and the Fe^0 active form of the iron porphyrin catalyst resulting in an adduct typically represented as Fe^ICO_2^- , although the actual electron distribution is more properly depicted through the contribution of resonance formulas $\text{Fe}^{II}\text{CO}_2^{2-}$ and Fe^0CO_2 .¹¹³ Spectroscopic investigation of iron tetraphenylporphyrin (FeTPP) intermediates with CO_2 was carried out by Mondal *et al.* under cryogenic conditions, upon a chemical reduction of the Fe-TPP catalyst.¹¹⁴ The authors isolated the Fe^ICO_2^- adduct, which was then readily protonated by weakly protic solvents to form a long-lived $\text{Fe}^I\dot{\text{C}}\text{OOH}$ species. In agreement with previous observations, this protonation step is believed not to be rate-determining: indeed, upon increasing the proton donor strength (*i.e.*, using phenol), the Fe^ICO_2^- complex was not detectable, since the Fe^0 intermediate is directly converted to a $\text{Fe}^I\dot{\text{C}}\text{OOH}$ intermediate. Both Fe^ICO_2^- and $\text{Fe}^I\dot{\text{C}}\text{OOH}$ intermediates were identified by resonance Raman spectroscopy. The Fe^ICO_2^- adduct displayed a signal in the low-frequency region at 590 cm^{-1} , attributed to stretching of the Fe-C bond, that shifted to 521 cm^{-1} in $\text{Fe}^I\dot{\text{C}}\text{OOH}$ upon protonation. The $\text{Fe}^I\dot{\text{C}}\text{OOH}$ intermediate also displayed a FT-IR signal at 1573 cm^{-1} , attributed to the C-O stretching of the COOH moiety. This represents a rare finding in terms of intermediate detection in the field of iron-catalyzed CO_2 reduction, since most commonly identified species are indeed inactive iron carbonyl complexes (*vide infra*). Furthermore, a recent infrared spectroelectrochemical investigation was

performed on a Fe porphyrin complex decorated at the *meso* positions with urea functionalities (described more in detail in Section 1.9). Indeed, a single signal at 1635 cm^{-1} was identified and attributed to a formal $\text{Fe}^{\text{I}}\text{CO}_2$ complex.¹¹⁵

The second protonation event involves $\text{Fe}^{\text{I}}\text{COOH}$ and leads to the cleavage of the C–O bond, with loss of one water molecule and formation of an iron carbonyl $\text{Fe}^{\text{II}}\text{CO}$. The $\text{Fe}^{\text{II}}\text{CO}$ adduct formation is suggested by the appearance of new anodic peaks in the CV of CO_2 -saturated solutions of Fe-porphyrin catalysts (as an example, the $\text{Fe}^{\text{I}}\text{CO} \rightarrow \text{Fe}^{\text{II}}\text{CO}$ re-oxidation peak may be appreciated in the return scan for Fe(TPP) in Figure 8). The $\text{Fe}^{\text{II}}\text{CO}$ complex is generated upon re-oxidation at -1.6 V vs SCE of a CO_2 -saturated solution of Fe-TPP in dimethylformamide (DMF) after electrolysis at a potential value at which CO_2 is catalytically reduced (-1.8 V vs SCE). Furthermore, spectroelectrochemistry (SEC) in the UV/visible range has provided evidence of such a $\text{Fe}^{\text{II}}\text{CO}$ intermediate, displaying a Soret band at 420 nm .¹¹¹ At this stage, a further one-electron reduction of Fe^{II} to Fe^{I} is needed in order to release CO from the iron coordination sphere; this is justified on the basis of the lower affinity to CO of Fe^{I} with respect to Fe^{II} . Incidentally, this last stage of the catalytic cycle is reminiscent of the well-known high affinity of heme complexes for CO.^{116,117} It is therefore possible to draw a parallel, based on the properties of the iron(II) porphyrin carbonyl complex, between these catalytic systems and the biochemical routes of blood poisoning involving carbon monoxide coordination to oxygen-binding heme proteins.

As a final remark, it is worth highlighting the crucial, twofold role of Brønsted acids in the Fe-porphyrin cycle: they are proton donors, *i.e.*, co-substrates in the reaction, and co-catalysts.^{118,119} Indeed, as well as Lewis acids,^{120–123} they participate in a push-pull scheme in which the iron complex injects electron density into CO_2 by back-donation, while the co-catalyst interacts with the substrate through its oxygen atoms by electrostatics and/or hydrogen bonding. This provides a stabilizing effect on the $\text{Fe}-\text{CO}_2$ adduct and weakens the C–O bond after the first protonation step. Outstanding catalytic performance could be

achieved by installing such co-catalytic units into iron's second coordination sphere. This strategy allows simultaneous activation of the CO₂ substrate, stabilization of key intermediates, and selectivity enhancement toward CO (*vide infra*).

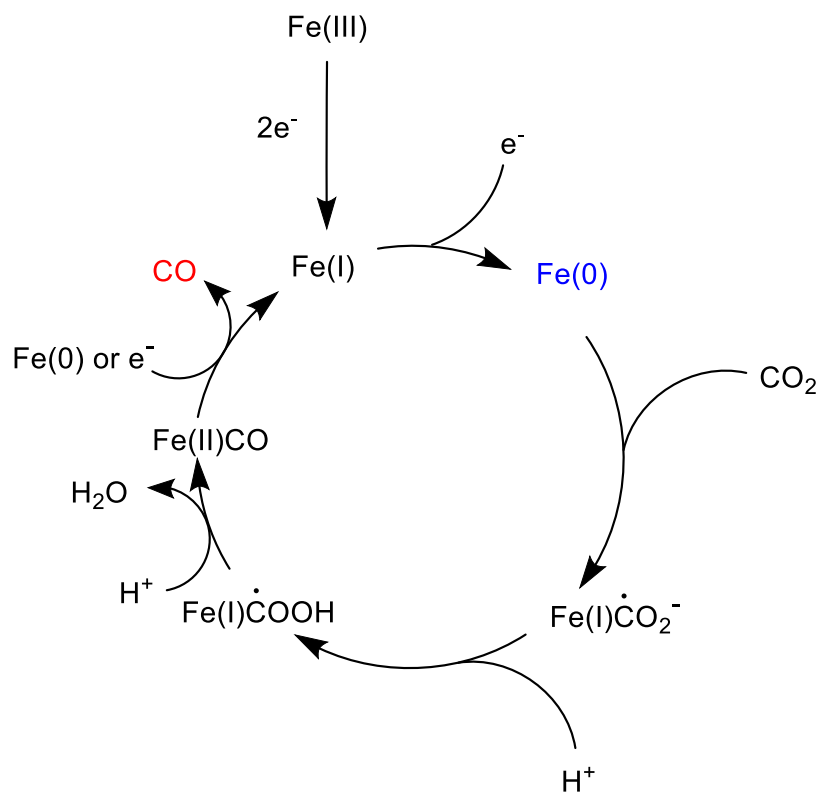


Figure 16. Catalytic cycle of the electrochemical reduction of CO₂ to CO catalyzed by iron porphyrins.

1.8.2 CO₂ Reduction by Iron Porphyrins to Methane

As discussed above, the release of CO from iron porphyrins involves a one-electron reduction of the Fe^{II}CO adduct, regenerating the Fe^I resting state. Under electrocatalytic conditions, CO release is fast since it occurs in the reaction–diffusion layer at the electrode, whose potential during electrolysis favors the Fe⁰ and Fe^I oxidation states. The fast release of CO by iron porphyrins has been known to drive the reduction of CO₂ to this 2e⁻/2H⁺ CO route for this class of catalysts. Conversely, when CO₂ reduction is conducted with photocatalytic systems (described in further detail in Paragraph 1.10), the Fe^{II}CO adduct may accumulate to a non-negligible extent, since its further reduction requires a bimolecular reaction with a molecular reductant in low steady-state concentration.¹²⁴ Therefore, subsequent reactions that involve participation of CO in the coordination sphere of the iron catalyst may occur. Indeed, two recent literature examples report that, under optimized photocatalytic conditions, the complete 8e⁻/8H⁺ reduction of CO₂ to CH₄ can be achieved with a remarkable selectivity of 14–15%, employing an iron catalyst bearing a quaternary ammonium-functionalized porphyrin ligand, Fe(*p*-NMe₃TPP), Figure 17. In the first report, *tris*[2-phenylpyridinato-C2,N]iridium(III), Ir(ppy)₃, was used as photosensitizer¹²⁴, while in a more recent work this role was played by a phenoxazine chromophore¹²⁵. These peculiar and novel examples highlight how tuning of the system allows new catalytic routes to be exploited by overcoming extrinsic mechanistic barriers.

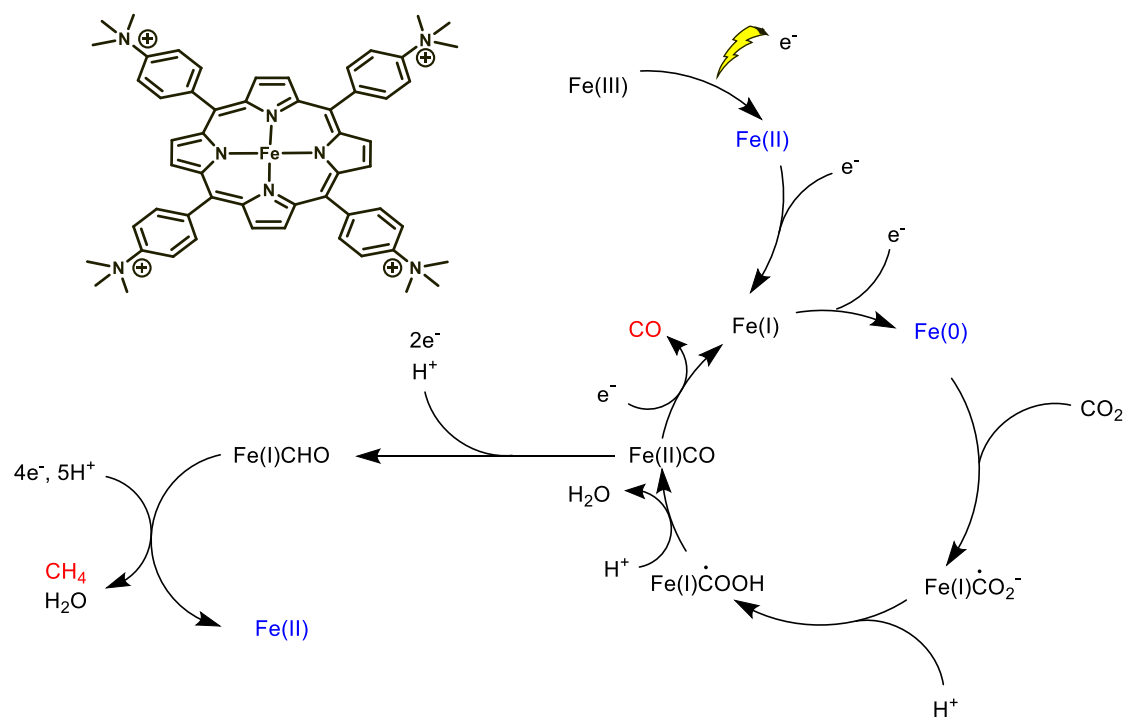


Figure 17. Photocatalytic cycle relative to CO₂ reduction to CO and CH₄ catalyzed by Fe(*p*-NMe₃TPP). Photoinduced electron transfer cycle steps, described more in detail in Paragraph, are simplistically represented as ET steps. Figure redrawn from ¹²⁴ under permission. Copyright 2017, Macmillan Publishers Limited, part of Springer Nature.

1.8.3 CO₂ Reduction by Iron Porphyrins to Formate

Recently, Margarit *et al.* achieved switching the selectivity of Fe-TPP from CO toward formate (up to 68% FE with phenol proton donor) by employing tertiary amine coadditives.¹²⁶ These Lewis bases (LB) act as monodentate ligands to iron in the *trans* position with respect to CO₂. This peculiarity is justified by an enhanced Fe→CO₂ electron density transfer upon coordination of the amine, inducing an increase of the basicity of the carbon atom of coordinated CO₂, and thus favouring the formic acid route (Figure 18). The back-bonding ability of the iron center in heme systems is indeed promoted by basic *trans* ancillary ligands; in this case a reactivity trend is observed in the series quinuclidine > trimethylamine > diisopropylethylamine. The reported CO-to-HCOOH change of

selectivity is remarkable, since in this case no iron hydride intermediate is involved toward the formation of formate, and thus the competitive evolution of hydrogen is negligible. It is worth highlighting that tertiary amines are often employed in photocatalytic cycles for the reduction of CO₂; the evaluation of their effect on the selectivity of the process in these systems should be thus considered. Interestingly, this strategy could be implemented by Dey and co-workers by installing tertiary base groups in the scaffold of a porphyrinoid Fe catalyst that could attain HCOOH catalytic production with 97% Faradaic efficiency with H₂O as the proton source (Figure 18).¹⁰⁷

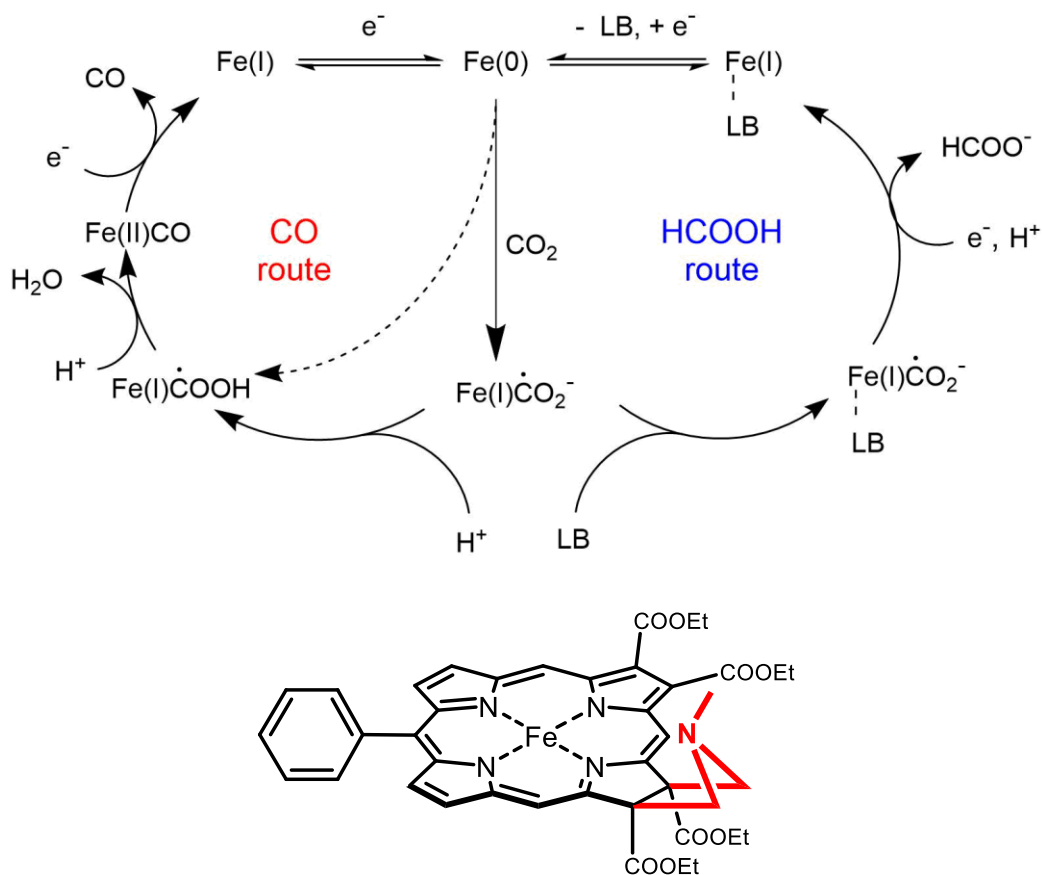


Figure 18. Top: catalytic cycle for iron porphyrins leading to CO or to formic acid in the presence of Lewis bases (LB). Bottom: structure of the tertiary amine-functionalized Fe porphyrinoid catalyst.

1.8.4 Non-heme Iron Mononuclear Complexes

Non-heme mononuclear iron complexes have been developed as another class of catalysts for CO₂ reduction, with mechanistic details and principles being common to both categories. However, differently from the previously discussed iron porphyrins, these systems share the common feature of operating through a formal Fe^I intermediate. Three of these catalysts deal with iron complexes with N₂O₂ tetradentate ligands: 2,9-bis(2-hydroxyphenyl)-1,10-phenanthroline (H₂dophen), 6,6'-di(3,5-di-*tert*-butyl-2-hydroxybenzene)-2,2'-bipyridine (^{tbu}dhbpy); the 2,2':6',2'':6'',2''':6'''-quaterpyridine (qpy) and 2,13-dimethyl-3,6,9,12,18-pentaazabicyclo[12.3.1]octadeca-1(18),2,12,14,16-pentaene (N5) provide instead nitrogen-based planar tetradentate and pentadentate motifs, respectively. Fe(dophen) catalyzes the reduction of CO₂ through an Fe^I intermediate, generated in DMF or dimethyl sulfoxide at E = -2.0 V vs Fc⁺/Fc, in the presence of proton donors. The nature of these latter has an impact on the selectivity of the process, where the main product is formate (FE up to 70%), while CO, C₂O₄²⁻, and H₂ were also observed. This observation was reasoned on the basis of two competitive pathways, one involving a postulated Fe-hydride intermediate, and the second one involving an η¹-C Fe-CO₂ adduct. The former is responsible for formate and H₂ evolution (see also previous paragraph; in this case SEC-IR suggested the involvement of an iron-formato species, Fe-OC(O)H, 1328 cm⁻¹); the Fe-CO₂ adduct is involved in CO and oxalate formation. SEC-IR revealed also the accumulation of an iron carbonyl species (Fe-CO, 1934 and 1881 cm⁻¹) before evolution of CO (2140 cm⁻¹). A similar scenario involving two competitive pathways was hypothesized for Fe(^{tbu}dhbpy), which shows a higher selectivity for formate (up to 68% FY at -2.5 V vs Fc⁺/Fc with phenol proton donor, with ca. 1% FE for CO). Also in this case the active Fe-hydride intermediate was postulated to form upon reduction of the Fe complex in the presence of phenol; conversely, an Fe-CO₂ intermediate was identified by a feature at 1804 cm⁻¹ in the SEC-IR, and was observed to convert into an iron-carbonyl species (1847-1941 cm⁻¹). These, however, release CO very slowly, and therefore

undergo competitive catalyst degradation. Formic acid is the main product observed also in the case of Fe(N5), a reaction which, however, does not involve the formation of an iron hydride. In this case, the reactivity occurs at the Fe^I state upon reaction with CO₂, forming an Fe^{III}-CO₂ adduct; the authors ascribed the favored selectivity for formate to fast isomerization of the CO₂ ligand into the formate-type adduct, with respect to a slow C-O bond cleavage that would lead to the formation of CO. Carbon monoxide was instead observed as the main product in the case of the analogous Co complex, under both electrochemical and photochemical conditions. Interestingly, this is one of few cases in which iron and cobalt centers bearing the same organic ligand both display CO₂ reduction catalysis. This Fe/Co similarity was observed also in the case of porphyrin derivatives, and of qpy complexes. Fe(qpy) is active for catalytic CO production in the presence of phenol as the proton donor with a high initial selectivity (>99%), and involving Fe^I intermediates. In particular, Fe(qpy) operates at a potential of E = -1.58 V vs Fc⁺/Fc (FY up to 48%). The TON, however, is limited to 8 for Fe(qpy). This limitation is again ascribable to competitive degradation pathways that lead to electrodeposition of iron nanoparticles at the working electrode. In the case of Fe(qpy), the critical step is a further reduction of an Fe^ICO intermediate, active in the catalytic cycle, to a non-productive Fe⁰CO (identified by a peak at 1854 cm⁻¹ in IR-SEC), with this latter being the one that undergoes demetallation and thus inducing electrodeposition of metallic iron. Interestingly, the durability of the Fe(qpy) catalyst is enhanced in photocatalytic cycles for reduction of CO₂, where the rate of the deleterious Fe^ICO → Fe⁰CO reduction is lowered since it is controlled by diffusion processes; Fe(qpy) thus reaches TON = 1880 with 97% catalytic selectivity with Ru(bpy)₃²⁺ as sensitizer and triethanolamine as sacrificial electron donor.

Recently, complexes of the polypyridine ligand 6-(1,1-bis(pyridin-2-yl)ethyl)-2,2'-bipyridine (bpyPY2Me) have been evaluated as catalysts for the CO₂-to-CO reduction. Variation of the ligand structure allowed the introduction of pendant moieties in the bipyridyl scaffold that produced a family of closely related ligands (bpy^RPY2Me). Their complexes have indeed proven effective catalysts in CH₃CN

in the presence of 11 M H₂O, acting through a proposed Fe^I(bpy^RPY2Me⁻) intermediate in which explicit redox activity of the ligand is invoked. Binding and activation of CO₂ was hypothesized to be followed by protonation to generate a postulated iron carbonyl intermediate from which CO release occurs. Interestingly, the best performance was obtained with the ligand bearing an ethylamine pendant acting as hydrogen bond donor and proton relay unit, Fe(bpy^{NHEt}PY2Me), reaching 81% Faradaic efficiency for CO evolution at -1.91 V vs Fc⁺/Fc and notably higher stability with regards to its simpler analogue Fe(bpyPY2Me). Despite the absence of direct experimental evidence to support the role of the NHEt pendant, it is interesting to comment that the other candidate for such features, bearing a phenolic group, promotes H₂ evolution while failing in CO₂ reduction. This was attributed to the higher (*circa* 10¹¹) acidity of the phenolic group with respect to the NHEt moiety, causing a dramatic shift in selectivity due to preferred formation of Fe hydrides in the former case.

Redox activity of the ligand has also proven valuable in a recent system based on the 2-4:6-8-bis(3,3,4,4-tetramethyldihydropyrrolo)-10-15-(2,2'-biquinazolino)-[15]-1,3,5,8,10,14-hexaene_{1,3,7,9,11,14}-N₆ (Mabiq) scaffold. Fe(Mabiq) acts as a competent catalyst in CH₃CN upon 2-electron reduction to produce its active form. Remarkably, electrolysis experiments conducted under CO₂ atmosphere at -1.85 V vs Fc⁺/Fc produced CO with 96% Faradaic efficiency and TON = 10. The active form of Fe(Mabiq) was chemically synthesized, thus allowing for *ex situ* characterization and reactivity probing. This approach allowed the authors to determine that the reduction events involve two distinct sites of the ligand scaffold producing a biradical macrocycle.

1.9 Role of the ligand on the catalytic activity

1.9.1 Inner coordination sphere

The mechanistic considerations provided highlight the paramount role of the electronic environment of the iron catalysts on the outcome of the catalytic reaction. The first coordination sphere of a metal ion strongly impacts on its redox chemistry, *i.e.* on the reduction potentials associated to its relevant oxidation states. Indeed, orbital interaction between the metal center and the donor atoms is first contributor to the electronic structure of the active site of a catalyst. Therefore, fundamental principles of coordination chemistry are to be called upon when designing *ex novo* a family of ligands for a catalytic application. In particular, σ and π donor/acceptor properties and Hard-Soft Acid Base (HSAB) theory are most useful guidelines when dealing with commonly encountered donors (N, O, S, P), that are to be substantiated by thorough investigation *via* electrochemical, spectroscopic, and computational studies. The foremost role of the donor atoms of a specific ligand is determining the stability of the complex in the several redox states that should be encompassed in catalytic reactions. The affinity of the metal center in its oxidation states for the donor sites justifies their relative stability and the propensity for transitioning from one to the other: for instance, ligands bearing softer donor sites will facilitate reduction from Fe^{III} to Fe^{II}, resulting in less negative E^0 values than analogous complexes with harder donors. A relevant example can be gathered by comparing the $E_{1/2}$ values for the quasi-reversible Fe^{III}/Fe^{II} redox couples of tripodal ligands complexes: when a pyridine N site in N,N,N-*tris*(2-pyridylmethyl)amine (TPMA) is replaced by a phenoxide (N-(2-hydroxybenzyl)-N,N-*bis*(2-pyridylmethyl)amine, ^{PhO}BPMA)^{127–130} (Figure 19), a staggering shift of $E_{1/2}$ in CH₃CN is observed, from -0.185 V vs Fc⁺/Fc to -0.55 V vs Fc⁺/Fc. Given no major influence by changes in the spin states of the complexes is at place, the observation is directly attributable to the influence of the ligand set on the conditional formation constants for complexes with the metal in the various oxidation states. In fact, Chatt *et al.* and Lever formulated parametrization criteria

to predict E^0 values for complexes upon addition of contributions by individual ligands, *i.e.* an electrochemical series.

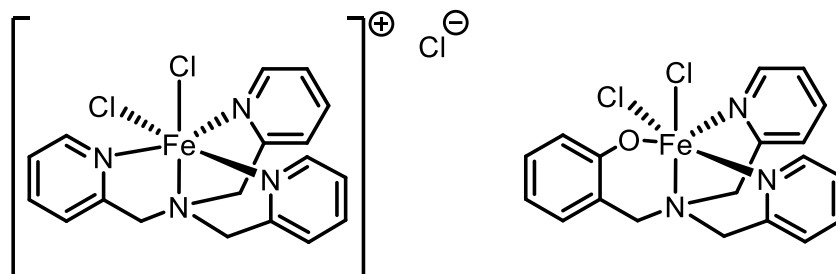


Figure 19. Chemical structures of $[Fe(TPMA)Cl_2]$ (left) and $[Fe(PhOBPMA)Cl_2]$.

Secondly, the nature of the donor sites can impact on the stability/reactivity of intermediates in catalytic cycles. Focusing on CO_2 electroreduction, stronger σ and π donors enhance π back-bonding towards π -accepting fragments. This results in weakened and more prone to cleavage C–O bonds in Fe– CO_2 intermediates, and in more stable Fe–CO adducts obtained in the subsequent steps. Therefore, the appropriate choice of a ligand platform not only impacts on fundamental properties of coordination compounds, but also determines mechanistic features contributing to significant performance outcome. In the literature examples described above, nitrogen donors are most widely exploited, given their versatility, *i.e.* their ability to form stable bonds with several transition metal redox states. Alkoxide or phenoxide groups are rarer, and generally their higher donor power is diluted in the coordination sphere of a metal ion by accompanying them with nitrogen sites.

1.9.2 Structure-activity relationships

Despite a very fine description of the influence of several electronic and structural factors could be provided based on the literature evidence, practical ligand design often relies on the choice of an overall appropriate ligand structure. Whenever synthetic chemistry allowed for exploring subtle variations of such parent ligand scaffold, precious information about the relationship between the redox properties of the resulting complexes and their catalytic activity has been obtained. While these studies are generally applicable to every metal complex acting as catalyst for any specific redox reaction, the following analysis will be restricted to iron complexes for the electrochemical reduction of carbon dioxide.

The natural descriptor of the redox properties of a given catalyst is the formal potential of its active form (E^0_{cat}). This can be related to the TOF_{max} values obtained through the analysis of electrochemical data (*vide supra*). It has been thoroughly demonstrated that the TOF_{max} directly responds to variations of E^0_{cat} , the latter in turn deriving from changes in the structure of ligands by merits of through-bond interactions.⁹¹ The general principle is that more demanding requirements for the generation of a catalytically active species will translate into a higher catalytic activity. This linear free energy relation (Eq. 23) implies that it is not allowed to decrease the overpotential for a catalytic reaction while increasing the TOF at the same time, relying only on through-bond electronic effects.

$$\log(\text{TOF}_{\text{max}}) \propto RT \ln(10) \log(k_{\text{cat}}) = a + b E^0_{\text{cat}} \quad (\text{Eq. 23})$$

The chemical significance of Eq. 23 lies in the driving force of the reaction between the active form of the catalyst and the substrate, in turn related to E^0_{cat} and to the E^0_{sub} . In several cases, this relationship has been shown to hold regardless from the considered ligand structures.⁴⁶ However, CO_2 reduction being a challenging reaction with differentiated mechanistic pathways and a variegated range of accessible products, directing the analysis towards a comparison between selected families of ligands is more appropriate. The discussion will therefore focus on Fe porphyrins, as a family of stable catalysts with a known

reaction mechanism and a wide synthetic space of the ligand scaffold allowing for systematic exploration of substituent effects.

Second-sphere effects prove to be the best strategy to break away from the linear free energy relationship described above, by gaining in maximum catalytic activity while not necessarily paying a price in terms of increase in overpotential. To overcome these limitations, a biomimetic approach has indeed been adopted: enzymatic reactions relying on metal ion active sites exploit a finely tuned secondary peptide environment. This allows for unmatched activity and selectivity of the biochemical processes carried out in the coordination sphere of the metal, without necessarily a direct influence on the electronic environment of the latter. Functional mimics aiming at metal enzyme-like activity therefore have been constructed by introducing groups in the structure of the ligands. These have the specific role of interacting with the reactants and/or key intermediates formed in the steps of the catalytic cycle and bound to the metal center. Groups possessing these peculiar functional and structural features are therefore indicated as secondary sphere effectors, where the expression is referred to the action sphere of the catalyst rather than the coordination sphere of the metal ion. Mainly, these effectors cover the key roles of proton and/or electron transfer relays. More synthetically challenging examples involve ligands displaying channel-like structures that provide a local environment promoting controlled reactant access to, or product release from the metal site, such as proton channels.¹³¹

The high stability, an almost quantitative selectivity for CO in the electrochemical CO₂ reduction and the synthetic tunability of the ligand ring offered fertile grounds for studying such second sphere effects in iron porphyrins. Ground-breaking studies were reported by Costentin, Robert, Savéant and co-workers. In 2012, a Fe porphyrin complex with phenolic groups installed in the *meso* aryl substituents of the ring was reported as catalyst for the CO₂-to-CO reduction in DMF with a staggering $\sim 10^2$ improvement in TOF₀ over Fe(TPP).¹³² The action of the local phenol groups is exerted through:

- i) A very high local concentration of functional groups mimicking the external proton source, *i.e.* phenol;
- ii) The ability of the phenol moieties to act as hydrogen bond donors stabilizing the Fe-CO₂ adduct (Figure 20);¹³³
- iii) A lowering in the energy barrier required for the further reduction of the Fe-COOH adduct.

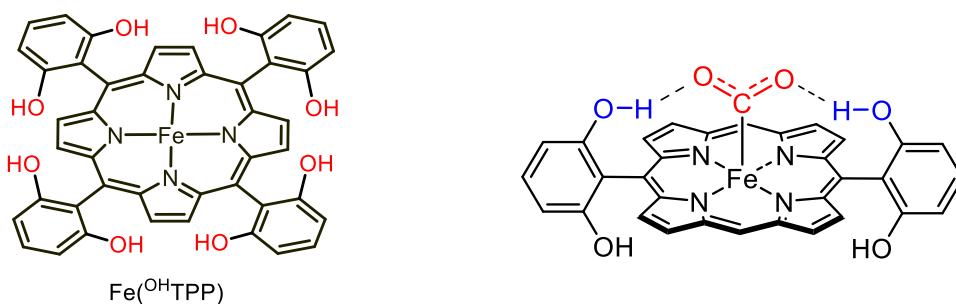


Figure 20. Left: chemical structure of Fe(O^HTPP). Right: stabilization of the Fe-CO₂ adduct by the phenol groups in the *meso* positions of Fe(O^HTPP).

As such, the boosting effect on catalysis is most clearly related to a complex mechanistic feature relying on supramolecular interactions between the catalyst and key intermediates. Specifically, catalysis improvement can be connected to stabilizing effects on high-energy intermediates intervening alongside with their further activation.

Further development of the catalyst in 2014 led the introduction in the porphyrin ring of perfluorinated aryl groups along with those bearing the phenolic functionalities (Figure 21). This was performed with the aim of lowering the overpotential for the reaction (*via* through-bond electron withdrawing effects) while at the same time increasing the catalytic rate over Fe(F²⁰TPP).³⁰

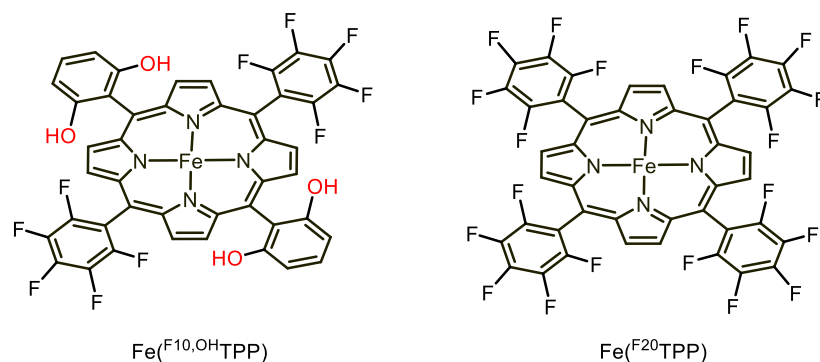


Figure 21. Left: chemical structure of $\text{Fe}(\text{F}^{10,\text{OH}}\text{TPP})$ bearing both phenol functionalities and perfluorinated rings. Right: chemical structure of $\text{Fe}(\text{F}^{20}\text{TPP})$ bearing four perfluorinated aryl rings.

Finally, the group's efforts culminated in 2016, when a water-soluble porphyrin catalyst was reported. The porphyrin scaffold was herein decorated with trimethylammonium (NMe_3^+) groups installed in the *ortho* positions of the *meso* rings, $\text{Fe}(\text{o-NMe}_3\text{TPP})$.⁹¹ These groups impart an electron withdrawing character to the ligand, thus shifting E^0_{cat} towards more positive potentials. Furthermore, the strong electrostatic stabilization exerted by the NMe_3^+ groups on the high-energy Fe-CO_2 adduct induces a boost in catalysis. The result is an enhancement of the catalytic rate, with TOF as high as 10^6 s^{-1} , at overpotentials as low as 220 mV, features representing the best performing molecular catalyst for CO_2 reduction. This outstanding result may be visualized in comparison to other entries in the Fe porphyrin family in terms of a considerable vertical $\log(k_{\text{cat}})$ gain with respect to the linear free energy relationship ($\log(k_{\text{cat}}) - E^0_{\text{cat}}$), represented by the blue star in Figure 22.

By comparison, the authors examined the Fe tetraarylporphyrin substituted in the *para* position of the *meso* rings, $\text{Fe}(\text{p-NMe}_3\text{TPP})$ (Figure 17).¹³⁴ This catalyst was originally studied for its solubility in water and its already remarkable features in electrocatalytic conditions ($\log(\text{TOF}_{\text{max}}) \approx 2.5 \cdot 10^3 \text{ s}^{-1}$, at $\eta = 539 \text{ mV}$), that led to its transfer to electrolyzers and to photocatalytic systems. Regardless, it exhibits a milder displacement from the linear free energy relationship (purple dot in Figure

22) than $\text{Fe}^{(o\text{-NMe}_3\text{TPP})}$). Indeed, through-space electrostatic stabilization is optimal when the NMe_3^+ groups are spatially closer to the catalytic center. Furthermore, the inductive, electron withdrawing (through-bond) effect of the NMe_3^+ groups is less effective in lowering the formal potential of the $\text{Fe}^{\text{I}}/\text{Fe}^0$ couple than in the *ortho* substituted analogue.

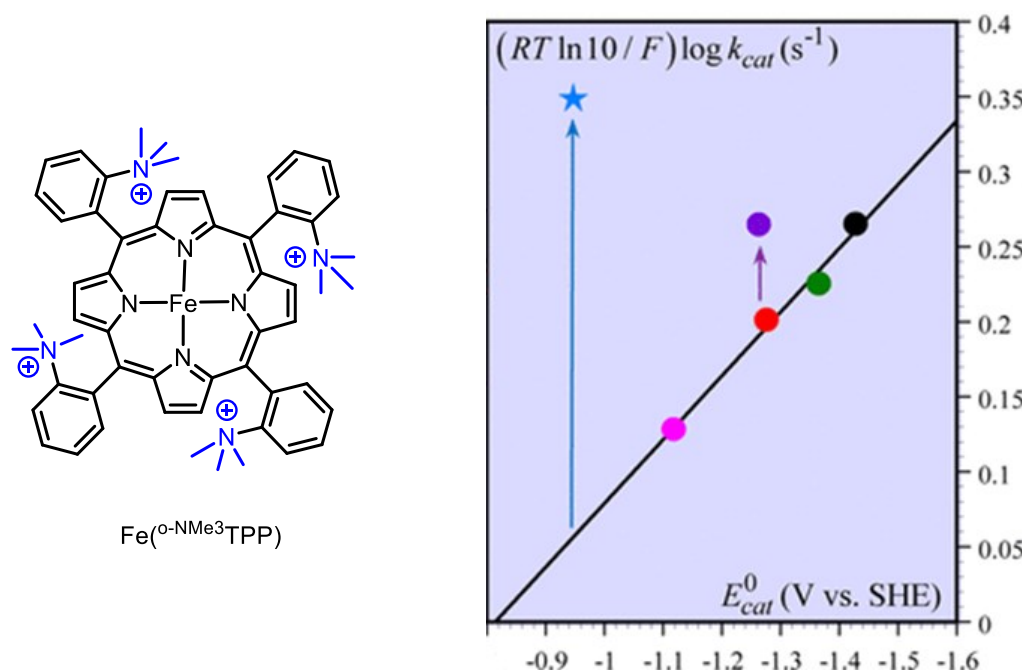


Figure 22. Left: chemical structure of $\text{Fe}^{(o\text{-NMe}_3\text{TPP})}$. Right: Correlation between $\log(\text{TOF}_{\text{max}}) = k_{\text{cat}}$ and E_{cat}^0 , recalling the through-structure substituent effect and showing the Coulombic interaction effects of positively charged substituents. Colour code: blue star (\star), $\text{Fe}^{(o\text{-NMe}_3\text{TPP})}$; purple dot (\bullet), $\text{Fe}^{(p\text{-NMe}_3\text{TPP})}$; magenta dot (\bullet), $\text{Fe}^{(\text{F}^{20}\text{TPP})}$; red dot (\bullet), $\text{Fe}^{(\text{F}^{15}\text{TPP})}$; green dot (\bullet), $\text{Fe}^{(\text{F}^{10}\text{TPP})}$; black dot (\bullet), $\text{Fe}(\text{TPP})$. Figure adapted with permission from ⁹¹. Copyright 2016 American Chemical Society.

This principle was profitably applied in further studies, employing superstructured porphyrins bearing amide substituents reminiscent of the picket-fence motif previously studied in oxygen activation chemistry.^{135–137} Other notable examples feature ionic liquid-derived moieties as substituents carried in the vicinity of the iron center, serving the same electrostatic stabilizing function as the trimethylammonium groups.¹³⁸ Lastly, Nocera and co-workers applied the peculiar “hangman” porphyrin motif to construct Fe-based catalysts with amide or phenol dangling proton relay groups.¹³⁹ The structures and key performance indicators of such systems are reported in Figure 23.

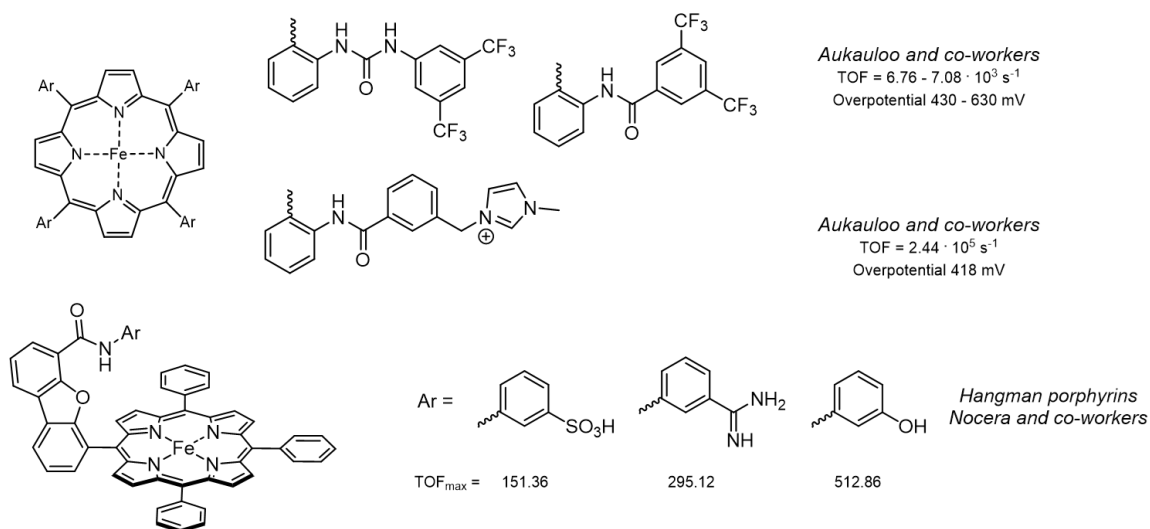


Figure 23. Chemical structures of superstructured Fe porphyrins imparting through-space effects to CO₂-to-CO electrochemical reduction.

Fine-tuning of second-sphere effects has been further studied using amide substituents as hydrogen bonding stabilizing groups in the *meso* site of Fe tetraarylporphyrins by Chang and co-workers.¹³⁷ A group of four structurally isomeric porphyrins, represented in Figure 24, was evaluated in the CO₂-to-CO electrochemical reduction reaction. The positional effect of the amide residues relative to the metal center was studied in the presence of a similar electronic environment for the four catalysts. As a result, a trend relating the position of the

NH amide groups to a vertical displacement of $\log(TOF_{max})$ from the linear free-energy relationship (Eq. 23) was established (Figure 24). The analysis demonstrated that the effect of the amide group on catalysis *via* hydrogen bonding could be directed towards efficient catalysis through optimal positioning. This report demonstrated quantitatively the impact of precisely installing residues in the proximity of the metal center, thus highlighting the potential of the biomimetic design approach.

Dey and co-workers have applied this principle by installing groups suitable for acting as proton transfer and/or hydrogen bonding relays on the four *meso* positions of Fe tetraarylporphyrins.¹³⁶ The authors studied the picket-fence porphyrin and two triazole derivatives, one bearing an ester moiety, comparing them with Fe(^{OH}TPP) and the Fe-*ortho*-2-amide porphyrin reported by Chang and co-workers (*vide supra*). A linear relationship between the pK_a of the hydrogen bonding/proton transfer relay group with the logarithm of the relative rate (and therefore $\log(TOF_{max})$ of the selected catalyst) was established (Figure 24). This interesting finding reflects the crucial role of managing PCET events in the action sphere of the catalyst.

The structure-activity relationships herein discussed highlight the importance, in molecular catalyst design, of considering electronic effects as well as supramolecular interactions in achieving fine control over the catalytic reaction. Indeed, the effort required for designing and synthesizing molecules following these principles is most often repaid with superior functional advantages.

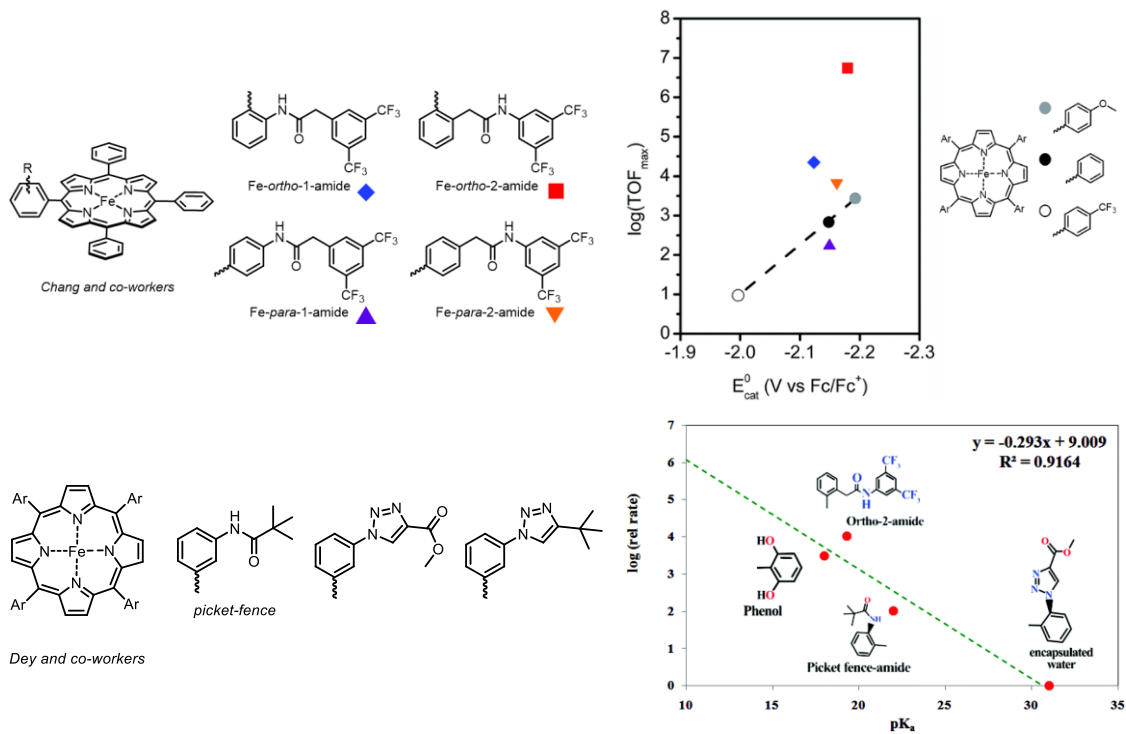


Figure 24. Top: correlation between $\log(TOF_{max})$ and E_{cat}^0 illustrating the through-space interactions that promote catalysis in the case of amide-functionalized superstructured Fe porphyrins. Figure reproduced with permission from ¹³⁷. Copyright 2018 Royal Society of Chemistry. Bottom: plot of $\log(\text{relative rate})$ with respect to the pK_a of the H-bonding residues. Figure reproduced with permission from ¹³⁶. Copyright 2019 Royal Society of Chemistry.

1.9.3 Redox activity of the ligand and catalyst stability

In typical descriptions of reaction mechanisms involving coordination compounds as catalysts, the focus is naturally posed on their active site, the metal center. The accessibility of different redox states, each with peculiar reactivity, is the key feature that confers metal complexes a paramount role as molecular catalysts in electrochemical reactions. However, this perspective is oftentimes clouded by overlooking the function of ligands in such processes. Indeed, the above discussion elucidated how ligands can be modified to allow for modulation of redox potentials or to enhance the reactivity of their complexes. Nonetheless, ligand direct redox activity is not rarely invoked in assisting redox events, as detailed for the Fe(Mabiq) catalyst. This is particularly relevant when exploring reactions beyond mildly cathodic potentials: while O₂ or NO reductive activation by iron complexes clearly revolves around their Fe^{II} and Fe^{III} states and their chemistry, no such clear-cut distinction can be applied *a priori* to CO₂ reduction catalysis. Functional catalysts can in fact display voltammetric waves leading to their active form attributable to mixed ligand- and metal-centered events or even to pure ligand-based reductions. The attribution of the character of such transformations *per se* is a subject of foundational molecular inorganic electrochemistry and computational chemistry research, while the relevance of the topic to catalysis is to be examined here.^{140–142}

Low-valent states of metal centers are usually characterized by low stability and their chemistry is easily impaired by disproportionation or demetallation with formation of metal nanoparticles. Redox-active (“non-innocent”) ligands can therefore act as electron reservoirs that mediate between the electrode and the metal center. The latter can drive reactions of the catalytic cycle relying on electrons “stored” in the ligand scaffold, with a lower degree of stress on the active site with respect to systems undergoing purely metal-based reductions. This crucial advantage is found in polypyridine and Schiff base complexes and metal porphyrins, where a partially reduced character of the ligand is invoked based upon experimental evidence or calculations. It is to be remarked nonetheless how

the reaction site in the complexes remains the metal, regardless from the nature of the reductions leading to the active form of the catalyst, as supported by thorough experimental evidence of metal-centered intermediates. An interesting topic to be investigated would then be the relation between the electronic state of the complex in its catalytically active form and in its bound state after interaction with a substrate (CO₂ binding to a “Fe⁰” center in iron porphyrins is a useful example). In particular, a formal description of the transition between two different electronic structures upon substrate binding could be extremely beneficial in understanding more in depth redox catalytic transformations.^{143–146}

It should also be mentioned that it is not infrequent to observe direct chemical involvement of a redox-active ligand in key chemical steps. In fact, proton-coupled electron transfer events occurring at the ligand have been proposed and supported as the formation routes of previously generically labelled “metal hydrides”. Chemically reversible reduction and protonation of key ligand sites can in fact assist further reactions of intermediates in the coordination sphere of the metal. A relevant case involves Ni porphyrins studied as catalysts for the electrochemical hydrogen evolution reaction.^{147–149}

Therefore, redox-active ligands can unlock the reactivity of their metal centers in their low-valent states allowing for a sophisticated multi-electron chemistry while preventing decomposition. However, ligand redox activity is also often the cause of chemical decomposition of the catalysts in operational regimes. This is expectable when the radical character of the ligand in the reduced complex is pronounced, so to allow for parallel ligand reactivity, e.g., passivation of the electrode *via* film formation or dimerization to produce “out of the cycle” species. Lastly, molecular design principles can be deployed as protective measures against otherwise unavoidable side-reactions of the ligand. For example, sterically encumbered groups may prevent radical dimerization thus enhancing catalyst stability. These aspects have been the focus of a most prolific research line featuring Manganese bipyridyl carbonyl complexes.⁷⁵ The considerations here outlined should then set researchers towards a rational case-by-case examination

of potential candidates as ligands to construct molecular catalysts for electrochemical reactions.

1.10 Photocatalysis

CO₂ catalytic reduction may be approached by using light as a primary source of energy, in artificial systems mimicking features and mechanisms of naturally occurring photosynthetic processes. Photocatalytic CO₂ reduction is in fact a major research frontier, steadily brought forward by authors globally. For these reasons, this Paragraph is intended as a brief overview of the most relevant aspects of photocatalysis applied to carbon dioxide reduction.

As stated above, photocatalytic systems rely on the use of light as the energy input for driving the target reaction. In the scope of reductive small molecule activation, the overall process may be divided into three main steps:

- i) light absorption;
- ii) catalyst activation by photoinduced electron transfer;
- iii) catalytic reaction.

Usually, this general scheme is interpreted in systems comprising three components: a light harvesting dye (photosensitizer), a catalyst, and a sacrificial electron donor (SD).

1.10.1 Photosensitizers

Light harvesting and conversion in the form of charge relies on the presence of molecules able to act as oxidizers or reductants in their excited state. Depending on the conditions and on the choice of catalyst and electron donor, the excited dye can act as both an oxidizer towards the electron donor or a reducing agent towards the catalyst. These routes, represented in Figure 25, are labeled reductive and oxidative emission quenching, respectively (*i.e.*, the adjectives

reductive and oxidative refer to the dye). The photocatalytic cycle is then closed by electron transfer from the reduced dye to the catalyst or from the electron donor to the oxidized dye.¹⁵⁰

Since the electron transfer reactions are usually bimolecular events relying on diffusion of the involved species, a sufficiently long excited state lifetime of the dye is a beneficial property for a photosensitizer.

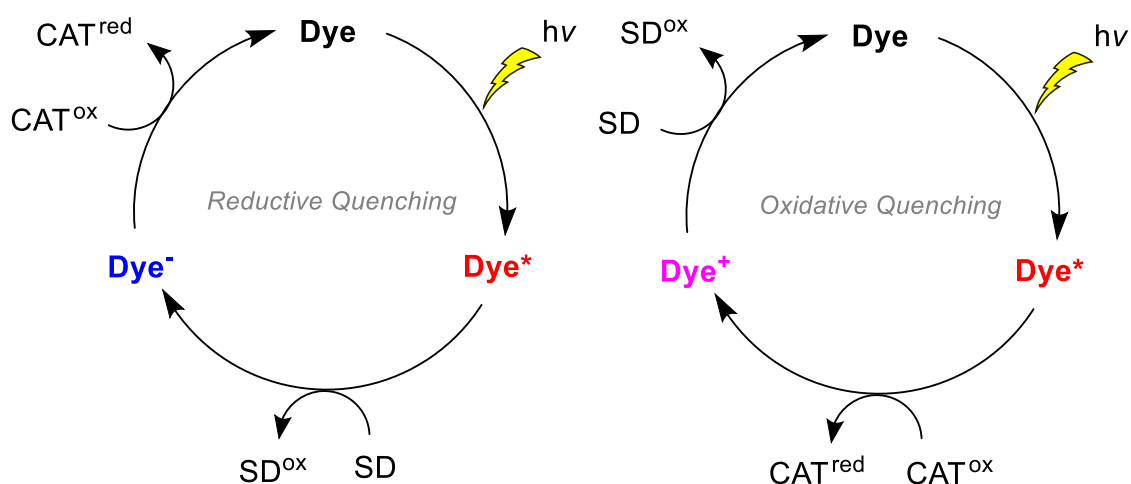


Figure 25. Mechanisms of reductive quenching (left) and oxidative quenching (right) routes in a three-component photocatalytic system constituted by a dye (photosensitizer), a catalyst (CAT) and a sacrificial electron donor (SD).

The thermodynamic requirements¹⁵¹ for each step are given by general equation describing the standard Gibbs free energy for electron transfer from a reductant R to an oxidant O, Eq. 24:

$$\Delta G_{ET}^0 = \frac{F}{RT} (E_R^0 - E_O^0) + w_r + w_p \quad (\text{Eq. 24})$$

Where E^0 is the standard reduction potential for the species R and O, while w_r and w_p are work terms associated with bringing the reactants (w_r), and the products (w_p) from infinity to reacting distance. These latter are often assumed to

be mainly electrostatic in nature, and expressed in terms of a general w_0 (Eq. 25) to be multiplied by the net sum of the charges of the reactants and products:

$$w_0 = \frac{e_0^2}{4\pi\epsilon_0\epsilon_s d} \quad (\text{Eq. 25})$$

Where e_0 is the elemental charge, $\epsilon_0\epsilon_s$ the dielectric constant of the medium, and d the reacting distance (of the order of a few Å).

In the case of a reductive quenching (Figure 25), the thermodynamics for electron transfer are therefore expressed through Equations 26a and 26b:

$$\Delta G_{RQ}^0(1) = \frac{F}{RT} \left(E_{SD^{•+}/SD}^0 - E_{dye^*/dye^{•-}}^0 \right) + w_r + w_p \quad (\text{Eq. 26a})$$

$$\Delta G_{RQ}^0(2) = \frac{F}{RT} \left(E_{dye/dye^{•-}}^0 - E_{cat}^0 \right) + w_r + w_p \quad (\text{Eq. 26b})$$

For an oxidative quenching, they result in Equations 27a and 27b:

$$\Delta G_{OQ}^0(1) = \frac{F}{RT} \left(E_{dye^{•+}/dye^*}^0 - E_{cat}^0 \right) + w_r + w_p \quad (\text{Eq. 27a})$$

$$\Delta G_{OQ}^0(2) = \frac{F}{RT} \left(E_{SD^{•+}/SD}^0 - E_{dye^{•+}/dye}^0 \right) + w_r + w_p \quad (\text{Eq. 27b})$$

The excited state standard potentials are in turn defined by Equations 28a and 28b:¹⁵²

$$E_{dye^*/dye^{•-}}^0 = E_{dye/dye^{•-}}^0 + \Delta G_{ES}/e_0 \quad (\text{Eq. 28a})$$

$$E_{dye^{•+}/dye^*}^0 = E_{dye^{•+}/dye}^0 - \Delta G_{ES}/e_0 \quad (\text{Eq. 28b})$$

The Gibbs free energy stored in the excited state, ΔG_{ES} (in eV), is often approximated to the energy of the first vibronic transition, E_{0-0} , experimentally obtained by the intersection of normalized optical absorption and emission

spectra of the dye. The standard potentials of the dye, on the other hand, are approximated to the half-wave potentials ($E_{1/2}$), when obtainable from cyclic voltammograms.

The mechanistic pathway followed by a specific photocatalytic system can be discerned by comparing the relative rates of electron transfer between the excited dye and either the electron donor or the catalyst. These latter are experimentally determined by emission quenching experiments, *i.e.* by comparing the emission intensity and the excited state lifetime of the dye in the absence and in the presence of increasing concentrations of electron donor or catalyst.

This theoretical background is necessary to provide choice criteria for potential dyes, matching the requirements of the catalytic systems expressed in terms of standard potential for each involved species.

Commonly used dyes are ruthenium and iridium polypyridyl compounds, the forerunners being *tris*-bipyridineruthenium(II), $\text{Ru}(\text{bpy})_3$, and *tris*-[2-phenylpyridinato-C2,N]iridium(III), $\text{Ir}(\text{ppy})_3$, and related derivatives. While precious mechanistic insights have been obtained using these highly performing dyes, their rare metal-based nature is incompatible with sustainable strategies. Therefore, several organic chromophores have been studied and proposed as molecular photosensitizers in photocatalytic CO_2 reduction schemes, such as phenoxazine, phenothiazine and phenazine dyes (Figure 26), along with copper complexes.^{124,151,153–159}

A step forward in the search for robust and sustainable photocatalytic systems is constituted by reports by Robert and co-workers. Indeed, purpurin, a naturally occurring anthraquinone chromophore (Figure 26), has been used as photosensitizer coupled to $\text{Fe}(\text{qpy})$ and $\text{Co}(\text{qpy})$ in DMF. Its application has then been transferred to aqueous photocatalysis by employing $\text{Fe}(\text{p-NMe}_3\text{TPP})$ as the catalyst.¹⁵¹ In a recent publication by Yuan *et al.*, purpurin was also used to form a coordination complex with Cu^{II} , thus obtaining a novel rare metal-free photosensitizer. Compared to purpurin, the complex exhibited a stronger reducing power in its excited state and a wider visible light absorption range.¹⁵⁹

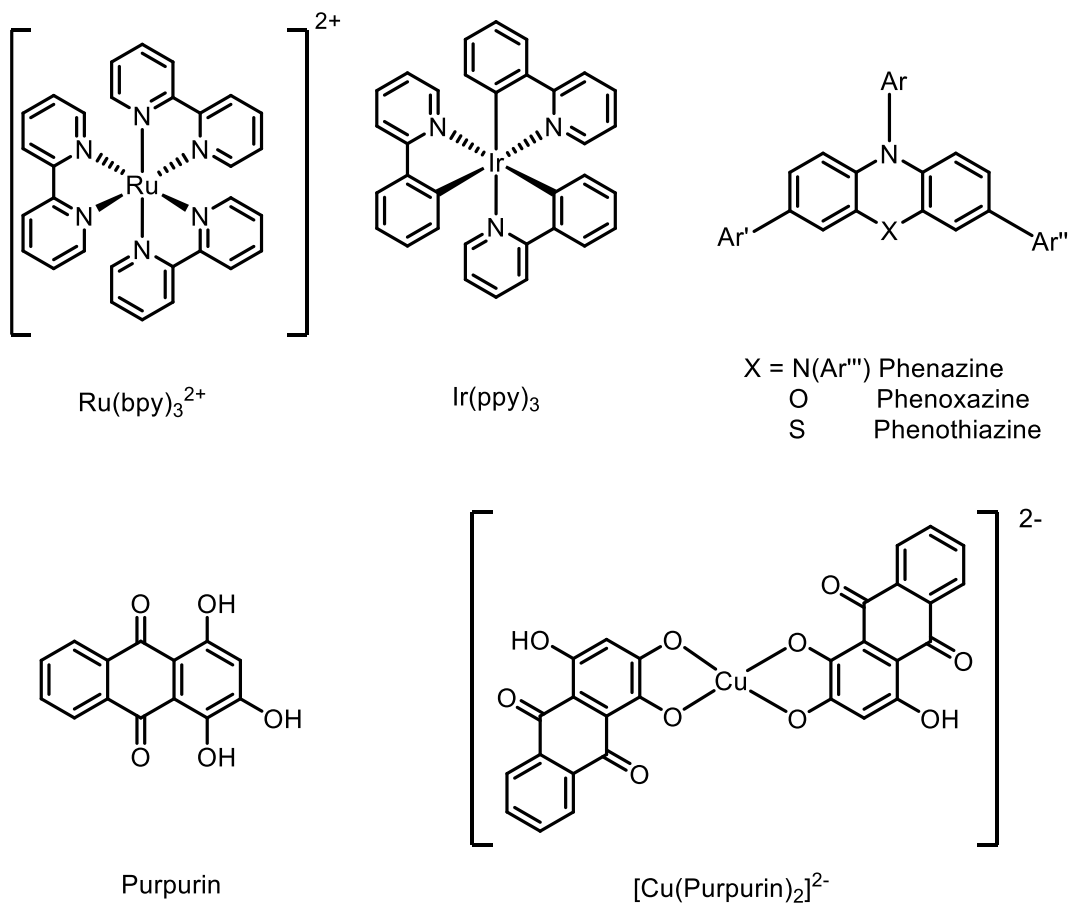


Figure 26. Chemical structures of dyes relevant to photocatalytic CO_2 reduction in three-component systems.

Finally, colloidal photocatalysts have also been recently explored in the field of metal-catalyzed CO_2 photoreduction, such as quantum dots¹⁶⁰ (CdS, CdSe, carbon-based), mesoporous graphitic carbon nitride (mpg- C_3N_4)⁹⁶ and covalent organic frameworks (COF's).

While the photophysical properties and mechanism of each photosensitizer would deserve particular attention, the topic is beyond the scope of the present thesis.

1.10.2 Sacrificial electron donors

The use of sacrificial reductants, *i.e.* substrates undergoing kinetically and thermodynamically facile oxidation, as electron donors is often chosen to focus solely on the target process. Most used are triethylamine (NEt₃), triethanolamine (TEOA), and 1,3-Dimethyl-2-phenylbenzimidazoline (BIH), employed in organic solvents, while EDTA and ascorbic acid are often encountered in aqueous photocatalysis (Figure 27).¹⁵⁰

Oxidation of tertiary amine derivatives occurs through electron abstraction from the nitrogen lone pair, typically followed by deprotonation (from the carbon site in alpha to the amine group) by a second amine molecule. The result is a neutral carbon-centered radical that can also act as reductant. Subsequent reactivity finally leads to fragmentation of the sacrificial amine, through a potential second oxidation event. In the case of BIH, no fragmentation occurs as part of its action mechanism, but rather a sequence of two electron and one proton transfer events leading to a stable aromatic cation. In both cases, the presence of a base to deprotonate the strongly acidic singly oxidized form of BIH is crucial to avoid charge recombination.

It should be noted that the irreversible nature of these oxidation events hampers a precise determination of the formal potential of the SD^{•+}/SD couples *via* electrochemical techniques, and that tabulated values also depend on the solvent nature and on proton concentration. Usually, sacrificial electron donors are present in a large excess with respect to the other components of the photocatalytic reaction mixture to ensure a non-rate limiting reservoir of electrons to feed the catalytic cycle. As a consequence, the reductive quenching pathway, when allowed thermodynamically, is often dominant and occurs through a pseudo-first order rate.

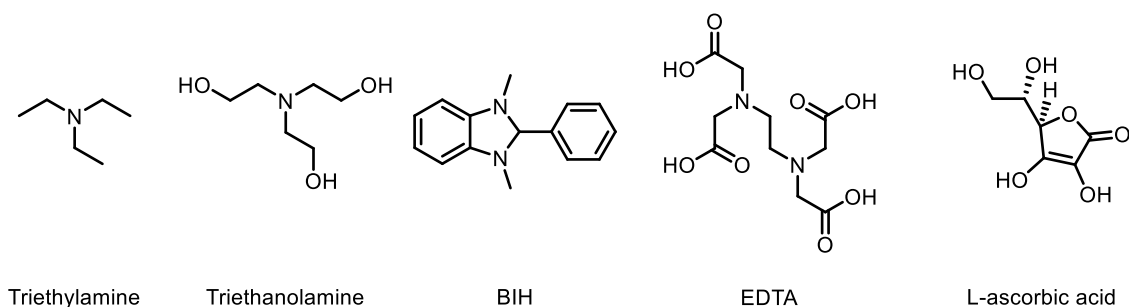


Figure 27. Chemical structures of commonly used sacrificial electron donors used in photocatalytic CO₂ reduction.

This reaction scheme allows to employ the same transition metal complexes used in electrocatalysis in photocatalytic processes, with reaction mechanisms being almost fully translatable. In fact, benchmarking of molecular catalysts and evaluation of their reaction mechanism is often fruitfully obtained by electrochemical methods and directed towards optimized photocatalytic schemes. However, paramount differences can arise in the reaction outcome. Indeed, multi-electron reduction processes, when translated from electrochemical catalysis to a photocatalytic regime, must rely on diffusional, light-induced electron transfers rather than on the presence of an electrode poised at a constant potential. Therefore, the steady-state profile of the intermediates differs chemically and spatially between the two regimes. Reaction intermediates can in fact accumulate and their reactivity be independently observed (*vide supra*).¹⁵⁸ Moreover, decomposition side-reactions related to the presence of a high local concentration of the active form of the catalyst in close vicinity to the electrode surface are generally by-passed in photocatalysis, therefore leading to more stable homogeneous systems.

1.10.3 Two-component systems

A last remark is due about the rarer two-component systems, exploiting photoactive compounds able to directly perform catalytic CO₂ reduction upon light absorption. Direct photoexcitation of metal catalysts is often harmful towards their chemical integrity, partly because of the energies carried by the required ultraviolet light. Such issue has been encountered in unsensitized CO₂ reduction by iron tetraphenylporphyrin¹¹¹ and Re^I(bpy)(CO)₃(X)¹⁶¹ (where X is an anionic monodentate ligand) under UV light irradiation. Notable heralds of two-component systems operating under visible light irradiation are based on a family of iridium photocatalysts, Ir(ppy)(^Rterpy)Cl, where ^Rterpy are 4'-aryl-substituted 2,2':6',2''-terpyridine ligands, able to produce CO selectively.¹⁶² In 2022, Yuan *et al.* reported a rare example of first raw photoactive compound constituted by a pentanuclear [Fe₂Na₃] complex employing purpurin as a ligand (Figure 28).¹⁶³ Interestingly, purpurin was found to act as a light harvesting unit able to manage PCET events functional to CO₂-to-CO reduction catalysis.

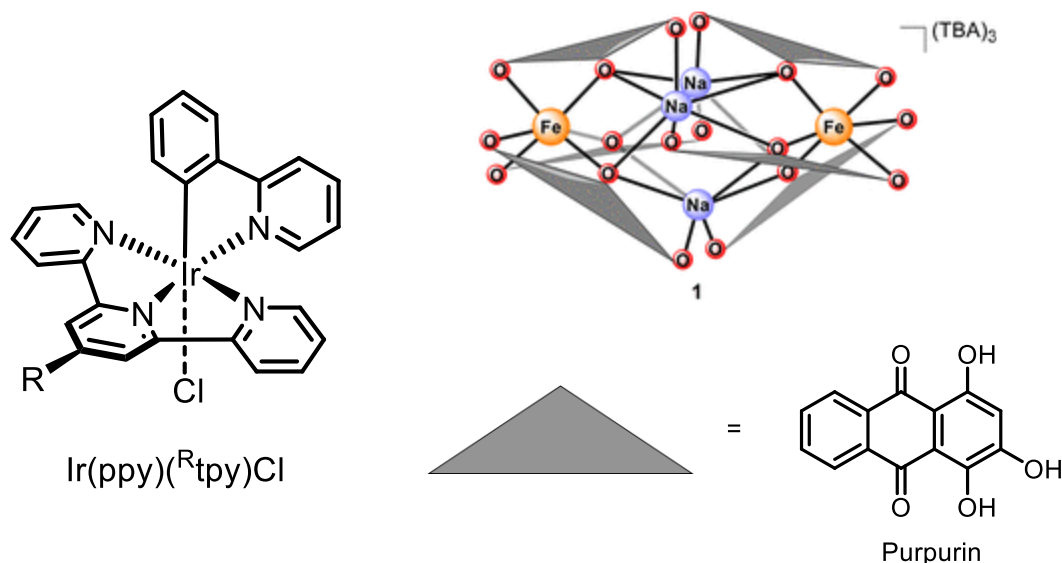


Figure 28. Left: chemical structure of Ir(ppy)(^Rterpy)Cl. Right: chemical structure of [Fe₂Na₃](Purpurin)₆. Figure adapted with permission from ¹⁵⁹. Copyright 2022 American Chemical Society.

This brief description of homogeneous photocatalytic CO₂ reduction should have highlighted their intrinsically variegated nature, originating from the multiple factors impacting on efficiency and stability. Indeed, failure of any photocatalytic system can eventually be observed, and the determination of its causes provides useful optimization criteria. Consumption of reagents or sacrificial electron donors driving catalysis to a halt is proper of stable systems, while decomposition of the dye and/or of the catalyst can underline chemical weaknesses of these key components.

The parameter used to rigorously quantify the overall efficiency is the photochemical reaction quantum yield Φ , defined by Eq. 29:¹⁶⁴

$$\Phi = \frac{N_p}{N_{hv}} \quad (\text{Eq. 29})$$

where N_p is the number of molecules of target product and N_{hv} the number of photons absorbed by the system. N_{hv} can be experimentally determined by using power meters or by chemical actinometry, not discussed herein.

Some reports also provide the quantum efficiency Φ_E (Eq. 30), a parameter accounting for the specific photochemical scheme considered:

$$\Phi_E = \frac{n_e}{n_d} (\Phi) \quad (\text{Eq. 30})$$

In Eq. 30 n_d is the number of electrons provided by each molecule of sacrificial electron donor and n_e the number of electrons required to produce a single molecule of target product. Incidentally, while the maximum photochemical quantum yield Φ_{\max} depends on the mechanism, $\Phi_{E,\max}$ is 1 by its definition.

Benchmarking of photocatalytic systems should report the photochemical quantum yield for the studied reaction. This should always be coupled to the TON_{\max} obtainable in a specific set of conditions to provide a more complete description of photocatalytic systems.

1.11 Chapter 2 and 3 Rationale

The present Chapter has served as a thorough introduction to the field of electrochemical catalysis for carbon dioxide reduction, with hints about photocatalysis. In the following chapters, the research contribution dealing with a novel family of iron complexes as catalysts for the CO₂-to-CO reduction is reported. Despite yet unchallenging performance with respect to the state of the art constituted by Fe porphyrins, we demonstrate the usability of our iron complexes as competent catalysts. The detailed mechanistic study provided paves the way for optimization of a family of catalysts with a wide synthetic space with large room for optimization.

Appendix 1

Appendix 1.1 – Computational simulation of electrochemical experiments

Electrochemical simulations (chronoamperometries and cyclic voltammetries) were obtained using the Electrochemical Simulation Package (ESP) written by Prof. Carlo Nervi (University of Torino). In the simulations, catalyst concentration was usually $1 \cdot 10^{-3}$ M. The heterogeneous rate constant (k_e) and the electron transfer coefficient (α) were consistently 0.12 cm s^{-1} and 0.5, respectively. A solid electrode with an area of $1 \cdot 10^{-2} \text{ cm}^2$ was considered.

Appendix 1.2 – Electrochemical study of iron porphyrin catalyst

The electrochemical study of iron(III) tetraphenylporphyrin chloride (Fe(TPP)Cl) was performed in the context of the Cyclic Voltammetry International School at the University of Paris Diderot, under the supervision of Prof. Marc Robert, Prof. Cyrille Costentin, Dr. Cédric Tard, Dr. François Mavré and Dr. Niklas von Wolff. Given the established scientific knowledge about the catalytic system considered, experimental data garnered during the School were used in the present Chapter (see Figure 8).

TPP and Fe(TPP)Cl were synthesized according to the literature procedures.^{165,166} Experiments were carried out in DMF, in the presence of 0.1 M tetrabutylammonium hexafluorophosphate (electrochemical grade) as supporting electrolyte and 1 mM Fe(TPP)Cl. Argon and carbon dioxide were withdrawn from high-purity reservoirs and bubbled through the electrolyte solutions for 15 minutes prior to measurements. A blanket of either gas was kept above the solutions during the experiments. Electrochemical experiments were run on a CHI potentiostat-galvanostat, using custom-made electrochemical cells and custom-made electrodes. The internal resistance was compensated using the positive feedback loop of the potentiostat. The working electrode was a glassy carbon (GC) electrode, the reference electrode a saturated calomel electrode (SCE) and the counter electrode a platinum wire. In between voltammetric experiments, the

working electrode was polished with a micrometric alumina paste on a micrometric cloth pad.

Appendix 1.3 – Synthetic procedure of 5,10,15,20-Tetraphenylporphin (TPP)

Propionic acid (150 mL) was introduced into a two-necked round bottom flask and brought to reflux. To the refluxing acid, 3 mL (46 mmol) of freshly distilled pyrrole and 4 mL (36 mmol) of benzaldehyde were simultaneously introduced by means of two syringes. The reaction was refluxed in the dark for 30 min, and then left to cool to room temperature. After filtration over a sintered glass filter, a brilliant purple solid was obtained, which was then washed with deionized water and with methanol, and finally dried. 980 mg (1.6 mmol, yield 4%) of product were obtained after column chromatography (eluent CH₂Cl₂).

¹H-NMR (300 MHz CDCl₃): δ 8.83 (s, 8H), 8.20 (d, J = 7.6 Hz, 8H), 7.81–7.71 (m, 12H). The NH protons could not be identified in the NMR spectrum.

UV/Vis: λ_{max} 417 nm, 514 nm, 549 nm, 590 nm, 646 nm.

ESI-MS: 615.4 m/z [MH]⁺.

Elemental analysis: calculated for C₄₄H₃₀N₄ C: 85.97% H: 4.92% N: 9.11 %.
Found C: 86.41% H: 5.00% N: 8.77%.

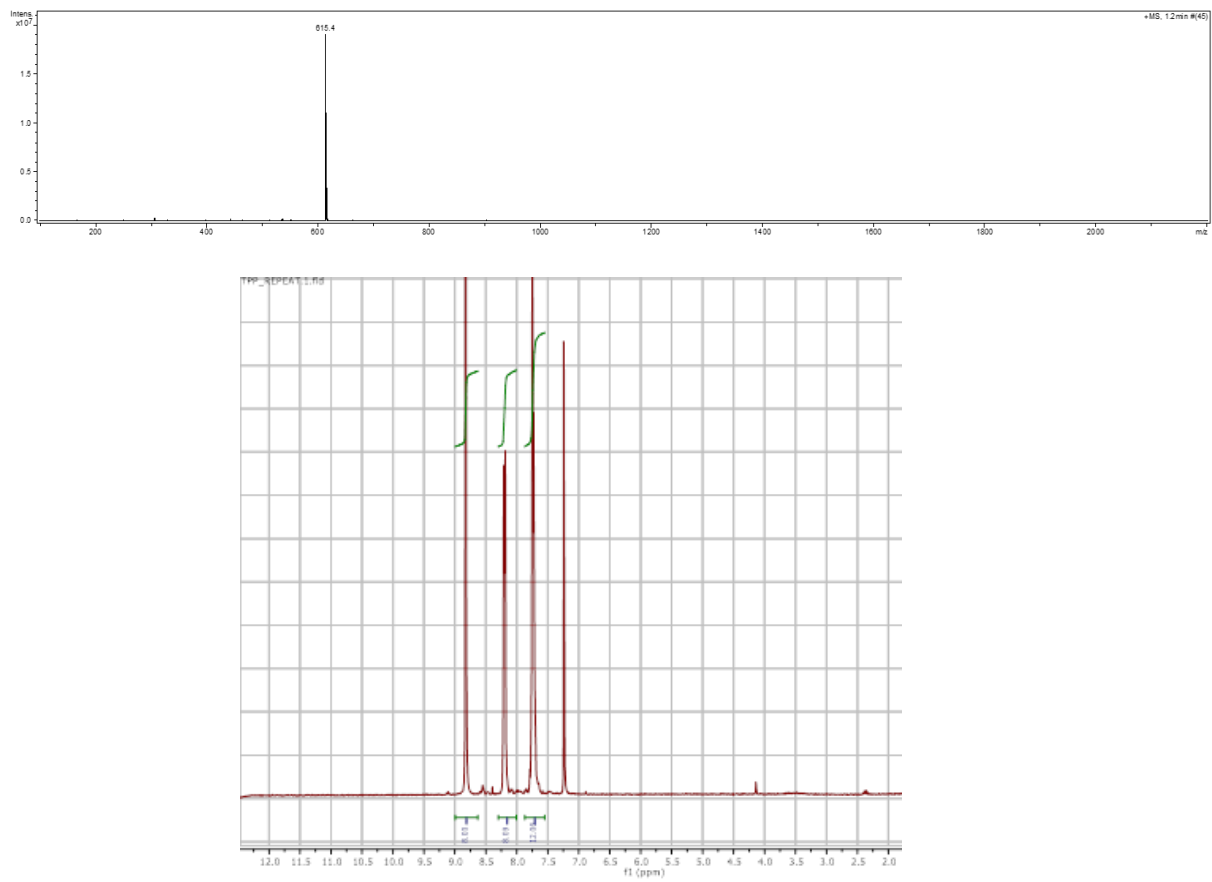


Figure 29. Top: ESI-MS spectrum of TPP in methanol. Bottom: ¹H-NMR spectrum of TPP in CDCl₃.

Appendix 1.4 – Synthesis of chlorido(5,10,15,20-Tetraphenyl-21H,23H-porphinato)iron(III) (Fe(TPP)Cl)

242 mg (0.394 mmol) of TPP were dissolved under stirring in 25 mL of HPLC-grade DMF. 5.42 g (27.26 mmol, 69 eq) of FeCl₂·4H₂O were added in small portions under stirring. The process resulted in evolution of heat. The reaction mixture was heated at 160 °C for 15 h. After the specified time, the reaction was left to cool to room temperature, then treated with 30 mL of deionized water and 0.5 mL of concentrated HCl. The mixture was stirred at room temperature for 15 minutes, then placed in an ice bath for an additional 10 minutes. The reaction mixture was filtered over a sintered glass filter. A purple wine solid was obtained and washed repeatedly with deionized water until the filtrate was colourless. The solid was transferred to an Erlenmeyer flask and treated abundantly with CH₂Cl₂ to dissolve selectively Fe(TPP)Cl and separate it from iron oxides formed during the reaction. A deep green solution was obtained and separated by filtration over paper from reddish powders. Incidentally, these latter were found to be soluble in aqua regia. The CH₂Cl₂ solution was brought to dryness with a gentle stream of N₂, producing 185 mg of a deep purple microcrystalline solid (0.262 mmol, yield 67%).

ESI-MS: 668.2 m/z [Fe(TPP)]⁺ (loss of Cl⁻).

UV/Vis: λ_{max} 416 nm, 511 nm, 570 nm.

Elemental analysis: calculated for C₄₄H₂₈N₄FeCl C: 75.07% H: 4.01% N: 7.96%. Found C: 74.42% H: 4.17% N: 7.10%.

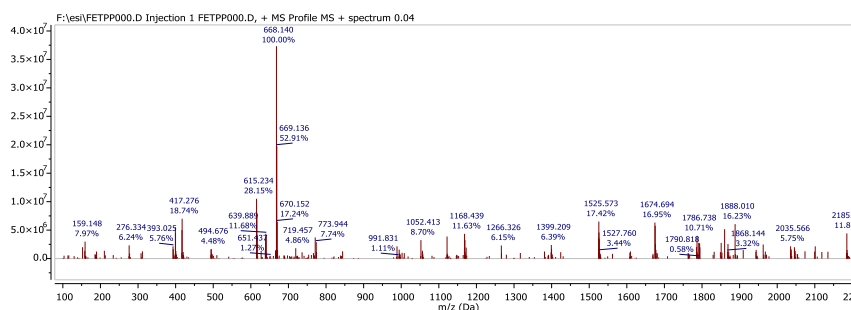


Figure 30. ESI-MS spectrum of 10⁻⁵ M Fe(TPP)Cl in methanol.

2. Electrochemical Conversion of CO₂ to CO by Fe^I Salophen complexes

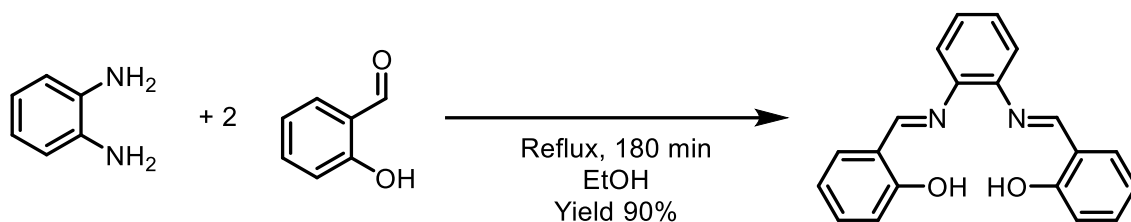
The following Chapter is the *compte rendu* of the work we carried out on the role of Fe(Salophen) complexes as molecular catalysts for the electrochemical reduction of CO₂. The work involved a collaboration between the Nano and Molecular Catalysis group and Prof. Marc Robert (Université Paris Diderot) and saw the contribution of other students (Roberto Altieri and Mirko Tagliapietra), in conducting preliminary investigations and key preparative-scale experiments.

2.1 Rationale

Different fields of catalysis have extensively used Schiff base-type complexes. Transition metal compounds of variously functionalized Schiff base ligands have been specifically used as Lewis acids and redox catalysts. Specifically, Salophen (N,N'-ortho-Phenylenebis(salicylimine)) ligand is easily synthesizable from commercially available reagents and represents a widely used ligand for metal catalysts in several fields.¹⁶⁷In particular, the electrochemical properties of Fe(Salophen)Cl have been the subject of seminal research in the field of electrocatalysis by Bond and co-workers, that identified sequential reduction of the Fe^{III} center to Fe^{II} and finally to Fe^I, with this latter species being electrocatalytically active towards reductive dehalogenation of benzyl halides.¹⁶⁸ Furthermore, the analogue cobalt(II) Salophen complex was reported as a CO₂-to-CO reduction electrocatalyst in DMF in the presence of Li⁺ by Isse *et al.*, involving an electrogenerated cobalt(I) active intermediate.¹²³ Indeed, several examples in the literature showed a common, privileged ligand choice for the design of cobalt and iron CO₂ reduction catalysts. These findings prompted us to study Fe(Salophen)Cl as a potential molecular catalyst for the electrochemical reduction of carbon dioxide. The work detailed herein accounts for the research done on the use of Fe(Salophen) complexes as molecular catalysts for CO₂ reduction.

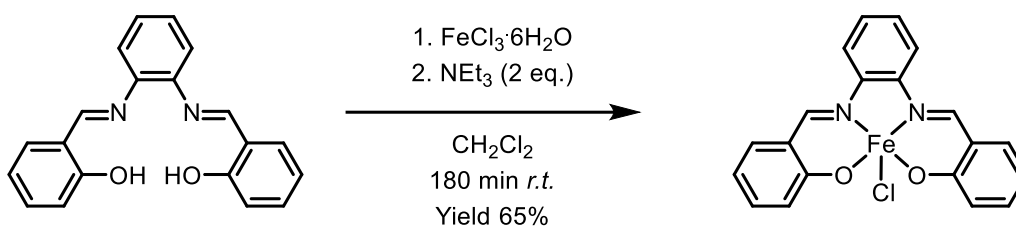
2.2 Synthesis of the Salophen ligand and of its iron complexes, $\text{Fe}(\text{Salophen})\text{Cl}$ and $\text{Fe}_2(\text{Salophen})_2(\mu\text{-O})$

Schiff base ligands are generally easily obtainable upon reaction of an aliphatic or aromatic diamine with salicylaldehyde derivatives. Specifically, the reaction of 1,2-diaminobenzene with two equivalents of salicylaldehyde in ethanol easily affords Salophen as orange crystals, according to Scheme 1.¹⁶⁸



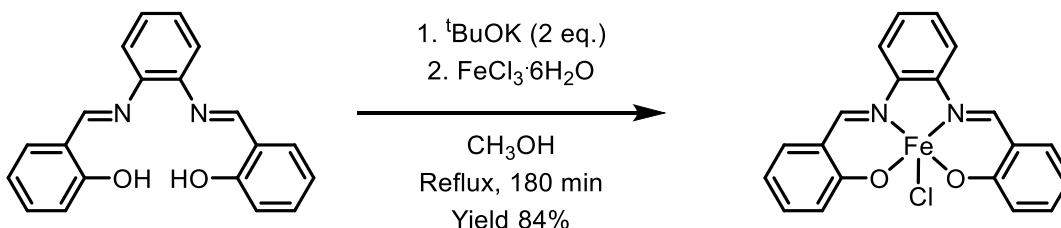
Scheme 1. Synthesis of the Salophen ligand.

Iron in its trivalent state can readily form two closely related coordination compounds with the Salophen ligand, a mononuclear and a dinuclear species. The formation of either complex is determined by the choice of reaction conditions and of the iron source. Specifically, mononuclear $\text{Fe}(\text{Salophen})\text{Cl}$ is obtainable when FeCl_3 is used as an iron salt precursor. The synthesis of $\text{Fe}(\text{Salophen})\text{Cl}$ requires the presence of a stoichiometric base to aid complex formation by deprotonating the phenol moieties. The first explored procedure is a variation of the literature synthesis, which requires triethylamine (NEt_3) as the base (Scheme 2).¹⁶⁸ NEt_3 was slowly added to a mixture of excess $\text{FeCl}_3 \cdot 6\text{H}_2\text{O}$ and Salophen in dichloromethane (DCM). After stirring the mixture for 2 hours, the organic phase was extracted with milli-Q water and dried. Upon evaporation of the solvent, $\text{Fe}(\text{Salophen})\text{Cl}$ was recovered in 65% yield.



Scheme 2. Synthesis of $\text{Fe}(\text{Salophen})\text{Cl}$ by using NEt_3 as a base.

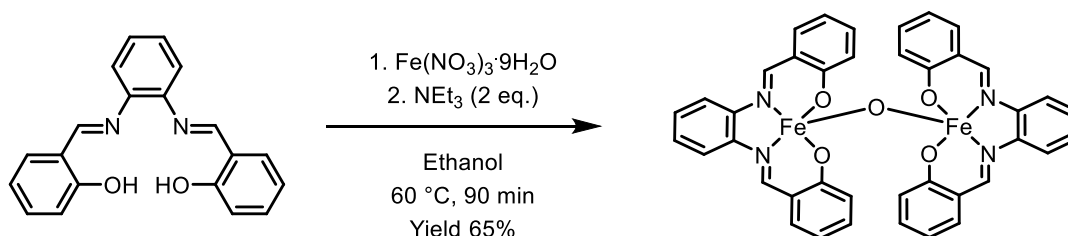
An alternative (Scheme 3) procedure was devised to synthesize $\text{Fe}(\text{Salophen})\text{Cl}$ while avoiding the extraction step. A stronger base (potassium tert-butoxide, ${}^t\text{BuOK}$) was used to quantitatively deprotonate Salophen generating its potassium salt in methanol.¹⁶⁹ A solution of $\text{FeCl}_3 \cdot 6\text{H}_2\text{O}$ (1.5 eq) in methanol was further added. After stirring under reflux, $\text{Fe}(\text{Salophen})\text{Cl}$ was isolated upon removal of the solvent and dissolution of the complex in DCM to remove insoluble inorganic salts. This procedure was proven effective in affording higher yields of the complex (>80%).



Scheme 3. Synthesis of $\text{Fe}(\text{Salophen})\text{Cl}$ using ${}^t\text{BuOK}$ as a base.

The use of ferric chloride is crucial when targeting a monomeric form of the iron-Salophen complex. Indeed, the use of any other Fe^{III} precursor leads preferentially to the dinuclear μ -oxo derivative. Literature reports featuring $\text{Fe}(\text{Salophen})$ with apical ligands different than the chloride ion rely either on their generation studied in solution or on the post-modification of $\text{Fe}(\text{Salophen})\text{Cl}$. Indeed, $[\text{Fe}(\text{Salophen})]\text{ClO}_4$ can be prepared by Cl^- displacement using AgClO_4 .^{170,171} Furthermore, Fe^{II} salts easily afford the dinuclear complex when the reaction is performed under oxygen-containing atmospheres, due to the high

sensitivity to O₂ of the divalent form of Fe(Salophen).^{172,173} In the present work, Fe₂(Salophen)₂(μ-O) was produced by allowing Fe(NO₃)₃·9H₂O to react with Salophen in the presence of NEt₃ in warm ethanol (Scheme 4). The complex was finally isolated as an orange solid upon centrifugation and washing with ethanol (yield 65%).



Scheme 4. Synthesis of Fe₂(Salophen)₂(μ-O).

2.3 Characterization of the complexes

Distinctive features between Fe(Salophen)Cl and Fe₂(Salophen)₂(μ-O) can be evidenced through electrospray ionization mass spectrometry (ESI-MS) and UV/visible spectroscopy (Figure 31 displays a comprehensive report of such data). In particular, ESI-MS spectra of both compounds exhibit an intense peak at $m/z = 370$, attributed to the [Fe(Salophen)]⁺ ion, while peaks attributed to dinuclear ions and centered at $m/z = 757$ ([Fe₂(Salophen)₂(μ-OH)]⁺) and 785 were observed only in the case of Fe₂(Salophen)₂(μ-O). Concerning UV/Vis spectroscopy, the two coordination compounds exhibit a notably different electronic absorption, consistent with literature references. A band peaking at 365 nm ($\epsilon = 1.3 \cdot 10^4 \text{ M}^{-1}\text{cm}^{-1}$) is observed for Fe(Salophen)Cl, while the dinuclear Fe₂(Salophen)₂(μ-O) complex is characterized by a redshifted maximum at 405 nm ($\epsilon = 2.0 \cdot 10^4 \text{ M}^{-1}\text{cm}^{-1}$); these spectral features, absent for the free ligand and characterized by high intensity and molar extinction coefficients, could therefore be appropriately described as charge-transfer bands between the Fe ions and the salophen ligand.

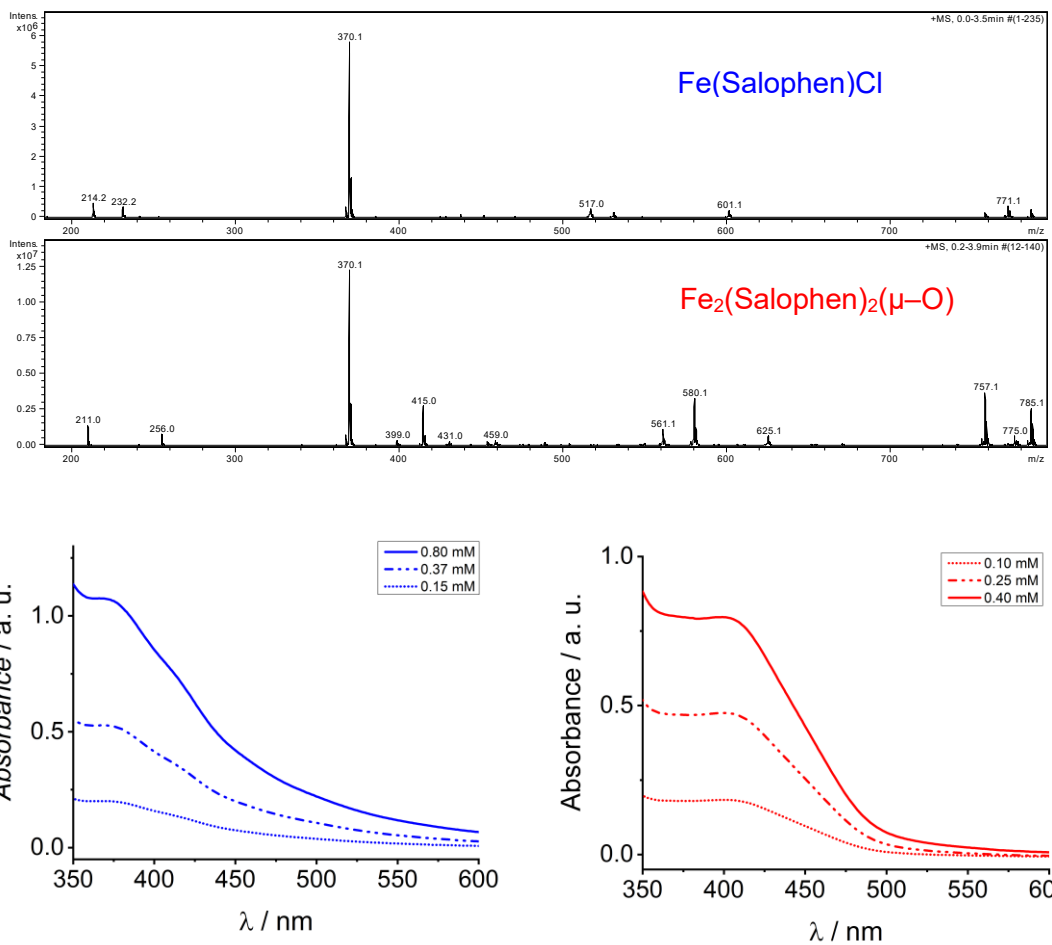


Figure 31. Top: ESI-MS spectra of 10^{-5} M $\text{Fe}(\text{Salophen})\text{Cl}$ in methanol, synthesized as per Scheme 2, and of 10^{-5} M $\text{Fe}_2(\text{Salophen})_2(\mu\text{-O})$ in methanol, synthesized as per Scheme 4. Bottom left: electronic absorption spectra of $\text{Fe}(\text{Salophen})\text{Cl}$ (0.15 ÷ 0.80 mM, blue traces). Bottom right: electronic absorption spectra of $\text{Fe}_2(\text{Salophen})_2(\mu\text{-O})$ (0.10 ÷ 0.40 mM, red traces).

2.4 Electrochemical properties of the complexes

The complexes were studied by means of cyclic voltammetry in acetonitrile (ACN), in the presence of 0.1 M tetraethylammonium tetrafluoroborate as supporting electrolyte, unless otherwise stated. Solutions were purged with N₂ to remove traces of O₂: this is a crucial step since the reduced forms of the complexes are reactive towards O₂ reduction. The working electrode was generally a glassy carbon disk electrode, the auxiliary electrode a gold disk electrode, and the reference electrode an Ag/AgCl (3 M NaCl) electrode. All potentials are reported against the ferricenium/ferrocene (Fc⁺/Fc) redox couple, added to the solutions as an internal standard.

2.4.1 Electrochemical Characterization of Fe(Salophen)Cl

Fe(Salophen)Cl displays a rich redox chemistry, proper of iron complexes with mixed-donor coordination spheres (Figure 32). As previously reported by Bond and co-workers, the starting Fe^{III} complex can undergo a quasi-reversible reduction at $E_{1/2} = -0.69$ V vs Fc⁺/Fc ($\Delta E = 77$ mV), attributed to the Fe^{III}/Fe^{II} conversion (wave A). This transformation is followed by a second cathodic event at $E_{1/2} = -2.01$ V vs Fc⁺/Fc (wave B). The latter process is ascribed to a Fe^{II} → Fe^I reduction, which however displays poor reversibility. The attribution relies on previous literature reports, based on the metal-centered reactivity of “Fe^I” with benzyl chloride.¹⁶⁸

The persistence of the chlorido ligand in the coordination sphere of Fe(Salophen) in the (+3), (+2), and (+1) oxidation states is met with general agreement, even in a coordinating solvent as ACN. However, successive reductions at the level of the iron complex result in an easier dissociation of the apical chloride, as observed in other iron complexes relevant to electrochemical catalysis schemes such as Fe porphyrins. This allows to represent the electrochemical reduction pathway leading from Fe^{III} to Fe^{II} *via* the formalism of “square schemes” (Scheme 5).³⁹

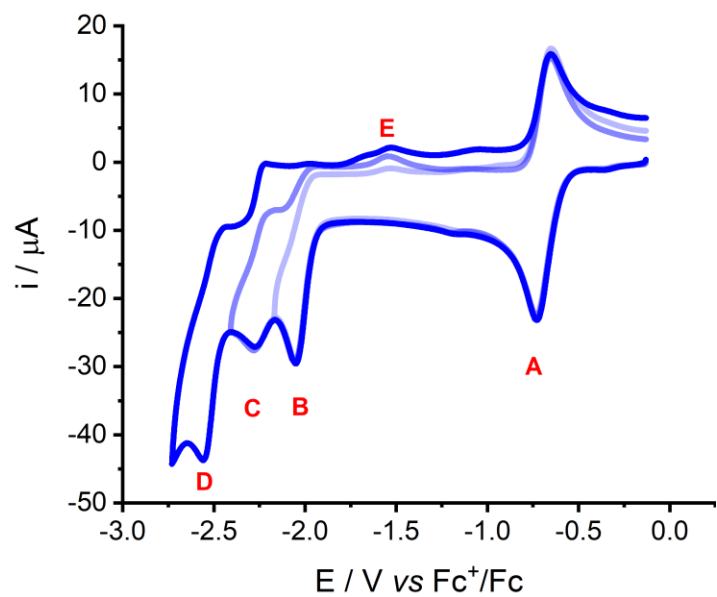
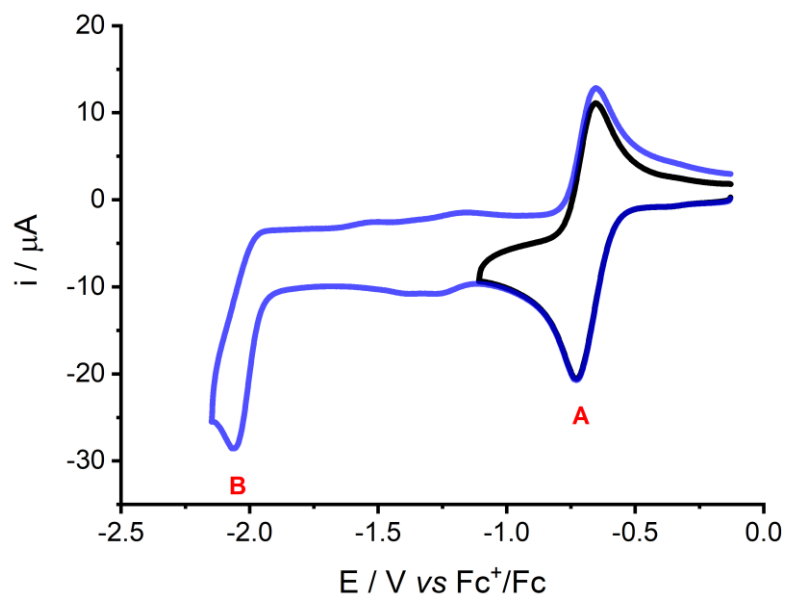
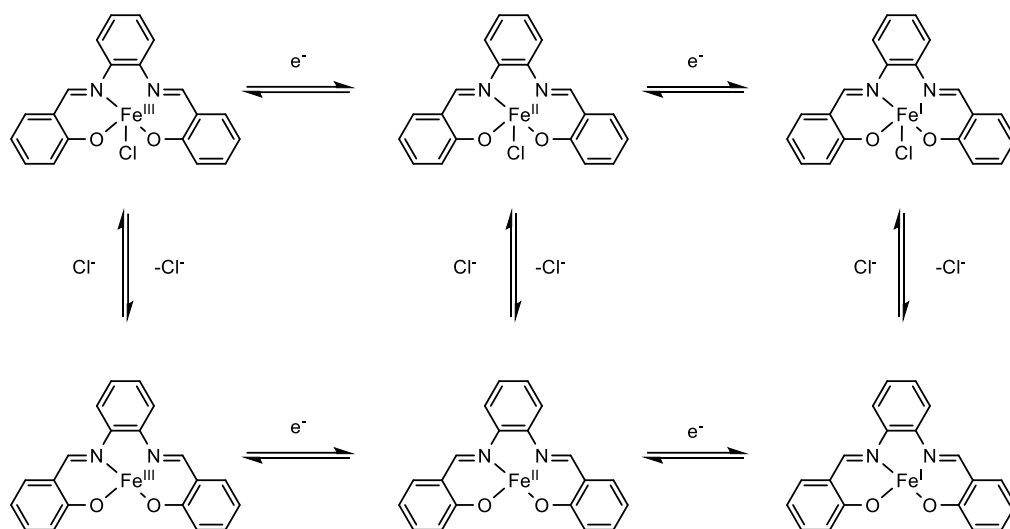


Figure 32. Top: CV traces under N_2 of 1 mM Fe(Salophen)Cl in ACN, restricted to the Fe^{III}/Fe^{II} (black trace) and Fe^{II}/Fe^I (blue trace) couples. Bottom: CV traces under N_2 of 1 mM Fe(Salophen)Cl in ACN, exploring potentials beyond the Fe^{II}/Fe^I couple. Scan rate: 0.1 V s^{-1} .



Scheme 5. Redox equilibria of Fe(Salophen)Cl involved at the level of the Fe^{III}/Fe^{II} and Fe^{II}/Fe^I couples.

Interestingly, two quasi-reversible one-electron reduction waves (wave C, $E_{1/2} = -2.20$ V vs Fc⁺/Fc and wave D, -2.48 V vs Fc⁺/Fc) may be observed upon increasing the explored potential range beyond the Fe^{II}/Fe^I cathodic peak. These redox events are likely ligand-based processes, given the redox-active nature of imine ligands as Salophen (*vide infra*). When the cathodic scan encompasses the cathodic peak D, a newly formed oxidation feature arises at $E_p = -1.53$ V vs Fc⁺/Fc, labeled peak E. The interpretation of such previously unreported findings is discussed in further detail in Section 2.10.

2.4.2 Electrochemical Characterization of Fe₂(Salophen)₂(μ-O)

For Fe₂(Salophen)₂(μ-O) (Figure 33) the first, quasi-reversible cathodic wave encountered in the forward scan is cathodically shifted ($E_{1/2} = -1.32$ V vs Fc⁺/Fc, $\Delta E = 100$ mV) and is attributed to the Fe^{III} to Fe^{II} reduction of both iron centers of the Fe–O–Fe μ-oxo bridge^{174–176}. The more negative potential required to reduce Fe^{III} to Fe^{II} in the dinuclear species with respect to the mononuclear one is in agreement with previous literature, and was observed also for iron porphyrin

analogues. This is likely attributed to electron transfer involving population of high energy π^* orbitals delocalized on the three Fe–O–Fe atoms in the dinuclear species. In addition, the non-reversibility of the wave was attributed to partial dissociation of the dinuclear species into two mononuclear units behaving independently. This was further confirmed by the two anodic peaks observed in the backward scan, at anodic peak potential $E_{p,a} = -1.28$ V vs Fc^+/Fc (re-oxidation of Fe^{II} to Fe^{III} in the dinuclear species) and at $E_{p,a} = -0.65$ V vs Fc^+/Fc , attributable to the re-oxidation of Fe^{II} to Fe^{III} in a mononuclear unit (Scheme 6). Regarding this last aspect, a similar behaviour was also observed for porphyrin analogues.¹⁷⁷ Scanning toward more negative potentials with $Fe_2(\text{Salophen})_2(\mu-O)$, a quasi-reversible wave at $E_{1/2} = -2.00$ V vs Fc^+/Fc was observed and attributed to the expected reduction of Fe^{II} to Fe^I in a mononuclear species.

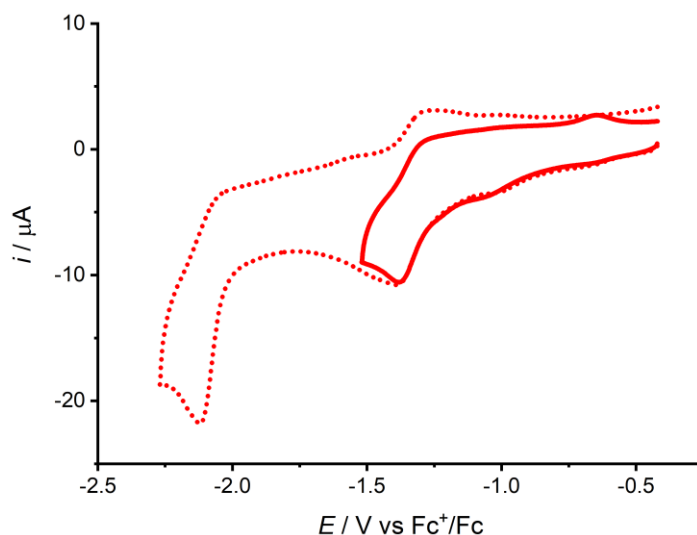
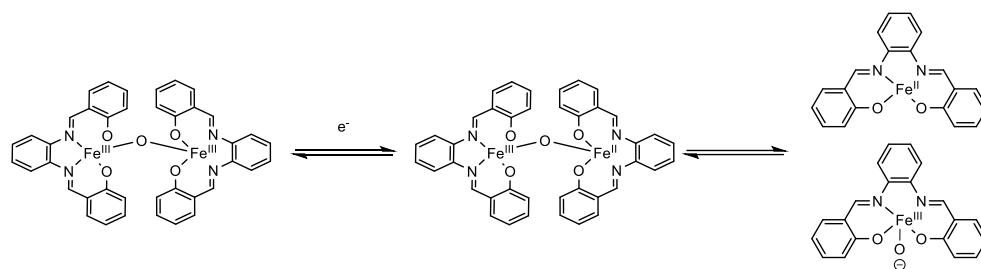


Figure 33. CV traces under N_2 of 0.4 mM $Fe_2(\text{Salophen})_2(\mu-O)$ in ACN. Scan rate: 0.1 $V s^{-1}$.



Scheme 6. Redox equilibria of $\text{Fe}_2(\text{Salophen})_2(\mu\text{-O})$ involved at the level of the $\text{Fe}^{\text{III}}/\text{Fe}^{\text{II}}$ couple in dinuclear and mononuclear species.

The formation of a common, mononuclear Fe^{I} species either starting from $\text{Fe}(\text{Salophen})\text{Cl}$ or from $\text{Fe}_2(\text{Salophen})_2(\mu\text{-O})$ was further confirmed by thin-layer spectroelectrochemistry in the UV/Vis region, that shows an identical absorption centered at 405 nm upon application of -2.00 V vs Fc^+/Fc potential for both complexes. The redshift with respect to the pristine Fe^{III} species is consistent with an iron-to-ligand charge transfer band from a reduced iron center.

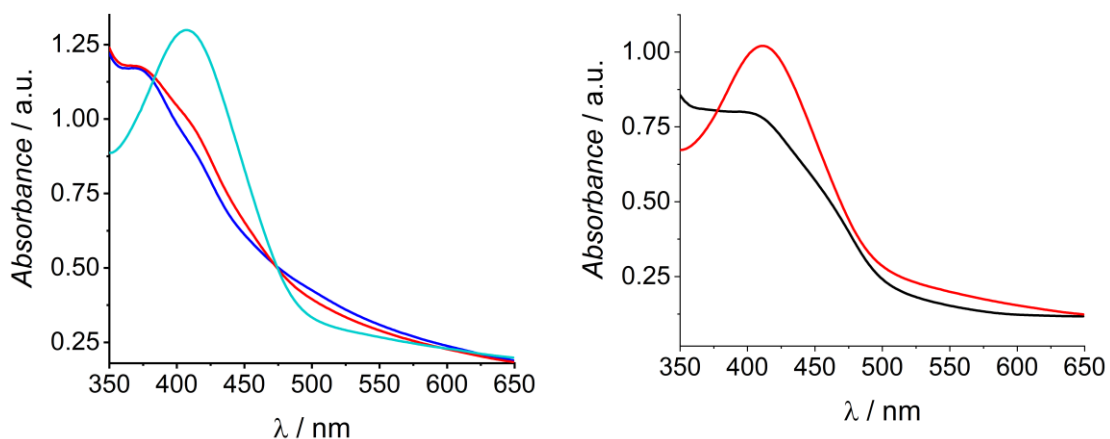


Figure 34. Left: spectroelectrochemistry in the UV/Vis region of $\text{Fe}(\text{Salophen})\text{Cl}$ at no applied potential (blue trace, Fe^{III} state), at -1.1 V vs Fc^+/Fc (red trace, Fe^{II} state), at -2 V vs Fc^+/Fc (cyan trace, Fe^{I} state). Right: spectroelectrochemistry in the UV/Vis region of $\text{Fe}_2(\text{Salophen})_2(\mu\text{-O})$ at no applied potential (black trace, $\text{Fe}^{\text{III}}\text{Fe}^{\text{III}}$ state), at -2 V vs Fc^+/Fc (red trace, Fe^{I} mononuclear state).

2.4.3 Interconversion of mononuclear and dinuclear species.

The distinctive spectral and electrochemical features of the mononuclear and dinuclear salophen-based Fe species allow their speciation in solution, and the investigation of their interconversion in the presence of Brønsted acids or bases or other chemical additives. From literature evidence and from chemical considerations regarding the nature of the complexes, the μ -oxo bridge binding the two Fe centers in the $\text{Fe}_2(\text{Salophen})_2(\mu\text{-O})$ should form between two mononuclear units in a base-induced condensation reaction.¹⁷⁶ Indeed, conversion of $\text{Fe}(\text{Salophen})\text{Cl}$ into $\text{Fe}_2(\text{Salophen})_2(\mu\text{-O})$ upon addition of NaOH was observed through cyclic voltammetry, that revealed the progressive abatement of the $\text{Fe}^{\text{III}}/\text{Fe}^{\text{II}}$ diagnostic peak for $\text{Fe}(\text{Salophen})\text{Cl}$ ($E_{1/2} = -0.69 \text{ V vs Fc}^+/\text{Fc}$), accompanied by a rise of the cathodic peak related to the dinuclear $\text{Fe}_2(\text{Salophen})_2(\mu\text{-O})$ ($E_{1/2} = -1.28 \text{ V vs Fc}^+/\text{Fc}$). Consistent results were obtained *via* spectrophotometric titration, upon addition of NaOH to a 0.8 mM solution of $\text{Fe}(\text{Salophen})\text{Cl}$ (Figure).

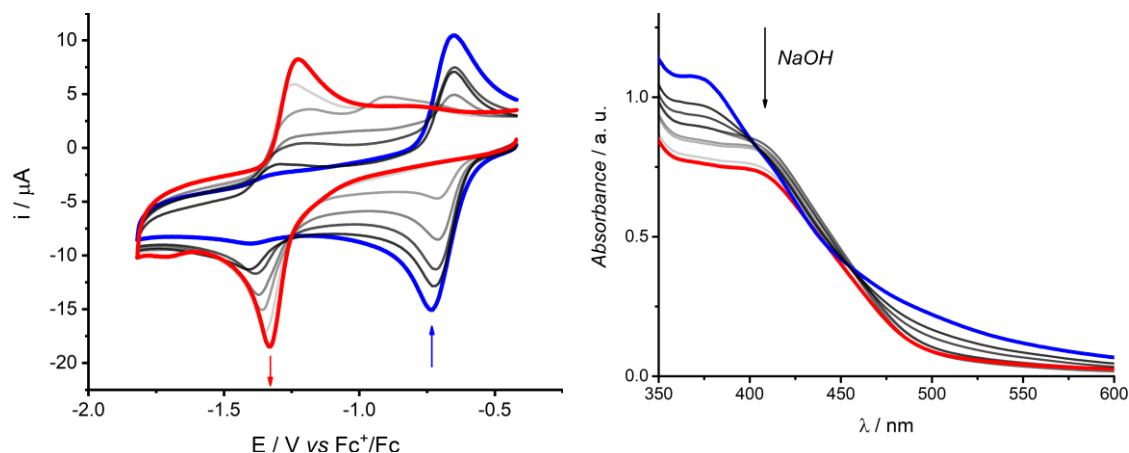
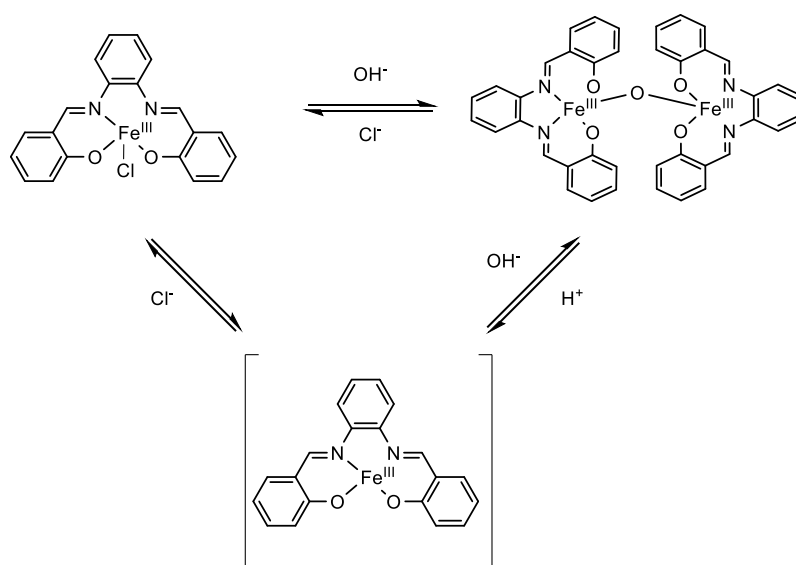


Figure 35. Left: CV traces under N_2 of 0.8 mM $\text{Fe}(\text{Salophen})\text{Cl}$ in ACN upon progressive addition of NaOH ; it is worth highlighting that in these CV the wave at -1.25 V attributed to the dinuclear species has a higher degree of reversibility with respect to the one registered for the $\text{Fe}_2(\text{Salophen})_2(\mu\text{-O})$ (see Figure 33); the reversibility of the process was indeed shown to depend on the presence of Lewis acid cations. Scan rate: 0.1 V s^{-1} . Right: electronic absorption spectra of 0.8 mM $\text{Fe}(\text{Salophen})\text{Cl}$ in ACN upon addition of NaOH , showing the progressive conversion to the dinuclear complex.

On the opposite site, protolysis of the μ -O bridge in the presence of Brønsted acids leads to the formation of mononuclear units $\text{Fe}(\text{Salophen})^+$ from $\text{Fe}_2(\text{Salophen})_2(\mu\text{-O})$; $\text{Fe}(\text{Salophen})^+$ may lead to the formation of $\text{Fe}(\text{Salophen})\text{Cl}$ in the presence of chloride ions. The reversible interconversion between mononuclear and dinuclear species can be summarized in Scheme 7; in particular, the conversion of dinuclear into mononuclear species in the presence of proton donors is of relevance since the presence of a proton source is typically needed when investigating the electrocatalysis of CO_2 reduction. The intrinsic instability of the μ -oxo bridge under the conditions for electrochemical CO_2 reduction hampers an evaluation of the impact of the nuclearity of the iron complex on the reactivity in the present case (*vide infra*).



Scheme 7. Proposed equilibria among mononuclear and dinuclear iron complexes with salophen ligand.

The acid chosen to study protolysis of the oxo bridge was acetic acid (HAc), mildly strong in CH_3CN ($\text{pK}_a = 23.51$).¹⁷⁸ Upon addition of acetic acid (Figure 36), an initial decrease of the peak current at -1.38 V vs Fc^+/Fc is observed, while a new cathodic peak at -1.11 V vs Fc^+/Fc arises. This latter undergoes a cathodic shift

up to -1.00 V vs Fc^+/Fc upon increasing the concentration of acetic acid. Finally, in the presence of 8.5 mM HAc, the only feature is a reversible wave, attributed to the $\text{Fe}^{\text{III}}/\text{Fe}^{\text{II}}$ couple of a mononuclear species ($E_{1/2} = -0.72$ V vs Fc^+/Fc , $\Delta E_p = 100$ mV). The proposed acid-induced cleavage of the μ -oxo bridge involves a protonated dinuclear complex $[\text{Fe}_2(\text{Salophen})_2(\mu\text{-OH})]^+$, formed in an acid:iron substoichiometric regime.

This μ -hydroxo bridged dinuclear complex dissociates forming two mononuclear units upon further protonation. The mononuclear salophen complex generated by the protolysis of the μ -oxo dinuclear compound, generically indicated as $\text{Fe}(\text{Salophen})^+$, likely bears acetate ligands that are not explicitly indicated. Indeed, hexacoordination is expected *via* the intervention of the conjugate base of the acid and/or by solvent molecules.

When the electrochemical behaviour of $\text{Fe}_2(\text{Salophen})_2(\mu\text{-O})$ is studied in acetonitrile with 0.1 M tetrabutylammonium chloride as both the supporting electrolyte and a chloride source (Figure 36), the feature attributed to the $\text{Fe}^{\text{III}}/\text{Fe}^{\text{II}}$ couple of $\text{Fe}(\text{Salophen})\text{Cl}$ is observed ($E_{1/2} = -0.67$ V vs Fc^+/Fc , $\Delta E_p = 60$ mV). The blue portion of the curve in Figure 36 encloses such feature. This indicates, as previously discussed, that the dinuclear complex may be subjected to conversion to $\text{Fe}(\text{Salophen})\text{Cl}$, induced by the presence of chloride anions.

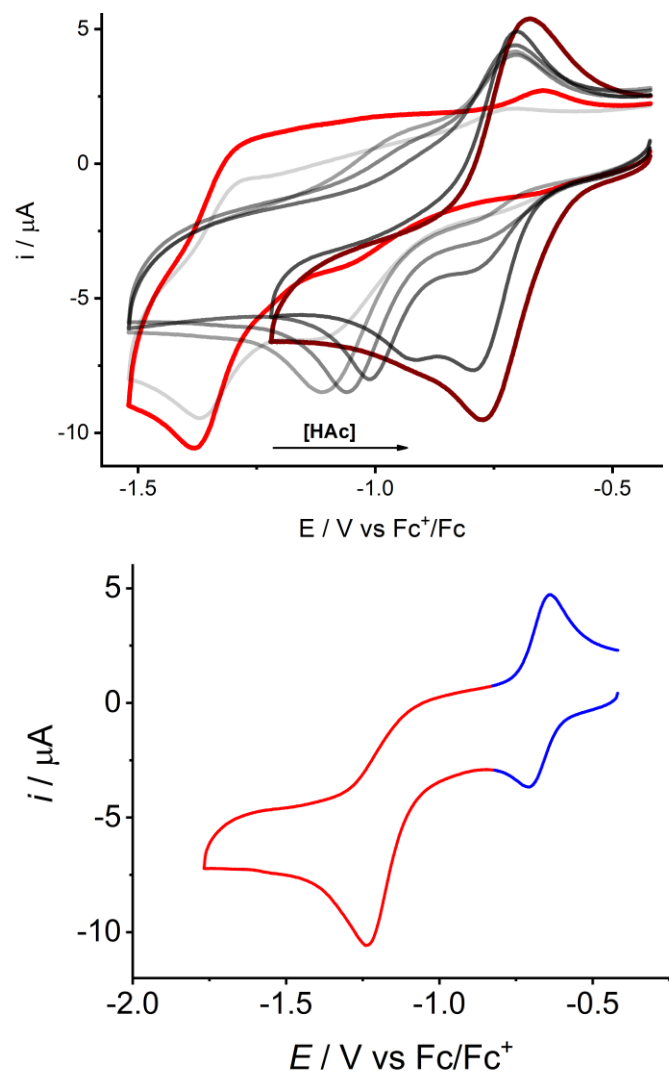


Figure 36. Top: CV traces under N_2 of 0.4 mM $Fe_2(Salophen)_2(\mu-O)$ in ACN upon addition of acetic acid. Bottom: CV trace of 0.4 mM $Fe_2(Salophen)_2(\mu-O)$ in the presence of 0.1 M tetrabutylammonium chloride (TBACl) as supporting electrolyte and chloride source; the blue and red parts of the CV trace indicate waves attributed to $Fe(Salophen)Cl$ and $Fe_2(Salophen)_2(\mu-O)$, respectively, with $Fe(Salophen)Cl$ forming from $Fe_2(Salophen)_2(\mu-O)$ in the presence of Cl^- from the support electrolyte. Scan rate: 0.1 Vs^{-1} .

2.5 Electrochemical behavior of Salophen Fe complexes in the presence of carbon dioxide

The voltammogram of CO₂-saturated (0.28 M in ACN) solutions of Fe(Salophen)Cl and Fe₂(Salophen)₂(μ-O) is reported in Figure 37. For what concerns the Fe^{III}/Fe^{II} couple, no significant changes are observed; the Fe^{II}/Fe^I reduction peak, however, is affected by the presence of carbon dioxide, undergoing a two- to three-fold enhancement of the cathodic peak current. The registered peak current increase might be regarded as an electrocatalytic contribution, as previously reported for the analogous Co^{II} complex, where the increase of cathodic current under similar conditions was attributed to the electrochemical reduction of CO₂ to CO with formation of carbonate.¹²³ Incidentally, the irreversible Fe^{II}/Fe^I peak shape, potential and current are similar for both mononuclear and dinuclear Fe catalysts, thus suggesting the occurrence of a redox process involving a common mononuclear Fe^I intermediate (*vide supra*).

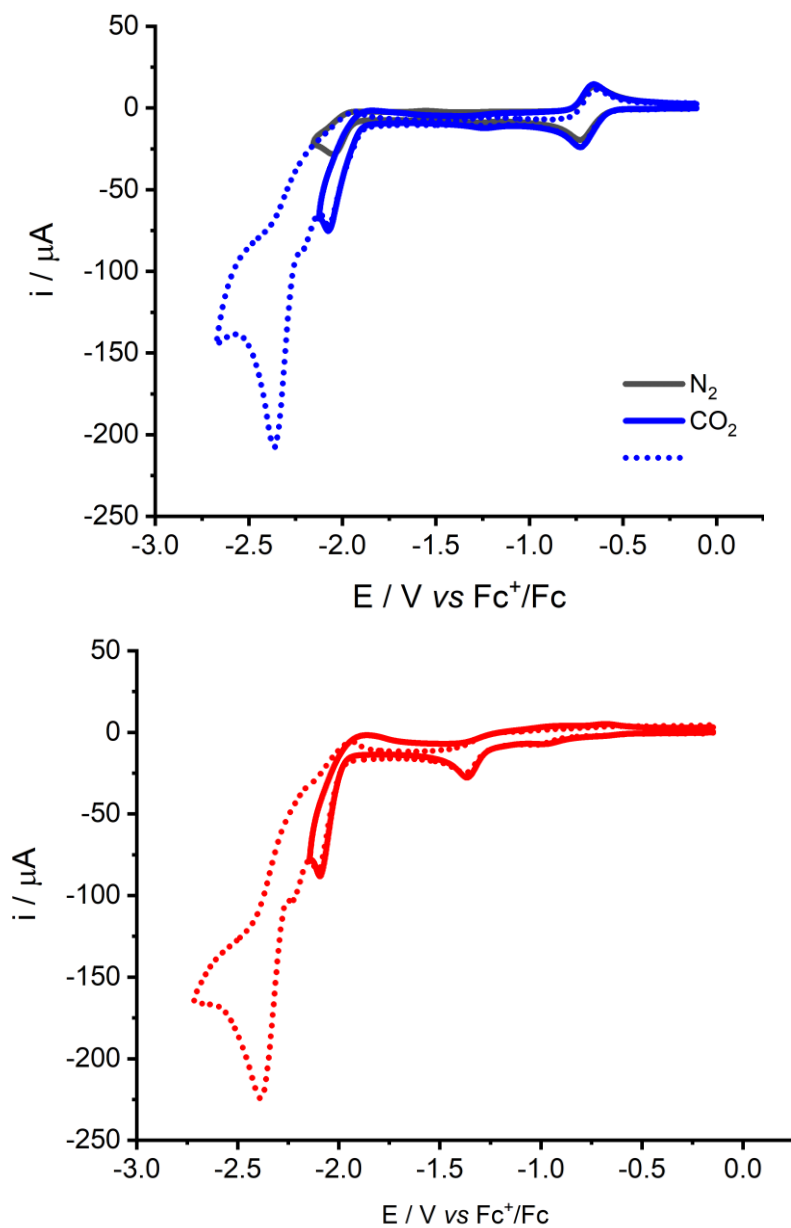


Figure 37. CV traces of 1 mM Fe(Salophen)Cl (top) and 0.5 mM Fe₂(Salophen)₂(μ-O) (bottom) in ACN under CO₂ atmosphere. For Fe(Salophen)Cl, the trace under N₂ atmosphere is provided for comparison (black trace). Scan rate: 0.1 Vs⁻¹.

A further confirmation came from similar traces observed under spectroelectrochemistry in the infrared region (SEC-IR), a widely exploited tool for characterizing binding and reduction of CO₂ at metal centers. The differential IR spectra obtained for Fe(Salophen)Cl and Fe₂(Salophen)₂(μ-O) along SEC-IR experiments in the presence of CO₂, conducted at the potential of the second reduction, are reported in Figure 38. The low frequency, intense positive absorptions bands at 1883 cm⁻¹ and 1913 cm⁻¹ are reasonably attributed to the C–O stretching in an iron-carbonyl intermediate, originated from iron-assisted C–O bond breaking of carbon dioxide¹⁷⁹. Consistently, oxide transfer to a second molecule of CO₂, in the presence of traces of water in the SEC cell, leads to hydrogen carbonate as supported by the positive absorptions bands at 1679, 1646 and 1306 cm⁻¹. Finally, the negative absorptions at 2357 and 2324 cm⁻¹ are ascribed to CO₂ consumption along the electrolysis.¹⁷⁹

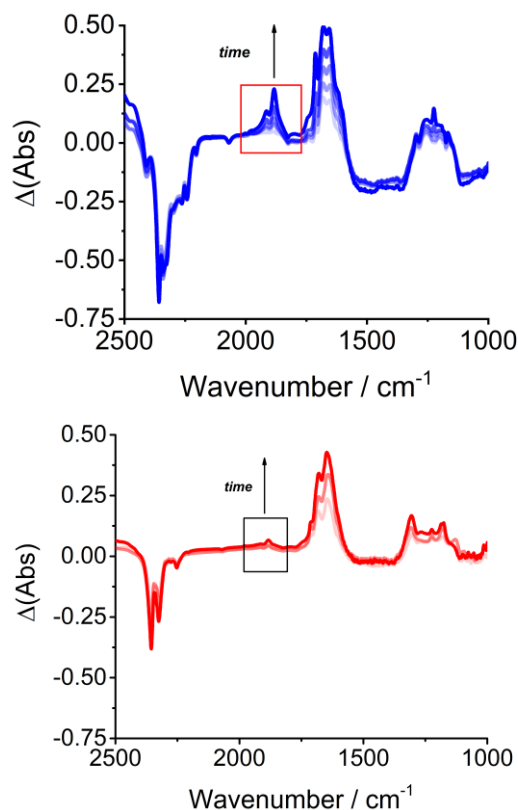


Figure 38. Spectroelectrochemistry in the IR range conducted at -2.1 V vs Fc⁺/Fc for 0.8 mM Fe(Salophen)Cl (top) and 0.4 mM Fe₂(Salophen)₂(μ-O) (bottom) in the presence of CO₂.

Fe^I reactivity towards CO₂ was further studied by *in situ* spectroelectrochemistry in the UV/Vis (SEC-UV/Vis). When electrolyzing a solution of Fe(Salophen)Cl at –2.1 V vs Fc⁺/Fc under a CO₂ atmosphere, the absorption maximum of Fe^I at 405 nm shifts to 385 nm in the presence of CO₂, which may be tentatively ascribed to the formation of the same iron carbonyl intermediate detected by SEC–IR (Figure 39, top). However, strongly informative evidence was garnered by *ex situ* SEC, performed to probe the reactivity of Fe^I towards CO₂ in conditions suitable to study CO₂ activation without turnover occurring. An electrolysis experiment was performed in a gas-tight electrochemical cell under N₂ atmosphere (Figure 39, bottom left; details about the experimental setup are provided in the Experimental Section of the present Chapter). A 0.8 mM Fe(Salophen)Cl solution was electrolyzed at –2.1 V vs Fc⁺/Fc to quantitatively generate the Fe^I species, thus obtaining a forest green solution. After the electrolysis, the solution was manipulated by cannulation to withdraw the Fe^I species for spectral analysis. The UV/Vis absorption spectrum (Figure 39, bottom right), registered under N₂ atmosphere, was found coherent with that of the Fe^I(Salophen) observed by *in situ* UV/Vis SEC, with a charge transfer optical band peaking at 405 nm. Afterwards, the reactivity of the Fe^I towards CO₂ was probed by bubbling CO₂ for 30 s into the Fe^I(Salophen) solution in the working compartment of the electrolysis cell. An instantaneous colour change of the Fe^I(Salophen) solution to bright orange was observed. The solution (incidentally found to be indefinitely stable in air) was withdrawn by cannulation under a pressure of CO₂ and analyzed by UV/Vis spectrophotometry. Features coherent with a Fe^{III} species were observed: this result suggests the reactivity of Fe^I intermediate towards CO₂, associated to the oxidation of the iron center.

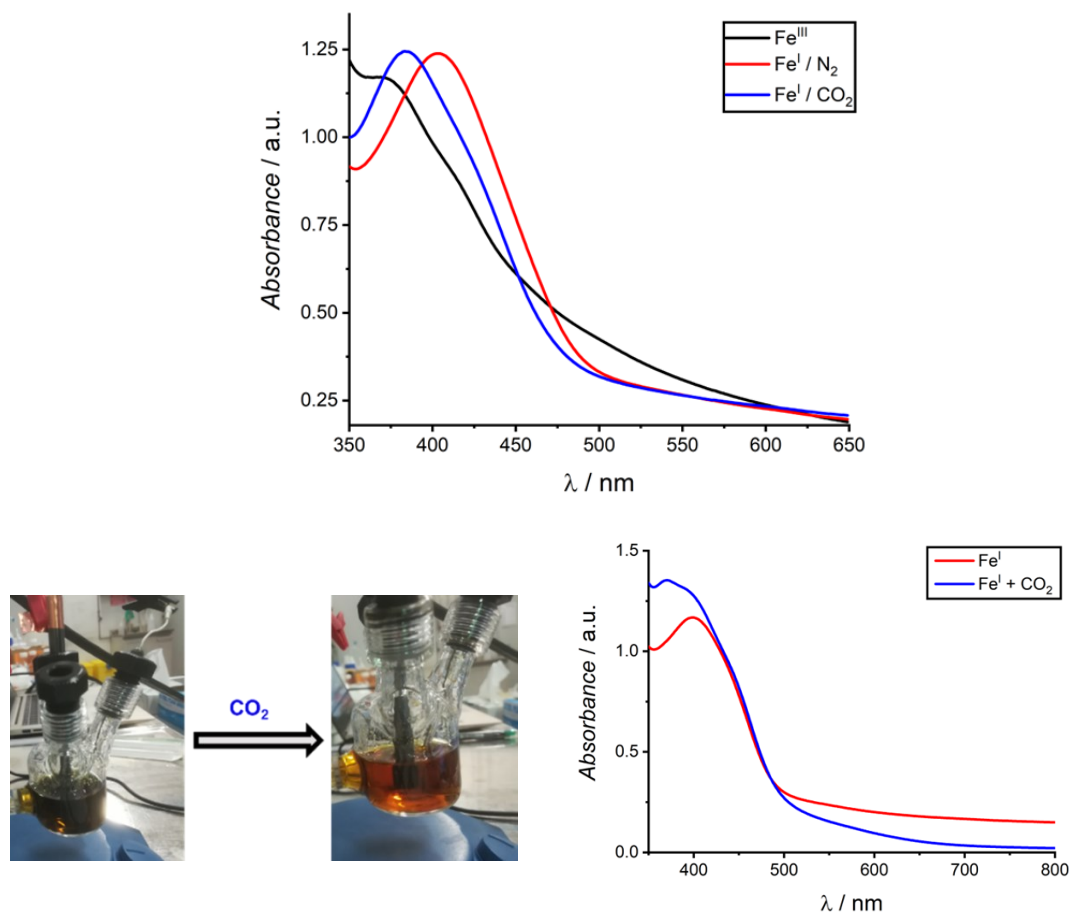


Figure 39. Top: spectroelectrochemistry in the UV/Vis of 0.8 mM Fe(Salophen)Cl under N₂ atmosphere at no applied potential (black trace), and at -2.1 V vs Fc⁺/Fc under N₂ (red trace) and CO₂ (blue trace) atmosphere. Bottom left: picture of the electrochemical cell containing Fe^I(Salophen) produced by electrolysis at -2.1 V vs Fc⁺/Fc before and after addition of CO₂. Bottom right: electronic absorption spectra of the Fe^I(Salophen) solution before (blue trace) and after (red trace) addition of CO₂.

Further evidence of reactivity and oxidation of Fe^I in the presence of CO₂ came from electron paramagnetic resonance (EPR) spectroscopy, performed in collaboration with Dr. Antonio Barbon (University of Padova) as *ex situ* EPR spectroelectrochemistry (Figure 40). For a frozen sample of the electrogenerated Fe^I state, a signal at 3450 G ($g \approx 2$) is observed at 80 K, which is consistent with a $S = 1/2$ for a d⁷ low-spin Fe^I;¹⁸⁰ in the sample treated with CO₂, the signal above disappears, while the appearance of a broad band at *circa* 3330 G and the raising

of a feature at 1600 G ($g \approx 4.3$) are observed. These features are consistent with a d^5 high-spin Fe^{III} with a high degree of rhombicity,¹⁷⁹ formed upon reaction of Fe^{I} with CO_2 . Interestingly, although indicative of a Fe^{III} state, this spectrum is different from the one of $\text{Fe}^{\text{III}}(\text{Salophen})\text{Cl}$, that displays a signal at low fields at $g = 8.6$ indicative of a smaller degree of rhombicity, likely ascribable to different apical ligands.

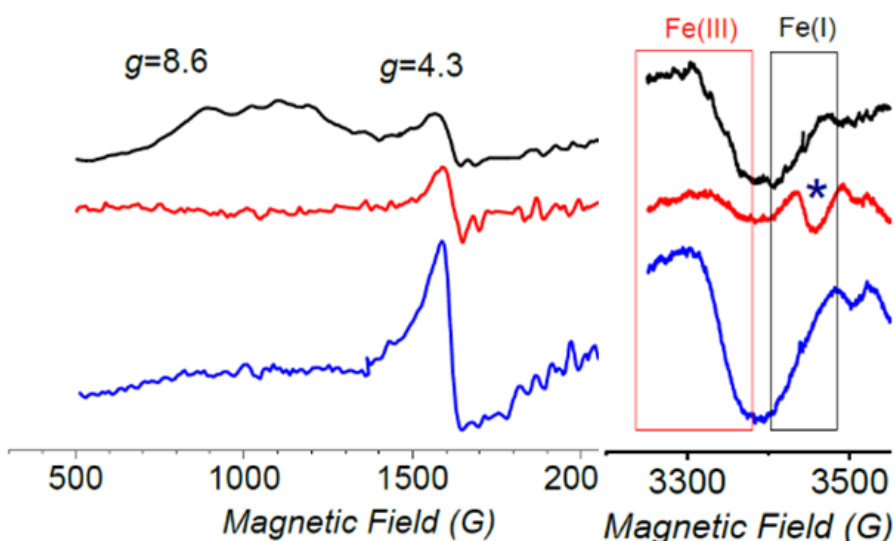


Figure 40. cw-EPR spectra in the regions $g = 4$ to 9 ca (left) and around $g = 2$ (right), relative to the position of most relevant Fe bands taken at 80 K for a series of samples: (black trace) $\text{Fe}(\text{Salophen})\text{Cl}$ prior to electrolysis (Fe^{III} state); (red trace) after electrochemical reduction to Fe^{I} state under inert atmosphere and (blue trace) after exposure to CO_2 (spectral characteristics of Fe^{III} , formed following Iron- CO_2 reaction). In the right panel the region for classical Fe^{III} bands is highlighted, as well as that for Fe^{I} (the only visible band is starred).

After the first peak observed under a CO_2 atmosphere, a further irreversible multi-electron cathodic wave was observed peaking at -2.40 V vs Fc^+/Fc (Figure 37). An analogous, composite peak is observed for $\text{Fe}_2(\text{Salophen})_2(\mu\text{-O})$. This latter wave is ascribed as well to electrocatalytic CO_2 reduction. The interpretation of

the voltammogram can be guided by insights based on previous studies on Fe(qpy) and Co(qpy) complexes by Cometto *et al.*⁵⁸ Specifically, the formation of a Fe–CO₂ adduct occurring at the level of the Fe^I species is indicated by the irreversible nature of the peak observed under CO₂ atmosphere. However, CO₂ binding is not the sole event occurring, the transformation being multi-electronic in nature and suggestive of a productive mechanism eventually leading to the Fe–CO adduct identified *via* SEC-IR. The catalytic transformation would therefore require further activation, being sluggish in the absence of proton donor coadjutants at the potential whereupon CO₂ binding by Fe^I is observed. Further reduction of the adduct could then provide a more efficient turnover under dry condition, in a scheme suggestive of two waves pertaining to the same catalytic reaction, *i.e.* CO₂-to-CO reduction. Nonetheless, this latter statement was not further investigated, on the premises here anticipated:

- i) Catalysis can be attained at the level of the first wave under optimized conditions;
- ii) Parasitic reactions leading to catalyst deactivation are more pronounced as the potential of the working electrode becomes more cathodic towards the potential of the second wave (*vide infra*).

Regardless, it is noteworthy that, when the potential is explored along voltammetric experiments, the level of both irreversible peaks observed under CO₂ in the absence of deliberately added proton donors, the Fe^{II} → Fe^{III} anodic peak remains unaltered. This indicates that, at least in the timescale of the CV, no appreciable degradation of the catalyst occurs.

Nonetheless, the current enhancement associated with the generation of the electroactive iron(I) species observed in the CV traces in the presence of CO₂ is modest. By assuming a reductive catalytic process in which carbon dioxide is involved, the observation may be related to the absence of a catalyst coadjutant, in particular of a suitable proton donor.

2.6 Electrochemistry in the presence of Phenol

The chemical and electrochemical properties of the iron salophen species were thus investigated in the presence phenol (PhOH) serving the function of Brønsted acid. Incidentally, acetic acid and water were also examined, although the unencouraging results (fast decomposition, inefficient catalysis) led us not to investigate catalysis in the presence of these proton donors.

In particular, phenol provided the most interesting results, based on its effectiveness as CO₂ reduction activity enhancer, already used in several literature examples of iron-based molecular catalysts.¹⁸¹ This particular CO₂-oriented selectivity of phenol with respect to other proton donors may be related to its mild acidity ($pK_a = 29.14$ in acetonitrile)¹⁷⁸, that hampers the formation of iron hydride intermediates and their subsequent reaction with protons to form hydrogen.

Binding interactions of Fe(Salophen) complexes with PhOH are relevant to CO₂ reduction catalysis, given the importance of proton-coupled electron transfer events in kinetically crucial steps. Specifically, the reactivity of Fe(Salophen)Cl and Fe₂(Salophen)₂(μ -O) was studied by means of cyclic voltammetry restricted to the Fe^{III}/Fe^{II} redox couple. A thorough discussion of the experimental results is provided in Appendix 2. Briefly, the complexes were found to be interacting with two molecules of PhOH. The interaction may be rationalized in terms of:

- i) Coordination of PhOH or PhO⁻ to the iron center, in competition with Cl⁻ binding; this contribution is believed to be the most substantial.
- ii) Association by means of protonation and/or hydrogen bonding with the ligand scaffold.

2.6.1 Fe^I reactivity towards phenol

When the potential was scanned to reach the potential range at which Fe^{II} is further reduced to Fe^I, in the presence of PhOH a multi-electron feature was registered as a peak-shaped wave at $E_p = -2.03$ V vs Fc⁺/Fc under N₂ atmosphere (Figure 41). This feature displayed peak currents invariably corresponding to 4 times those associated with the one-electron Fe^{III} → Fe^{II} reduction peak. The peak potential and current values were proven independent on the concentration of PhOH in the range 0.1 ÷ 2 M, thus leading to exclude a catalytic process. Based on the outcome of electrolysis experiments (*vide infra*), we are brought to hypothesize a ligand-centered reduction event occurring when the complex is reduced beyond the Fe^{II} state in the presence of a proton donor. Similar findings were reported for the free Salophen ligand and its Co complex, both undergoing electrochemical saturation of the imine functionalities in the presence of PhOH. At the present state, the possible role of the metal center in assisting such process, e.g., mediation of the hydrogenation of C=N bonds in an intramolecular fashion, is cautiously left void of attribution.¹⁸²

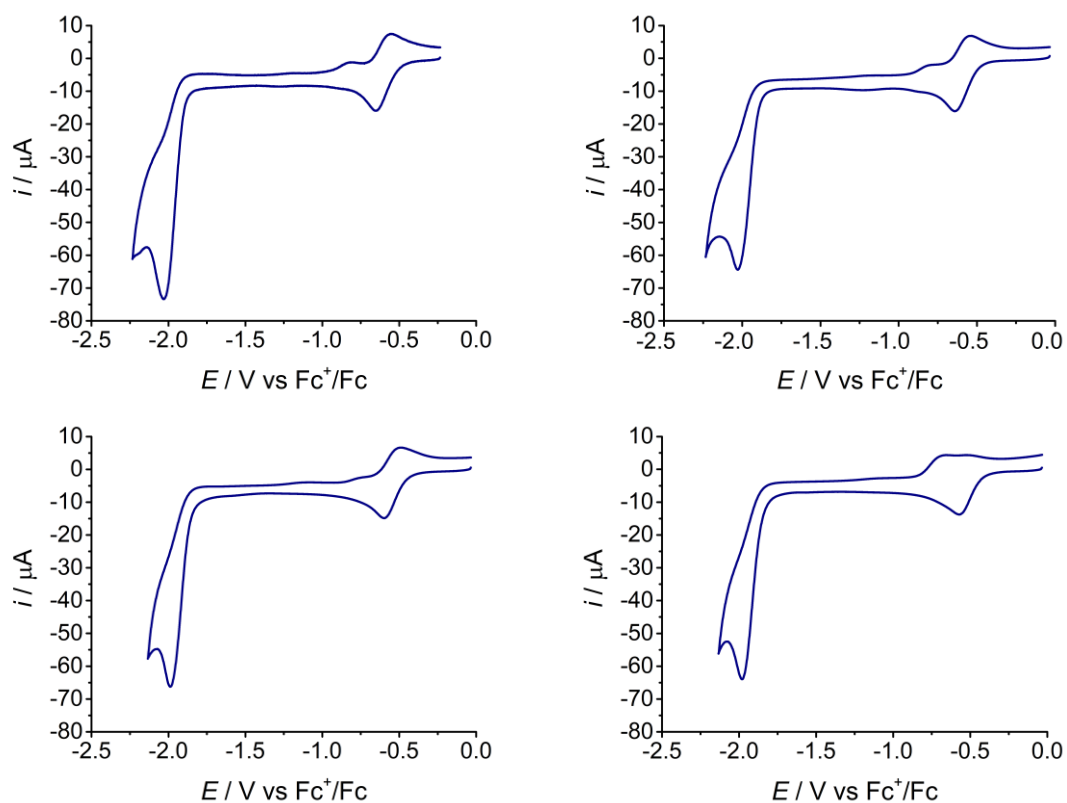


Figure 41. CV traces under N_2 atmosphere of 0.8 mM Fe(Salophen)Cl in ACN in the presence of PhOH 0.3 M (top left), 0.5 M (top right), 1.0 M (bottom left), 2.0 M (bottom right). Scan rate: 0.1 Vs^{-1} .

2.6.2 Catalytic CO_2 reduction in the presence of phenol

The scan towards more negative potentials is accompanied by the increase of the expected, intense and irreversible wave attributed to CO_2 reduction, at the potential of the $\text{Fe}^{\text{II}}/\text{Fe}^{\text{I}}$ couple. The peak potential E_{p,CO_2} is observed at $-1.99 \text{ V vs Fc}^+/\text{Fc}$, independently from phenol concentration, while the peak current i_{p,CO_2} raises from -86 to $-136 \mu\text{A}$ (corresponding to -1.22 to -1.92 mAcm^{-2}) upon increase of [PhOH], Figure 42. A visual analysis of the voltammogram reveals a peak-shaped wave,^[31,55] suggesting the interference of secondary phenomena competing with catalysis (*vide infra*; increase of the scan rate up to 10 Vs^{-1} did not change the current profile to an “S-shaped” wave).

Almost superimposable waves were observed in the voltammograms under CO_2 of $\text{Fe}(\text{Salophen})^+$ species deriving from $\text{Fe}_2(\text{Salophen})_2(\mu\text{-O})$ at the same nominal

iron concentration (0.8 mM, Figure 43), since the presence of phenol induces protolysis and cleavage of the Fe–O–Fe μ -oxo group, leading to the generation of the mononuclear Fe(Salophen)⁺ (Schemes 6 and 7 and previous discussion).

The catalytic wave of CO₂ reduction is followed by a further intense wave, characterized by a peak current of ca –130 μ A and by a peak potential that depends on phenol concentration and falls in the range –2.17 \div –2.00 V vs Fc⁺/Fc, with less negative values observed at high concentration of phenol. At the highest phenol concentrations employed (1 and 2 M), this wave partially superimposes with the catalytic wave of CO₂ reduction (Figure 42). Similar waves, observed also in the CV under N₂, are attributed to ligand-based reductions, eventually leading to catalyst demetallation and electrodeposition (further evidence will be provided by electrolysis experiments, *vide infra*).

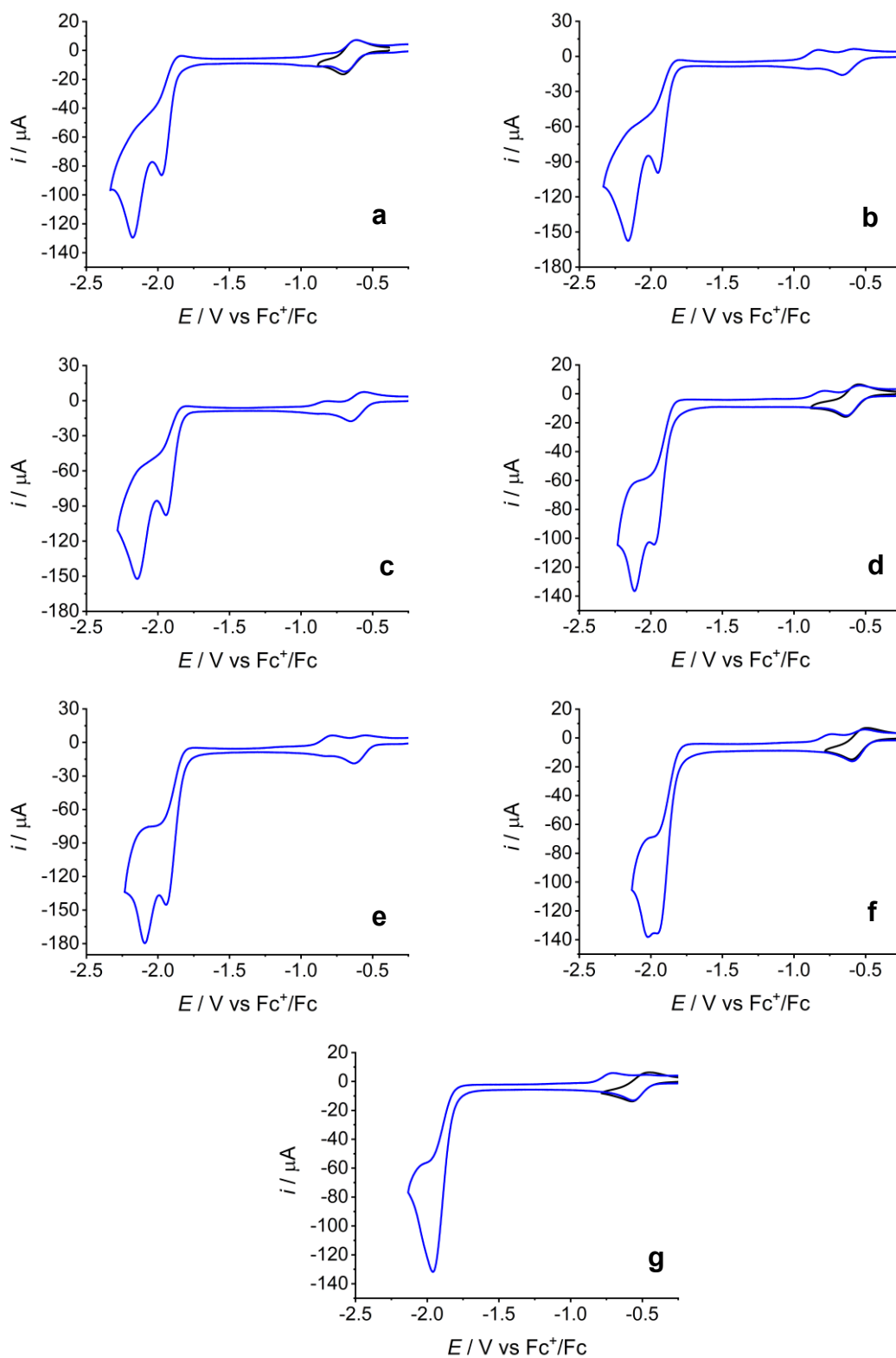


Figure 42. CV traces of 0.8 mM Fe(Salophen)Cl in ACN under CO_2 atmosphere in the presence of PhOH 0.1 M (a), 0.2 M (b), 0.3 M (c), 0.5 M (d), 0.6 M (e), 1 M (f), 2 M (g). Scan rate: 0.1 Vs^{-1} .

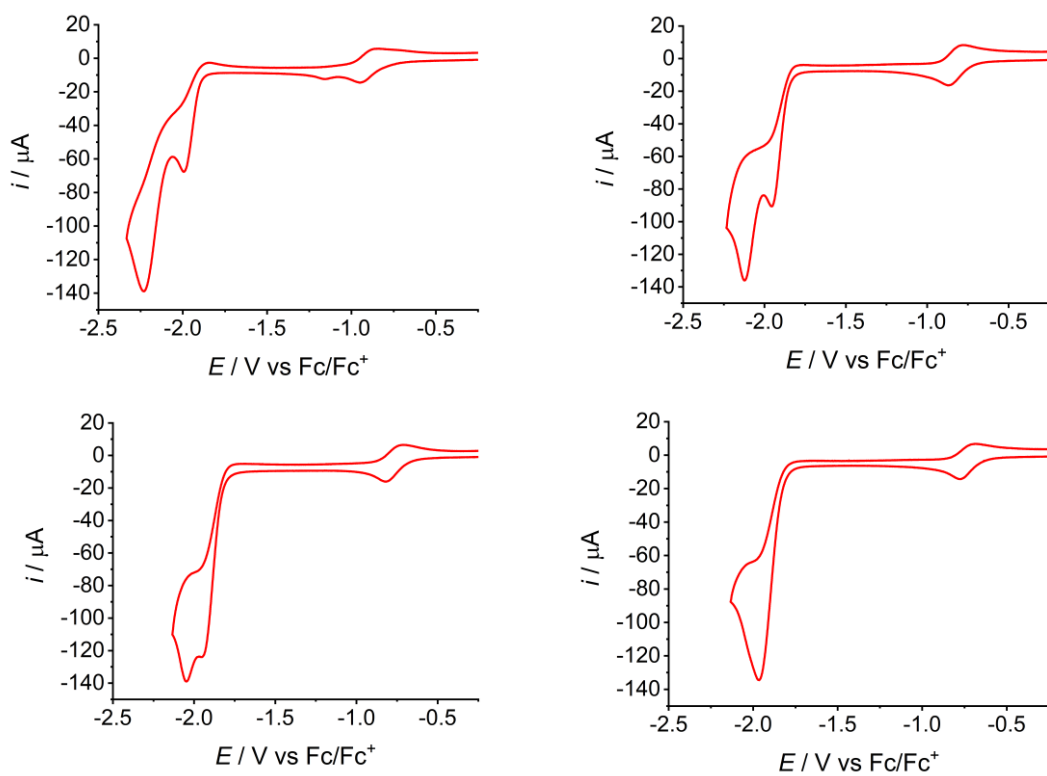


Figure 43. CV traces of 0.4 mM $\text{Fe}_2(\text{Salophen})_2(\mu\text{-O})$ in ACN under CO_2 atmosphere in the presence of PhOH 0.1 M (top left), 0.5 M (top right), 1 M (bottom left), 2 M (bottom right). Scan rate: 0.1 Vs^{-1} .

2.7 Preparative scale CO₂-to-CO electrochemical reduction

In order to characterize the electrochemical processes associated with these cathodic waves, constant potential electrolysis experiments (CPE) were conducted by employing a 2 cm² glassy carbon working electrode. Concerning the reaction products, both CO and H₂ were detected along the electrolysis, while no formic acid, methanol and other soluble products were observed. A control experiment employing ¹³CO₂ led to the formation of ¹³CO, thus confirming carbon dioxide as the source of the produced carbon monoxide (Figure 44).¹²⁴

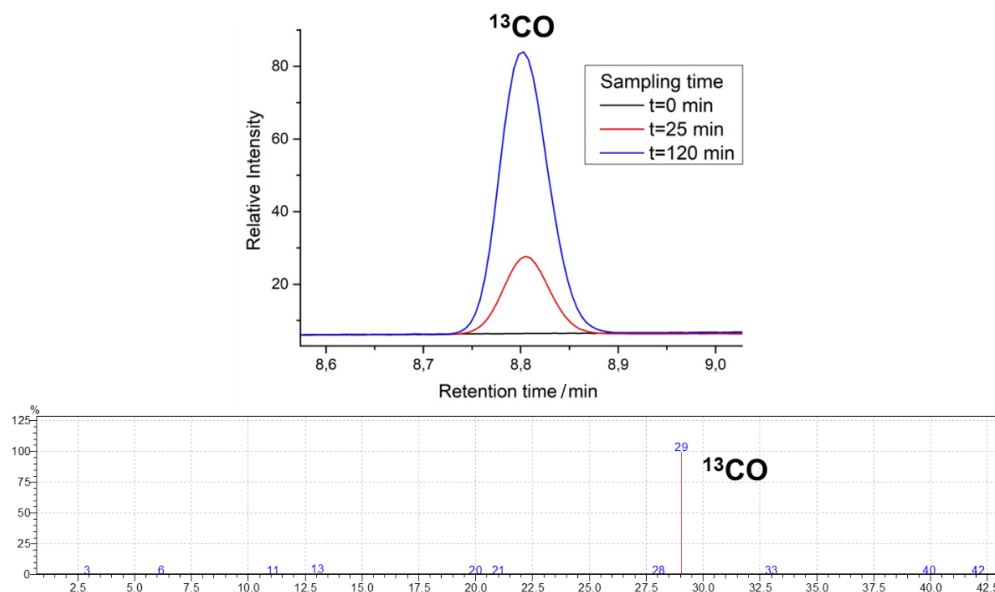


Figure 44. Top: chromatographic peak of ¹³CO at increasing electrolysis time. Bottom: mass spectrum of the eluted ¹³CO.

Interestingly, the formation of CO and H₂ showed markedly different profiles along the electrolysis, as can be appreciated in Figure 45, reporting the turnover number of Fe(Salophen)Cl for CO and H₂ (top left), the selectivity for CO (top right) and the Faradaic efficiency (bottom) as a function of the charge passed during electrolysis, normalized per iron center (Table 3). In particular, employing PhOH in the range 0.1 ÷ 1 M, CO was detected from the beginning of the electrolysis with selectivity in the range 90 ÷ 99% and Faradaic efficiency up to 59%, while

CO production suffers from a slowing down after *circa* 10 electrons passed per iron center (total TON for CO production of 3, with 0.5 M [PhOH]). Conversely, the H₂ profile showed an initial lag time followed by a rising of production, concomitant to the depletion of CO formation, that leads to a drop in selectivity of the process towards CO after *circa* 10 electrons passed per iron center in electrolysis (Figure 45; results are summarized in Table 3).

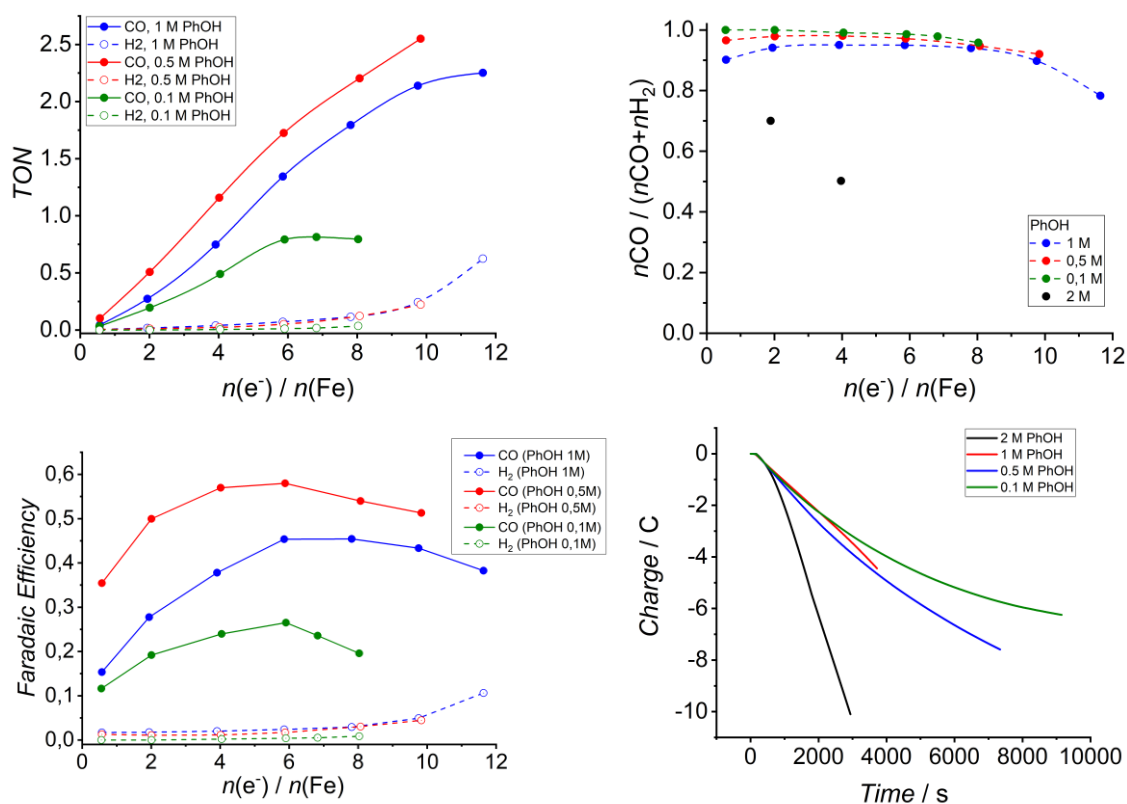


Figure 45. TON for CO and H₂ (top left), selectivity for CO (top right) and Faradaic efficiency (bottom left) vs the charge passed along electrolysis experiments (maximum electrolysis time was 3 h), normalized per Fe center as a function of phenol concentration (0.1÷1 M; regarding selectivity, two data points for the electrolysis at 2 M PhOH are also shown); charge vs time profiles in electrolysis experiments as a function of phenol concentration (0.1÷2 M) (bottom right). The CPE experiments were performed at -2.0 V vs Fc^+/Fc ; $Fe(Salophen)Cl$ 0.8 mM; tetraethylammonium tetrafluoroborate 0.1 M; 20 mL ACN saturated with CO_2 , at different concentrations of PhOH.

n(e ⁻)/n(cat)		F.E. CO (%)	F.E. H ₂ (%)	Selectivity F.E.(CO)·100/ (F.E.(CO)+F.E.(H ₂))
Phenol 2.0 M				
1.9		30	14	68
4.0		23	22	51
20		5	70	7
Phenol 1.0 M				
0.57		15.5	1.7	90
1.96		27.9	1.8	94
3.91		38.2	2.0	95
5.86		45.9	2.4	95
7.81		45.9	3.0	94
9.76		43.8	5.0	90
11.64		38.7	10.7	78
Phenol 0.5 M				
0.57		35.9	1.3	96
2.01		50.5	1.1	98
4.02		57.6	1.2	98
5.88		58.6	1.7	97
8.07		54.6	3.1	95
9.83		51.9	4.5	92
Phenol 0.1 M				
0.56		11.7	<0.1	>99
2.01		19.4	<0.1	>99
4.04		24.2	0.21	99
5.91		26.8	0.38	99
6.83		23.8	0.52	98
8.03		19.8	0.87	96

Table 3. Results of CPE experiments were performed at -2.0 V vs Fc^+/Fc ; $Fe(Salophen)Cl$ 0.8 mM; tetraethylammonium tetrafluoroborate 0.1 M; 20 mL ACN saturated with CO_2 , at different concentrations of PhOH.

The UV/Vis analysis of the electrolysis solution shows the fingerprint signatures of mononuclear $\text{Fe}(\text{Salophen})^+$ with a $\sim 20\%$ abatement of intensity with respect to a freshly prepared solution at the same nominal concentration (Figure 46), indicating partial catalyst decomposition. Reutilization of this solution in a new electrolysis, after polishing the working electrode, restores the production of CO; this result speaks in favour of a surface modification of the glassy carbon working electrode, originated from the decomposition of the iron catalyst, as responsible for the observed change of selectivity of the process towards hydrogen evolution. The change of catalytic regime was even more pronounced at a higher phenol concentration of 2 M, where a lower initial CO selectivity and its faster drop were observed (Figure 45).

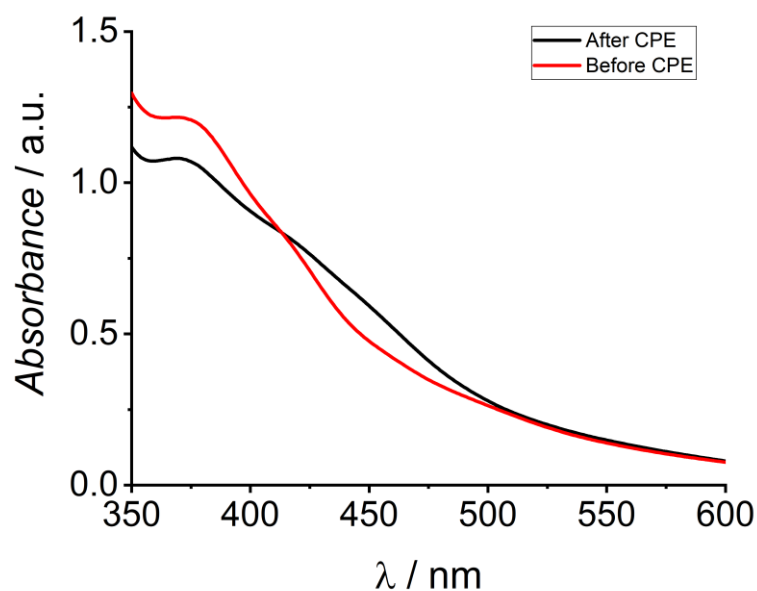


Figure 46. Electronic absorption spectra of a 0.8 mM $\text{Fe}(\text{Salophen})\text{Cl}$ solution in acetonitrile, in the presence of 0.1 M tetraethylammonium tetrafluoroborate and 0.5 M PhOH before (red trace) and after (black trace) CPE at -2.0 V vs Fc^+/Fc under CO_2 .

Indeed, after the electrolysis experiment the glassy carbon working electrode surface was found to be covered by iron-based nanoparticles originated from electrodeposition of the iron molecular precursor at the electrode, with rough surface and dimensions up to 100 nm, as revealed by Scanning Electron

Microscopy (SEM, Figure 47). *Ex-situ* X-Ray Photoemission Spectroscopy (XPS) showed peaks at binding energies of 726 and 711 eV associated to Fe 2p_{3/2} and Fe 2p_{1/2} transitions, typical of iron oxide formed upon air exposure of the electrode (Figure 47).

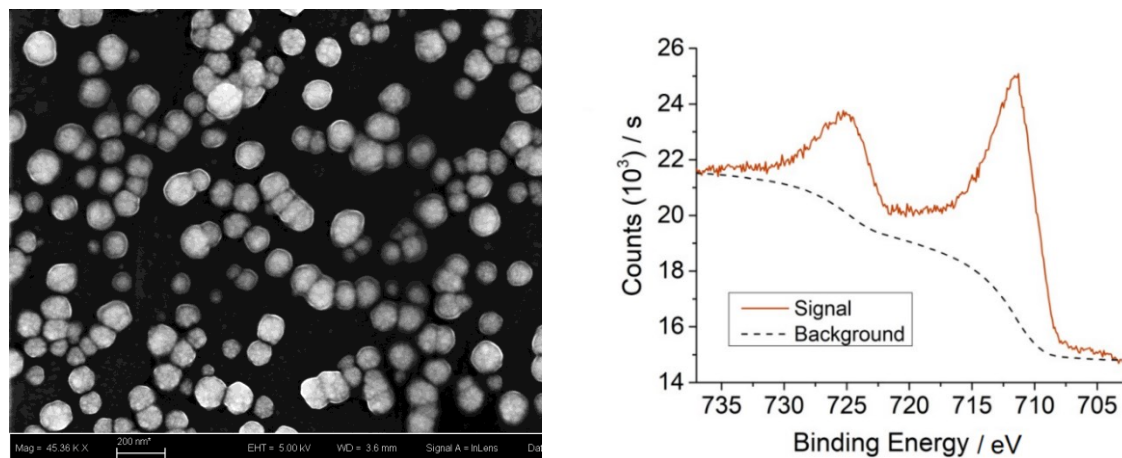


Figure 47. Left: SEM image of the iron nanoparticles on the glassy carbon electrode surface after CPE of a Fe(Salophen)Cl solution. Right: XPS spectrum of the iron nanoparticles, exhibiting Fe^{III} signals due to the electrode being exposed to the air.

The electrodeposition of the nanoparticles could likely originate from ligand demetallation upon a further reduction of Fe^I to “Fe⁰” intermediates, as observed in the case of the Fe(qpy) catalyst.¹⁸³ The direct utilization of the unpolished glassy carbon electrode in a CPE experiment, conducted in the absence of Fe complexes in solution, led to immediate, continuous and stable production of H₂ (current density = 0.6 mAcm⁻², Faradaic efficiency in the range 65 ÷ 80%), while no CO was detected. Interestingly, methane was also observed as electrolysis product, and confirmed to be electrogenerated from carbon dioxide from a labelling experiment with ¹³CO₂ (Figure 48), with a Faradaic efficiency of 1 ÷ 2 %; this value corresponds to a partial current density for methane generation in the range 6 ÷ 12 μAcm⁻², slightly inferior to the one obtained in the case of Fe nanoparticles electrodeposited from Fe(qpy), 27 μAcm⁻². The yield and selectivity of methane generation likely depend on nanoparticles size, shape and composition.⁹⁵

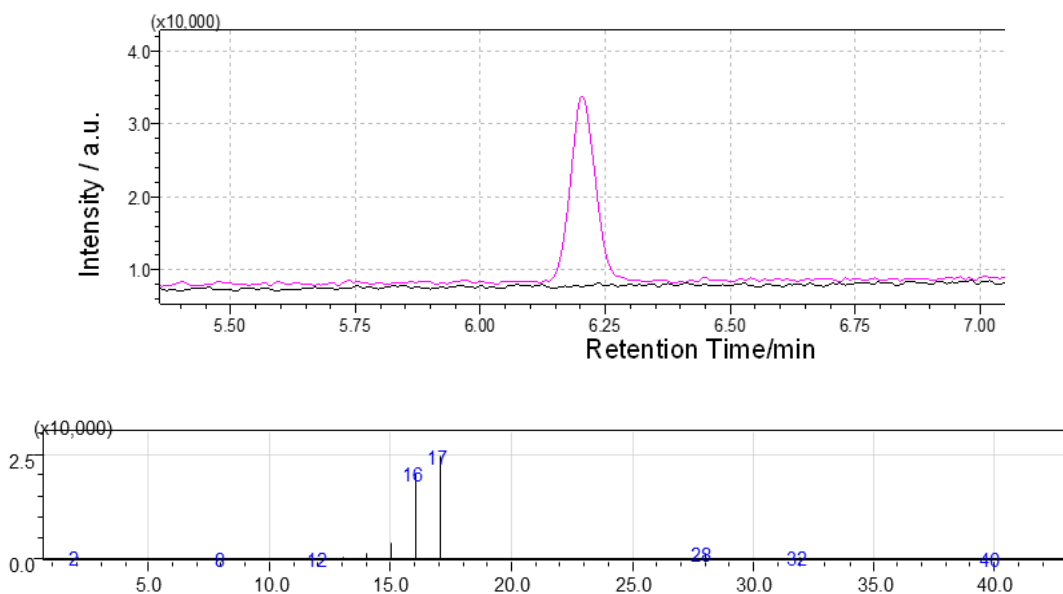


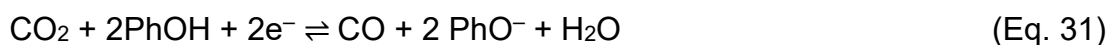
Figure 48. Top: chromatographic peak of CH_4 detected under electrolysis experiments with $^{13}\text{CO}_2$. Bottom: mass spectrum of the eluted $^{13}\text{CH}_4$. CPE experiments performed under CO_2 atmosphere on a 2 M PhOH solution without the iron Salophen complex, employing as the working electrode the glassy carbon plate bearing the nanostructured iron layer. Applied potential = -2.0 V vs Fc^+/Fc ; average current density in a 1 h experiment = 0.6 mAcm^{-2} with a 2 cm^2 carbon plate working electrode (geometric area).

2.8 Homogeneous vs heterogeneous electrocatalytic routes and benchmarking

The results above can thus be interpreted on the basis of competitive homogeneous and heterogeneous electrocatalytic pathways having different preferential products. The former is carried out by the molecular Fe^{I} Salophen intermediate and leads to selective CO_2 reduction to CO. The latter is driven by the heterogeneous iron nanoparticles formed upon electrodeposition from the molecular precursor, and is mainly oriented towards proton reduction to H_2 with formation of CH_4 as a minor product.

With the identification of CO as the product of the homogeneous electrocatalytic reduction of CO_2 by Fe Salophen species, it is possible to determine the metrics

for catalyst benchmarking. The overpotential can be calculated from the difference between the peak potential E_{p,CO_2} of the catalytic curve previously determined (Table 4) and the E^0 for the CO_2/CO couple under the adopted conditions. In organic solvents $E^0(CO_2/CO)$ is related to the following equation (Eq. 31), and depends on the activity of the species including the acidity of the proton donor, PhOH in the present case:



This was recently estimated in acetonitrile as -0.72 V vs the standard hydrogen electrode (SHE), resulting in $E^0(CO_2/CO) = -1.34$ V vs Fc^+/Fc after converting the potential to the Fc^+/Fc couple (E vs SHE = E vs $Fc^+/Fc + 0.624$ V).^{126,139} Therefore, the overpotential at the peak of the wave in the presence of phenol can be calculated as per Eq. 32:

$$\eta = -(E_{p,CO_2} - E_{CO_2/CO}^0) = (1.99 - 1.34) V = 0.65 V \quad (\text{Eq. 32})$$

The k_{cat} of the iron complex at different phenol concentrations (in the range $0.1 \div 0.6$ M, where the wave of CO_2 reduction is clearly distinguished from the wave leading to electrodeposition, Figure 42), can be estimated subjecting the voltammograms to the FOWA treatment. FOWA enables determination of the rate constant by analysis and fitting of a CV scan at the foot of the catalytic wave, where low charge has passed and side phenomena can be assumed negligible. The approach for data treatment through the FOWA is provided in Appendix 2.

The plots show profiles with a maximum, as expected in the presence of side phenomena; the linear fitting is applicable only in a restricted range of low ($E - E^0_{Fe(III)}$) values, providing slopes that can be associated to the k through Eq. 33, where the concentration of CO_2 substrate is equal to 0.28 M in acetonitrile. The catalytic constants k_{cat} (Table 4) can then be calculated from Eq. (3):

$$k_{cat} = k[CO_2] \quad (\text{Eq. 33})$$

[PhOH], M	E_{p,CO_2} , V vs Fc ⁺ /Fc	i_p , mA (i_p , mA·cm ⁻²)	k_{cat} , S ⁻¹
–	– 2.07	– 41 (– 0.58)	0.60±0.03
0.1	– 1.99	– 86 (– 1.22)	291±15
0.2	– 1.99	– 91 (– 1.29)	421±20
0.3	– 1.99	– 98 (– 1.39)	531±26
0.5	– 1.99	– 100 (– 1.41)	1016±50
0.6	– 1.99	– 108 (– 1.53)	1250±60
1	– 1.99	– 136 (– 1.92)	n.d.
2	– 1.99	– 132 (– 1.87)	n.d.

Table 4. Electrocatalytic parameters for reduction of CO₂ to CO by Fe(Salophen)Cl determined from CV experiments. An uncertainty of ±5 % should be considered for the i_p and k_{cat} values reported.

The k_{cat} values show a linear dependence on phenol concentration, while the plot of $\log(k_{cat}/k_{cat,0})$ vs $\log([PhOH]/[PhOH]_0)$ shows a slope of 0.82 (Figure 49), suggesting a first order dependence in the catalytic cycle of CO₂ reduction to CO. A catalytic scheme can thus be postulated, involving a 1e⁻ / 2H⁺ reduction of a Fe^I-CO₂ adduct to generate a Fe-CO intermediate and release water. Upon further reduction, regeneration of the Fe^I resting state would close the catalytic cycle (Figure 50). It is worth to mention that the initial catalyst activation (reduction of Fe^{III} to Fe^I active state) can also account for the low Faradaic efficiency observed at the initial stage of the electrolysis ($n(e^-)/n(Fe) < 4$, see Figure 45).

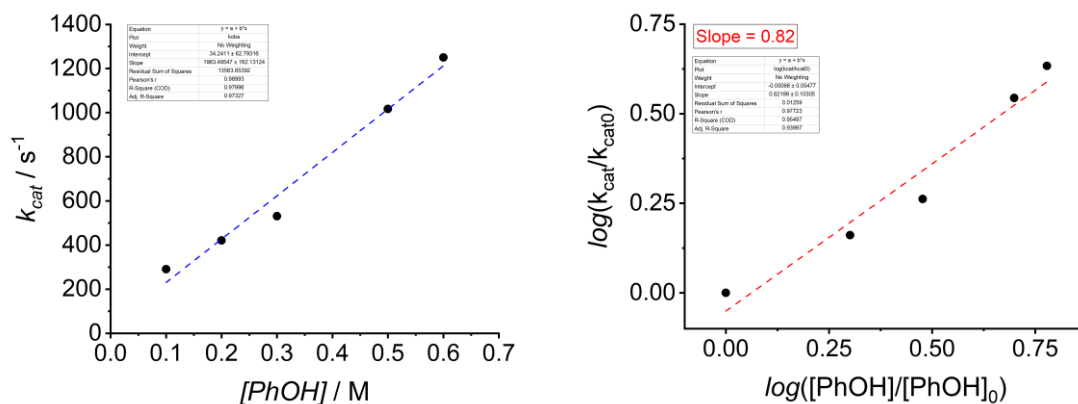


Figure 49. Left: plot of the values of k_{cat} calculated by FOWA as a function of the concentration of phenol, displaying a linear dependence. Right: plot of $\log(k_{cat}/k_{cat,0})$ as a function of $\log([\text{PhOH}]/[\text{PhOH}]_0)$, with a slope of approximately 1. The values of $[\text{PhOH}]_0 = 0.1$ M was arbitrarily chosen.

After determination of η and of k_{cat} , the values obtained at $[\text{PhOH}] = 0.6$ M were plotted in Figure 50 as a catalytic Tafel plot to allow for benchmark comparison with literature data. Iron Salophen is catalyzing CO_2 electrochemical reduction at relatively low overpotential (in the range of several literature benchmarks based also on noble second and third row transition metals). The catalytic rate k_{cat} (or turnover frequency, TOF) is high, although it is one order of magnitude lower with respect to the one observed for the iron tetraphenyl porphyrin (k_{cat} up to 10^4 s^{-1}),^{14,33} the forerunner of this class of CO_2 reduction catalysts. The notable improvement of catalytic performance for iron porphyrins in the latest years^{34,35} suggests a large margin of catalyst optimization also for Fe(Salophen) catalyst. With this regard, a tetracationic iron porphyrin $\text{Fe}(\text{o-NMe}_3\text{TPP})$ ³⁵ gives a clear outstanding performance catalyst with respect to the average, both in terms of low overpotential and of high k_{cat} ; this win–win condition was ascribed to a favourable supramolecular interaction of the catalyst with carbon dioxide: a similar approach can thus be envisaged for iron salophen species, by proper functionalization of the ligand scaffold.^{68,69}

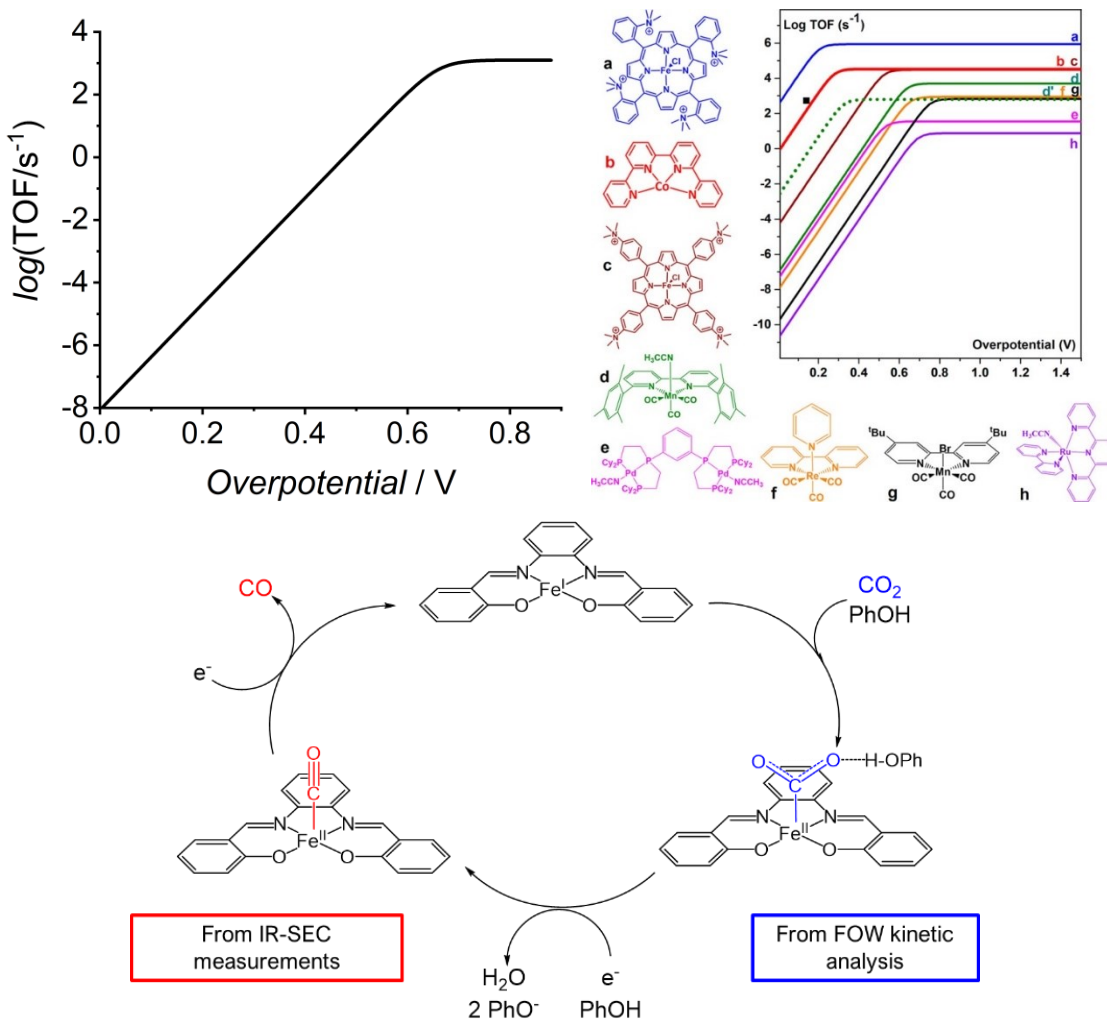


Figure 50. Top left: catalytic Tafel plot for the reduction of CO_2 to CO by $\text{Fe}(\text{L})\text{Cl}$ in acetonitrile, in the presence of 0.6 M phenol ($k_{\text{cat}} = 1250 \text{ s}^{-1}$, Table 4). E^0 , the potential of the $\text{Fe}^{\text{II}}/\text{Fe}^{\text{I}}$ couple in the absence of CO_2 and phenol, is set to -2.00 V vs Fc^+/Fc . Top right: Catalytic Tafel plot for benchmarking electrocatalysts for CO_2 reduction. Reprinted with permission from ⁵⁸. Copyright 2018, American Chemical Society. Bottom: proposed catalytic cycle based on the experimental observations.

The limited TON_{CO} reached in optimized electrochemical catalytic regimes is justified by the low stability of the Fe^{I} intermediate. Indeed, the metal-centered reactivity towards CO_2 is eventually impaired by electrode passivation at $[\text{PhOH}] \leq 0.5 \text{ M}$. However, deposition of Fe-based particles eventually leading to a heterogeneous catalytic regime is observed only when the proton donor

concentration is increased further (Figure 51). Incidentally, when examining the CV traces in the presence of carbon dioxide, merging of the second wave with that ascribed to the catalytic process is observed as the concentration of PhOH increases. This observation, ascribable to ligand electrochemical saturation that becomes more facile as the concentration of protons becomes higher, leads to two implications:

- i) As the ligand-centered decomposition pathway overwhelms the metal-based CO₂ reduction process, kinetic interrogation of the CV response is prevented. Specifically, the FOWA approach fails for [PhOH] ≥ 1 M, the catalytic process being completely masked, consistently with the low selectivity for CO observed in preparative electrolysis.
- ii) Comparison between the voltammetric behaviour observed under CO₂ atmosphere in the absence and in the presence of PhOH is restricted to the first wave (Fe^{II} → Fe^I), since the alleged metal-based reactivity observed at higher overpotentials in the absence of proton donors suffers from competition by the non-catalytic reduction processes when PhOH is introduced.

A primary task will be first to stabilize the catalyst towards the observed electrodeposition of heterogeneous Iron based materials. In this regard, reductive activation of the Fe(qpy) catalyst through a photochemical cycle has shown to improve the catalyst durability with respect to the electrochemical conditions.⁹⁶ Indeed, the utilization of the title Fe(Salophen) catalysts in light activated cycles is currently on going and will be reported in due course.

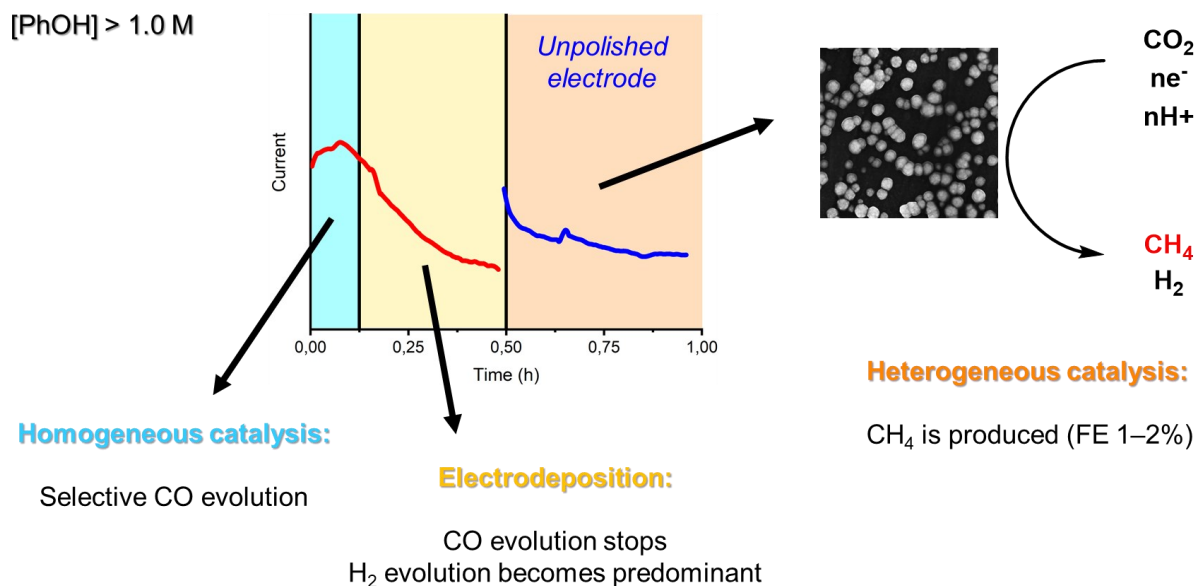
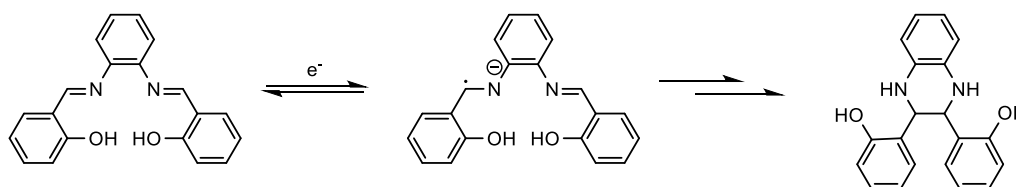


Figure 51. Schematized representation of the transition from the homogeneous catalytic regime leading to CO₂-to-CO reduction by Fe^I(Salophen) to a heterogeneous regime in which iron nanoparticles deposited on the carbon working electrode promote H₂ evolution and CO₂ reduction to CH₄. The scheme is structured based on the evolution of the electrolysis current from the homogeneous regime (red trace, cyan background) followed by increase (red trace, yellow background). Deposition of iron nanoparticles on the working electrode leads to an electrocatalytically active material (blue trace, orange background). Note that the cathodic current increases towards negative values, as per the IUPAC convention followed throughout the Thesis.

2.9 Electrochemical characterization of the Salophen ligand in acetonitrile

As part of control experiments protocols, the voltammetric behaviour of the ligand was studied in acetonitrile in the presence of 0.1 M tetraethylammonium tetrafluoroborate as supporting electrolyte. The interpretation of the experimental data has been carried out based on a previous report by Isse *et al.*¹⁸² Voltammograms of Salophen recorded at 0.1 Vs⁻¹ display a first irreversible peak at -1.98 V vs Fc⁺/Fc, followed by a weaker, ill-defined irreversible peak at -2.29 V vs Fc⁺/Fc (Figure 52). This first system of peaks is attributed to the formation of a radical anion upon reduction of the redox-active C=N bonds. The radical anion has been proposed to evolve to a saturated form upon stepwise proton transfer and intramolecular cyclization steps (Scheme 8)¹⁸².



Scheme 8. Electrochemical processes leading to reductive saturation and cyclization of the Salophen ligand.

A second, irreversible wave peaking at -2.69 V vs Fc⁺/Fc has been attributed to the reduction of the conjugate base of Salophen, generated by the homogeneous chemical reactions following the first electron transfer. However, certain attribution was not provided in the original report, and it is not inconsiderate to hypothesize that the second reduction step could target the radical anion to produce a more basic dianion.

Interestingly, the accumulation of the conjugate base of Salophen in the reaction-diffusion layer can be traced by cyclic voltammetry (Figure 52). As proposed by Isse *et al.*, it is obtained through proton transfer from the substrate to the singly or doubly reduced form of the ligand. The Salophen conjugate base (Salophen²⁻) may indeed be detected on the reverse scan, since the irreversible oxidation peak

of the phenolate is detectable in the range -0.40 V and -0.19 V vs Fc^+/Fc . Incidentally, anodic detection of Salophen^{2-} is more easily attained on a glassy carbon electrode than on Hg working electrodes used in the aforementioned 1996 work. The attribution is supported by *in situ* deprotonation of Salophen with 2 equivalents of sodium *tert*-butoxide. The deep yellow solution of the Salophen dianion sodium salt displays an irreversible oxidation peak arising at -0.07 V vs Fc^+/Fc , ascribed to phenoxide moieties oxidation. Incidentally, the more anodic peak potential with respect to those observed by generating the anion at the electrode is justifiable by invoking the stabilizing effect of Na^+ on the phenoxide groups.

When Salophen is reduced at the electrode, its conjugate base is generated to a higher extent as the explored cathodic potential window is enlarged and as the scan rate is increased. The former observation is consistent with an increase in basicity of the progressively more reduced forms of the Schiff base. The increase in oxidation peak current of the phenoxide anions is compatible with a reversible nature of the chemical steps following the cathodic electron transfer events that lead to the generation of Salophen^{2-} .

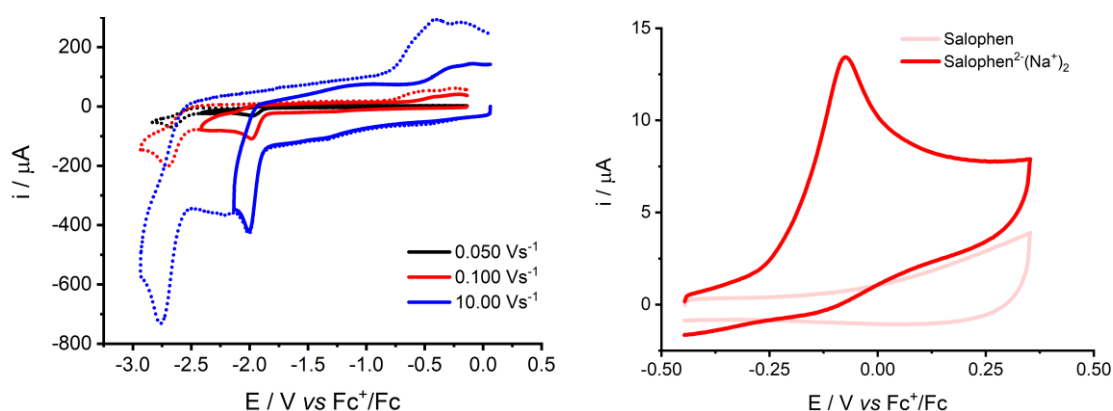


Figure 52. Left: CV under N_2 atmosphere of 1 mM Salophen in ACN with 0.1 M tetraethylammonium tetrafluoroborate at varying scan rates (0.050 Vs^{-1} , black trace; 0.100 Vs^{-1} , red trace; 10.00 Vs^{-1} , blue trace). Right: CV traces under N_2 of 1 mM Salophen in ACN with 0.1 M tetraethylammonium tetrafluoroborate before (pale red coloured trace) and after (deep red coloured trace) neutralization with 2 equivalents of tBuONa . Scan rate: 0.1 Vs^{-1} .

Upon analyzing the electrochemical response of Salophen under CO₂ atmosphere (Figure 53), an irreversible peak is observed at $-1.94\text{ V vs Fc}^+/\text{Fc}$, anodically shifted by 40 mV with respect to the first reduction peak observed for N₂-purged solutions, with 1.6 times increase in peak current. Such observation is consistent with CO₂ binding by the basic and nucleophilic reduced C=N bonds of Salophen. A more detailed insight on the reaction may be gathered based on the increase in the oxidation peaks of the phenoxide anion under CO₂ atmosphere. Indeed, such redox features are barely appreciable at 0.1 Vs^{-1} in the absence of carbon dioxide. Their more pronounced nature in the presence of CO₂ may be indicative of a faster, likely intramolecular proton transfer step from the phenol groups, occurring in the reduced form of Salophen after CO₂ binding. At this stage, we thus propose that the Schiff base ligand may undergo electrochemically induced carboxylation, but no electrosynthetic experiment has been devised to characterize the products of such reaction. It may be of interest to investigate the electrochemical carboxylation of Salen-type Schiff bases to target chiral α,α' -diamino acids. Indeed, ethylenediamine-*N,N'*-bis(2-hydroxyphenylacetic acid), Scheme 9, potentially obtainable from carboxylation of Salen, is a commercially employed chelator for iron, with widespread agrochemical applications.

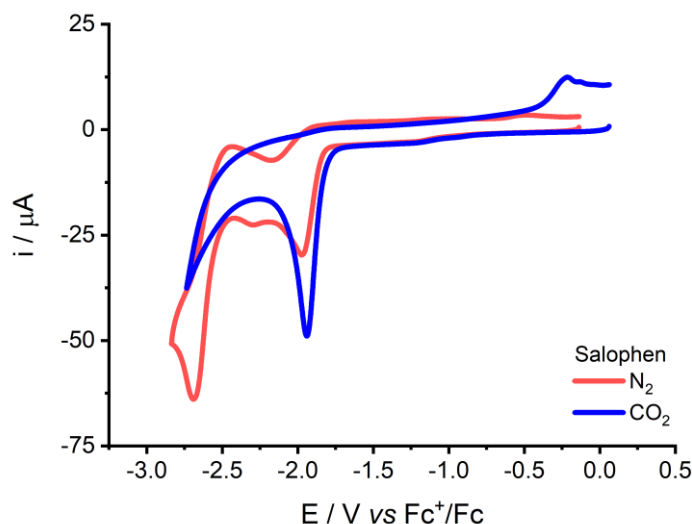
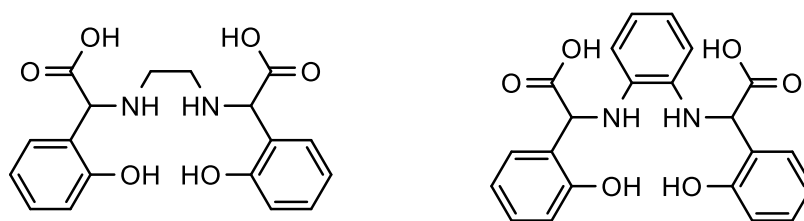


Figure 53. CV traces of 1 mM Salophen in acetonitrile with 0.1 M tetraethylammonium tetrafluoroborate under N₂ (red trace) and CO₂ (blue trace) atmosphere. Scan rate: 0.1 Vs^{-1} .



Scheme 9. Chemical structures of ethylenediamine-N,N'-bis(2-hydroxyphenylacetic acid) (left) and phenylenediamine-N,N'-bis(2-hydroxyphenylacetic acid) (right).

As previously reported, the redox activity of the ligand occurs at potentials very close to those required for the generation of low-valent intermediates in Fe(Salophen) complexes. However, the metal-based reactivity towards CO₂ catalytic reduction is unequivocally distinguished from the reactivity of the ligand alone. Indeed, Fe complexes display unique voltammetric features and their electrochemical reduction leads to competent Fe–CO species from which evolution of the CO product is obtained. Therefore, iron Salophen complexes are confirmed to productively direct the redox activity of the ligand to unlock the redox chemistry of low-valent metal-centered intermediates competent to the higher reactivity involved in CO₂ reduction.

2.10 Higher nuclearity compounds as products of ligand-based electrochemistry

Since the first works by Floriani and co-workers, the variegated chemistry of transition metal Salophen complexes undergoing reductive transformations has been explored.^{169,172,184–189} Indeed, over the last decades, it has been proven that Mn, Ni, Co and Fe Salophen derivatives can react with stoichiometric chemical reductants to form polynuclear complexes. Such reactions involve ligand-based reductions by the chemical reductant, followed by radical-radical coupling to yield mononuclear subunits connected by the newly formed C–C bonds between reduced Salophen ligands (Figure 54 reports an example based on a Co(Salophen) analogue).

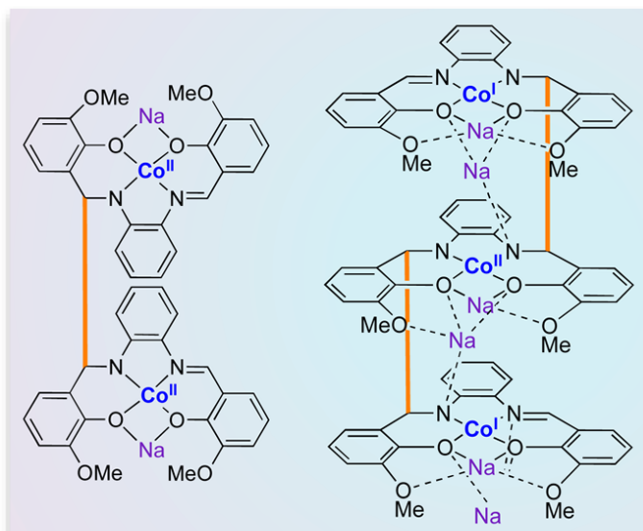


Figure 54. Polynuclear structures assembled upon C=N reduction by Na metal and subsequent radical-radical coupling in Co(Salophen) analogues. Figure reproduced with permission from ¹⁸⁹. Copyright 2017 American Chemical Society.

Formation of the polynuclear species strongly relies on the nature of the reductant: the employed chemical species is indeed metallic sodium, which acts as a stepwise one-electron donor, contextually generating hard Lewis acid cations. These latter serve the function of templating agents by interacting with the

phenoxide moieties during the assembly of the polynuclear structure. The nature of the Lewis acid cation impacts on the overall process, alkali cations with smaller ionic radii (Na^+ , Li^+) being able to guide the assembly of the polynuclear complexes better than larger cations (K^+). The synthetic outcome of these reactions strongly depends also on the choice of solvent, several structures being further accessible and mutually interconvertible by changing the reaction medium. As a last remark, formation of polynuclear complexes upon bielectronic reduction is a peculiarity of complexes bearing Salophen and its closely related analogues constructed from 1,2-phenylenediamine. Such specific reactivity is in fact not shared with Salen or other Schiff bases deriving from aliphatic diamines. The literature justification is based on the planar nature of Salophen and of its complexes, that facilitates the approach between mononuclear units in the coupling steps leading to higher structure assembly. Indeed, analogous complexes bearing the non-planar Salen ligand do not undergo a similar reduction pathway.

These considerations highlight the need of great care when considering the redox chemistry of low-valent metal complexes bearing the Salophen ligand. Indeed, polynuclear compounds generated by chemical reduction can display metal-centered reactivity towards nucleophiles such as alkyl iodides or CO_2 . Trinuclear cobalt and iron Salophen complexes have been reported as reductants towards the bielectronic transformation of CO_2 into CO and CO_3^{2-} . Interestingly, exploiting the reactivity of these complexes results in overall disruption of their polynuclear structure, eventually affording the mononuclear starting $\text{M}(\text{Salophen})$ units. The authors generally interpreted these results as an ability of these compounds to exploit the reductively coupled C–C bonds as electron reservoirs and shuttles, able to store electrons and direct them towards the transition metal ions when required for metal-centered redox chemistry.

When comparing the outcome of chemical vs electrochemical reduction of a specific molecule, the intrinsically different nature of the reductant can play a key role on the obtainable products. In the case of a solid, chemically inert electrode,

electron transfer thermodynamics and kinetics are finely dictated by the potential at which the former is poised. Chemical reductants, on the other hand, possess a definite reducing power, formalized by their standard potential, that may not be easily varied. When considering a chemical reductant, its stoichiometry is instead the most easily controllable experimental parameter. Furthermore, reductants in homogeneous phase (e.g., cobaltocene) act *via* reaction steps that differ from the interfacial mechanism between a substrate and an electrode. Alkali metals, despite their heterogeneous nature with respect to the M(Salophen) complexes present in solution, act as sacrificial reductants, releasing non-innocent cations directly involved in the polynuclear structure assembly. Therefore, formation of metal clusters starting from M(Salophen) may result in a different outcome which may be completely suppressed when considering the electrochemical regime. Specifically, ligand-based dimerization involving reduced forms of the complexes in the vicinity of the electrode surface might be the prevailing reaction when unaided by alkali ions, instead of the formation of higher aggregates. A powerful example is the case of Co(Salophen), which can be reduced by Li or Na to form di- or trinuclear complexes. When studied at an electrode surface in the presence of Li⁺ cations, the mononuclear nature of the Co^I complex is instead retained, as reported by Isse *et al.*¹²³

In 2020, Mazzanti and co-workers reported the formation of tri- and hexanuclear high-spin aggregates upon reduction of Fe^{II}(Salophen) with Na metal, [Na₆Fe₃(tris-cyclo-salophen)(py)₉] and [Na₁₂Fe₆(tris-cyclosalophen)₂(THF)₁₄], represented in Figure 55.¹⁷² Their structure is based on a formally macrocyclic ligand generated by reductive coupling of three Salophen units, tris-cyclosalophen. In each trinuclear subunit, two Fe sites display a N₃O₂ coordination motif, while the third has a N₂O primary coordination sphere, the phenoxide groups also interacting with Na⁺ ions. These complexes are able to induce the CO₂-to-CO conversion as stoichiometric reductants, regenerating the starting Fe^{II}(Salophen) mononuclear units.

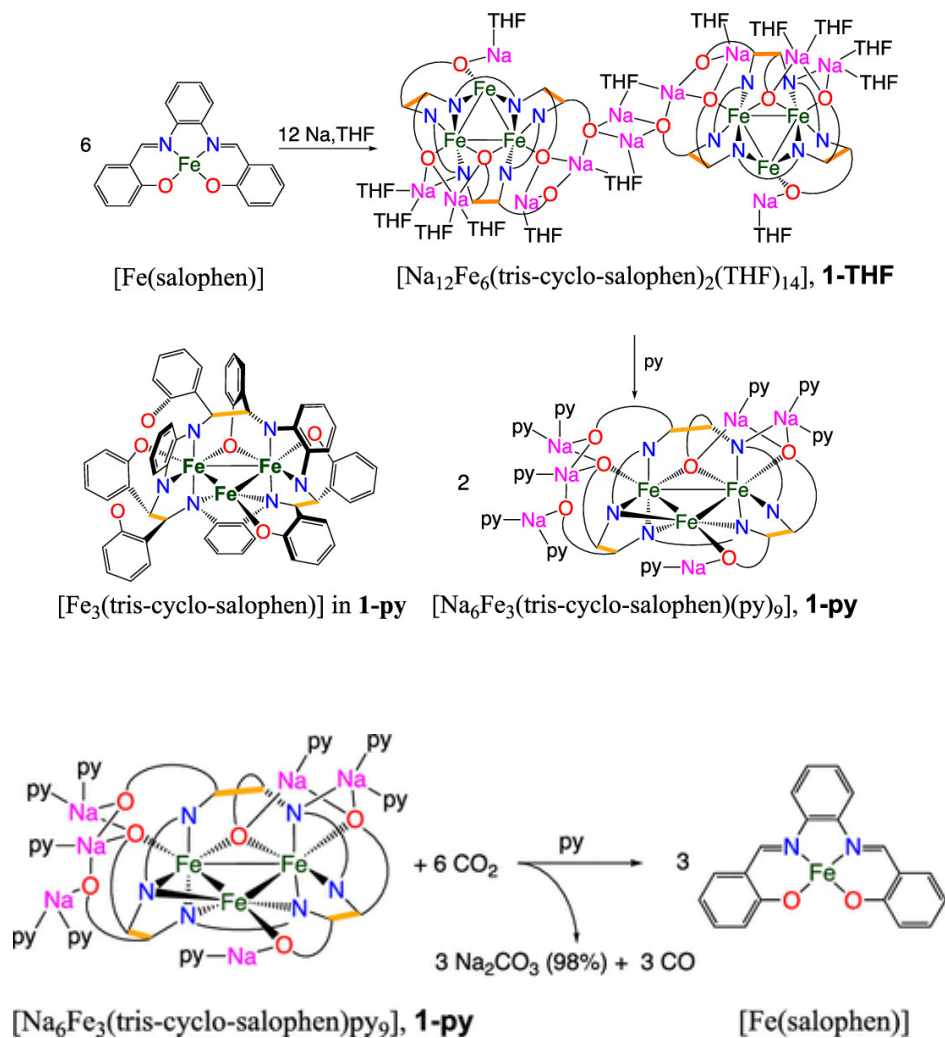


Figure 55. Top: synthesis of $[\text{Na}_6\text{Fe}_3(\text{tris-cyclo-salophen})(\text{py})_9]$ and $[\text{Na}_{12}\text{Fe}_6(\text{tris-cyclo-salophen})_2(\text{THF})_{14}]$ by $\text{Fe}^{\text{II}}(\text{Salophen})$ reduction with Na metal. Bottom: proposed stoichiometric CO_2 reduction reaction to CO and carbonate by $[\text{Na}_6\text{Fe}_3(\text{tris-cyclo-salophen})(\text{py})_9]$ in pyridine (py). Figures reproduced with permission from ¹⁷². Copyright 2020 American Chemical Society.

The synthesis of the polynuclear aggregates requires the use of 2 equivalents of sodium metal per $\text{Fe}^{\text{II}}(\text{Salophen})$ unit, resulting in a twofold reduction of the starting mononuclear complex. Considering the voltammetric behaviour of $\text{Fe}(\text{Salophen})\text{Cl}$, this would correspond to reducing the complex beyond the third one-electron wave. CO_2 binding and activation at the Fe site is instead observed at the level of the second cathodic process ($\text{Fe}^{\text{II}} \rightarrow \text{Fe}^{\text{I}}$). To probe the possible

formation of C–C bonded aggregates, cyclic voltammograms were recorded on Fe(Salophen)Cl solutions in the presence of NaClO₄ as a source of Na⁺ ions. These latter are introduced under the assumption that their presence in the reaction-diffusion layer might assist the assembly of polynuclear species, in combination with the Faradaic processes induced by the electrode. The electrode/Na⁺ system is therefore intended as a mimic of sodium metal as chemical reductant.

A due comparison with the electrocatalytic behaviour of Fe(Salophen)Cl is herein proposed. Indeed, experimental evidence of mononuclear intermediates has been provided through SEC-IR, cyclic voltammetry and kinetic investigation of the role of the proton donor in the catalytic mechanism. Furthermore, CO evolution observed in optimized conditions is consistent with a steady catalytic reaction rather than a stoichiometric process.

Under these premises, controlled addition of Na⁺ in the form of aliquots of a 1 M NaClO₄ solution in acetonitrile to a N₂-purged 1 mM solution of Fe(Salophen)Cl was performed, registering two cyclic voltammograms after each addition. When Na⁺ is added in a 1:1 stoichiometric ratio with respect to Fe(Salophen)Cl, the Fe^{III} → Fe^{II} (A) and Fe^{II} → Fe^I (B) waves are mostly unaffected, the latter undergoing a negligible E_p anodic shift by 10 mV (the peak labelling is the one adopted in Figure 32). The major change in the voltammetric response is however observed at the level of the third reduction peak (C), which cathodically shifts to –2.38 V vs Fc⁺/Fc. Upon increasing [Na⁺] to reach a 2:1 ratio with respect to Fe(Salophen)Cl, the nominal stoichiometry required for the synthesis of the clusters, the wave becomes irreversible and its cathodic current increases. At 3:1 Na : Fe ratio, the wave turns into a multi-electron, composite irreversible peak. Furthermore, the Fe^{II} → Fe^{III} anodic peak is progressively abated as [Na⁺] increases.

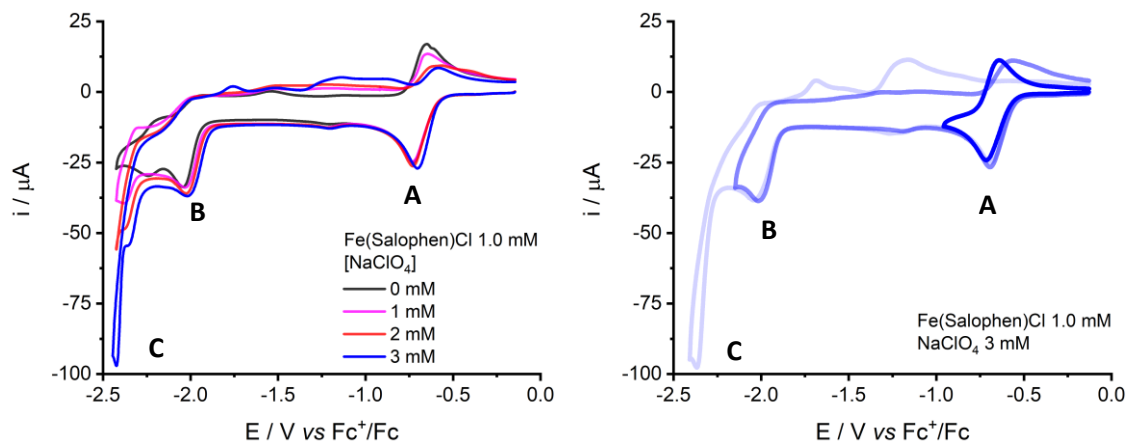


Figure 56. Left: CV traces under N_2 atmosphere of 1 mM Fe(Salophen)Cl in ACN in the presence of 0.1 M tetraethylammonium tetrafluoroborate and in the absence (black trace) and with increasing $[NaClO_4]$: 1 mM (magenta trace), 2 mM (red trace), 3 mM (blue trace). Sodium perchlorate was added in the form of a 1.0 M solution of the salt in acetonitrile. Right: CV traces under N_2 atmosphere of 1 mM Fe(Salophen)Cl in ACN in the presence of 0.1 M tetraethylammonium tetrafluoroborate and in the presence of 3 mM $NaClO_4$, with increasing potential window. Scan rate: 0.1 Vs^{-1} .

When the concentration of Na^+ is further increased to reach a $Na^+ : Fe$ 12:1 ratio, the $Fe^{III} \rightarrow Fe^{II}$ and $Fe^{II} \rightarrow Fe^I$ peaks remain unaltered. However, the current associated with peak C further increases, while the wave undergoes curve crossing on the reverse scan. Such observation points to the generation of a species oxidized at more positive potentials than those required for its generation. Curve crossing is often associated with evolution of a solution species to a molecular or nanoparticulate deposit on the electrode surface, as clearly detailed by Dempsey and co-workers.⁵⁰ The modification of the electrode surface is supported by running a second scan without polishing the working electrode: indeed, the voltammetric profile shows a clearly different behaviour from the first cyclic voltammogram. Incidentally, the anodic peak associated with the restoration of the starting Fe^{III} complex is completely abated on the anodic scan when $Na^+ : Fe > 6:1$. These findings suggest that, in the presence of sodium cations, a ligand-based process is triggered leading to new species deposited on the electrode surface.

The analysis of the voltammetric response in the anodic scan as $[\text{Na}^+]$ is increased also provides useful insights (Figure 57). Indeed, as the cathodic scan encompasses waves B and C in the presence of sodium ions, anodic irreversible peaks are observed at $-1.72\text{ V vs Fc}^+/\text{Fc}$ and $-1.03\text{ V vs Fc}^+/\text{Fc}$ (this latter being constituted by two coalescing peaks). The peak current of these new systems of signals increases with $[\text{Na}^+]$. Furthermore, their shape varies in between scans when an unpolished electrode is tested.

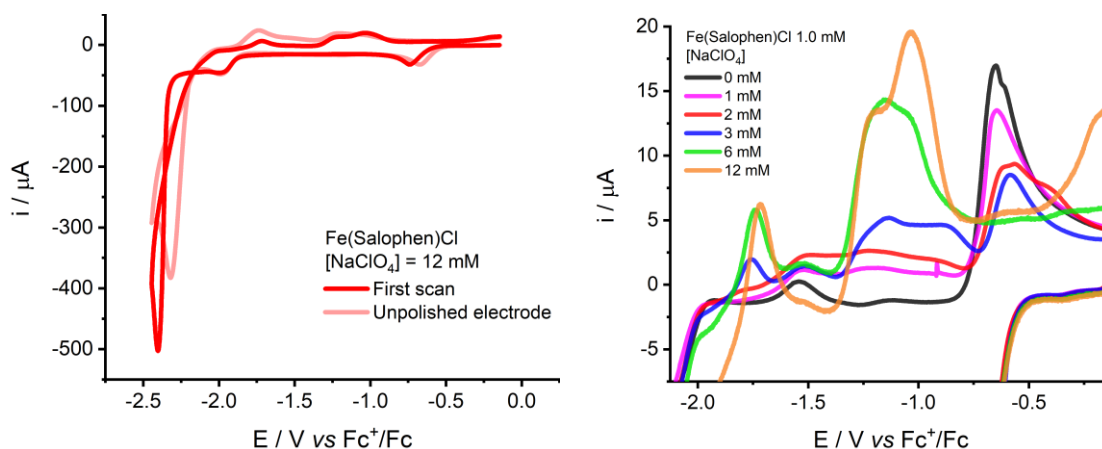
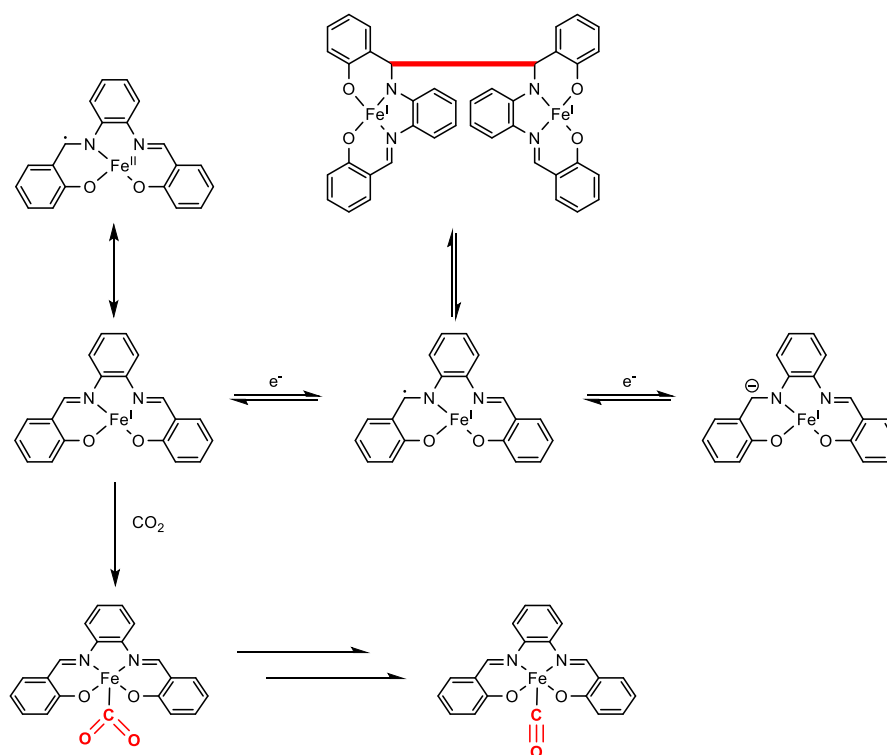


Figure 57. Left: CV traces under N_2 of 1 mM Fe(Salophen)Cl in acetonitrile in the presence of 0.1 M tetraethylammonium tetrafluoroborate and 12 mM NaClO_4 with a pristine (deep red trace) and an unpolished (pale red trace) glassy carbon working electrode. Right: CV traces of 1 mM Fe(Salophen)Cl and increasing $[\text{NaClO}_4]$, with focus on the anodic scan.

A preliminary attribution of these newly formed waves involves deposition of redox active species on the electrode surface occurring in the presence of Na^+ under cathodic conditions. While a deeper investigation would be required to ascertain the nature of these experimental observations, the influence of alkali cations on the reduction chemistry of Fe(Salophen)Cl is clearly appreciated. This leads to hypothesize that, in the presence of Lewis acid coadjutants, ligand-ligand reductive coupling might occur within the electrode interphase, leading to formation of adsorbed species. To study the nature of these latter, the electrode surface should be analyzed by means of microscopy, provided that the adsorption strength is sufficient to grant post-electrolysis recovery. Under this assumption, the anodic feature D observed in the absence of Na^+ at $E_p = -1.53\text{ V vs Fc}^+/\text{Fc}$

(see Figure 32) may be attributed as well to oxidation of species generated by reductive coupling. Ligand-ligand coupling should therefore be occurring at the level of the third redox couple of Fe(Salophen), albeit at a low degree when unaided by Na⁺. A consequence of this attribution is that the redox couple C is a ligand-based process that leads to pairing of Fe(Salophen) units, which benefits from the assistance of Lewis acid cations. To ascertain the nature of the transformation and compare it with the chemical reduction process, the electrochemical analysis of authentic samples of [Na₁₂Fe₆(tris-cycloalophen)₂(THF)₁₄] or [Na₆Fe₃(tris-cyclo-salophen)(py)₉] should be performed.

In this scenario, it is possible to propose that multi-electron processes leading to oligo- or polymerization of Fe(Salophen) pertain to the domain of ligand reductive chemistry, distinct from the mononuclear, metal-based reactivity involved in electrocatalytic CO₂ reduction (Scheme 10).



Scheme 10. Alleged ligand-based electrochemical processes parallel to the metal-centered reactivity towards CO₂.

2.11 Experimental section

2.11.1 Materials and methods

NMR spectra were recorded on a Bruker Avance-300 MHz instrument. ^1H -NMR spectra were registered in CDCl_3 and referenced to its residual isotopic impurity ($\delta = 7.26$ ppm). CDCl_3 was treated by passing it through basic aluminium oxide prior to preparing the samples. NMR spectra were processed using MestReNova 12.0.2. ESI-MS spectra were acquired with an Agilent Technology LC/MSD Trap SL, interfaced to an Agilent 1100 binary pump. All mass spectra were registered upon flow injection of samples diluted in methanol or acetonitrile. The eluent phase was chosen as pure HPLC-grade methanol. FT-IR spectra were recorded with a Jasco 4000 spectrophotometer. Samples were embedded in glassy potassium bromide pellets (*circa* 1% w/w), prepared with a dedicated manual hydraulic press. Electronic absorption spectra were recorded with a Perkin Elmer Lambda 45 spectrophotometer. A 1 mm optical path quartz cuvette was used in all measurements.

2.11.2 Electrochemical setup

2.11.2.1 Cyclic voltammetry (CV)

CV experiments were performed with a BASi EC Epsilon potentiostat-galvanostat.

Working electrode (WE): glassy carbon, 3 mm \varnothing (BASi or BioLogic).

Auxiliary electrode (also indicated as counter electrode, CE): gold, 1.6 mm \varnothing (BASi).

Reference electrode (RE): Ag/AgCl (3 M NaCl) (BASi). All measurements were referenced against the ferricenium/ferrocene (Fc^+/Fc) redox couple by adding ferrocene as internal standard.

To minimize Ohmic drop, the internal resistance was compensated by means of the positive feedback loop of the electrochemical workstation (to an extent of 85 – 95%).

HPLC-grade solvents (Carlo Erba) and electroanalytical-grade electrolytes (Sigma) were used without further purification. Ultrapure (mQ) water was employed. The glass electrochemical cell was kept closed during measurements with a PTFE lid annexed to the potentiostat-galvanostat. Inert gas (N₂) or CO₂ were introduced into the cell by means of a PTFE pipe, equipped with a needle. A gas trap filled with CH₃CN was interposed before the cell, to avoid evaporation of the solution in the latter.

The glassy carbon electrodes were polished with SiC paper (Struers) 2000 grit, then 4000 grit (in sequence), then with 3 μm, 1 μm, 0.25 μm diamond paste (DP Paste, Struers) on DP Dur (for 3 μm and 1 μm pastes) and DP Nap (for 0.25 μm paste) pads (Struers).

In between polishing steps, the electrodes were sonicated for 60 s in ethanol, then rinsed with methanol and dried with a N₂ stream. Once prepared, the electrodes were used for the experiments. In between each CV measurement and at the end of the experimental sessions, the electrodes were polished with 1 μm DP Paste, sonicated in ethanol for 60 s, rinsed with methanol and dried with N₂.

After each series of CV experiments, the electrochemical cell was carefully rinsed with ethanol, acetone, and deionized water; afterwards, the cell and the magnetic stirrer were sonicated for 5-10 min with a HCl 0.1 M/ethanol/acetone 1:1:1 (v/v) mixture. The cell and the stirrer were then rinsed again with deionized water, ethanol, and acetone and dried in an oven. The cell was kept protected from dust by covering it with aluminium foil. The described cleaning procedure was modified by adding a preliminary washing step when working with phenol: the WE, the stirrer, and the cell were rinsed and sonicated for 5 minutes in an aqueous 0.1 M NaOH solution.

2.11.2.2 Constant potential electrolysis (CPE)

CPE experiments were performed by means of an AMEL 7050 potentiostat-galvanostat. The solutions were electrolyzed in a 6-neck-2-compartment custom made cell with known inner volume, realized by Mauro Meneghetti (glassblower in the Department of Chemical Sciences of the University of Padova). The two compartments were separated by a porous glass frit.

Working electrode: glassy carbon stick (SIGRADUR, HTW) or glassy carbon plate.

Reference electrode: Ag/AgCl (3 M NaCl) (BASi).

Auxiliary electrode: platinum wire.

Connection between the WE and the potentiostat-galvanostat was constituted either by an electrolytic copper wire carefully wrapped at the top of the electrode or by a copper tape. The cell was tightly closed with rubber septa (gas inlet/outlet necks) or with rubber seals in which the electrodes were inserted. A CO₂-saturated environment was generated by bubbling CO₂ separately into the two compartments, the gas reservoir being connected to a Y junction with two stopcocks. Syringe needles piercing the rubber septa allowed gas inlet and outlet. Experiments were run under stirring of both compartment solutions, after removing all needles from the cell.

The same cleaning procedures described above were adopted for the CPE-dedicated cell and for the glassy carbon stick. During CPE experiments in the presence of phenol, the CE became covered in a dark carbonaceous material resulting from phenol oxidation in the anodic compartment. Cleaning of the wire was achieved by sonicating in acetone for 15 minutes and successively rinsing with the same solvent. Gaseous product analysis was performed by gaschromatography (GC) with a thermoconductimetric detector (TCD) and a mass spectrometer (MS). Solution species were analyzed by ionic chromatography (IC) and ¹³C-NMR spectrometry.

2.11.2.3 Infrared spectroelectrochemistry (SEC-IR)

IR-SEC experiments were performed by employing a Thermo Nicolet Nexus FT-IR spectrophotometer, equipped with a LabOmak UF-SEC cell. A schematic view of the cell is provided in Figure 58. The three-electrode system was enclosed between two calcium fluoride optical windows, held together by four quick-nuts, between which a 0.2 mm thick compartment could be filled with the solution to be analysed. The electrodes used were:

Working electrode (WE): platinum gauze.

Reference electrode (RE): silver wire (acting as pseudoreference).

Auxiliary electrode (CE): platinum gauze.

Irradiation occurred through the solution in the cell where the working electrode was placed, in order to register spectral changes induced by application of the potential at the WE. Preliminary CV analysis allowed to set the appropriate potential for CPE experiments. During the electrolysis, multiple infrared spectra were recorded. Solutions were prepared using 0.1 M tetraethylammonium tetrafluoroborate as the supporting electrolyte and acetonitrile as the solvent. All solutions were degassed with CO₂ for 15 minutes before running the IR-SEC experiments and kept in a sealed container under CO₂ atmosphere.

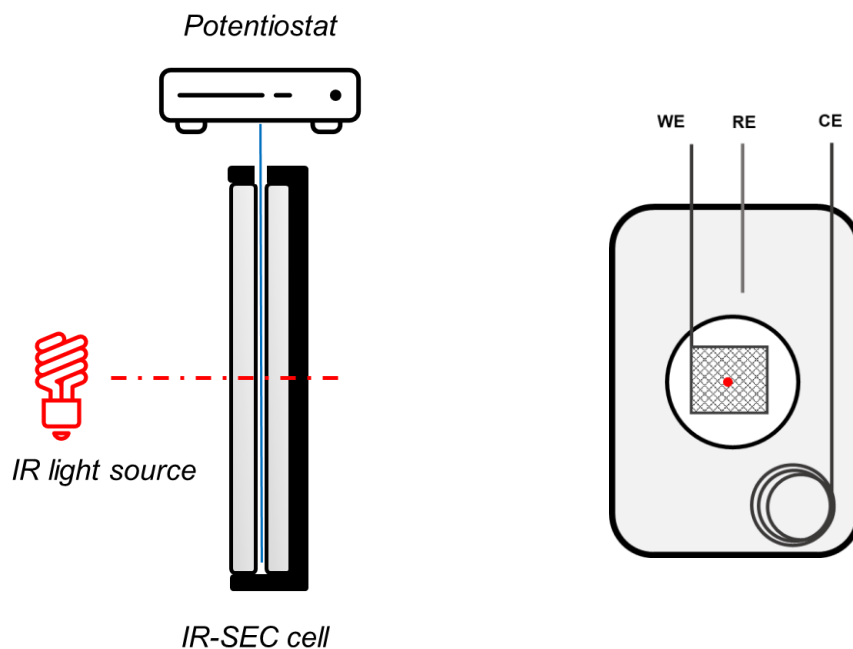


Figure 58. Schematic view of the SEC-IR cell. Left: side view; right: front view, with explicit indication of the three electrodes.

2.11.2.4 UV/Vis spectroelectrochemistry (SEC-UV/Vis)

SEC-UV/Vis experiments were performed by employing an Agilent Cary 5000 spectrophotometer, equipped with a 0.5 mm optical path quartz spectroelectrochemistry cell (BASi EF-1362). A schematic view of the cell is provided in Figure 59.

The electrodes used were:

Working electrode: platinum gauze.

Reference electrode: Ag/AgCl (3 M NaCl) (BASi).

Auxiliary electrode: platinum wire.

The reference and auxiliary electrodes were kept in the space above the thin layer of solution in which the working electrode was held. Irradiation occurred through the 0.5 mm optical window containing the working electrode. Spectroelectrochemistry experiments were performed as described above for IR-

SEC. Solutions were prepared using 0.1 M tetraethylammonium tetrafluoroborate as the supporting electrolyte and acetonitrile as the solvent. All solutions were deoxygenated by sparging the solution in the cell with N₂ or CO₂ for 40 seconds prior to performing the experiments.

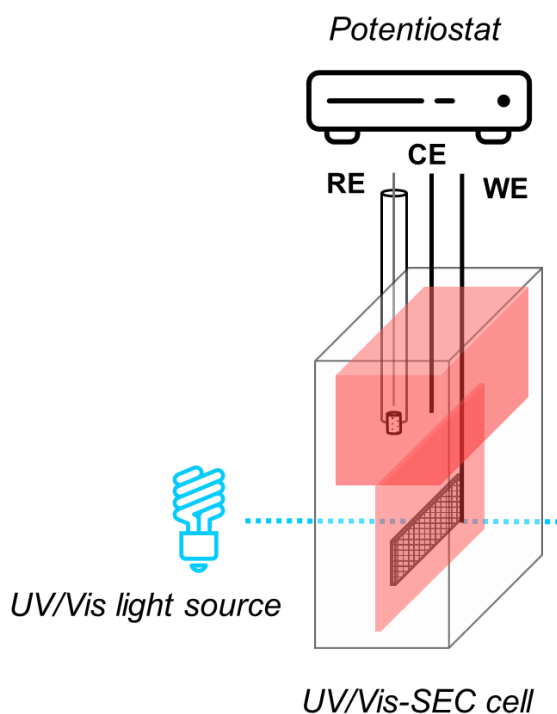


Figure 59. Schematic view of the UV/Vis-SEC cell.

2.11.3 Electron Paramagnetic Resonance (EPR) spectroscopy

EPR spectra were obtained by Dr. Antonio Barbon (University of Padova) with a Bruker ELEXSYS instrument operating at X-band, equipped with a dielectric cavity inserted inside a CF935 cryostat (Oxford). Temperature was stabilized at 80 K with a thermostated cold nitrogen flow. The solutions were transferred in the tubes from the electrolysis cell *via* cannulation with N₂ or CO₂ gases, and immediately frozen under liquid nitrogen.

2.11.4 Synthetic procedures

2.11.4.1 Synthetic procedure of Salophen ligand

o-phenylenediamine (1.08 g, 10.0 mmol) was suspended in 25 mL ethanol in a round-bottom flask. Subsequently, salicylaldehyde (2.10 mL, 19.7 mmol) was added to the reaction mixture. The liquid phase immediately exhibited a yellow colour. The reaction mixture was stirred under reflux for 3 hours. After the indicated time, an orange solid was observed, that settled from the pale-yellow supernatant. The solid was recovered by filtration and washed carefully with mQ water (x 3), cold ethanol (x 3), and diethyl ether (x 5). The orange solid was then dried under a vacuum and weighted (2.88 g, 9.1 mmol, yield = 90%).

$^1\text{H-NMR}$ (300 MHz CDCl_3): δ 13.03 (s, 1H), δ 8.64 (s, 1H), δ 7.41-7.20 (m, 4H), δ 7.09-6.86 (m, 2H)

FT-IR (KBr, cm^{-1}): 3055(w, br), 1618 (s), 1562 (m), 1481 (m), 1402 (w), 1362 (w), 1276 (s), 1192 (s), 1150 (m), 1045 (w), 910 (s), 830 (w), 640 (w), 581 (w), 529 (w).

ESI-MS: 317 m/z, $[\text{MH}]^+$.

Elemental analysis: Calculated for $\text{C}_{20}\text{H}_{16}\text{N}_2\text{O}_2$ C: 75.93% H: 5.10% N: 8.86%
Found C: 75.63% H: 4.98% N: 8.85%.

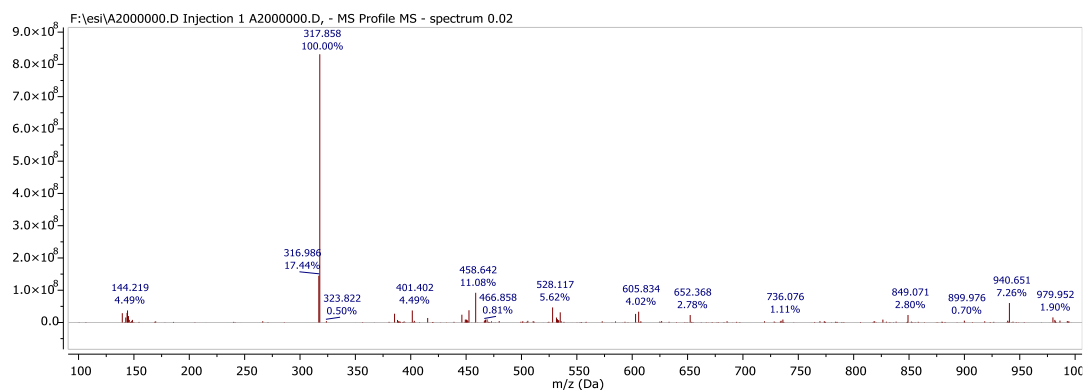


Figure 60. ESI-MS spectrum of 10^{-5} M Salophen in methanol.

2.11.4.2 Synthetic procedures of Fe(Salophen)Cl

Synthetic procedure with triethylamine

The synthesis of Fe(Salophen)Cl was performed through a slight modification of the literature procedure. Salophen ligand (111 mg, 0.35 mmol, 1 eq) was dissolved under stirring in 10 mL of CH₂Cl₂ at room temperature in a round-bottom flask. Iron(III) chloride hexahydrate (97 mg, 0.36 mmol, 1.03 eq) was subsequently added to the mixture. The bright yellow suspension immediately turned dark brown, no solid being visible to the bare eye. The reaction mixture was left under stirring for 1 hour. Triethylamine (98 μL, 0.702 mmol, 2 eq) was dissolved in 2 mL of CH₂Cl₂ and then slowly added to the reaction mixture. Upon addition of triethylamine, the mixture turned dark reddish-brown. After 2 hours, the solution was extracted with mQ water (x 3) to remove triethylammonium chloride and iron chloride excess. The organic phase was then recovered and dried. Upon slow evaporation of the solvent, a dark brown powder was obtained, that was washed with cold methanol (x 3) and dried. Weighed 92 mg, 0.23 mmol (yield 65%).

ESI-MS: 370 m/z [Fe(Salophen)]⁺ (loss of Cl⁻).

FT-IR (KBr, cm⁻¹): 1635 (m), 1605 (m), 1577 (m), 1535 (m), 1462 (w), 1436 (w), 1378 (m), 1316 (w), 1257 (m), 1234 (w), 1198 (w), 1147 (w), 1127 (w), 923 (w), 873 (w), 860 (w), 813 (w), 759 (w), 741 (w), 615 (w), 536 (w).

Elemental analysis: calculated for C₂₂H₂₂N₂O₄ClFe C: 56.25% H: 4.72% N: 5.96%. Found C: 56.40% H: 3.40% N: 5.90%. The proposed formula corresponds to Fe(Salophen)Cl·2CH₃OH.

Synthetic procedure involving potassium tert-butoxide

Salophen ligand (419 mg, 1.32 mmol, 1 eq) was suspended in 50 mL of methanol. ^tBuOK (297 mg, 2.64 mmol, 2 eq) was then added under stirring. After 10 minutes, the reaction mixture became a clear orange solution. FeCl₃·6H₂O (535 mg, 1.98 mmol, 1.5 eq) dissolved in 5 mL of CH₃OH was added dropwise to the reaction mixture under stirring. The deep green mixture was heated at reflux under stirring for 3 h. After the specified time, the reaction mixture was brought to dryness with the aid of a rotary evaporator and the residues were treated with 30 mL of CH₂Cl₂. The brown solution obtained was filtered over paper to remove insoluble salts, and then dried with a gentle stream of N₂ to afford Fe(Salophen)Cl as a microcrystalline dark brown powder (450 mg, 1.11 mmol, yield 84%).

ESI-MS: 370 m/z [Fe(Salophen)]⁺ (loss of Cl⁻).

Elemental analysis: calculated for C₂₀H₁₄N₂O₂ClFe C: 59.22% H: 3.48% N: 6.91%. Found 58.96% H: 3.54% N 6.43%.

Synthetic procedure of Fe₂(Salophen)₂(μ-O)

Salophen ligand (40 mg, 0.13 mmol, 1 eq) was suspended under stirring in 10 mL of ethanol at room temperature. Iron(III) nitrate nonahydrate (57 mg, 0.14 mmol, 1.1 eq) was subsequently added to the mixture, together with further 5 mL of solvent. The bright yellow suspension immediately turned dark green. No solid was visible to the bare eye. The solution was heated at 50°C, and upon addition of triethylamine (35 μL, 0.25 mmol 2 eq), the mixture turned dark brown. In the first 30 seconds after the addition, precipitation of a red solid was observed. Heating up to 60 °C and stirring was applied for an additional 1 h. Afterwards, stirring and heating were stopped. The solid product settled, leaving a supernatant brown solution. The product was isolated by centrifugation and washed with ethanol (x 3). Weighed 66 mg, 0.09 mmol (yield = 56%).

Elemental analysis: Calculated for $C_{40}H_{32}N_4O_7Fe_2$ C: 60.63% H: 4.07% N: 7.07%
Found C: 60.63% H: 4.07% N: 7.07%. The proposed formula corresponds to
 $Fe_2(Salophen)_2(\mu-O)\cdot 2H_2O$.

FT-IR (KBr, cm^{-1}): 1635 (m), 1609 (m), 1580 (m), 1536 (m), 1462 (w), 1445 (w),
1437 (m), 1379 (w), 1343 (w), 1320 (w), 1190 (w), 1148 (w), 1124 (w), 1031 (w),
920 (w), 872 (w), 855 (w), 819 (w), 809 (w), 755 (w), 607 (w), 535 (w).

ESI-MS: 370 m/z ($[Fe(Salophen)]^+$), 757 m/z ($[Fe_2(Salophen)_2(\mu-OH)]^+$).

Appendix 2

Appendix 2.1 – $\text{Fe}_2(\text{Salophen})_2(\mu\text{-O})$ characterization in dichloromethane

The electrochemistry of dinuclear $\text{Fe}_2(\text{Salophen})_2(\mu\text{-O})$ was further examined in CH_2Cl_2 using 0.1 M tetrabutylammonium hexafluorophosphate as supporting electrolyte (the change of quaternary ammonium salt was imposed by the lower solubility of tetraethylammonium tetrafluoroborate in dichloromethane). The first reduction of the complex occurs in a quasi-reversible fashion at $E_{1/2} = -1.47$ V vs Fc^+/Fc ($\Delta E = 86$ mV), indicated as peak A in Figure 61.

Interestingly, the reversibility of the redox couple is higher than in acetonitrile, the anodic feature being more well-defined. Such observation is suggestive of a higher degree of stability of the oxo bridge, further corroborated by the absence of anodic features associated with $\text{Fe}^{\text{II}} \rightarrow \text{Fe}^{\text{III}}$ conversion in mononuclear complexes. Close to the first oxidation feature observed in the return scan (peak B), a couple of anodic irreversible peaks is observed, at -1.21 V vs Fc^+/Fc and -1.12 V vs Fc^+/Fc , respectively indicated as peaks C_1 and C_2 . Upon increasing the scan rate, peaks C_1 and C_2 merge into a single anodic feature at -1.40 V vs Fc^+/Fc .

Generation of the Fe^{I} complex is instead detected as an irreversible cathodic peak at -2.00 V vs Fc^+/Fc , peak D. Comparison of the peak heights of peaks A and D suggests that the voltammetric peaks observed when reducing $\text{Fe}_2(\text{Salophen})_2(\mu\text{-O})$ in dichloromethane are two-electron features. A stepwise reduction of the two Fe^{III} centers in $\text{Fe}_2(\text{Salophen})_2(\mu\text{-O})$ is reasonably expected, albeit no distinct voltammetric waves being observable. The better-defined reversibility of the A/B peak couple and the attribution to two-electron reduction processes would therefore be indicative of a higher chemical stability of the reduced complex in dichloromethane towards oxo bridge dissociation. In the frame of this hypothesis, peaks B and $\text{C}_{1,2}$ may be attributed to the slower

stepwise reduction of the iron centers in the bridge, giving rise to a multiple set of peaks as opposed to the single Fe^{III}-to-Fe^{II} wave observed on the forward scan.

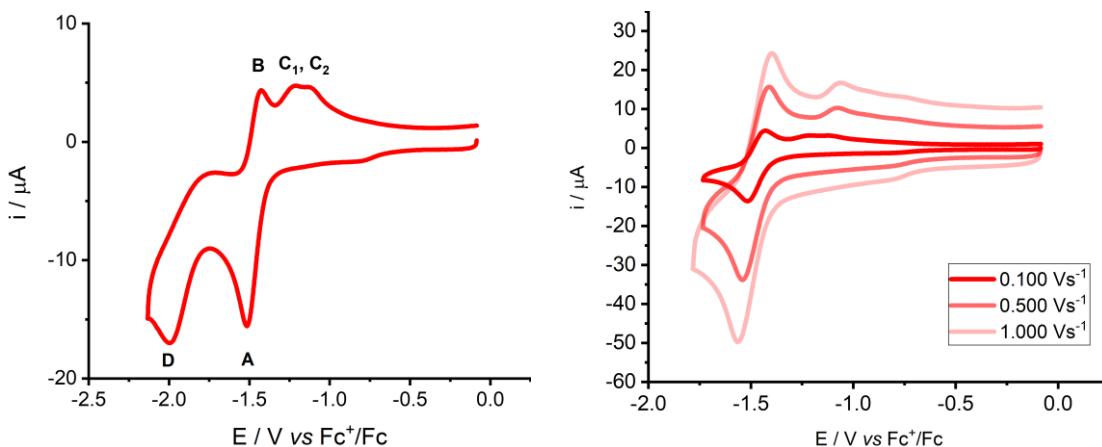


Figure 61. CV traces of 0.5 mM Fe₂(Salophen)₂(μ-O) under N₂ in dichloromethane in the presence of 0.1 M tetrabutylammonium hexafluorophosphate. Left: trace recorded at 0.1 Vs⁻¹, highlighting the Fe^{III}/Fe^{II} and Fe^{II}/Fe^I redox couples; right: traces recorded at variable scan rates, focusing on the Fe^{III}/Fe^{II} couple.

Appendix 2.2 – Binding of phenol to Fe(Salophen)Cl and Fe₂(Salophen)₂(μ-O)

In the presence of increasing concentration of phenol, the $E_{1/2}$ of the Fe^{III}/Fe^{II} couple progressively shifts to less negative values ($E_{1/2}$ values in the range between -0.66 V and -0.51 V vs Fc⁺/Fc, Figure 62), indicative of a preferential binding of phenol to the Fe^{II} center. The anodic potential shift can indeed be fitted according to Eq. 34:

$$E_{1/2}^{PhOH} = E_{1/2}^0 + \frac{RT}{nF} \cdot \ln\{1 + \beta_2[\text{PhOH}]^2\} \quad (\text{Eq. 34})$$

Where $E_{1/2}^{PhOH}$ is the half-wave potential of the Fe^{III}/Fe^{II} couple in the presence of PhOH, $E_{1/2}^0$ the one observed in the absence of PhOH, and β_2 is the formation constant of Fe^{II} salophen adduct with two phenol moieties ($n = 1$ in the Fe^{III}/Fe^{II} couple); fitting of the traces provides $\beta_2 = 170 \pm 11 \text{ M}^{-2}$.

The parabolic fit in Figure 62 (right) exploits the parabolic form of Equations 35a and 35b:

$$E_{1/2}^{PhOH} = E_{1/2}^0 + \frac{RT}{F} \cdot \ln\{1 + \beta_2[PhOH]^2\} \quad (\text{Eq. 35a})$$

$$\exp\left[\left(\frac{F}{RT}\right)(E_{1/2}^{PhOH} - E_{1/2}^0)\right] = 1 + \beta_2[PhOH]^2 \quad (\text{Eq. 35b})$$

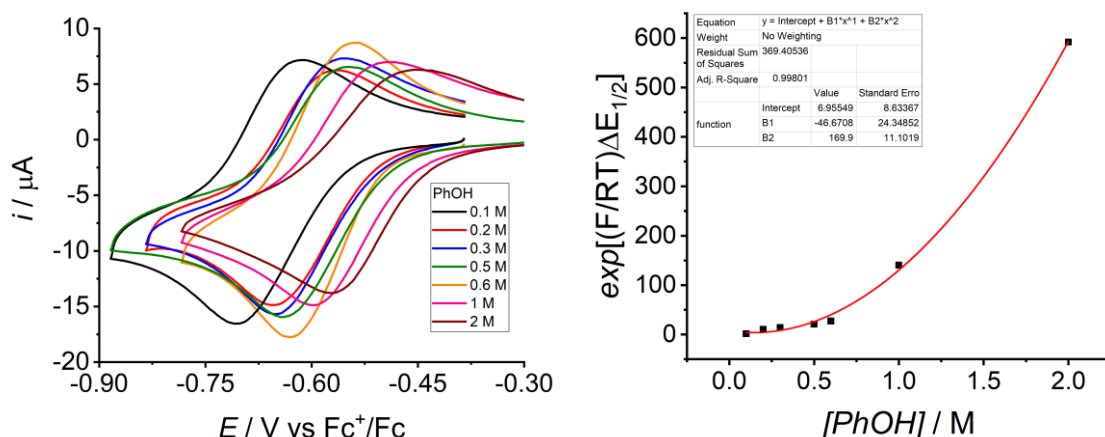


Figure 62. Left: CV traces under N_2 of 0.8 mM Fe(Salophen)Cl in ACN in the presence of 0.1 M tetraethylammonium tetrafluoroborate with different concentrations of phenol. Right: plot of Eq. 35b as a function of $[PhOH]$, with the proposed parabolic fit.

The anodic shift observed is attributed to a binding event that might in turn be ascribed to coordination of two molecules of phenol to the iron center and protonation of a Salophen phenoxide moiety. As a further remark, the separation between the cathodic and anodic peaks (ΔE_p) increases with increasing $[PhOH]$, from 95 mV (0.1 M PhOH) to 120 mV (2 M PhOH). This observation and the comparison between the shape of the cathodic and anodic traces of the Fe^{III}/Fe^{II} couple when $[PhOH] = 2 \text{ M}$ suggests partial dissociation of the chloro ligand upon the first reduction event. These observations pertain to a more complicated scenario involving multiple ligand-exchange equilibria. Based on previous observations by Nichols *et al.*¹⁰¹, we considered also the possible intervention of protonation equilibria of the complex upon its reduction in the presence of PhOH,

i.e. PCET events contributing as well to the observed effect of chemical reactions on the electrochemical behaviour of the target molecule.

A similar behaviour is displayed by $\text{Fe}_2(\text{Salophen})_2(\mu\text{-O})$ when studied in the presence of a high concentration of phenol. However, in this latter case, phenol has a twofold role: first, it acts as a Brønsted acid towards the starting dinuclear Fe^{III} complex, inducing protolysis of the μ -oxo bridge and generating two mononuclear iron units (indeed, when the lowest 0.1 M phenol concentration is used, an irreversible cathodic peak at -1.13 V vs Fc^+/Fc is still observed, that is attributed to residual $[\text{Fe}_2(\text{Salophen})_2(\mu\text{-OH})]^+$). Second, phenol binds to the complex and causes the progressive anodic shift of the $\text{Fe}^{\text{III}}/\text{Fe}^{\text{II}}$ $E_{1/2}$ value (Figure 63)

In order to quantitatively describe the binding events competing to the mononuclear complex $\text{Fe}(\text{Salophen})^+$ the knowledge of the $E_{1/2}$ value for the $\text{Fe}^{\text{III}}/\text{Fe}^{\text{II}}$ couple in the absence of phenol would be required. However, the $\text{Fe}^{\text{III}}/\text{Fe}^{\text{II}}$ wave for the mononuclear complex is observed only upon protolysis of a different starting species, $\text{Fe}_2(\text{Salophen})_2(\mu\text{-O})$, and therefore the Brønsted acid is required in solution as well. This implies that protolysis of the μ -oxo bridge by phenol may not be conceptually disjointed from the binding process, the system not being suited for description with a single equation. Although further investigation of the matter was felt to be beyond the purpose of the present work, an attempt to relate the shift of the $E_{1/2}$ for the $\text{Fe}^{\text{III}}/\text{Fe}^{\text{II}}$ couple for $\text{Fe}(\text{Salophen})^+$ was made by means of Eq. 36:

$$\exp\left[\left(\frac{F}{RT}\right)E_{app}^0\right] = (1 + \beta_2[\text{PhOH}]^2) \cdot \exp\left[\left(\frac{F}{RT}\right)E_{\frac{1}{2}}\right] \quad (\text{Eq. 36})$$

The fitting outcome (Figure 63) reveals a similar trend as that discussed for $\text{Fe}(\text{Salophen})\text{Cl}$, suggestive of binding of two molecules of phenol to the iron complex.

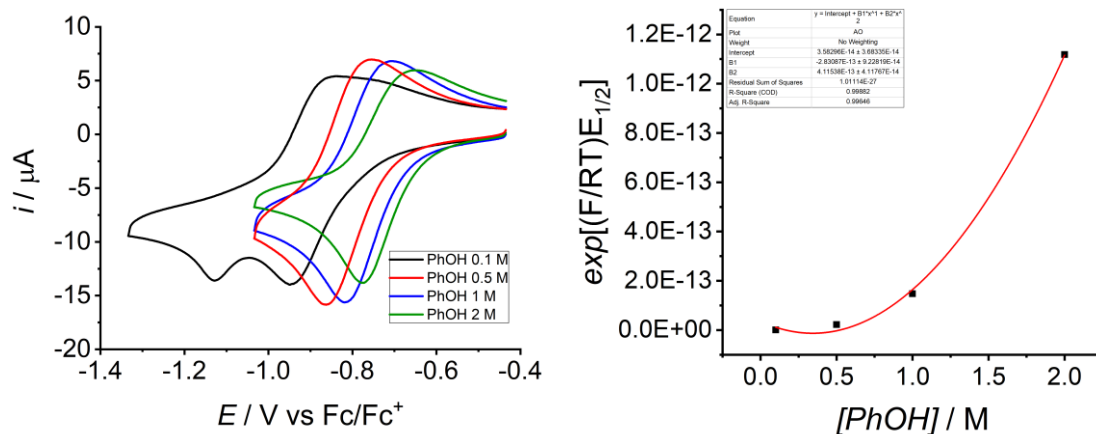


Figure 63. Left: CV traces under N_2 atmosphere of 0.4 mM $\text{Fe}_2(\text{Salophen})_2(\mu\text{-O})$ in ACN in the presence of 0.1 M tetraethylammonium tetrafluoroborate with different concentrations of phenol. Right: plot of Eq. 36 as a function of $[\text{PhOH}]$, with the proposed parabolic fit.

Appendix 2.3 – Competitive binding of chloride and phenol

As discussed previously, dissociation of chloride is promoted by reduction from Fe^{III} to Fe^{II} , with the simultaneous binding of PhOH . This is corroborated by the electrochemical behaviour of the $\text{Fe}(\text{Salophen})\text{Cl}$ complex when tetrabutylammonium chloride is used as both the supporting electrolyte and a chloride ion source, in the presence of 2 M PhOH (Figure 64). A cathodic shift of the $E_{1/2}$ value is indeed observed (from $-0.51 \text{ V vs Fc}^+/\text{Fc}$ to $-0.63 \text{ V vs Fc}^+/\text{Fc}$), coherent with the effect of coordination, the chloride binding event being more favourable for Fe^{III} than Fe^{II} . Furthermore, the ΔE_p is notably diminished upon introduction of excess chloride to the value of 73 mV, approaching electrochemical reversibility. This is attributed to an overall inhibited chloride dissociation process.

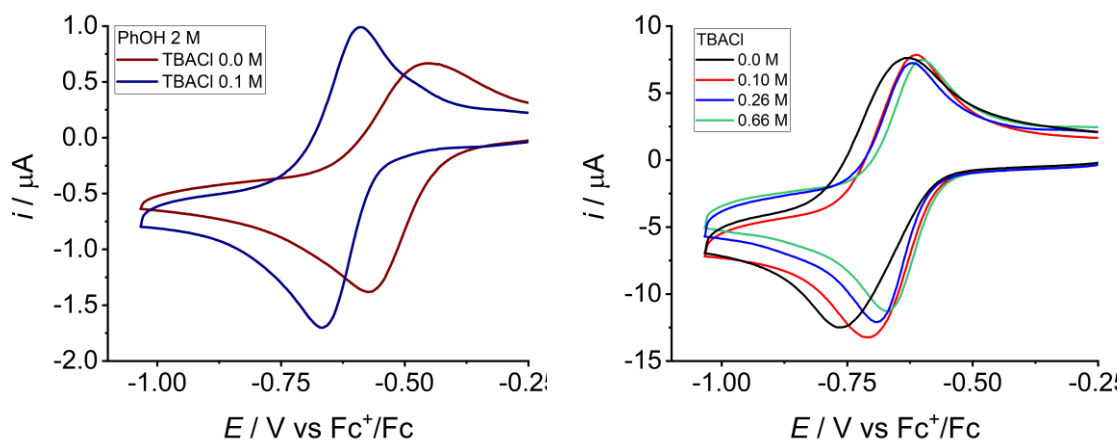


Figure 64. Left: CV traces under N_2 atmosphere of 0.8 mM $Fe(Salophen)Cl$ in the presence of 0.1 M tetraethylammonium tetrafluoroborate in the absence (wine trace) and in the presence (navy trace) of 2 M PhOH. Right: cyclic voltammetry traces under N_2 of 0.4 mM $Fe_2(Salophen)_2(\mu-O)$ in the presence of 2 M PhOH and increasing [TBACl].

An analogous approach may be followed for $Fe(Salophen)^+$ generated by protolysis of $Fe_2(Salophen)_2(\mu-O)$ in 2 M PhOH. The effect of an external source of chloride anion on the electrochemical behaviour of the mononuclear species can thus be studied. Upon increasing [TBACl], the $E_{1/2}$ anodically shifts from an initial value of -0.70 V vs Fc^+/Fc to -0.63 V vs Fc^+/Fc , converging to the same value obtained for $Fe(Salophen)Cl$ in the presence of [TBACl] = 0.1 M (Figure 64). The binding of chloride to $Fe(Salophen)^+$ produces a decreased ΔE_p , from 133 mV when no external chloride is introduced, to a saturation value of 69 mV, reached when [TBACl] = 0.26 M. These observations lead to hypothesize the same electrochemical regime is reached in the presence of excess $[Cl^-]$ regardless of the starting mononuclear iron complex. The binding event quantitatively translates into a linear Nernstian plot of the cathodic Fe^{III}/Fe^{II} peak potential with respect to $\log([TBACl])$, with a slope of +50 mV (Figure 65), consistent with slow chloride dissociation. However, the same does not hold for the $E_{1/2}$ value, its trend being affected by a nearly constant anodic peak potential. These observations combined suggest the chloride ligand is being subjected to slow dissociation upon electrochemical reduction.

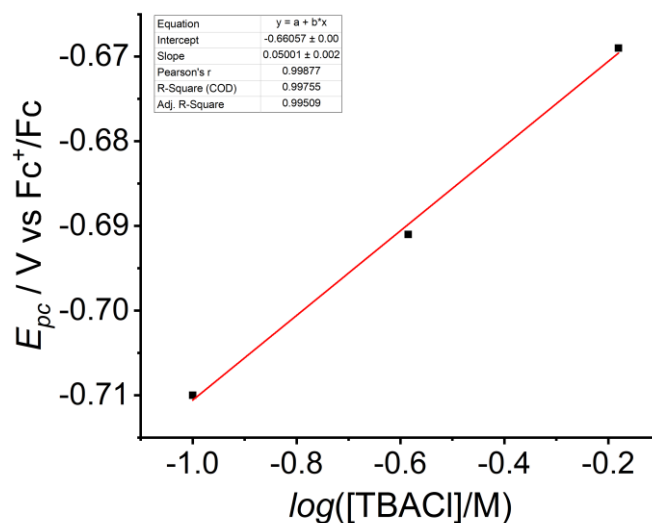


Figure 65. Plot of the Fe^{III}/Fe^{II} cathodic peak potential as a function of the logarithm of [TBACl], with the proposed linear fit.

Given the discussion developed so far, the difference between the Fe^{III}/Fe^{II} $E_{1/2}$ value for the two mononuclear complexes at every value of [PhOH] is ascribed to the presence of the chloro ligand.

When the potential is scanned to the Fe^{II} → Fe^I reduction wave in the presence of phenol (*vide supra*), a new oxidation feature is observed for Fe(Salophen)Cl (Figure 66, blue trace). The peak potential of the new feature (−0.63 V vs Fc⁺/Fc) coincides with that of the anodic Fe^{III}/Fe^{II} peak observed for the mononuclear unit deriving from protolysis of Fe₂(Salophen)₂(μ-O) (Figure 66, red trace). The appearance of new anodic features is indeed not observed when considering CV traces of the protolyzed Fe(Salophen)⁺ (Figure 43).

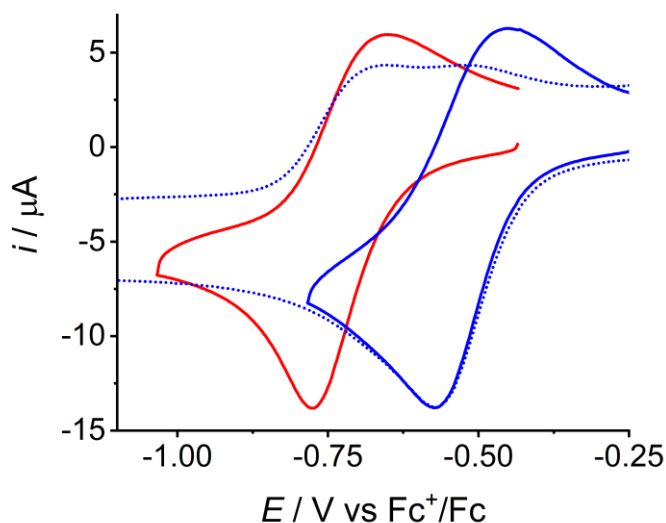


Figure 66. CV traces in ACN under N_2 atmosphere of 0.8 mM $Fe(Salophen)Cl$ (blue traces), restricted to the Fe^{III}/Fe^{II} couple (full trace) or registered upon scanning to -2.10 V vs Fc^+/Fc (dotted trace) in the presence of 2 M PhOH and 0.1 M tetraethylammonium tetrafluoroborate; CV trace of $Fe_2(Salophen)_2(\mu-O)$ (0.4 mM) in the presence of 2 M PhOH, tetraethylammonium tetrafluoroborate (red trace).

It is proposed that irreversible dissociation of the chlorido ligand occurs substantially when reaching potentials at which irreversible electrochemical processes occur in the presence of phenol. The system then follows an anodic pathway involving a mononuclear iron complex lacking chloride in the coordination sphere of the metal center.

Similar results are indeed obtained in the CV under N_2 and CO_2 atmosphere, with the concentration of phenol that impacts on the Cl^- displacement, as suggested by the increase of intensity of the wave at -0.75 V vs Fc^+/Fc when increasing the amount of phenol.

Appendix 2.4 – Foot-of-the-wave-analysis

The Foot of the wave analysis (FOWA) approach was followed to extract kinetic information from the voltammetric trace of 0.8 mM Fe(Salophen)Cl in the presence of PhOH (0.1 – 0.6 M) as the proton donor. The analysis, described in detail by Costentin *et al.* and discussed in Chapter 1, consists in elaborating the cyclic voltammogram of the catalyst, producing a plot of the normalized current as a function of the parameter $1 / \{1 + \exp[(F / RT)(E - E^0_{\text{cat}})]\}$, where F is the Faraday constant, E the potential (independent variable in the CV trace) and E^0_{cat} the standard potential of the Fe^{II}/Fe^I active redox couple of the catalyst, here approximated to the half-wave potential. In the incipient portion of the function, corresponding to the foot of the catalytic wave, the influence of side-phenomena causing the catalytic wave to deviate from a pure kinetic shape are attenuated. This region can be therefore fitted to a linear function, Eq. 9 applying to its slope, as reported in Figure 67.

Knowing the concentration of CO₂ in saturated acetonitrile (0.28 M), the kinetic constant can be calculated and then converted to $k_{\text{cat}} = k \cdot [\text{CO}_2]$.

It should be mentioned that in the present case, the determination of the k_{cat} with the FOWA is subject to uncertainty, due to the narrow interval of linearity in the fitting and due to the variation of $E_{1/2}$ of the Fe^{II}/Fe^I couple under the catalytic conditions.

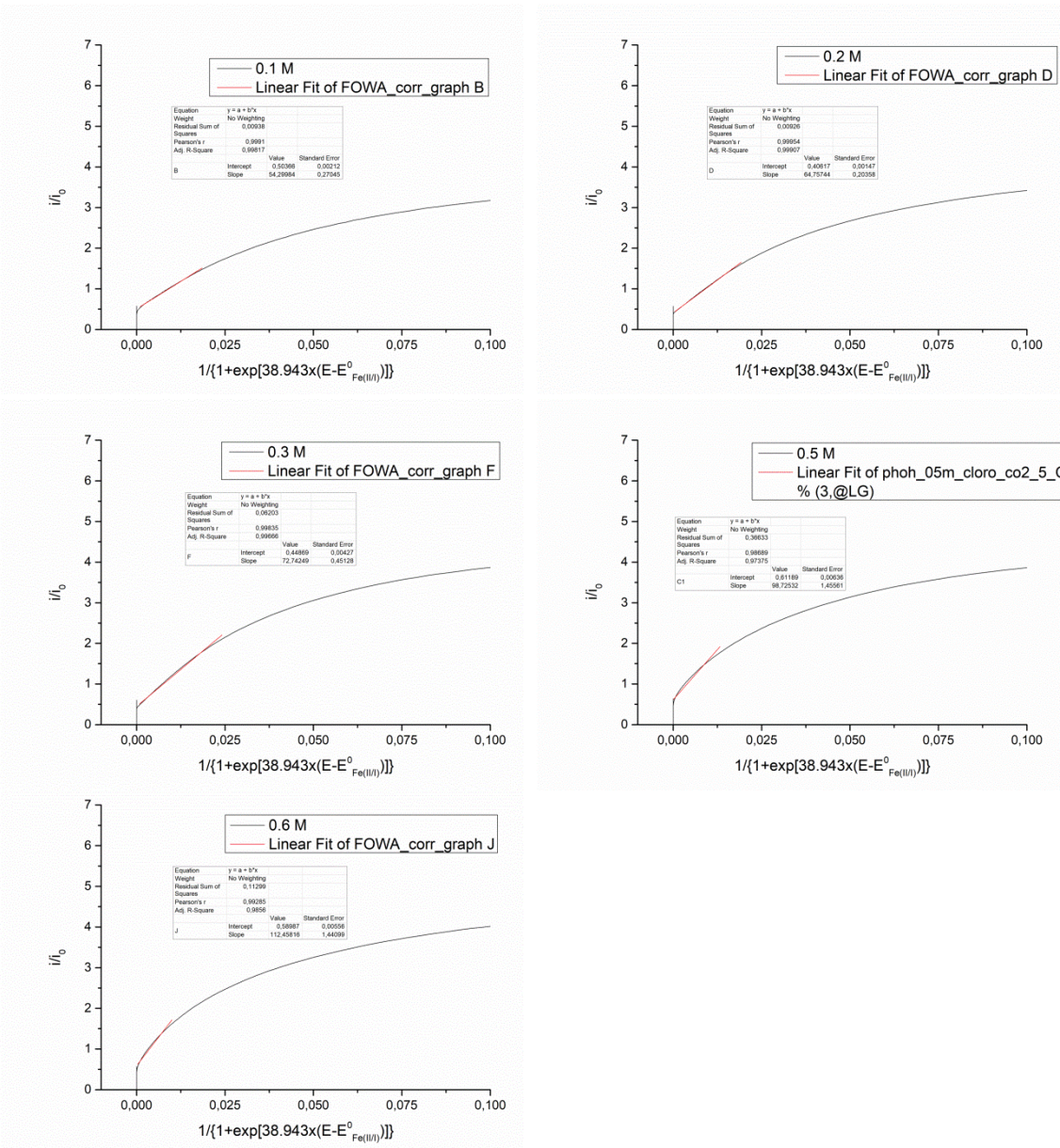


Figure 67. Fitting of Foot-of-the-wave-analysis of CV traces of 0.8 mM Fe(Salophen)Cl under CO₂-saturated solutions, at different concentrations of phenol, in the range 0.1 ÷ 0.6 M.

3. Fe^I intermediates bearing N₂O₂ Schiff base ligands: study of the effects of ligand electronic properties and of the proton donor on reactivity with CO₂

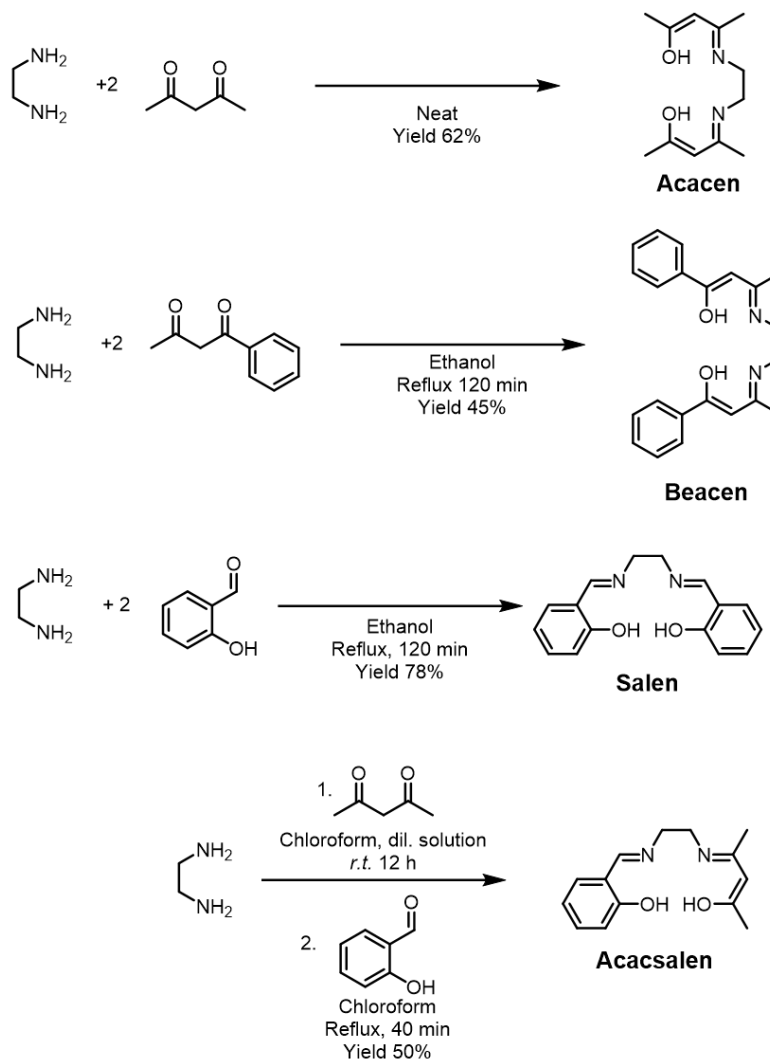
The present Chapter revolves around the developments based on the findings described in Chapter 2, explored within the Nano and Molecular Catalysis Group in the University of Padova. My contribution has been the conceptualization of the research and its experimental development. Francesco Crisanti and Daniel Civettini contributed as well to the experimental work as Master's students, while Density Functional Theory (DFT) calculations were performed by Prof. Andrea Sartorel.

3.1 Rationale

The promising results on Fe(Salophen) prompted us to approach the study of Fe complexes bearing N₂O₂ Schiff base ligands to constitute a proper family of CO₂ reduction catalysts. The ligands chosen for the synthesis of the complexes derived from ethylenediamine and β -diketones and/or salicylaldehyde. Interestingly, previous reports explored the redox chemistry of such complexes only in the domain of the Fe^{III}/Fe^{II} couple.¹⁷⁴ We demonstrated that a formal Fe^I redox state is also accessible, and explored its reactivity towards carbon dioxide reduction. Spectroscopic, electrochemical and spectroelectrochemical investigation allowed to gain information about the family of catalysts and to quantitatively correlate the effect of substituents in their ligand structure to the redox properties. Finally, we evaluated their performance in promoting CO₂ electrochemical reduction, obtaining useful metrics for describing the overall performance of the Fe N₂O₂ Schiff base catalyst family.

3.2 Synthesis and characterization of the complexes

The ligands investigated were synthesized *via* imine condensation of 1,2-diaminoethane with β -diketones (acetylacetone, benzoylacetone) or salicylaldehyde, following literature procedures (Scheme 11). Briefly, N,N'-ethylene-bis(acetylacetoneimine) (Acacen) and N,N'-ethylene-bis(benzoylacetoneimine) (Beacen) were obtained allowing two equivalents of β -diketones to react with 1,2-diaminoethane. A similar protocol was followed in the reaction of two equivalents of salicylaldehyde with the same diamine to produce N,N'-bis(salicylaldehyde)-1,2-phenylenediamine (Salen). Finally, stepwise condensation of one equivalent of acetylacetone and, subsequently, of salicylaldehyde, afforded the mixed-structure ligand N,N'-ethylene-(acetylacetoneimine)(salicylideneimine) (Acacsalen). The identity and purity of the ligands were confirmed by $^1\text{H-NMR}$, $^{13}\text{C-NMR}$, elemental analysis and ESI-MS.



Scheme 11. Synthesis of the Schiff base ligands involved in the study.

The synthesis of Fe^{III} derivatives was then approached. The procedure chosen involved the use of ^tBuOK as a strong base to quantitatively deprotonate the ligands, followed by treatment of the reaction mixture with excess FeCl₃·6H₂O. The complexes, soluble in dichloromethane, could be recovered upon dissolution and subsequent removal by filtration of the inorganic salts (KCl and excess ferric chloride). Solvent evaporation afforded Fe(L)Cl complexes in high yield (84-98%), where L corresponds to the Schiff base ligand. The iron complexes were finally characterized by means of elemental analysis and ESI-MS to confirm their identity

and purity. Further details are reported in the Experimental Section to the present Chapter.

The electrochemical properties of the iron complexes were investigated by cyclic voltammetry in acetonitrile solutions containing 0.1 M tetraethylammonium tetrafluoroborate, and are summarized in Table 5; Figure 68 (black traces under N_2) reports the CV traces of Fe(Salen)Cl, Fe(Beacen)Cl, Fe(Acacen)Cl and Fe(Acacsalen)Cl.

Although the redox-active nature of Schiff base ligands is well-established (see also previous chapter), common electrochemical features encompassing these coordination compounds are two stepwise monoelectronic reduction processes attributed to metal-based couples, Fe^{III}/Fe^{II} and Fe^{II}/Fe^I , in which chloride binding equilibria are coupled to the electrochemical process driven by the working electrode potential (with analogy to Scheme 5, drawn for Fe(Salophen)Cl).

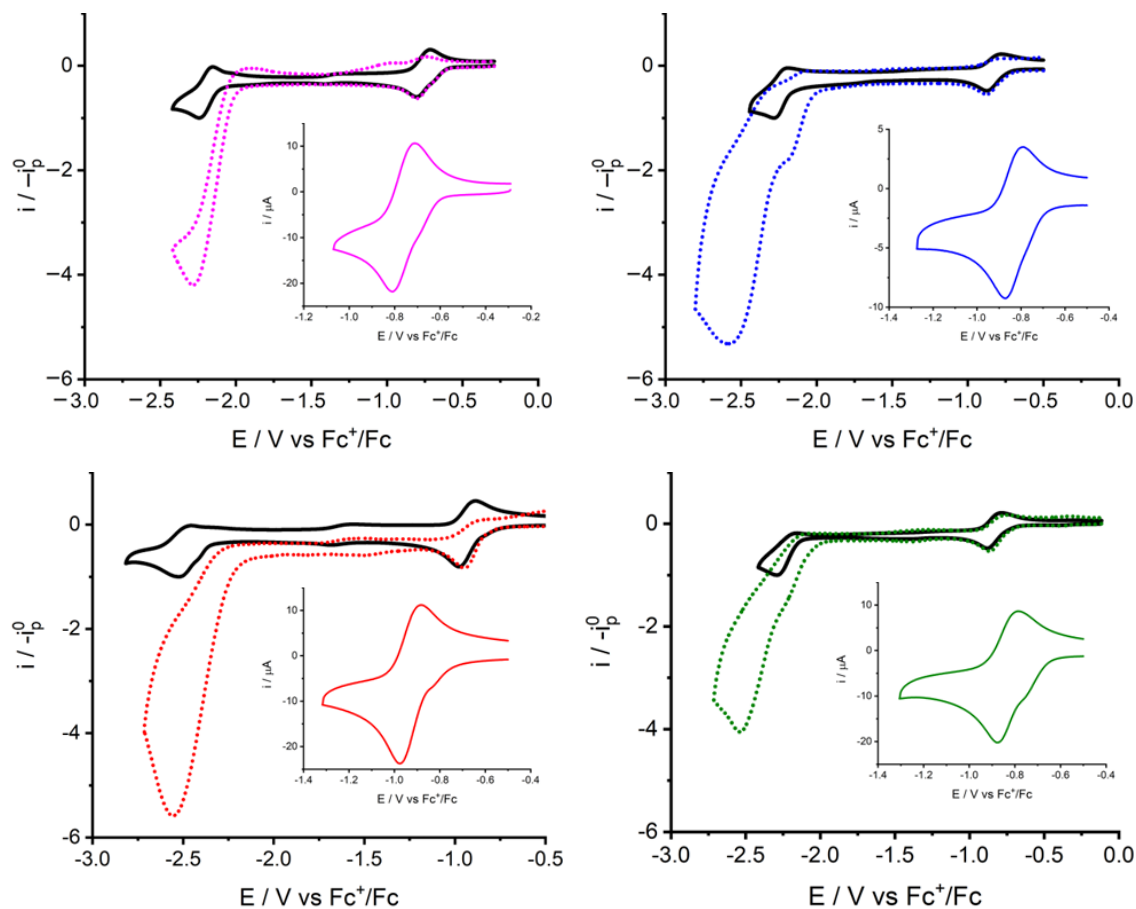


Figure 68. CV traces of 1 mM Fe(L)Cl complexes in acetonitrile in the presence of 0.1 M tetraethylammonium tetrafluoroborate under N₂ (black traces) and CO₂ (coloured dotted traces) atmospheres. Top left: Fe(Salen)Cl; top right: Fe(Beacen)Cl; bottom left: Fe(Acacen)Cl; bottom right: Fe(Acacsalen)Cl. Insets represent CV traces restricted to the Fe^{III}/Fe^{II} couples under N₂ atmospheres. Scan rate: 0.1 Vs⁻¹.

The electrochemical behaviour of the complexes at the level of their Fe^{III}/Fe^{II} couples, first described by Carré *et al.*¹⁷⁴, is typical of a quasi-reversible transformation. Specifically, all Fe^{III}/Fe^{II} waves display ΔE in the range 80 ÷ 100 mV, as summarized in Table 5, coherently with competition between the coordinating solvent and the chloride anion for the apical coordination site in the Fe^{III} and Fe^{II} states.

The second cathodic wave, encountered at more negative potentials, displays quasi-reversible features, depending on the Schiff base ligand coordinated to the

iron ion. The structural and electronic analogies justifying the group categorization of the iron complexes herein described are manifest in the accessibility of a formal, low valent Fe^I state (the formation of a Fe^I intermediated was corroborated by electron paramagnetic resonance (EPR) spectroscopy for Fe(Salophen), coupled to *ex* and *in situ* spectroelectrochemistry, as discussed in Chapter 2).

The electronic properties of the Schiff base ligands and their direct influence on the redox potentials of the Fe^{III}/Fe^{II} and Fe^{II}/Fe^I couples have been evaluated on the basis of the σ -donor strength of the N₂O₂ ligand; interestingly, in the series of coordination complexes examined in this work, correlations are observed between the Fe^{III}/Fe^{II} and Fe^{II}/Fe^I reduction potentials and the energy of the highest occupied molecular orbital of the ligands involved in σ -donation (HOMO-2), as predicted by DFT calculations at the B3LYP/6-311+g(d,p) level of theory: slopes of -0.40 ± 0.04 and of -0.84 ± 0.11 V/eV are observed for the Fe^{III}/Fe^{II} and Fe^{II}/Fe^I couples, respectively (Figure 69). Notably, the almost double slope value observed for the Fe^{II}/Fe^I couples with respect to Fe^{III}/Fe^{II} ones indicate a higher impact of the nature of the ligand on the reduction potentials of the former couple. This could be ascribed to the fact that the Fe^{III}/Fe^{II} transition is expected to be charge neutral upon loss of the Cl⁻ ligand, while the Fe^{II}/Fe^I transition is expected to generate a negative charge at the complex.

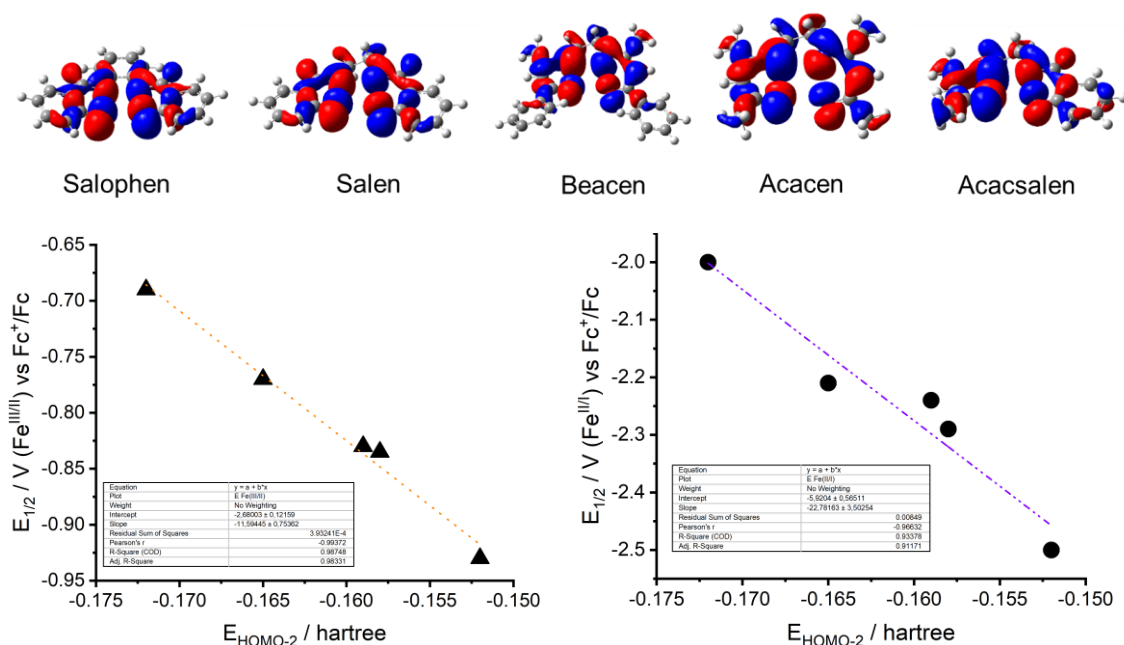


Figure 69. Top: visual representations of the HOMO–2 orbitals of the ligands in their dianionic forms. Bottom left: plot of the $E_{1/2}$ of the $\text{Fe}^{\text{III}}/\text{Fe}^{\text{II}}$ couples as a function of the energy of the HOMO–2 orbital of the ligand (σ -donating). Bottom right: plot of the $E_{1/2}$ of the $\text{Fe}^{\text{II}}/\text{Fe}^{\text{I}}$ couples as a function of the energy of the HOMO–2 orbital of the ligand (σ -donating).

Characterization of the Fe^{I} intermediates in the series of complexes was further performed via SEC-UV/Vis. Figure 70 reports the absorption traces of the iron N_2O_2 complexes upon application of the potentials associated to the second reduction waves (-2.21 and -2.24 V vs Fc^+/Fc for $\text{Fe}(\text{Salen})$ and $\text{Fe}(\text{Beacen})$, and -2.50 and -2.25 V vs Fc^+/Fc for $\text{Fe}(\text{Acacen})$ and $\text{Fe}(\text{Acacsalen})$, respectively). Consistent UV/Vis spectral changes were observed, and in particular:

- i) bleaching of the initial absorption of the Fe^{III} species at 464 and 311 nm for $\text{Fe}(\text{Salen})\text{Cl}$, 490 and 270 nm for $\text{Fe}(\text{Acacen})\text{Cl}$ and 492 and 293 nm for $\text{Fe}(\text{Beacen})\text{Cl}$, attributed to ligand-to-metal charge transfer bands, LMCT;

- ii) rising of new bands at 344 nm for Fe(Salen), 295 nm for Fe(Acacen) and 354 nm for Fe(Beacen), respectively, attributed to metal-to-ligand charge transfer bands (MLCT) proper of the electron rich Fe^I state.
- iii) In the case Fe(Acacsalen)Cl, bleaching of the band at 475 nm is contextual with two absorption features rise at 308 and 379 nm, respectively. These two MLCT components are expected on the basis of the peculiar character of the asymmetric Acacsalen ligand, bearing both the acetylacetonimine and salicylideneimine fragments. Incidentally, the two absorption maxima observed for Fe^I(Acacsalen) are similar to those observed separately for Fe^I(Acacen) (288 nm) and for Fe^I(Salen) (354 nm).

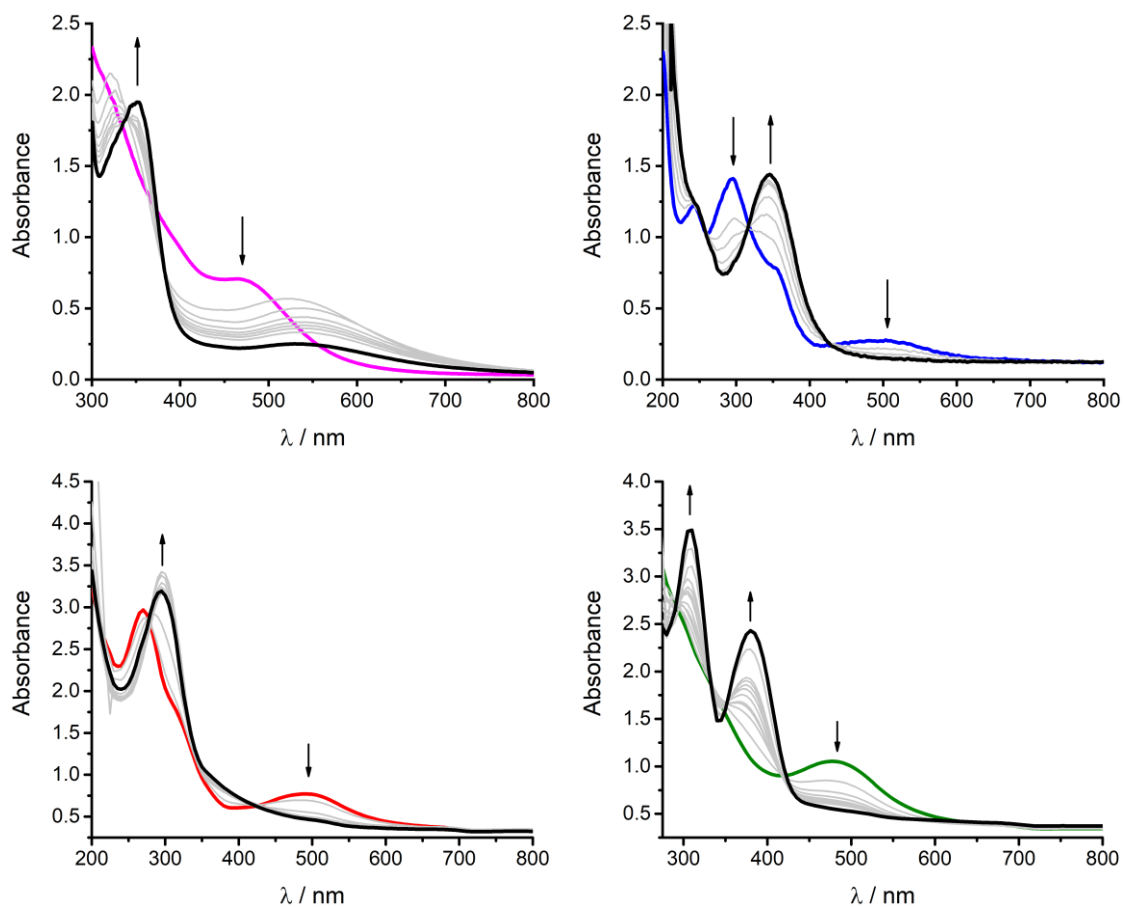


Figure 70. SEC-UV/Vis traces under N_2 atmosphere of 1 mM Fe(Salen)Cl (top left), Fe(Beacen)Cl (top right), Fe(Acacen)Cl (bottom left) and of Fe(Acacsalen)Cl (bottom right) in ACN, at the potentials corresponding to the generation of the formal Fe^I state.

The energy of the MLCT band observed for the Fe^I intermediates correlates linearly with the redox potential of the Fe^{II}/Fe^I couple; the trend shows that the more negative the potential of the Fe^{II}/Fe^I couple, the higher the energy of the MLCT band (absorption shifted towards the blue region of the spectrum, Figure 71). Indeed, spectroelectrochemistry provides the experimental basis for the correlation between redox and spectroscopic features related to the electronic properties of the ligands, thus allowing for a group categorization of the Schiff base iron complexes.

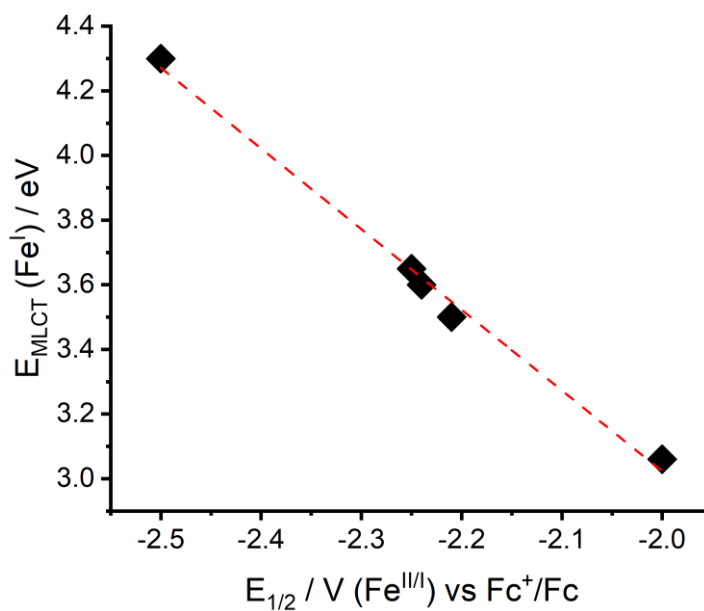


Figure 71. Plot of the energy of the MLCT band in Fe^I intermediates vs the $E_{1/2}$ of the Fe^{II}/Fe^I couple. In the case of 1 mM $Fe(Acacsalen)Cl$, the energy plotted is the average of the energies of the two MLCT experimentally observed at 308 and 379 nm (see Table 5).

Iron Complex	$E_{1/2} (V) vs. Fc^+/Fc, V$ ($\Delta E, mV$)		$\lambda_{MAX} Fe^I$	$-i_{CO_2}/i_{N_2}$
	$Fe^{II/I}$	$Fe^{II/I}$		
$Fe(Salen)Cl$	-0.77 (98)	-2.21 (89)	354	-4.2
$Fe(Acacen)Cl$	-0.93 (93)	-2.50 (68)	288	-5.6
$Fe(Beacen)Cl$	-0.83 (81)	-2.24 (93)	344	-5.3
$Fe(Acacsalen)Cl$	-0.83 (91)	-2.25 (131)	308, 379	-4.1

Table 5. Electrochemical and spectroscopic characterization of iron complexes employed in this work.

3.3 Reactivity of Fe^I towards carbon dioxide

In the presence of carbon dioxide, the voltammetric traces of the iron complexes display intense, irreversible peak-shaped waves at the level of the Fe^{II}/Fe^I couple (see the i_{CO_2}/i_{N_2} parameter summarized in Table 6, where i_{CO_2} is the peak current of the wave under CO₂, and i_{N_2} is the peak current of the one-electron cathodic wave of the Fe^{II}/Fe^I couple under dinitrogen atmosphere). The features of the wave observed under CO₂ atmosphere are indicative of an electrocatalytic event involving the active Fe^I intermediate generated at the electrode, as evident in Figure 68. In the case of Fe(Beacen)Cl, the wave observed in the presence of CO₂ is composed of two contributions. A pre-wave, observed at -2.20 V vs Fc⁺/Fc (positively shifted by 80 mV with respect to the cathodic Fe^{II}/Fe^I peak under N₂ atmosphere), is followed by the more intense wave peaking at $E_p = -2.58$ V vs Fc⁺/Fc. Such observation is likely ascribable to two different reduction pathways - associated to different reduced intermediates - of which the second, generated at more cathodic potentials, is involved in a faster catalytic reaction. The first cathodic wave observed in the presence of CO₂ could therefore be reasonably attributed to a slower process, proceeding through an adduct obtained as the irreversible association between CO₂ and the reduced Fe^I complex, as previously observed in the case of a Fe(qpy) and Fe(Salophen)Cl complexes (see Chapter 2).⁵⁸ We anticipate that in the presence of proton donors (*vide infra*), the subsequent catalytic current will enhance at this potential, most likely due to a protonation-first pathway of the reduced adduct, promoting the catalytic transformation.

Furthermore, the electrocatalytic process impacts on the behaviour observed in the backward anodic scan. Indeed, the backward anodic trace recorded in the presence of CO₂ displays an abatement of the Fe^{II} → Fe^{III} reoxidation wave. In the case of Fe(Salen)Cl, a new anodic peak ($E_p = -0.93$ V vs Fc⁺/Fc) arises, 210 mV more negative than the Fe^{II}/Fe^{III} oxidation peak (Figure 68). These observations are ascribable to chemically irreversible transformations

of the complexes induced by the applied potential in the presence of CO₂ acting as substrate. These processes might involve loss or exchange of apical ligands in the coordination sphere of the iron ion, as already discussed for Fe(Salophen)Cl. Fe(Acacen)Cl and Fe(Beacen)Cl, on the other hand, undergo complete abatement of the Fe^{II} → Fe^{III} backward anodic wave. Such observation is suggestive of a strong impact of the electrocatalytic process on the stability of iron complexes with β-diketoiminato ligands.

Reactivity of the Fe^I species with CO₂ was further supported by two complementary experiments:

i) isolation of Fe^I species upon constant potential electrolysis under inert atmosphere, followed by addition of carbon dioxide (in the absence of applied potential), that led to an immediate colour change of the solution (see pictures in Figure 72); in the case of Fe(Salophen), reactivity of Fe^I with CO₂ under analogous conditions was associated to a redox process involving oxidation of Fe^I to Fe^{III} by CO₂, as supported by EPR evidence. Notably, no reduced products of CO₂ were detected under these conditions (in particular carbon monoxide), suggesting that a further reduction of the Fe^I-CO₂ adduct is required in order to close the cycle and release the products (*vide infra*).

ii) SEC-UV/Vis analysis in the presence of CO₂, where the diagnostic MLCT features of Fe^I intermediate are blue-shifted with respect to those observed under dinitrogen (Figure 72). In particular, the absorption maximum shifts from 354 to 345 nm for Fe(Salen)Cl and from 344 nm to 332 nm for Fe(Beacen)Cl; in the case of Fe(Salophen)Cl, the MLCT shifts from 405 nm to 385 nm in the presence of CO₂, suggesting the reactivity of the complex towards CO₂, and the likely formation of an iron carbonyl adduct.

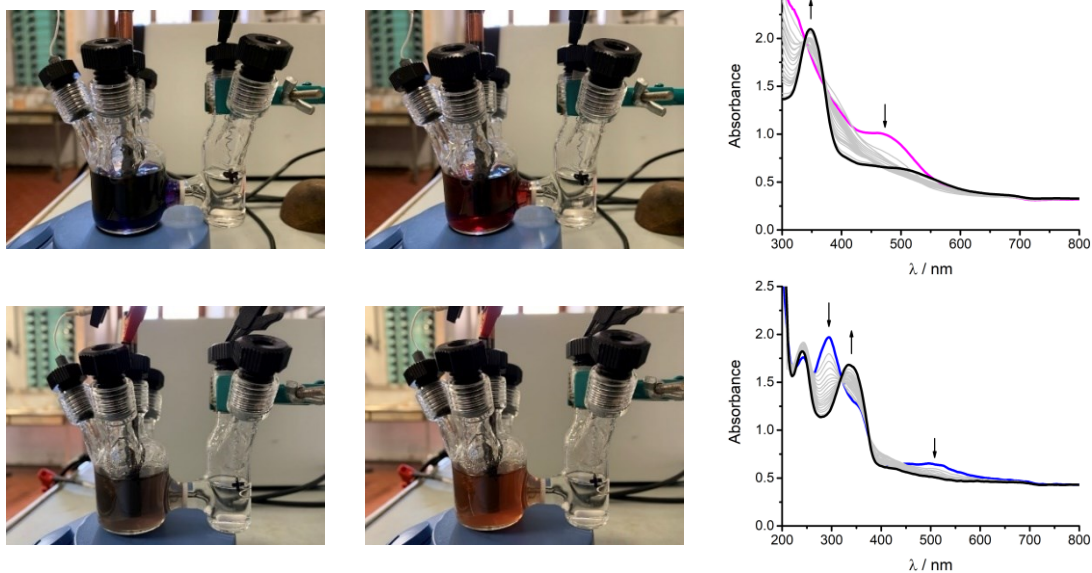


Figure 72. Pictures of the gas-tight electrochemical cell containing the Fe^I species electrogenerated from 1 mM Fe(Salen)Cl (top) and Fe(Beacen)Cl (bottom) in ACN before (left) and after (mid) addition of CO₂. Right: SEC-UV/Vis traces under CO₂ atmosphere of 1 mM Fe(Salen)Cl (top) and Fe(Beacen)Cl bottom at the potential associated with the generation of Fe^I.

3.4 Effect of Proton Donors and Electrolysis

In order to evaluate and characterize the putative electrocatalytic reduction of CO₂ in the presence of the iron complexes, the use of a proton donor adjunctant was considered. Following the indication of a previous screening conducted with Fe(Salophen), phenol (PhOH, pK_a = 29 in acetonitrile) was first considered, since it provided high selectivity for CO formation, also supported by ¹³CO₂ labelling experiments. Trifluoroethanol was also evaluated (TFE, pK_a = 35.4 in acetonitrile, although a value of 25.1 was estimated in the presence of CO₂ due to the reaction of the trifluoroethoxide conjugate base with CO₂ to give the CF₃CH₂OCO₂⁻ carbonate)^{73,190}, since it was recently used in combination with Mn-based and Fe porphyrin CO₂ reduction catalysts. The concentration of 0.3 M for TFE was selected as the one providing the maximum current in a CV screening with Fe(Acacen)Cl. The effect of the proton donors in the presence of CO₂ was first investigated by CV (Figure 73), by choosing 0.3 M and 0.5 M as the concentrations of TFE and PhOH, respectively.

The major effect is a further current increase of the cathodic wave at the level of the Fe^{II}/Fe^I couple, as indicated by the i_{CO_2}/i_{N_2} ratio (Table 6). This is coherent with a more efficient catalytic process, highlighting the beneficial role of mild proton donors in facilitating the further evolution of the putative Fe–CO₂ intermediate upon its stabilization by hydrogen bonding and stepwise protonation. Notably, the presence of trifluoroethanol led to the observation of the Fe^{II} → Fe^{III} re-oxidation wave in the backward scans, likely indicative of a more efficient cycle, with a lower impact on the chemical stability of the catalytically active molecular species (*vide supra*).

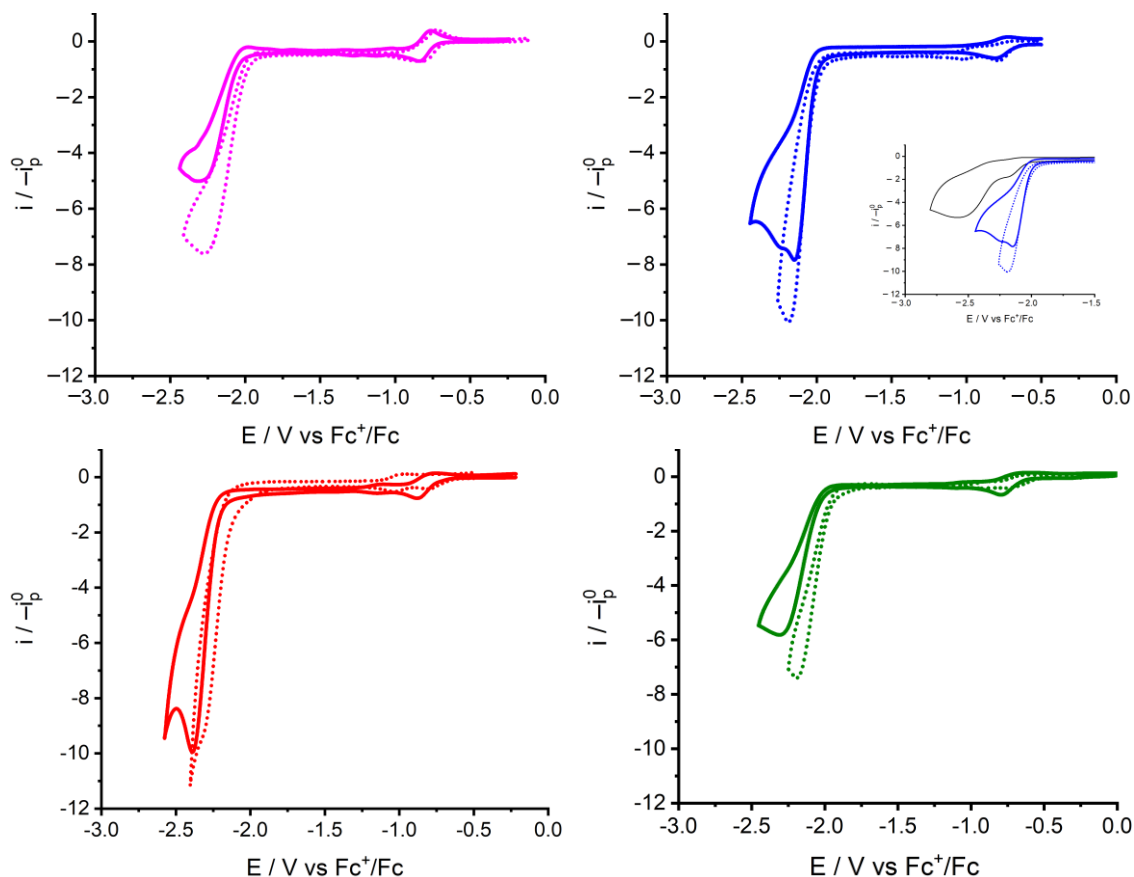


Figure 73. CV traces of 1 mM Fe(L)Cl complexes under CO₂ atmosphere in the presence of 0.3 M TFE (full traces) and 0.5 M PhOH (dotted traces). Top right (magenta traces): Fe(Salen)Cl; top left (blue traces): Fe(Beacen)Cl; bottom left (red traces): Fe(Acacen)Cl; bottom right (green traces): Fe(Acacsalen)Cl. Scan rate: 0.1 Vs⁻¹.

Constant potential electrolysis was then performed in order to identify and quantify the products associated with the electrocatalytic waves, and to evaluate the stability of the systems. Three general considerations can be summarized as follows (Figure 74 and Table 6):

- i) Carbon monoxide (CO) and hydrogen (H₂) were the sole product identified; NMR analysis according to the procedure reported by Nichols *et al.*¹⁰¹ did not reveal the production of HCOO⁻.

ii) In all cases, the overall Faradaic efficiency of the process for CO and H₂ production was significantly lower than the ideal value; this is ascribed to both the need for pre-reducing the Fe^{III} to the active Fe^I state, and the consumption of reducing equivalents by the iron complexes leading to their inactivation and decomposition, as demonstrated by the drop of electrolysis current over time and by the marked changes in the UV/Vis spectra after electrolysis (see Paragraph 3.6 for a thorough discussion). Non-quantitative Faradaic yields are not unusual in the electrochemical reduction of CO₂ with coordination complexes, especially when low TON are achieved.

iii) The use of phenol as the proton donor led to a marked impact on the catalytic selectivity of the process (as defined in Chapter 1) depending on the iron complex. In particular, while high selectivity for CO was observed in the case of Fe(Salophen) and Fe(Salen), H₂-oriented selectivity was recorded for Fe(Acacen), Fe(Acacsalen), and Fe(Beacen), as shown in Table 6 and Figure 73, *i.e.*, for the species where the Fe^I intermediate is generated at more negative potentials and is thus expected to be more prone to a direct reaction with proton donors.

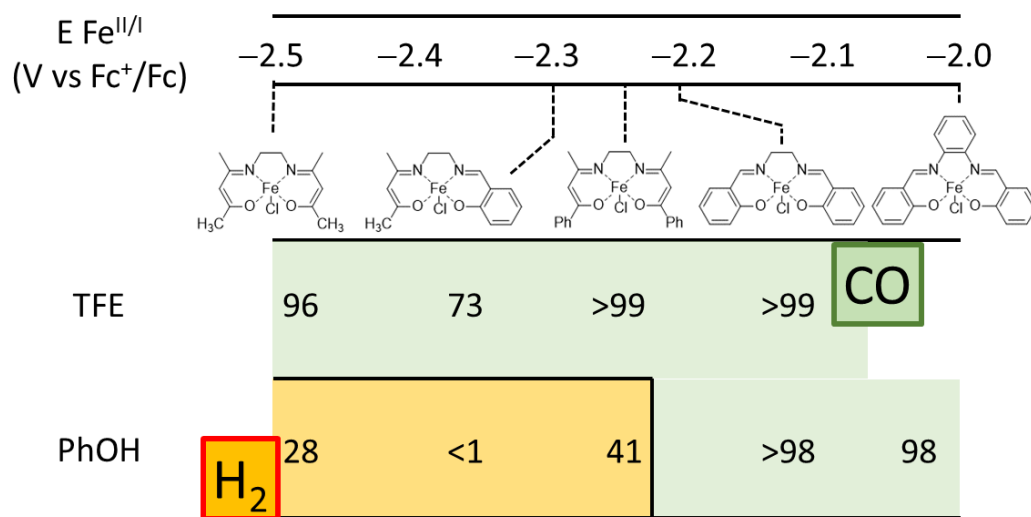


Figure 74. CO vs H_2 selectivity in CPE experiments with Iron complexes, depending on the proton donor. The selectivity was compared after the same charged passed, in particular at two electrons per iron catalyst (see Table 6), and used as performance indicators in the series.

Iron Complex	Proton Donor	E_p (V vs. Fc^+/Fc)	$-i_{CO_2}/i_{N_2}$	FY, CO (FY, H_2)	CO vs H_2 Selectivity
Fe(Salophen)Cl	PhOH 0.5 M	-1.99	-4.3	50 (1)	98
Fe(Salen)Cl	PhOH 0.5 M	-2.25	-7.6	40 (<0.5)	>98
	TFE 0.3 M	-2.29	-5.0	21 (<0.1)	>99
Fe(Acacen)Cl	PhOH 0.5 M	-2.31	-9.7 [1]	5.5 (13.7)	28
	TFE 0.3 M	-2.31	-10.0	13.5 (0.55)	96
Fe(Beacen)Cl	PhOH 0.5 M	-2.18	-10.0	10 (14.4)	41
	TFE 0.3 M	-2.15	-7.8	42 (<0.1)	>99
Fe(Acacsalen)Cl	PhOH 0.5 M	-2.19	-7.4	<1 (14.8)	<1
	TFE 0.3 M	-2.31	-5.8	18 (6.6)	73

Table 6. Electrochemical reduction of CO_2 with iron complexes in the presence of phenol (PhOH) or trifluoroethanol (TFE) proton donors.

3.5 Fe(Salen) as catalyst for the electrochemical CO₂-to-CO reduction

From a catalytic perspective, Fe(Salen)Cl appears the most promising candidate in the reduction of CO₂. Fe(Salen)Cl allowed to maintain a selectivity > 98 % along electrolysis after 25 and 20 electrons passed per Iron center with PhOH and TFE, respectively, reaching a turnover number for CO production of 4.6 and 2.6 with PhOH and TFE, respectively. Although still limited, the TON values confirm the possibility for Fe(Salen) to operate catalytically; for the sake of comparison, a TON of 8 and a Faradaic efficiency of 48% for CO were found under electrochemical conditions for one of the most recently investigated catalyst for reduction of CO₂ to CO, *i.e.*, Fe(qpy);⁵⁸ 3 TONs were registered for Fe(Salophen) with PhOH. The slightly higher stability of Fe(Salen) with respect to Fe(Salophen) could be associated to the more negative potential required for the reduction of the imine bond, which can be responsible for nucleation of Fe clusters and to the electrodeposition of Fe(0) nanoparticles.¹⁷²

Benchmarking of Fe(Salen)Cl was proposed on the basis of the overpotential (η) and the rate constant (k_{cat}), whose estimation can be directly obtained by the CV analysis. η was determined from the difference between the peak potential of the catalytic wave and the standard reduction potential associated with the CO₂/CO evaluated in the same conditions ($E^0(\text{CO}_2/\text{CO}) = -1.34$ vs Fc^+/Fc , *vide supra*): in the presence of 0.5 M PhOH, η results 0.91 V, significantly higher than the one observed for Fe(Salophen) under similar conditions, $\eta = 0.65$ V. The observation may be justified on the basis of the increased electron donating character of Salen ligand that requires a more negative potential to generate the Fe^I species. Concerning k_{cat} , given the impossibility of reaching an “S-shaped” wave typical of pure kinetic conditions operating at higher scan rates, a foot-of-the-wave analysis (FOWA) was conducted on the cyclic voltammogram, providing an estimation of $k_{\text{cat}} 5 \cdot 10^4$

s^{-1} (under the same conditions, Fe(salophen) exhibited $1 \cdot 10^3 \text{ s}^{-1}$). These key performance indicators are summarized in the Catalytic Tafel plot (Figure 75).

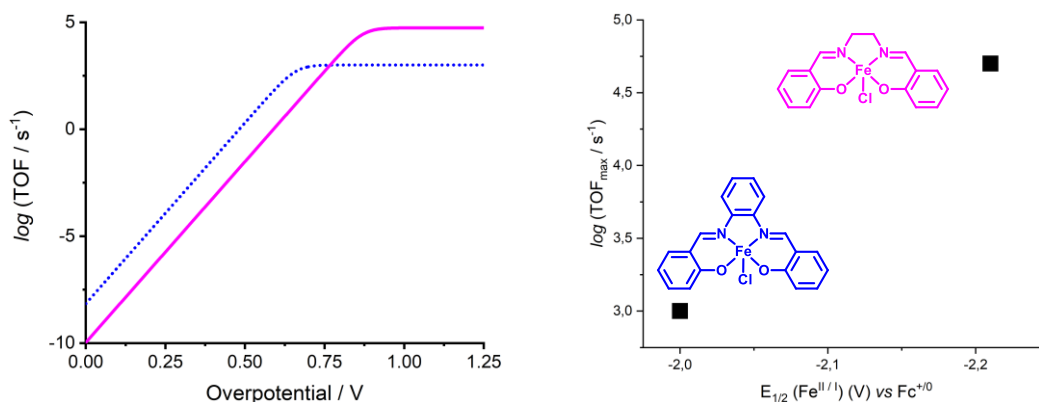


Figure 75. Left: catalytic Tafel plots for Fe(Salophen) (blue, dotted trace) and Fe(Salen) (magenta, solid trace) for the reduction of CO_2 to CO in acetonitrile, in the presence of 0.5 M phenol. Right: structure-activity relationship between Fe(Salophen)Cl and Fe(Salen)Cl.

3.6 Catalyst decomposition

A final point of discussion deals with the initial CO vs H_2 selectivity observed in CPE experiments, and its relationship with catalyst stability. The selectivity for CO of Fe(Salen) was supported by the persistence of the spectroscopic features of the Fe^{I} intermediate along SEC-UV/Vis experiments in the presence of both proton donors employed (Figure 76). Regarding catalyst stability, a subsequent electrolysis on a Fe(Salen) solution previously employed (25 electrons passed per iron center, with 0.5 M PhOH as the proton donor) displayed a lower current (<10% with respect to the first electrolysis) and negligible activity toward CO_2 reduction. The spectroscopic features of acetonitrile solutions after electrolysis pertain to Fe(Salen), albeit with ~30% absorbance decrease at the end of preparative experiments both using PhOH and TFE.

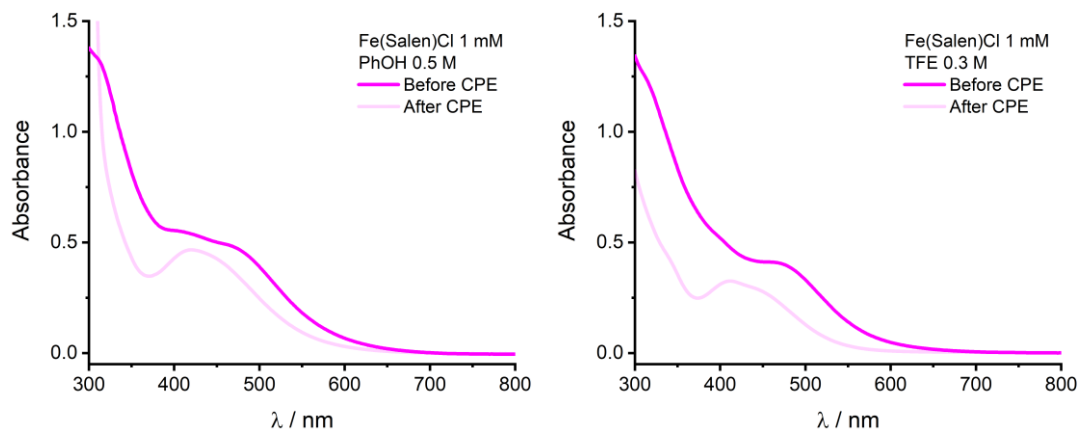


Figure 76. Electronic absorption spectra of Fe(Salen)Cl before (full traces) and after (dotted traces) CPE at -2.3 V vs Fc^+/Fc in the presence of CO_2 and 0.5 M PhOH (left) or 0.3 M TFE (right).

These results are coherent with Faradaic decomposition side-processes of Fe(Salen) to inert species. Regardless, CO_2 reduction occurring through a molecular pathway is supported by the lack of any activity of the working electrode at the end of the CPE experiments. Indeed, the working electrode used in “unpolished tests” (*i.e.*, CPE experiments in which the initial surface state of the working electrode was not restored, run in electrolyte solutions without the catalyst) pass only a limited amount of charge, displaying negligible activity towards proton reduction and no activity towards CO_2 reduction. Eventual deposition of electroactive iron particles on the carbon electrode would instead produce an electrode prone to enhanced H_2 evolution in the presence of proton donors. It is also worth mentioning that in this latter case CO_2 reduction to CH_4 could reasonably be observed, with FE values in the $1 \div 3\%$ range as previously discussed.

This indicates a limited degree of reactivity of $Fe^I(Salen)$ with PhOH and TFE, thus favouring its reactivity with CO_2 and supporting the observed CO_2 -to- CO reaction pathway. A further evidence is provided by the CV traces of Fe(Salen)Cl in the presence of PhOH and TFE under N_2 atmosphere, where no current discharge attributable to H_2 production at the level of the Fe^{II}/Fe^I

couple could be observed, Figure 77). Indeed, introduction of PhOH and TFE results in an irreversible feature peaking at E_p -2.15 V vs Fc^+/Fc and -2.23 V vs Fc^+/Fc , respectively, that is coherent with similar observations discussed for Fe(Salophen).

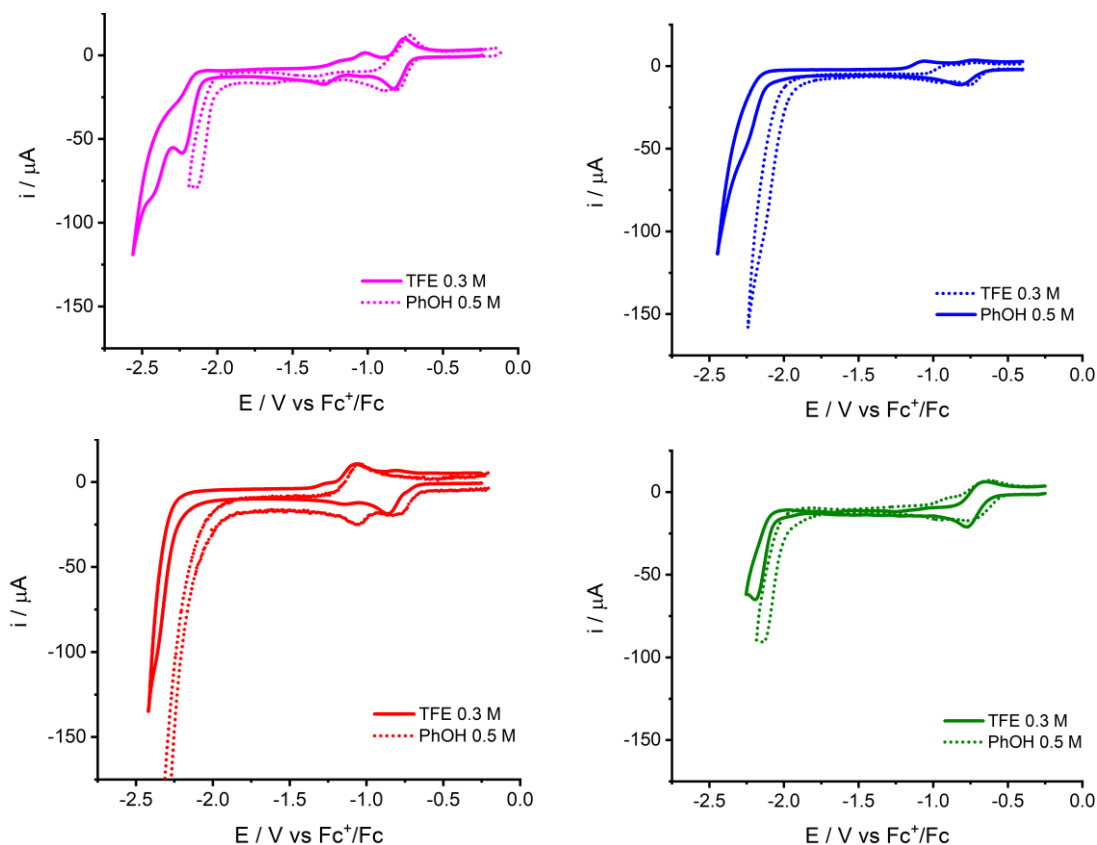


Figure 77. CV traces of the 1 mM Fe(L)Cl in ACN under a N_2 atmosphere in the presence of 0.3 M TFE (full traces) or 0.5 M PhOH (dotted traces). Top left (magenta traces): Fe(Salen)Cl; top right (blue traces): Fe(Beacen)Cl; bottom left (red traces): Fe(Acacen)Cl; bottom right (green traces): Fe(Acacsalen)Cl.

Specifically, we attribute these waves to reaction of the proton donors with the reduced form of the complex at the level of the C=N bonds (a structural motif shared with Fe(Acacsalen) as well), with a selectivity that is switched towards a productive, metal-based reactivity when CO_2 is introduced.

On the contrary, Fe(Beacen) and Fe(Acacen) display sharp, ill-defined multi-electron cathodic features at the level of the Fe^{II}/Fe^I couple that are reflective of the inherent proneness to chemically impacting transformations of the β -diketylminato complexes observed in electrolysis. Indeed, for Fe(Acacen)Cl, Fe(Beacen)Cl and Fe(Acacalen)Cl, the nature of the proton donor determines the observed products, and in particular on the initial CO vs H₂ selectivity (Table 6). While the use of TFE favours CO formation (selectivity 96, > 99 and 73% for Fe(Acacen)Cl, Fe(Beacen)Cl and Fe(Acacalen)Cl, respectively), the presence of phenol switches the process towards H₂ production already in the early stage of the experiment (associated to a drop in CO vs H₂ selectivity: 28, 41, <1 % for Fe(Acacen)Cl, Fe(Beacen)Cl and Fe(Acacalen)Cl, respectively).

The influence of the proton donors on the stability of the complexes can be further discussed in terms of the different change in the electronic absorption spectral profile for the iron complexes that can be observed in pre- and post-electrolysis conditions in the presence of TFE or PhOH (Figure 78). The application of the CPE cathodic potential to the CO₂-saturated solutions of Fe(Beacen), Fe(Acacen) or Fe(Acacalen) in the presence of TFE induces an irreversible bleaching of the spectral features of the complexes in the visible region even after the exposure of the electrolyzed mixtures to the air. These latter, incidentally, undergo a drastic colour change, turning yellow with formation of a fine precipitate. Such observations may indicate irreversible chemical disruption of the complexes into inactive species. Identification of the decomposition products was not attempted; nonetheless, the loss of the Fe^{II} \rightarrow Fe^{III} anodic peak in CV under CO₂ atmosphere (Figure 68) is supportive of Fe poisoning as a result of electrocatalytic CO₂ reduction. To investigate such hypothesis, a spectroelectrochemical analysis in the infrared region (SEC-IR) was attempted to detect Fe carbonyl intermediates that are expected to form in electrocatalytic regimes (see Chapter 2 for experimental details of the SEC-IR experiment). However, the analysis failed to reveal absorption features ascribable to stretching motions of iron-carbonyl intermediates, as was instead

observed in the case of Fe(Salophen). This could be due to an enhanced reactivity of such intermediates towards decomposition, although the interference of platinum working electrode at the negative potential used in our setup should be also considered.

Phenol, on the other hand, has a different effect on the electronic absorption spectra of the post-electrolysis solutions: for all three complexes, new spectral features in the visible region arise, still ascribed to an irreversible transformation of the starting compounds. The spectra, however, display charge transfer absorptions consistent with Fe^{III} molecular compounds, while in no case an abatement in absorbance could be observed that would otherwise indicate decomposition of the complexes as the outcome of the electrolysis experiments.

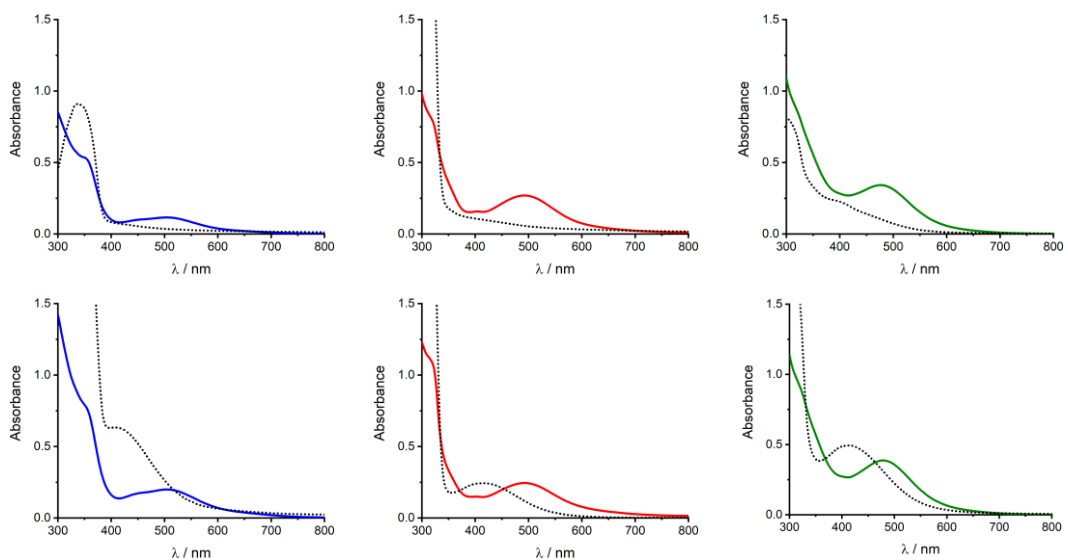


Figure 78. Electronic absorption spectra of 1 mM Fe(L)Cl before (full, coloured traces) and after (black, dotted traces) CPE under a CO₂ atmosphere in the presence of 0.3 M TFE (top) or 0.5 M PhOH (bottom). Left: Fe(Beacen)Cl; mid: Fe(Acacen)Cl; right: Fe(Acacsalen)Cl.

These results suggest a direct reactivity of electrogenerated Fe^{I} species in this series with phenol, as confirmed by CV (raise of the cathodic current at the level of the $\text{Fe}^{\text{II}}/\text{Fe}^{\text{I}}$ couple in the presence of PhOH under N_2 atmosphere, Figure 76) and by SEC-UV/Vis experiments. We approached the electrogeneration of the Fe^{I} intermediate under N_2 atmosphere in the presence of PhOH for $\text{Fe}(\text{Beacen})\text{Cl}$ as a representative case (Figure 79). The diagnostic feature of Fe^{I} species is significantly abated, while new absorptions raise in the 400 ÷ 800 nm region. Conversely, in the presence of TFE a similar spectroscopic outcome with respect to the one previously discussed in the absence of proton donors is observed (raising of the MLCT band at 340 nm, see Figure 70 and related discussion).

The reactivity of $\text{Fe}^{\text{I}}(\text{Beacen})$ (and related analogues) with phenol can potentially involve both the iron centre and the ligand. The H_2 evolution observed for the β -diketyl-derived complexes in the presence of phenol (Table 6) could be possibly associated to formation of iron hydride intermediates, and to their further reaction with a second phenol equivalent (metal hydrides with sufficient hydricity could be also responsible for formate production, that however was not detected in this case). Iron hydride generation might also be assisted by previous protonation of the methine site, ultimately producing a hydride-transfer relay in the ligand scaffold (Scheme 12). Indeed, protonation of the imine group or of the methine carbon in β position to the imine and enolate can be considered to occur under cathodic conditions, and both processes could account for the Faradaic decomposition of the catalysts.^{191,192} The presence of the methine group is likely responsible for the low selectivity for CO under electrolysis conditions for $\text{Fe}(\text{Beacen})$, $\text{Fe}(\text{Acacen})$ and $\text{Fe}(\text{Acacsalen})$, when PhOH is employed. On the other hand, in conditions in which selective CO_2 reduction could be attained (TFE 0.3 M), catalyst poisoning is the more plausible cause of deactivation (current drops after 3 electrons passed per iron centre)

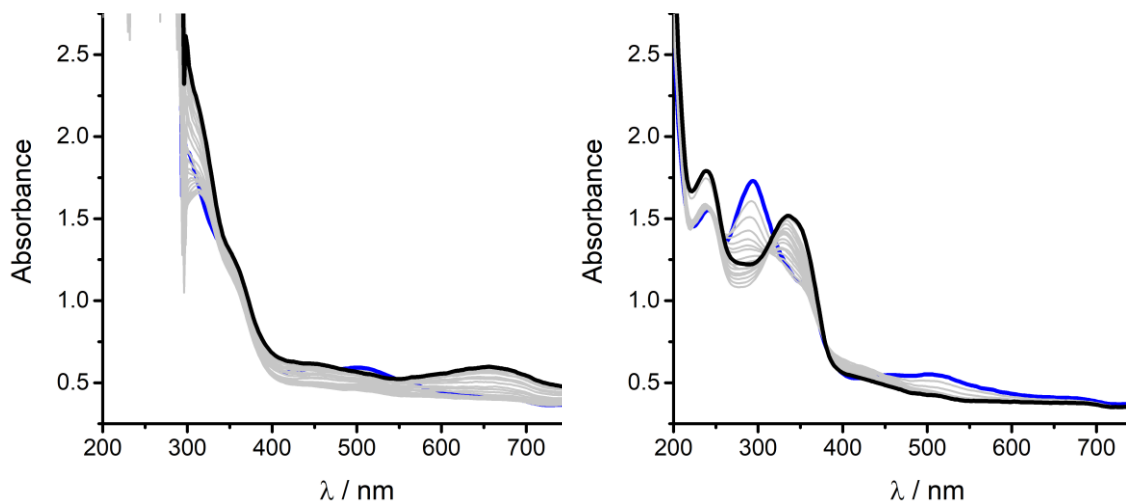
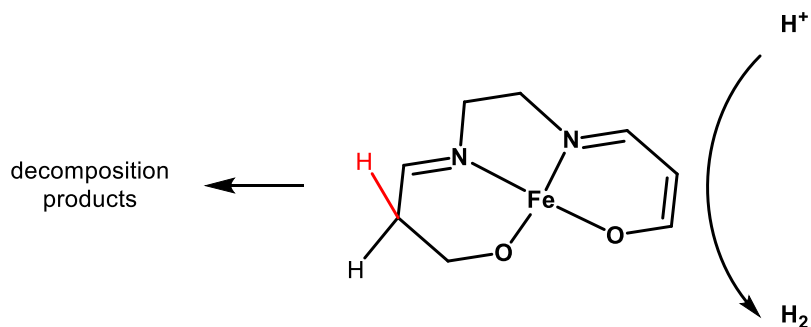


Figure 79. UV/Vis SEC of Fe(Beacen)Cl in ACN under a N₂ atmosphere at the potential corresponding to generation of Fe^I, in the presence of 0.5 M PhOH (left) or 0.3 M TFE (right).



Scheme 12. Proposed intermediate derived from β-ketoiminato Fe complexes, involved in catalyst decomposition and hydrogen evolution catalysis.

3.7 Conclusions

We have reported an electrochemical investigation of four $\text{Fe}^{\text{III}}(\text{N}_2\text{O}_2)\text{Cl}$ complexes (N_2O_2 is a tetradentate Schiff base ligand), and their potential application in the reduction of carbon dioxide. The main results can be summarized as follows:

i) The $\text{Fe}^{\text{III}}(\text{N}_2\text{O}_2)\text{Cl}$ complexes display two metal-based reductions, involving $\text{Fe}^{\text{III}}/\text{Fe}^{\text{II}}$ and $\text{Fe}^{\text{II}}/\text{Fe}^{\text{I}}$ couples; the potential associated with the $\text{Fe}^{\text{II}}/\text{Fe}^{\text{I}}$ couple, relevant to reactivity with CO_2 , correlates with the electronic character of the N_2O_2 ligand (in terms of the energy of the highest occupied σ -donating orbital) and with the energy of the metal-to-ligand charge transfer absorption of the Fe^{I} intermediate, determined by SEC-UV/Vis.

ii) The Fe^{I} intermediates react with CO_2 , as proven by CV, UV/Vis analysis of the electrogenerated intermediates upon addition of CO_2 , and SEC-UV/Vis investigation.

iii) For $\text{Fe}(\text{Salen})\text{Cl}$, in the presence of phenol or trifluoroethanol proton donors, the process is associated with the selective reduction of CO_2 to CO (no H_2 and formate were detected along with the electrolysis); in the presence of 0.5 M phenol, key performance indicators are an overpotential of 0.91 V, a catalytic rate constant of $5 \cdot 10^4 \text{ s}^{-1}$, and a turnover number of 4. CO_2 reduction occurs through a homogeneous route, and the transformation of $\text{Fe}(\text{Salen})$ into an electrochemically inert species occurs.

iv) In the case of $\text{Fe}(\text{Acacen})\text{Cl}$, $\text{Fe}(\text{Beacen})\text{Cl}$, and $\text{Fe}(\text{Acacsalen})\text{Cl}$, the production of CO is observed only with TFE proton donor, while phenol leads to the evolution of H_2 from the early stage of electrolysis. In all cases, the electrolysis current drops suddenly after three electrons passed per iron center, indicating a higher instability of these species, likely associated with the protonation under cathodic conditions of the ketylacetoneimine pendant of the ligands. This intrinsic limitation therefore hampers the use of these iron complexes as catalysts for CO_2 -to-CO reduction. Moreover, the active detrimental role of ligand structural features

imposes a distinction in the originally devised category of N_2O_2 Schiff base ligands, between the Salen-type derivatives and those obtained from β -diketones.

The structure-reactivity correlations involving active low-valent Fe intermediates and the indications on the selectivity and stability of the coordination complexes under cathodic conditions and depending on the proton donor nature can be valuable in the design of more efficient and more robust catalysts. Furthermore, the results herein discussed confirm the possible categorization of Salen-type ligands as functional scaffold for constructing a competent family of Fe catalysts for the electrochemical reduction of carbon dioxide. Given the wide synthetic space allowing for fine-tuning of structural and electronic properties of the Schiff base ligands, this section is concluded with confidence in the possible expansion of the scope of these complexes.

3.8 Experimental section

3.8.1 Synthesis of the Schiff base ligands

Acacen and Beacen were synthesized according to the procedure reported by McCarthy *et al.*¹⁹³ Acacsalen was synthesized following the procedure described by Biswas *et al.*¹⁹⁴ and Costes *et al.*¹⁹⁵ Salen was prepared by following the procedure reported by Guieu *et al.*¹⁹⁶

3.8.1.1 N,N'-ethylene-bis(acetylacetonimine) (Acacen)

Ethylenediamine (0.72 mL, 10.7 mmol) was slowly added to acetylacetonone (2.2 mL, 21.4 mmol). A rapid and vigorous reaction afforded a white solid, which was subsequently recrystallized from dichloromethane-hexane after filtration over cellulose to remove yellow oily by-products. The product was obtained as a crystalline white solid in 62% yield (1.47 g) after 3 recrystallization steps.

¹H-NMR (300 MHz, CDCl₃): δ 10.85 (s, 2H), δ 4.96 (s, 2H), δ 3.38 (m, 4H), δ 1.96 (s, 6H), δ 1.87 (s, 6H).

¹³C-NMR (200 MHz, CDCl₃): δ 195.53, 162.82, 96.17, 43.53, 28.88, 18.68.

ESI-MS: 225.0 m/z [MH]⁺.

Elemental analysis: calculated for C₁₂H₂₀N₂O₂ C: 64.26%, H: 8.99%, N: 12.49%.
Found C: 64.55% H: 9.59% N: 12.59%.

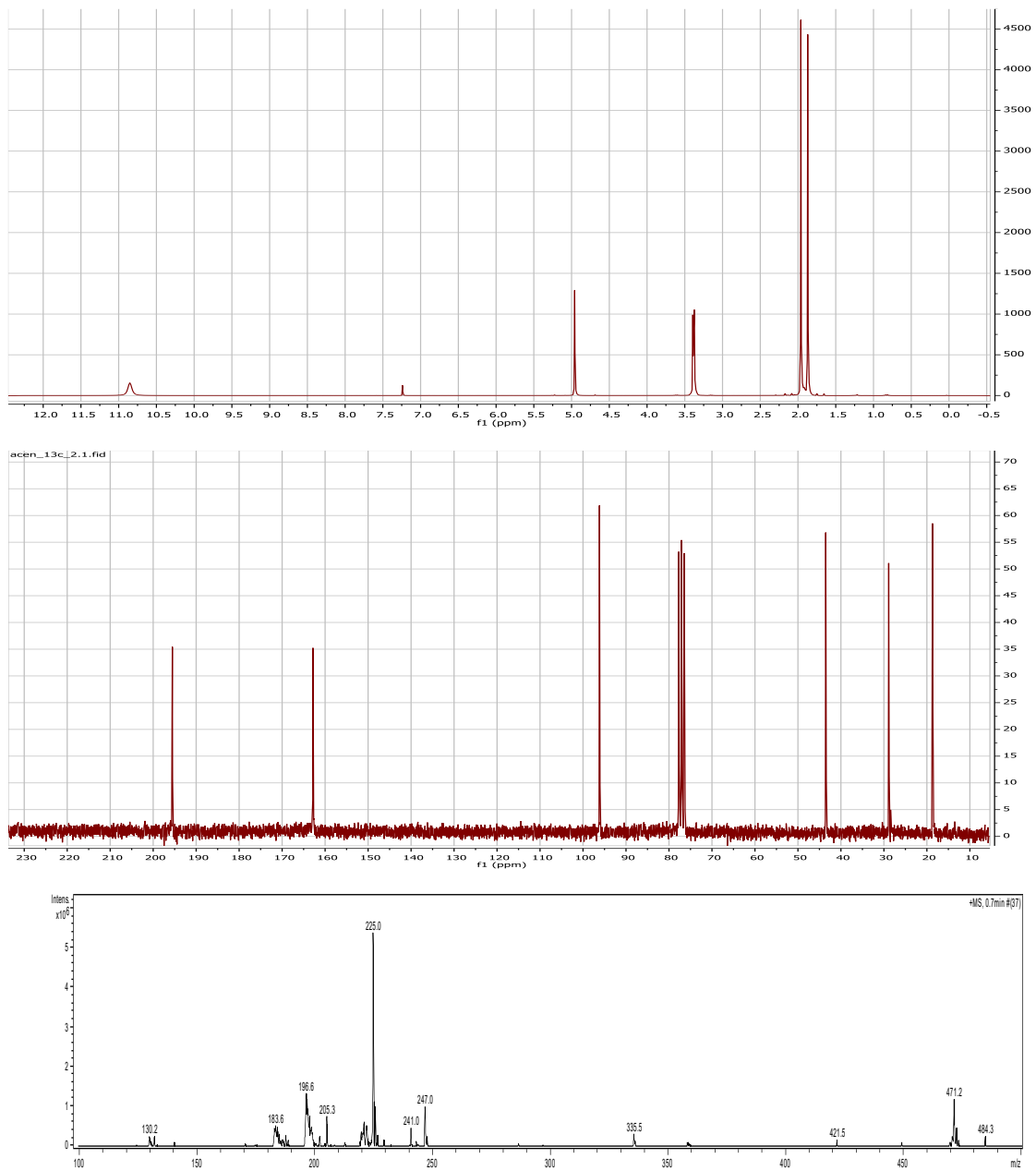


Figure 80. Characterizations of the Acacen ligand. Top: $^1\text{H-NMR}$; mid: $^{13}\text{C-NMR}$; bottom: ESI-MS of Acacen (10^{-5} M in methanol).

3.8.1.2 N,N'-ethylene-bis(benzoylacetoneimine) (Beacen)

Benzoylacetone (2.190 g, 11.0 mmol) was dissolved in 20 mL of ethanol. The pale-yellow solution was heated under stirring, and subsequently treated with a solution of ethylenediamine (0.45 mL, 0.406 g, 6.75 mmol) in 10 mL of ethanol. The yellow reaction mixture was refluxed for 120 minutes. After the specified time, the reaction mixture was allowed to cool to room temperature. Upon cooling, the product precipitated as a white solid, which was isolated by filtration and thoroughly washed with diethyl ether and dried. Yield 45% (1.06 g).

$^1\text{H-NMR}$ (300 MHz, CDCl_3): δ 11.57 (s, 2H), δ 7.85 (m, 4H), δ 7.40 (m, 4H), δ 5.71 (s, 2H), δ 3.58 (m, 4H), δ 2.08 (s, 6H).

$^{13}\text{C-NMR}$ (200 MHz, CDCl_3): δ 188.33, 164.86, 140.16, 130.68, 128.22, 126.95, 93.00, 43.82, 19.28.

ESI-MS: 349.2 m/z $[\text{MH}]^+$.

Elemental analysis: calculated for $\text{C}_{22}\text{H}_{24}\text{N}_2\text{O}_2$ C: 75.83% H: 6.94% N: 8.04%.
Found C: 75.83% H: 7.32% N: 8.02%.

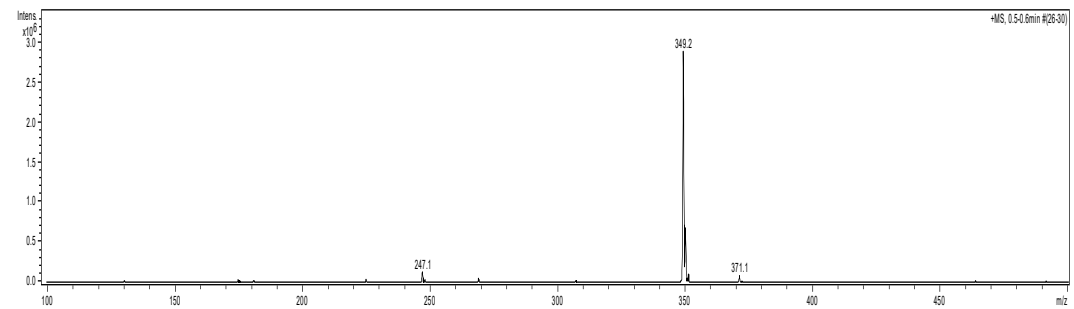
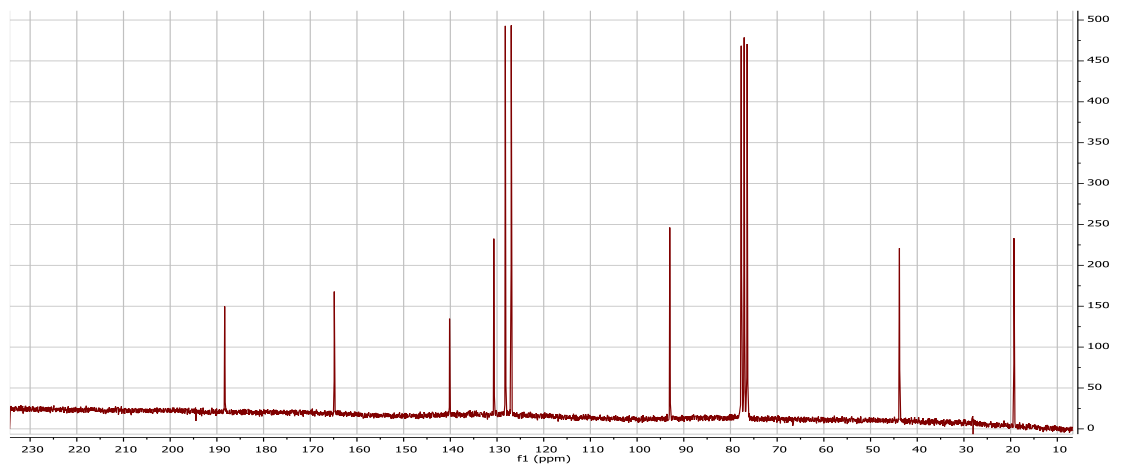
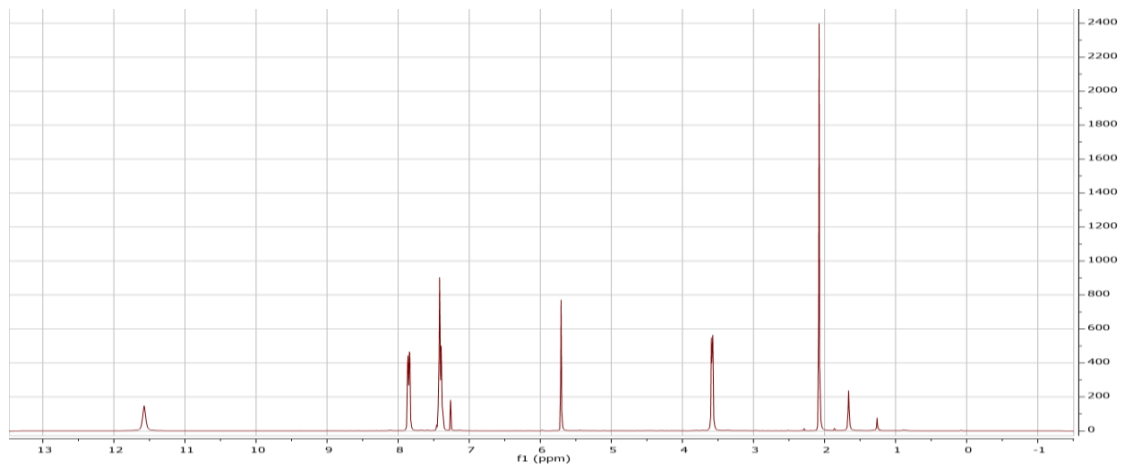


Figure 81. Characterizations of the Beacen ligand. Top: $^1\text{H-NMR}$; mid: $^{13}\text{C-NMR}$; bottom: ESI-MS of Beacen (10^{-5} M in methanol).

3.8.1.3 N,N'-ethylene-(acetylacetonimine)(salicylideneimine) (Acacsalen)

Ethylenediamine (0.72 mL, 10.7 mmol) was dissolved in 50 mL of chloroform in a 250 mL round bottom flask. A solution of acetylacetonone (1.1 mL, 10.7 mmol) in 50 mL of chloroform was slowly added to the vigorously solution of ethylenediamine, by means of a dripping funnel, over the course of 3 hours. The reaction mixture was further stirred at room temperature for a total time of 12 hours. After the specified time, the pale-yellow solution was concentrated by rotary evaporation to 40 mL. To the so obtained mixture, a solution of salicylaldehyde (1.10 mL, 10.32 mmol) in 30 mL of chloroform was added. The deep yellow mixture was refluxed for 40 minutes, then filtered over cellulose and concentrated to 10 mL by rotary evaporation. Finally, the product was obtained by addition of hexane as a golden yellow solid in 50% yield (1.28 g).

$^1\text{H-NMR}$ (300 MHz, CDCl_3): δ 12.96 (s, 1H), δ 10.89 (s, 1H), δ 8.33 (s, 1H), δ 7.26 (m, 2H), δ 6.88 (m, 2H), δ 4.95 (s, 1H), δ 3.74 (t, $J = 5.2$ Hz, 2H), δ 3.57 (t, $J = 5.0$ Hz, 2H), δ 1.96 (s, 3H), δ 1.88 (s, 3H).

$^{13}\text{C-NMR}$ (200 MHz, CDCl_3): δ 195.3, 167.05, 163.01, 160.90, 132.55, 131.68, 118.80, 118.64, 116.98, 95.88, 59.87, 43.49, 28.80, 18.92.

ESI-MS: 247.0 m/z $[\text{MH}]^+$.

Elemental analysis: calculated for $\text{C}_{14}\text{H}_{18}\text{N}_2\text{O}_2$ C: 68.27% H: 7.37% N: 11.37%.
Found C: 65.65%, H: 7.24%, N: 10.74%.

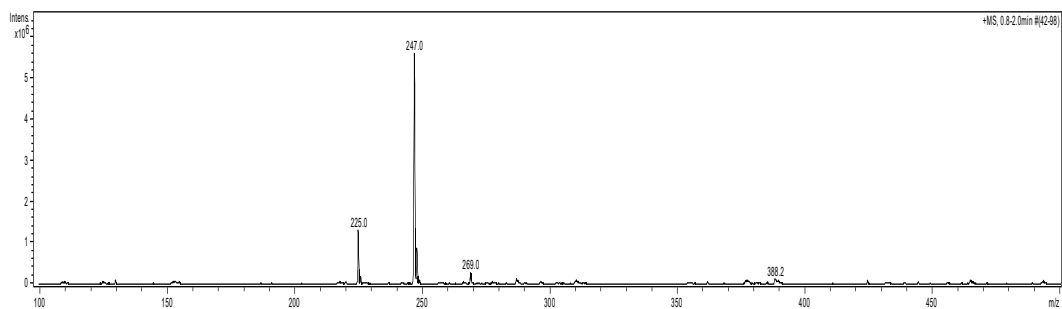
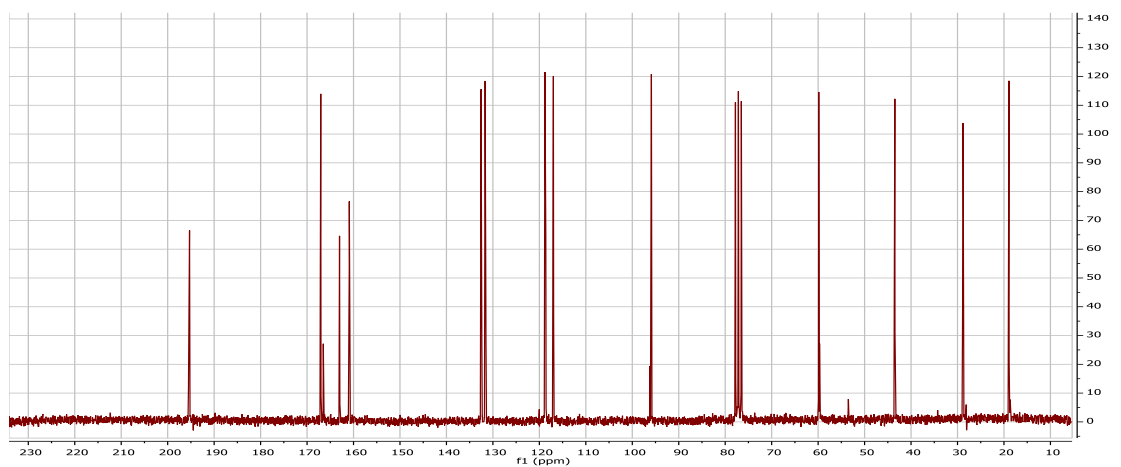
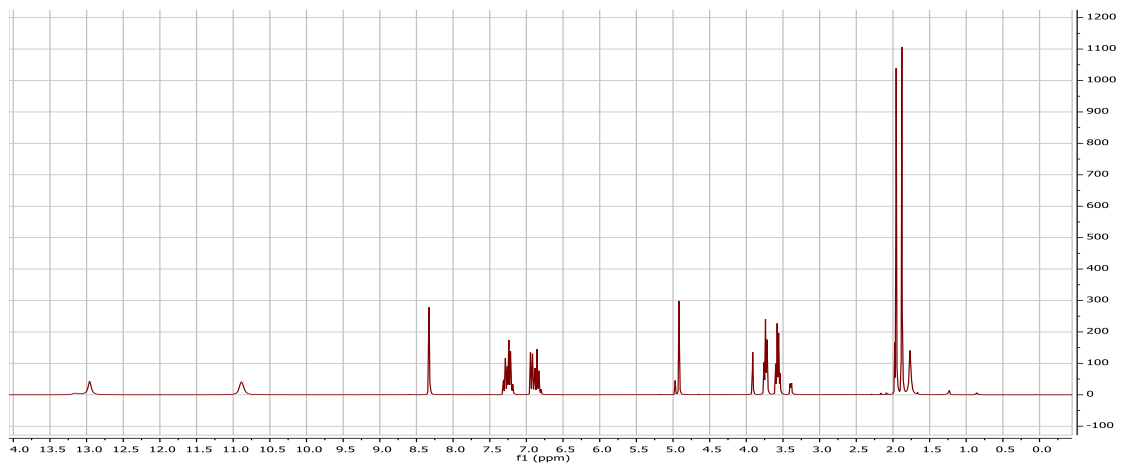


Figure 82. Characterizations of the Acacsalen ligand. Top: $^1\text{H-NMR}$; mid: $^{13}\text{C-NMR}$; bottom: ESI-MS of Acacsalen (10^{-5} M in methanol).

3.8.1.4 N,N'-ethylene-bis(acetylacetonimine) (Salen)

Salicylaldehyde (0.81 mL, 7.6 mmol, 2 eq.) dissolved in 30 mL of ethanol was treated with a solution of ethylenediamine (0.25 mL, 3.8 mmol, 1 eq) in 20 mL of ethanol. The reaction mixture rapidly turned bright yellow and was refluxed under stirring for 2 hours. After the specified time, the yellow mixture was allowed to cool to room temperature, observing the precipitation of yellow crystals. These latter were recovered by filtration and thoroughly washed with cold ethanol and hexane and dried in vacuum. Yield 78% (0.78 g).

$^1\text{H-NMR}$ (300 MHz, CDCl_3): δ 8.35 (s, 2H), δ 7.33-7.16 (m, 5H), δ 6.73-6.69 (m, 3H), δ 3.93 (s, 4H).

$^{13}\text{C-NMR}$ (200 MHz, CDCl_3): δ 166.52, 161.02, 132.41, 131.49, 118.68, 116.97, 59.77.

ESI-MS: 269.1 m/z $[\text{MH}]^+$.

Elemental analysis: calculated for $\text{C}_{20}\text{H}_{16}\text{N}_2\text{O}_2$ C: 71.62, H: 6.01, N: 10.44. Found C: 71.59% H: 6.21% N: 10.42%.

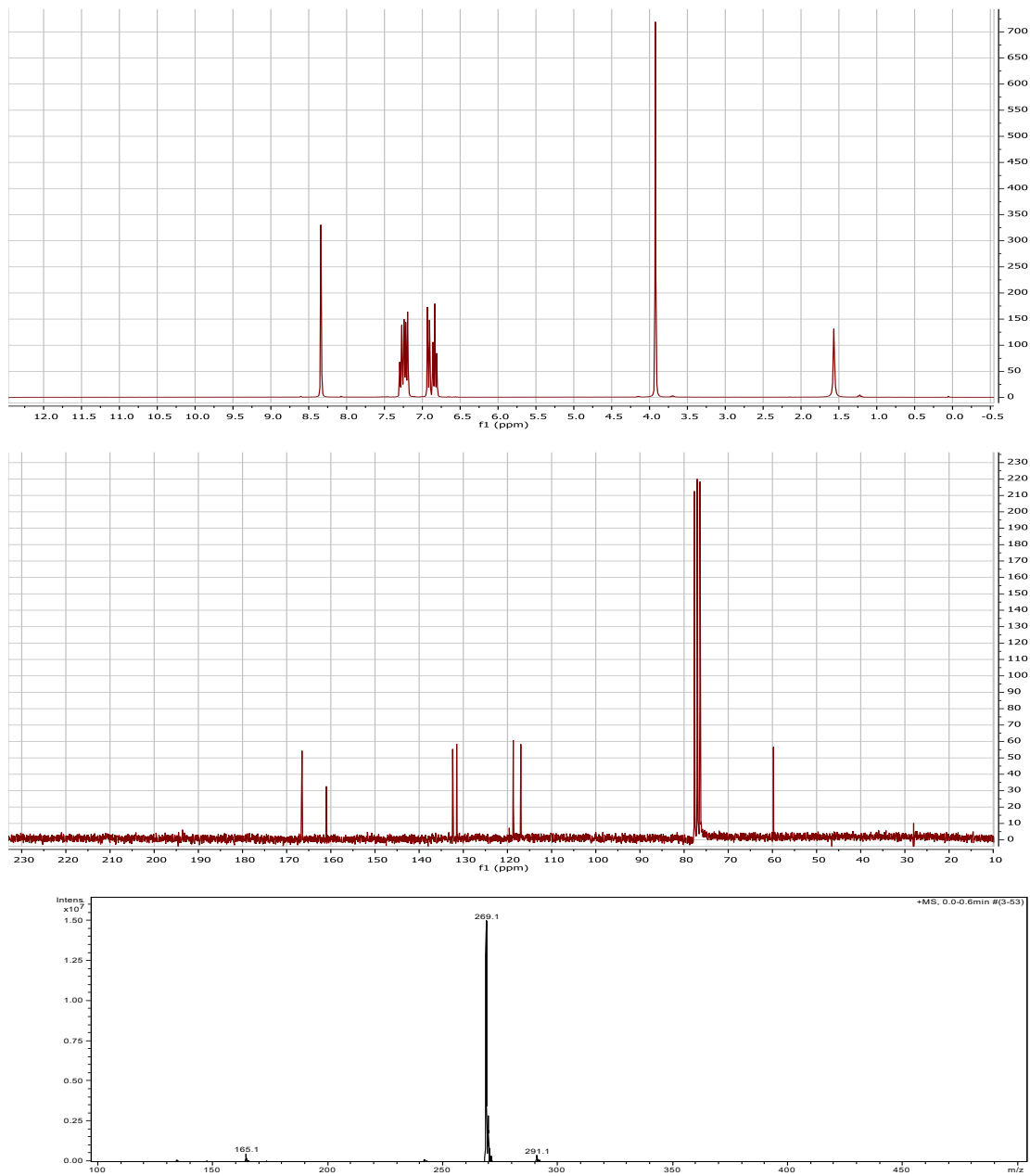


Figure 83. Characterizations of the Salen ligand. Top: $^1\text{H-NMR}$; mid: $^{13}\text{C-NMR}$; bottom: ESI-MS of Salen (10^{-5} M in methanol).

3.8.2 Synthesis of the Iron complexes

Iron(III) complexes of ligands deriving from the condensation between β -diketones and ethylenediamine were synthesized by a modification of the procedure published by Cisterna *et al.*¹⁹⁷, involving quantitative deprotonation of the ligand with potassium *tert*-butoxide (^tBuOK) in methanol to produce its conjugate dianionic base, subsequently metalated with iron(III) chloride hexahydrate. Fe(salen)Cl was synthesized by following the procedure reported for the synthesis of Fe(Salophen)Cl.

3.8.2.1 N,N'-ethylene-bis(acetylacetonimine)chloroiron(III), Fe(Acacen)Cl

203 mg of Acacen ligand (0.91 mmol) were dissolved in 80 mL of methanol and treated at room temperature with 203 mg (1.81 mmol, 2 eq.) of ^tBuOK. After stirring the mixture for 20 minutes, a solution of FeCl₃·6H₂O (260 mg, 0.96 mmol, 1.05 eq.) in 10 mL of methanol was added dropwise to the mixture, which rapidly turned deep red. After refluxing under stirring for 3 hours, the mixture was concentrated to dryness by rotary evaporation and treated with CH₂Cl₂ to dissolve the product. The deep red solution was filtered to remove insoluble salts (KCl and the excess of iron(III) salt). CH₂Cl₂ was removed with a gentle stream of dinitrogen, thus affording Fe(Acacen)Cl as a dark purple microcrystalline solid (260 mg, yield 91%).

ESI-MS: 278.1 m/z [Fe(Acacen)]⁺ (loss of Cl⁻).

Elemental analysis: calculated for C₁₂H₁₈N₂O₂FeCl C: 45.96% H: 5.79% N: 8.93%. Found C: 45.99% H: 6.21% N: 8.72%.

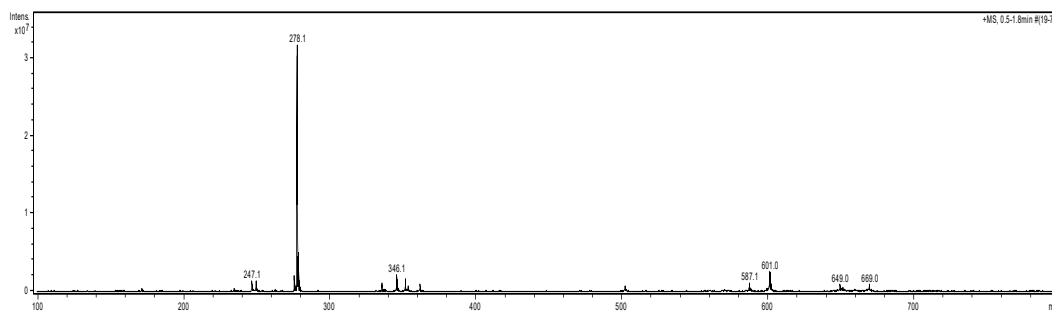


Figure 84. ESI-MS spectrum of Fe(Acacen)Cl 10^{-5} M in methanol.

3.8.2.2 N,N'-ethylene-bis(benzoylacetoneiminato)chloroiron(III), Fe(Beacen)Cl

122 mg (0.35 mmol) of Beacen ligand were suspended in 50 mL of methanol, heated under stirring until complete dissolution of the solid, and treated with 78 mg (0.70 mmol, 2 eq.) of t BuOK. After 15 minutes, the mixture turned yellow. 100 mg of FeCl₃·6H₂O (0.37 mmol, 1.06 eq.) dissolved in 10 mL of methanol were added dropwise, inducing a colour change in the mixture, which turned deep purple. The reaction mixture was refluxed under stirring for 4 hours. After the specified time, the mixture was concentrated to dryness by rotary evaporation and treated with CH₂Cl₂ to dissolve the iron complex, leaving the inorganic salts undissolved. The latter were filtered off, and the product was obtained as a purple powder after removing the solvent with a gentle stream of dinitrogen. 129 mg (yield 84%) of product were obtained.

ESI-MS: 402.1 m/z [Fe(Beacen)]⁺ (loss of Cl⁻).

Elemental analysis: calculated for C₂₂H₂₄N₂O₃FeCl C: 60.37% H: 5.07% N: 6.40%. Found C: 57.42% H: 5.07% N: 5.90%. The experimental analysis provides results coherent with the presence of one molecule of water per molecule of metal complex, Fe(Beacen)Cl·H₂O.

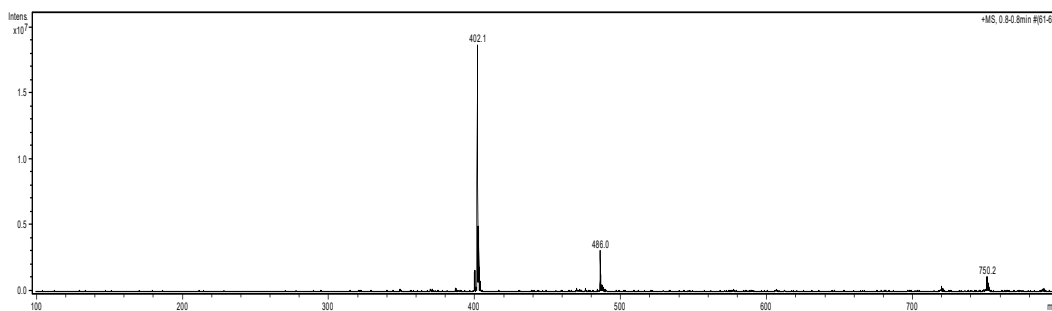


Figure 85. ESI-MS spectrum of Fe(Beacen)Cl 10^{-5} M in methanol.

3.8.2.3 N,N'-ethylene-(acetylacetonimine)(salicylideneimine), Fe(Acacsalen)Cl

99 mg (0.40 mmol) of Acacsalen ligand were dissolved in 30 mL of methanol and treated under stirring with 90 mg (0.80 mmol, 2 eq.) of *t*BuOK. The mixture was stirred for 30 minutes. After the specified time, a solution of 115 mg (0.43 mmol, 1.06 eq.) of FeCl₃·6H₂O in 10 mL of methanol was added dropwise, obtaining a deep purple mixture which was refluxed under stirring for 3 hours. The solvent was removed by rotary evaporation, and the product dissolved in CH₂Cl₂. The insoluble inorganic salts were filtered off. The product was obtained as a wine-coloured microcrystalline solid after removing the solvent with a gentle stream of dinitrogen. 134 mg of product were obtained (yield 98%).

ESI-MS: 300.1 m/z [Fe(Acacsalen)]⁺ (loss of Cl⁻).

Elemental analysis: Calculated for C₁₄H₁₆N₂O₂FeCl C: 50.11% H: 4.81% N: 8.35%. Found C: 48.23% H: 4.80% N: 7.72%.

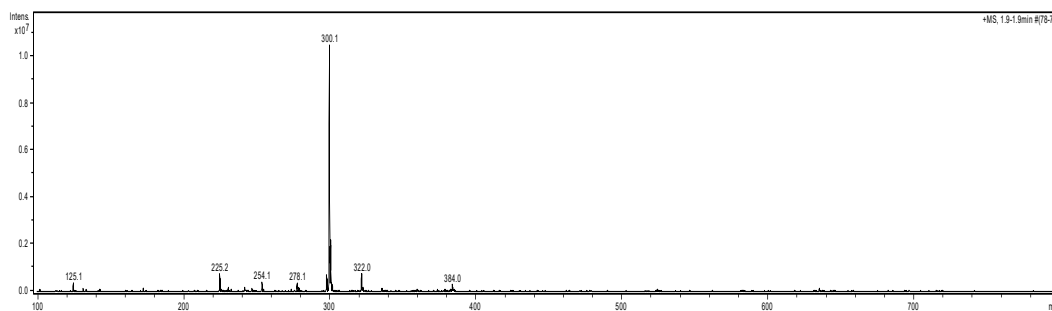


Figure 86. ESI-MS spectrum of Fe(Acacen)Cl 10^{-5} M in methanol.

3.8.2.4 N,N'-ethylene-bis(acetylacetonimine)chloroiron(III), Fe(Salen)Cl

75 mg (0.28 mmol) of Salen were dissolved in 30 mL of CH_2Cl_2 . To the yellow solution, 86 mg (0.32 mmol, 1.1 eq.) of $\text{FeCl}_3 \cdot 6\text{H}_2\text{O}$ were added, resulting in a red suspension. After 1 h of stirring at room temperature, 42 μL (0.30 mmol, 2 eq) of triethylamine, dissolved in 15 mL of CH_2Cl_2 , were added dropwise to the reaction mixture. The mixture is further stirred at room temperature for 4 h, resulting in a dark red solution. The solvent was removed by rotary evaporation and the product redissolved in CH_2Cl_2 . Solid residues were removed by filtration, and CH_2Cl_2 was removed with a gentle stream of N_2 . The dark purple solid thus obtained was finally washed with cold (-20°C) absolute ethanol to remove triethylammonium chloride and dried under vacuum. Yield 42% (42 mg).

ESI-MS: 322.0 m/z. $[\text{Fe}(\text{Salen})]^+$ (loss of Cl^-).

Elemental analysis: Calculated for $\text{C}_{20}\text{H}_{14}\text{N}_2\text{O}_2\text{FeCl}$ C: 53.74% H: 3.95% N: 7.83%. Found C: 52.80% H: 4.01% N: 7.60%.

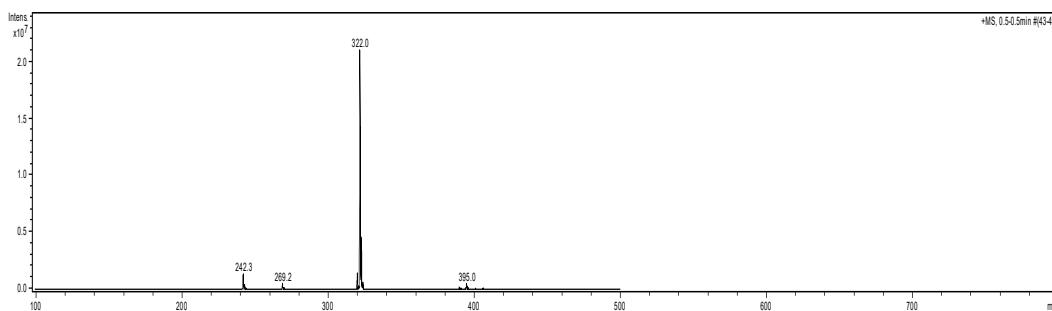


Figure 87. ESI-MS spectrum of Fe(Salen)Cl 10^{-5} M in methanol.

3.8.3 Electrochemical methods

3.8.3.1 Cyclic voltammetry

Cyclic voltammetry experiments were conducted with a three-electrode system controlled by a BASi EC Epsilon potentiostat-galvanostat. The working electrode was a glassy carbon disk electrode (BioLogic, nominal diameter 3 mm), the auxiliary electrode a platinum electrode (BASi), the reference electrode an Ag/AgCl/NaCl (3 M) electrode (BASi); potentials were then referenced to the ferricenium/ferrocene (Fc^+/Fc) couple upon addition, at the end of each experiment session, of ferrocene to the analyte solutions as internal standard, the $E_{1/2}$ of which was measured by running a cyclic voltammogram. Between each voltammetric experiment, the working electrode was polished with a 1 μm diamond paste (Struers) on a DP Nap microfiber cloth (Struers), rinsed with methanol, sonicated in ethanol, rinsed again and gently dried with N_2 gas. At the end of each experiment session, the same treatment was applied to both working and auxiliary electrodes, while the reference electrode was gently rinsed with deionized water, methanol, and dried with N_2 gas. Analyte solutions were prepared with HPLC-grade solvents (Carlo Erba) and electrochemical-grade supporting electrolytes (Sigma, purity >99.0%), used without further purification. The solutions were purged with dinitrogen or carbon dioxide gas, the headspace of the cell being also degassed to prevent dioxygen contamination.

3.8.3.2 Constant potential electrolysis

Constant potential electrolysis experiments were performed with a Metrohm Autolab PGSTAT204 potentiostat-galvanostat controlled by Nova 2.1.4 software. The cell generally employed for preparative electrolyses was a custom-made 6-necked 2-compartment glass cell, the two compartments being separated by a porous glass frit. The cell and the experimental procedure were previously described (see Experimental Section of Chapter 2. Figure 88 represents the cell assembled during gas saturation of the solutions before electrolysis). The working electrode was a glassy carbon rod (SIGRADUR, HTW), the auxiliary electrode a platinum wire, and the reference electrode an Ag/AgCl/NaCl (3 M) electrode. The reference electrode was separated from the bulk analyte solution by means of a custom-made gas-tight salt bridge filled with electrolyte solution. The tip of the salt bridge was equipped with a CoralPor® frit, while the body of the reference electrode was fit inside the upper part of the bridge. This latter was constituted by a screw joint allowing the content of the bridge to be sealed by means of a PTFE O-ring. Care was taken to remove any obstruction offered by gas bubbles to the electrolytic contact between the solutions across the junction.



Figure 88. Gas-tight electrolysis cell used throughout the study. The working compartment, containing the coloured solution, and the auxiliary compartment, are shown being degassed. Electrodes and connections are assembled as described in the text. The salt bridge housing the RE is visible.

3.8.3.3 UV/Visible absorption spectroelectrochemistry

UV/Visible absorption spectroelectrochemistry experiments SEC-UV/Vis experiments were performed by employing Varian Cary 50 Bio spectrophotometer, equipped with a 0.5 mm nominal optical path quartz spectroelectrochemistry cell (BASi EF-1362). The electrodes used were a platinum gauze working electrode, a platinum wire auxiliary electrode, and an Ag/AgCl/NaCl (3 M) reference electrode, using the setup previously described. Solutions were prepared using 0.1 M tetraethylammonium tetrafluoroborate as the supporting electrolyte and acetonitrile as the solvent. All solutions were degassed by sparging dinitrogen or carbon dioxide for 10 minutes in sealed vials and kept under an atmosphere of the same gas. Manipulation of solutions was performed

via cannulation. Control experiments on aerated solutions were run to confirm the quality of the reported experimental data in regard to the removal of dioxygen.

3.8.3.4 Electrolysis gaseous product quantification

Gaseous product analysis was performed by gaschromatography, using an Agilent Technologies 7890A GC equipped with a thermoconductimetric detector and a 5975C VL MSD mass spectrometer. Gas samples of known volume were withdrawn from the headspace of the electrolysis cell by means of a gastight Hamilton syringe. Quantification of the gaseous species was achieved by external calibration of the instrument, upon construction of a calibration curve by injection of known volumes of pure gas (Figure 89).

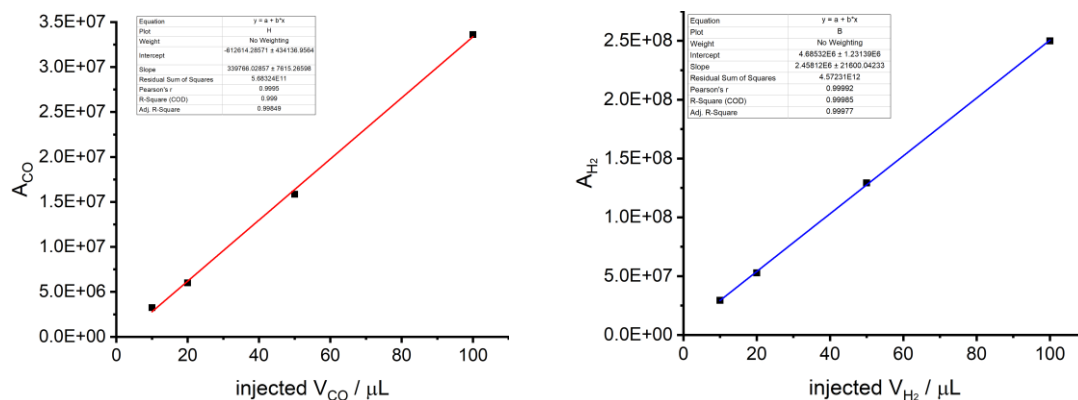


Figure 89. External calibration curves for CO (left) and H₂ (right).

The external calibration provided the response factor k_{gas} relating the measured peak area associated with the analyte gas (A_{gas}) to the injected volume of gas (V_{gas}) (Eq. 37):

$$A_{gas} = k_{gas} \times V_{gas} \quad (\text{Eq. 37})$$

When a gas sample of known volume (V_{inj}) was withdrawn from the electrolysis cell and analyzed *via* GC, the peak area associated to the analyte gas could be therefore used to determine its volume V_x (Eq. 38). The volume concentration of the analyte gas in the headspace of the cell (ζ_x) could be determined from the ratio between V_{gas} and V_{inj} (Eq. 39).

$$V_x = A_x/k_{gas} \quad (\text{Eq. 38})$$

$$\zeta_x = V_x/V_{inj} \quad (\text{Eq. 39})$$

By multiplying ζ_x by the independently determined volume of the headspace (V_{HS}), the total volume of gas could be calculated ($V_{x,tot}$) (Eq. 40), and converted into moles of analyte gas by using the ideal gas law (Eq. 41).

$$V_{x,tot} = \zeta_x \times V_{HS} \quad (\text{Eq. 40})$$

$$n_x = \frac{PV_{x,tot}}{RT} \quad (\text{Eq. 41})$$

Where P is the pressure (assumed as 1 atm), the temperature 298 K, and R the ideal gas constant, $0.08206 \text{ LatmK}^{-1}\text{mol}^{-1}$.

SECTION 2.

Hybrid photoactive catalytic materials for photoelectrochemical water oxidation to O₂

The following Section is dedicated to Mark Joseph Ferrari

4 Dye-catalyst dyads as constituents of Photoelectrochemical Cells

4.1 Introduction

Artificial photosynthesis relies on the fixation of naturally abundant solar energy into the form of chemical bonds. Such task has been traditionally interpreted following a biomimetic, compartmental approach. This draws inspiration from the natural photosynthetic systems, in which light absorption and subsequent photoinduced charge separation provide the driving force for the redox transformations leading to NADPH and ATP synthesis. These reductive dark reactions are fed by the water oxidation process, necessary to provide the reducing equivalents.^{198–201} In artificial photosynthetic schemes, the dual nature of the photoinduced redox transformations is most clearly interpreted in photoelectrochemical cells (PEC's); these devices are traditionally composed of two photoelectrodes, where light absorption and conversion into separated electrons and holes take place. Holes (describable as oxidizing equivalents) are employed at the anodic compartment to drive an oxidation reaction, usually the oxidation of water (or oxygen evolution reaction, OER). On the other hand, electrons are driven to the cathode, which is designed to be catalytically active towards processes such as small molecules reduction (Figure 90). Most notable are the fuel-forming hydrogen evolution (HER) and carbon dioxide reduction reactions.^{202–206}

The photoanodic compartment is usually regarded as a key component of a PEC. The core structure of photoanodes is composed of a semiconductor, often a nanostructured n-type semiconducting metal oxide (SCO) film, interfaced with a transparent conducting oxide (TCO) such as fluorine-doped tin oxide (FTO) or indium tin oxide ($\text{In}_2\text{O}_3 \cdot \text{SnO}_2$, ITO). Most notably, dye-sensitized photoanodes have been extensively studied and applied in dye-sensitized solar cells (DSSC's) and water splitting dye-sensitized photoelectrochemical cells (WS-PEC's). In

these latter, the semiconductor is interfaced with a dye that extends the light absorption, and with a catalyst that accelerates the target chemical reaction.

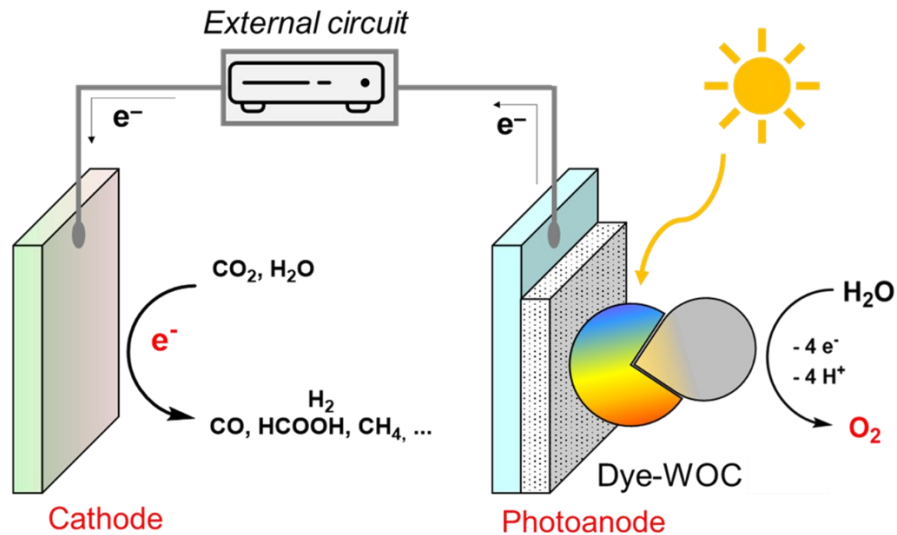


Figure 90. Fuel-synthesizing photoelectrochemical cell constituted by a photoanode, based on a dye and a Water Oxidation Catalyst, and a dark cathode.

The photoanode of WS-PEC's operates through a light-activated catalytic cycle, in which the dye is involved in three key steps:

- i) light absorption;
- ii) electron transfer to the SCO, resulting in injection; electrons in turn diffuse through the SCO film until they reach the back contact and are collected by the cathode through an external circuit.
- iii) electron transfer from the WOC, resulting in oxidation of the latter; this process can be constituted by a series of lateral ET events between neighboring dye and WOC sites.

These notions constitute the basics of dye-sensitized photoelectrochemical cells (DSPEC's).

4.1.2 Semiconductors

The components of dye-sensitized photoelectrodes must be carefully designed to produce an efficient system. Particularly, the thermodynamics and kinetics of injection of photogenerated charges into the conduction band of the semiconductor must allow for efficient competition against charge recombination.^{207–215} Typical examples of SCO substrates with an appropriate band structure for constructing photoanodes are SnO₂, TiO₂, and WO₃. In other reports, nanostructured porous conducting oxides as ITO have been used as substrates. Several strategies have been devised to favor and accelerate charge injection while counteracting recombination, such as growing overlayers of semiconducting (e.g., TiO₂ over SnO₂) or insulating (Al₂O₃ over TiO₂) oxide polyatomic layers over the SCO film to produce core-shell structures. Secondly, electronic states between the valence and conduction bands of the SCO can act as trap states, lowering the injection efficiency. The nature and energetic properties of these states are highly dependent on SCO composition, morphology, and synthetic route. Also, SCO film structure and thickness determine the time required for electrons diffusing towards the TCO contact. Lastly, the attainable dye (and WOC, *vide infra*) loading is a crucial parameter that strongly depends on SCO morphology. Micrometer thick, mesoporous SCO films allow for the highest loadings, despite imposing a longer path for injected electrons to travel in order to reach the TCO. This consideration highlights the need to consider film morphology, in turn related to the synthetic protocols that are followed to obtain the SCO-functionalized electrode.^{207–215}

More recently, organic visible light absorbing-semiconductors have been applied to WS-PEC's, with the most notable example being carbon nitride. Choosing organic semiconducting materials allows for direct bandgap excitation with visible light, while an additional notable feature is the applicability of molecular design principles to the organic material, the optoelectronic and redox features of which may be finely tuned to attain the desired properties. Notably, polymeric films containing chromophore monomers have been reported. In more recent years,

the emerging topic of photoactive Covalent Organic Frameworks entered the field of photoelectrochemistry, as nanoporous organic semiconductors. Nonetheless, despite the innovative nature of these materials, performance and device scalability still favor SCO-based PEC's.^{216–218}

4.1.3 Dyes

Given the low absorption in the visible region displayed by traditionally employed semiconducting oxides, such as TiO₂ and SnO₂, dyes need to be introduced. Dyes are usually molecular chromophores, able to harvest visible photons and inject photoexcited electrons into the conduction band (CB) of the semiconductor.

To be applied as photosensitizers for a specific photoanodic system, dyes must satisfy several requirements:^{219–221}

- i) Extended absorption in the visible region (especially challenging for $\lambda > 500$ nm);
- ii) Robustness and durability in the operational environment;
- iii) High oxidizing power of the oxidized state, to match with the required potential of the catalyst for OER or for other target oxidation processes;
- iv) High reducing power of the excited or reduced states, to provide the driving force for injecting electrons in the conduction band of the SCO (oxidative quenching of the dye).

As an alternative to this mechanism, the dye in its excited state can promote oxidation of the catalyst (reductive quenching of the dye), followed by electron injection in the semiconductor from the reduced form of the dye.

It should be remarked that, unlike in photocatalytic systems (discussed in Chapter 1), a long excited state lifetime is not a paramount requirement for dyes to be employed on photoelectrodes. Indeed, the residence of dyes at the interphase with a semiconducting electrode allows for fast charge transfer, thus bypassing the need for the excited state to survive for long times.

The thermodynamic requirements at points iii and iv are formalized as detailed in Chapter 1 and must be expressed through appropriate redox potentials of the dye. Specifically, a dye can inject an electron in the conduction band of a semiconductor if either its excited (in oxidative quenching) or reduced (in reductive quenching) states lie at higher energies (*i.e.*, more negative potentials) than the conduction band edge of the semiconductor. Seminal works by T. E. Mallouk and co-workers employed ruthenium *tris*(bipyridyl) complexes as dyes for TiO₂-based photoanodes. More recently, attention was directed to organic chromophores as sustainable and efficient substitutes for rare metal-based dyes. Relevant classes of dyes are porphyrins (as free-base and in the form of metal complexes), subporphyrins, boron-dipyrromethenes (BODIPY), triaryl amines, diketopyrrolopyrroles, and perylene bisimides (PBI). These are represented in Figure 91.

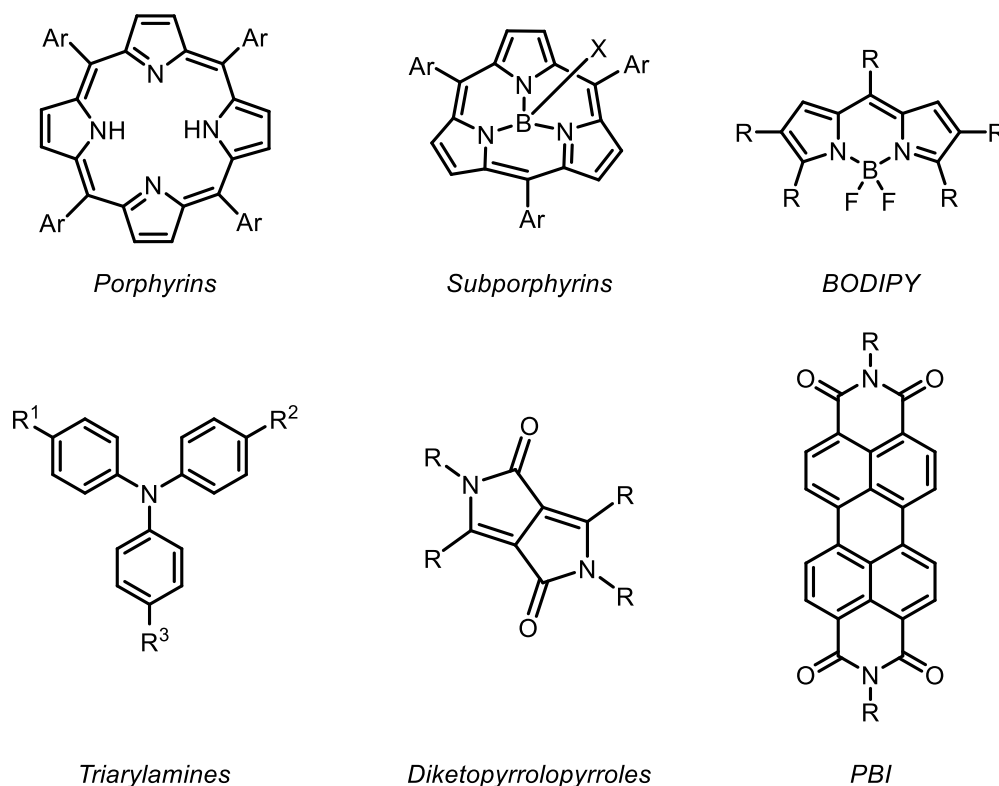


Figure 91. Structures of visible-absorbing dyes commonly used in photoelectrochemical cells.

Molecules of each category have been applied in photoanodes for the OER. A paramount aspect of photoanode preparation is the introduction of dyes on the surface of a SCO. The stability of the dye at the surface and its electronic communication with the underlying semiconductor is heavily dependent on the chemical interactions between the two and should therefore be addressed when designing molecular dyes. The most effective strategy to include molecular dyes on the surface of photoelectrodes relies on the presence of anchoring moieties in their structure.^{222–224} Anchors are functional groups that can bind to metal oxides. The most used linkers are based on carboxylic, phosphonic, and hydroxamic acids, or silatranes. More exotic interactions involve catechol-type molecules binding to oxides in a bidentate chelating fashion *via* phenoxide groups (e.g., alizarin).^{225–227} The nature of the anchoring group determines the stability of the SCO-dye interface towards hydrolysis. Furthermore, the dye-SCO (or dye-catalyst, *vide infra*) bond is crucially involved in the photoinduced electron transfer processes leading to electron injection into the metal oxide. Indeed, this latter process is more efficient when electron transport is mediated by direct bonds between the ET partners. Other (less efficient) strategies involve deposition of dyes *via* solution methods, relying solely on physical interactions between dye molecules and SCO upon solvent removal. These principles have been clearly elucidated by Brudvig and co-workers in 2017, and further integrated in later years (Table 7).^{222,223} A final remark on the choice of the appropriate anchoring group is related to the synthetic effort for adding such anchors in the chromophore core. The most commonly chosen groups are the carboxylate and the phosphonate, owing to the ease of dye synthetic protocol modification to introduce and subsequently hydrolyze alkyl esters for obtaining the desired dyes.

Semiquantitative description of dyes on photoanodes may be safely carried out under the assumption of applicability of photophysical and chemical properties in diffusional systems (see Chapter 1). This view might need refinement when explicitly considering the effect of aggregation. Briefly, multiple layers of weakly dye molecules may offer dispersive relaxation pathways counteracting electron diffusion towards the back contact.

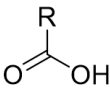
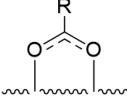
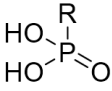
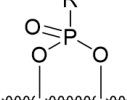
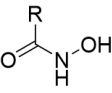
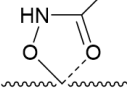
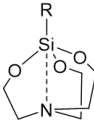
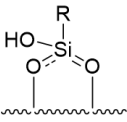
Anchoring group	Binding mode	H ₂ O stability	Electron injection
		pH < 4	Efficient
		pH < 7	Moderate
		2 < pH < 10.25	Efficient
		2 < pH < 11	Moderate

Table 7. Main features of anchoring groups used to chemically link dyes to oxide surfaces. Material adapted with permission from ²²². Copyright 2017 Royal Society of Chemistry.

A second phenomenon that may be enhanced on the surface of photoelectrodes is symmetry breaking charge separation (SBCS). It is a process in which two identical chromophore molecules closely interacting (*i.e.*, in an aggregated state) form a charge separated state upon photon absorption. The formation of a charge separated excited state (by symmetry breaking charge transfer, SBCT) and its subsequent evolution to an ion couple are facilitated in a polar environment. SBCS has been observed predominantly in organic chromophores, among which PBI dyes are the most relevant. When SBCS is active in photocatalytic or photoelectrochemical regimes, the independent redox reactivity of the chromophore radical anion and cation may in principle be exploited towards injection and oxidation processes, respectively. Albeit less reactive than a singlet excited state, the photogenerated ion couple typically displays longer lifetimes.

4.1.4 Water Oxidation Catalysts (WOC)

Dyes can manage the oxidation of facile redox reactants, such as I^- used in DSSC's, or other one-electron sacrificial donors. However, dyes alone are most often unable to drive the 4-electron, 4-proton oxidation of water to O_2 , albeit matching the thermodynamic requirements. The inertness of the targeted reactant therefore introduces the need for a water oxidation catalyst (WOC) as an additional component.

The WOC is fed by the oxidized form of the dye (or by the excited state of the dye, in the case of the reductive quenching mechanism), and the photocatalytic cycle is repeated until the WOC reaches its active state and the water oxidation catalytic process is initiated (dark cycle) (Figure 92).

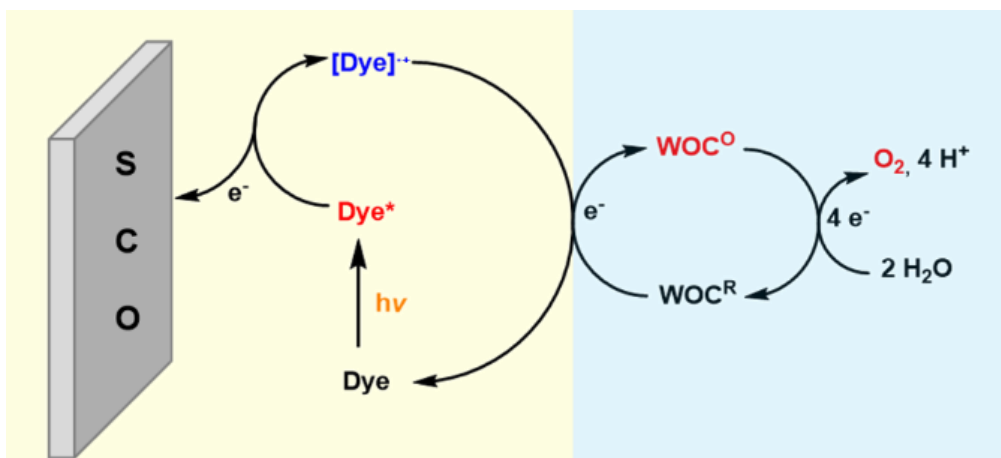


Figure 92. Action mechanism of a water-oxidizing photoanode composed by a SCO, a dye, and a WOC. The dye is represented acting *via* oxidative quenching, commonly encountered for $Ru(bpy)_3$ analogues.

Catalysts employed in the literature are transition metal-based and either molecular or nanoparticulate in nature. Ruthenium and iridium complexes have proven crucial in seminal studies, given the possibility of tuning their redox and catalytic properties through ligand design, along with the mechanistic tools applicable to the *operando* study of molecular catalysts. Indeed, research on

reaction mechanisms of water oxidation catalyzed by transition metal complexes has heavily relied on Ru and Ir-based catalysts (Figure 93). Further developments targeted first-row transition metal complexes in the scope of more sustainable systems, especially based on iron, manganese, cobalt, and copper.^{164,228–236}

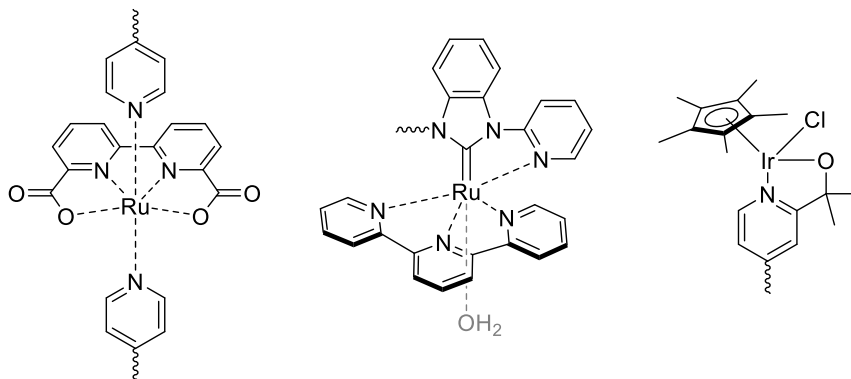


Figure 93. Chemical structures of relevant Ru and Ir molecular WOC's.

Aside from promoting the water oxidation reaction, the presence of a fast WOC is needed to avoid charge accumulation at the dye. Failing to provide turnover at the level of the photocatalytic cycle can in fact result in dye bleaching (or photo-fading), especially for organic chromophores becoming chemically vulnerable in their oxidized forms. Efficient electronic communication between semiconductor film, dye and catalyst is therefore paramount to avoid sluggish steps in the electron transfer chain. Another factor contributing to efficiency losses is back electron transfer from the dye to the WOC and the direct scavenging of injected electrons by the oxidized form of the WOC (charge recombination). These processes and the energy levels of the components involved are pictorially represented in Figure 94.

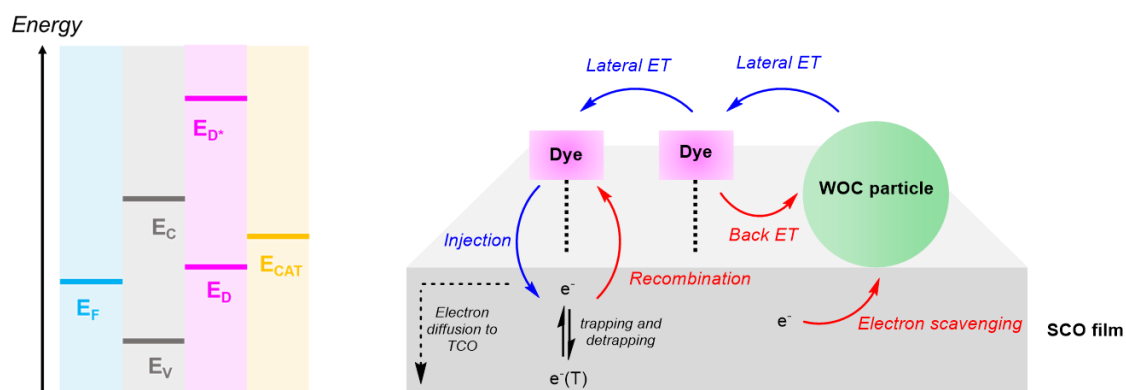


Figure 94. Right: pictorial energy levels of photoanode constituents. Left: schematical view of the directional ET processes involved during operation of photoanodes. Figure redrawn with permission from ²³⁷. Copyright 2014 American Chemical Society.

These preliminary considerations highlight the need for an integrated multi-disciplinary approach combining semiconductor chemistry and physics, organic and inorganic synthesis, molecular photophysics, and electrocatalysis.

4.1.5 Dye-catalyst dyads

As previously discussed, a smart and efficient managing of the electron transfer events is a mandatory requirement for a functional device. From the standpoint of a photoelectrode constituted by a SCO, a dye and a WOC, this calls for optimization of the interactions between the couples SCO-dye and dye-WOC. The dyadic approach, in which the catalyst and the dye are directly bound together by means of chemical interactions, allows to attain controllable dye : catalyst ratio values, an aspect that is particularly relevant when multi-electron transformations are being targeted. Researchers have devoted molecular design and synthetic efforts for producing pre-assembled dye-WOC functional dyads. For the sake of clarity, the dyadic nature of these systems is to be intended as regarding the dual components connected by chemical interactions and serving the functions of dye and catalyst, regardless from the stoichiometry of the resulting assembly.

The issue of electronic communication between connected redox centers has been examined at the molecular level by considering the importance of the spatial interactions between partners in an electron transfer reaction. Indeed, the Marcus theory clarifies the impact of thermodynamics on the kinetics of electron transfer and regulates the ET chain between multiple partners. A paramount role is covered by nature and length of the spacer (“bridge”) between these latter, determining the distance between the redox centers and the ability to open preferential long-range electron transfer pathways.

Over several decades, donor-acceptor biomimetic dyads have fueled extremely detailed studies of the mechanisms of photoinduced energy and electron transfer. The body of work on fixed-distance donor-acceptor dyads has indeed shed light on electron transport in photosynthetic centers and in redox proteins. The Marcus theory has been further confirmed and applied for finer understanding of *in vivo* electron transfer reactions occurring in living systems. Ultimately, the principles of natural photosynthesis have been followed in the design of dye-catalyst molecular dyads relying on this historically preponderant research. A well-defined molecular structure with a known dye : catalyst ratio represents the main strength point of

molecular dyads with regards to their electrochemical and photophysical characterization. However, artificial molecular systems suffer from heavily demanding synthetic efforts that may afford only a limited degree of properties tuning, especially of the dye : catalyst ratio. In the scope of functional devices, it must also be considered how the stability issues often associated with molecular catalysts may not be avoidable, thus impairing the outcome of elegant design work. Examples of molecular dyads employ either ruthenium-based or organic dyes and molecular complexes of ruthenium as catalysts for water oxidation, that were studied on TiO₂-based photoanodes.

Molecular dyadic systems relying on supramolecular interactions or hybrid dyads built upon surface functionalization of nanostructured catalysts therefore represent a more appropriate strategy to produce elements displaying efficient photoinduced electron transfer features applicable to PEC's. Recently,^{238,239} our research group reported a biomimetic supramolecular assembly of cationic perylene bisimides chromophores interacting through electrostatics with a central ruthenium polyoxometalate WOC, [(PBI)₅(Ru₄POM)], where Ru₄POM stands for [Ru₄(μ-O)₄(μ-OH)₂(H₂O)₄(γ-SiW₁₀O₃₆)₂]¹⁰⁻. This complex (Figure 95) represents a testimony to the key role of spatial organization of chromophores around a catalytic center in producing efficient functional models of Photosystem II (PSII). Its performances were studied on photoanodes constituted by WO₃, reaching photocurrents of 44 μAcm⁻² under 1 Sun illumination with almost quantitative Faradaic efficiency for O₂ evolution. Through refinement of the supramolecular approach, it was then possible to further improve the performances of the system. This was achieved by functionalizing the PBI chromophores with tetraethylene glycol (TEG) cross-linkers, thus introducing hydrophilic domains in the vicinity of the catalytic centers of Ru₄POM in superstructured assemblies of [(PBI^{TEG})₅(Ru₄POM)]. Indeed, inverse-opal ITO photoelectrodes based on such supramolecular system displayed a staggering 340% improvement over the simpler parent.²³⁹

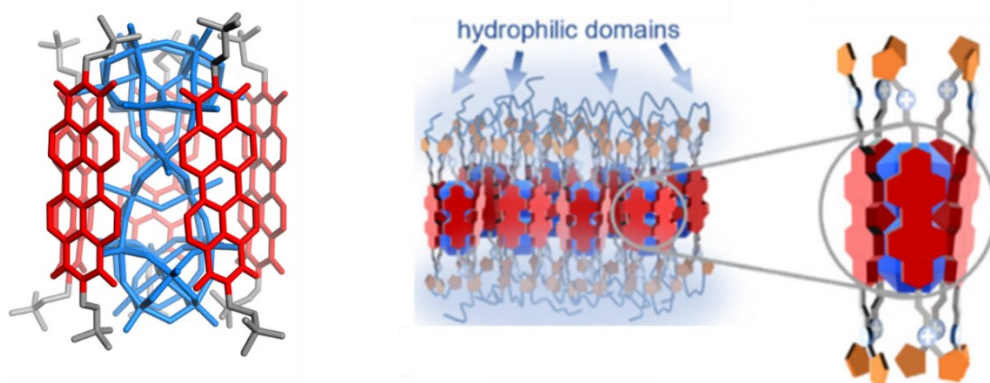


Figure 95. Structures of $[(\text{PBI})_5(\text{Ru}_4\text{POM})]$ (left) and $[(\text{PBI}^{\text{TEG}})_5(\text{Ru}_4\text{POM})]$ (right). Figures reproduced with permission from ^{238,239}. Copyright 2019 the Authors, under exclusive licence to Springer Nature Ltd.; Copyright 2022 American Chemical Society.

Literature addressing the issue of electron transfer kinetics in dyadic assemblies have also been reported involving colloidal oxide particles as WOC and molecular dyes. However somewhat scarcer, examples of such sort are appealing given the tendency of nanostructured catalysts to display higher activity and/or better stability than molecular complexes.

Historically relevant studies involve state-of-the-art dye and catalyst, Ru^{II} polypyridine derivatives and colloidal hydrated iridium oxide, respectively. Indeed, mechanistic studies²⁴⁰ of the electron transfer reaction between $\text{Ru}(\text{bpy})_3^{2+}$ and IrO_x relevant to the water oxidation reaction date back to 2004. In these, it was demonstrated that the rate-limiting step in the overall water oxidation in the presence of persulfate as sacrificial electron acceptor was in fact the electron transfer between the oxidized dye and iridium oxide. A tailored synthesis method employed Ru^{II} polypyridine analogues bearing dicarboxylic groups in the periphery of one of the bipyridyl ligands, thus able to act as capping agents in the synthesis of the iridium oxide particles. Furthermore, the heteroleptic complexes were directly connected to a TiO_2 film by a phosphonate anchor in the structure of another bipyridyl ligand (Figure 96). By bridging the dye and the catalyst through a direct chemical interaction, the rate of electron transfer between the

oxidized dye and IrO_x was increased by two orders of magnitude.^{212,241} This effect is indeed ascribable to both a higher local concentration of the dye on the surface of the catalytically active material and a stronger degree of electronic coupling between the two components. The result is therefore a pre-organized system prone to intrinsically faster inner-sphere electron transfer.

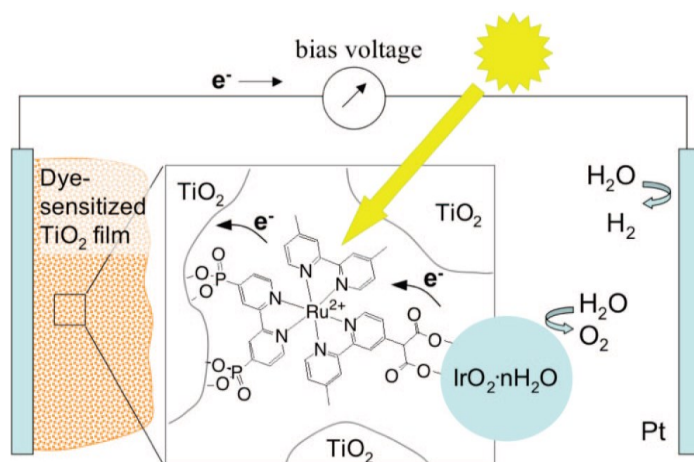


Figure 96. Photoelectrochemical cell featuring a TiO_2 -based photoanode functionalized with a Ru-sensitized hydrated Ir oxide nanoparticles. Figure reproduced with permission from ²⁴¹. Copyright 2009 American Chemical Society.

Later developments kept exploiting iridium oxide, the surface of which could be functionalized by either a free-base porphyrin dye bearing dicarboxylate moieties in its *meso* aryl rings or by its Pd complex introduced as stabilizers during IrO_x synthesis (Figure 97).²⁴² Fluorescence quenching experiments demonstrated the close electronic interaction between the colloidal catalyst and the porphyrin, possibly resulting from electron transfer from the former to the excited state of the dye (reductive quenching route). Despite encouraging preliminary observations, however, the hybrid dyad was not further investigated in photocatalytic or photoelectrocatalytic regimes.

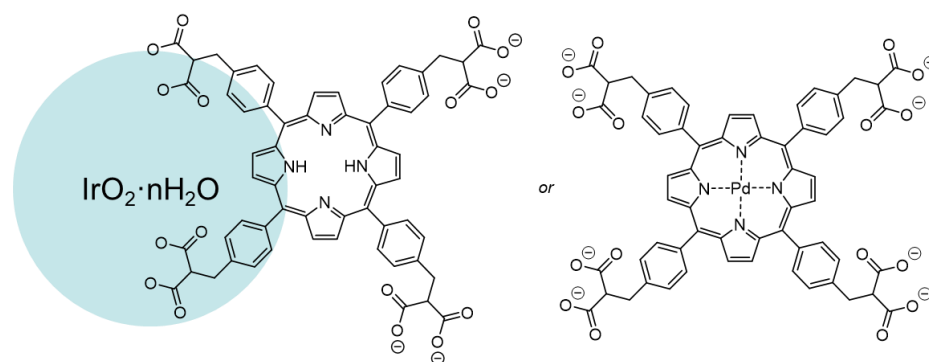


Figure 97. Hydrated iridium oxide nanoparticles functionalized on their surface by freebase and Pd porphyrins studied by Mallouk and co-workers.²⁴²

A key step in the development of photoactive hybrid materials for the OER was recently published by Sala and co-workers. They reported the synthesis of cobalt oxide nanoparticles decorated with analogues of $\text{Ru}(\text{bpy})_3^{2+}$ on their surface ($\text{RuPS}@Co_3O_4$), represented in Figure 98.²⁴³ These hybrid dyads were studied under visible light irradiation, catalyzing the OER through light absorption by the ruthenium complex in the presence of persulfate as sacrificial electron acceptor. Photophysical studies provided evidence for the dye acting through its normally observed mechanism, *i.e.* oxidative quenching of the excited state of the dye by persulfate. Indeed, findings highlighted no significant difference in the light harvesting action mechanism by the photosensitizer followed by electron transfer to $\text{S}_2\text{O}_8^{2-}$. However, the role of the direct chemical and electronic interaction between dye and catalyst was clearly appreciable by comparing the catalytic performance of the $\text{RuPS}@Co_3O_4$ dyad with the system composed by the “unbound” RuPS and Co_3O_4 . Indeed, photocatalytic O_2 evolution is relevant only in the former case, thus confirming the power of the dyad approach. Nonetheless, comparative studies of such materials in immobilized systems may provide insights in the beneficial role of the latter beyond colloidal catalysis. These would therefore constitute the premises for novel photoelectrochemical devices.

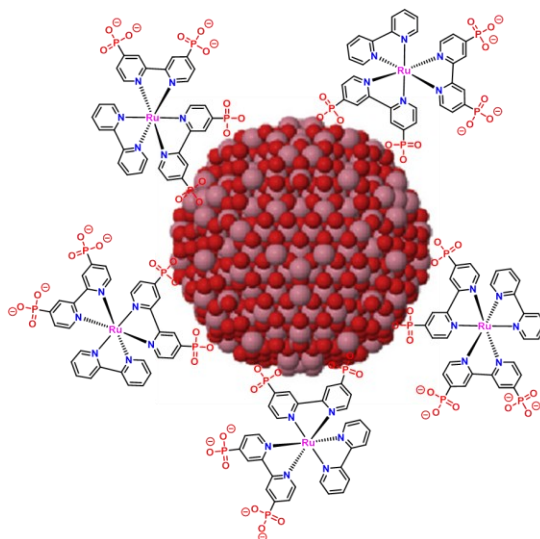


Figure 98. Cobalt oxide-Ru dye hybrid nanoparticles (RuPS@Co₃O₄) studied for photocatalytic water oxidation by Sala and co-workers. Figure adapted with permission from ²⁴³. Copyright 2018 Elsevier.

To date, rare-metal free dye-catalyst dyads for promoting either photocatalytic or photoelectrochemical OER have not been reported. In 2014, Finke and co-workers have reported photoanodes based on organic semiconducting PBI films (Figure 99).²²⁰ The dye was functionalized with phosphonic acid pendants at the nitrogen sites, thus acting as a potential binding moieties for transition metal ions and oxides. By using this strategy, researchers were able to guide the photoelectrochemical growth of cobalt oxide nanoparticles (CoO_x) bound to the phosphonate moieties of the visible light-absorbing film, starting from aqueous solutions of Co²⁺ salts. The photoanodes displayed 80% FE for O₂ evolution with maximum IPCE 0.12%, limited by the low optical absorption by the thin films. Despite the interesting system based on a versatile approach, the cobalt oxide WOC-PBI films were not comprehensively characterized from the compositional and morphological standpoint. Indeed, while the direct chemical interaction between the PBI molecules and the cobalt oxide particles was proven crucial to the efficacy of the device, the loosely controllable synthetic approach prevented the formation of a well-controlled dyad.

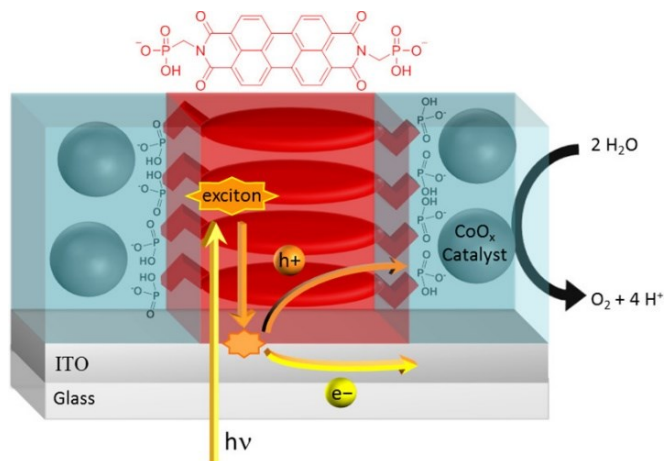


Figure 99. Scheme of the photoanode based on cobalt oxide-PBI, published by Finke and co-workers. Figure reproduced with permission from ²²⁰. Copyright 2014 American Chemical Society.

The undefined structure of the PBI-CoO_x assembly was proven as a device flaw in later reports, in which SnO₂ films were sensitized with phosphonate-bearing PBI's and functionalized by photoelectrochemical growth of CoO_x. In this latter system, CoO_x was proven to grow preferentially on SnO₂, rather than exploiting the chemical interaction between the $\sim\text{PO}_3^{2-}$ anchoring groups and Co^{2+} ions.

4.1.6 From molecular to nanostructured WOC: the case of cobalt oxide

The design principles described in Chapter 1 have been profitably directed to attain effective molecular catalysts operating at low overpotentials and reaching high TOF and TON values. However, stability issues associated with molecular species have been found to be commonly accompanying their usage in electrochemical regimes.

Especially first-row transition metal complexes, when studied in conditions relevant to water oxidation, tend to undergo decomposition to their oxides, producing heterogeneous catalytic films at the electrode surface. Stable devices could benefit from the presence of nanostructured transition metal oxides as WOC, more tolerant to the operational conditions. The most active heterogeneous catalyst is indeed hydrated iridium oxide ($\text{IrO}_x \cdot n\text{H}_2\text{O}$), thoroughly studied in the best performing TiO_2 -based photoanodes (*vide supra*). However, the inapplicability of iridium-based devices on a large scale calls for resorting to base metal-containing catalysts.

Nanostructured cobalt oxide has proven a valid electrocatalyst, able to oxidize water to O_2 with overpotentials as low as 350–400 mV in basic electrolyte.²⁴⁴ More recently, cobalt oxide catalysts have been proven as effective also under acidic medium. This would represent a viable alternative to iridium-based catalysts, given the abundancy of the source metal, even though ethical controversies about its supply have been raised and should be kept in consideration.

Co_3O_4 is a mixed-valence oxide with a spinel structure containing Co^{2+} ions at the T_d sites and Co^{3+} ions at the O_h sites. The surface of Co_3O_4 crystals is partially oxidized to $\text{Co}^{\text{III}}\text{OOH}$, the oxidation degree depending on the applied electrode potential. Further surface oxidation provides $\text{Co}^{\text{IV}}\text{O}_2$, producing anodic voltammetric features that precede the catalytic water oxidation onset. The OER mechanism catalyzed by cobalt oxide has been thoroughly studied both in nanocrystals and molecular models in the last decade.^{245–250}

Briefly (Figure 100), a two-electron oxidation at two neighboring $\text{Co}^{\text{III}}\text{OH}$ sites produces two $\text{Co}^{\text{IV}}\text{O}$ oxo sites involved in nucleophilic attack towards water. The resulting peroxy intermediate subsequently evolves to a superoxo fragment and finally to O_2 upon two further oxidation steps. It should be highlighted how each oxidation step is a PCET involving proton abstraction by a base in the reaction medium.

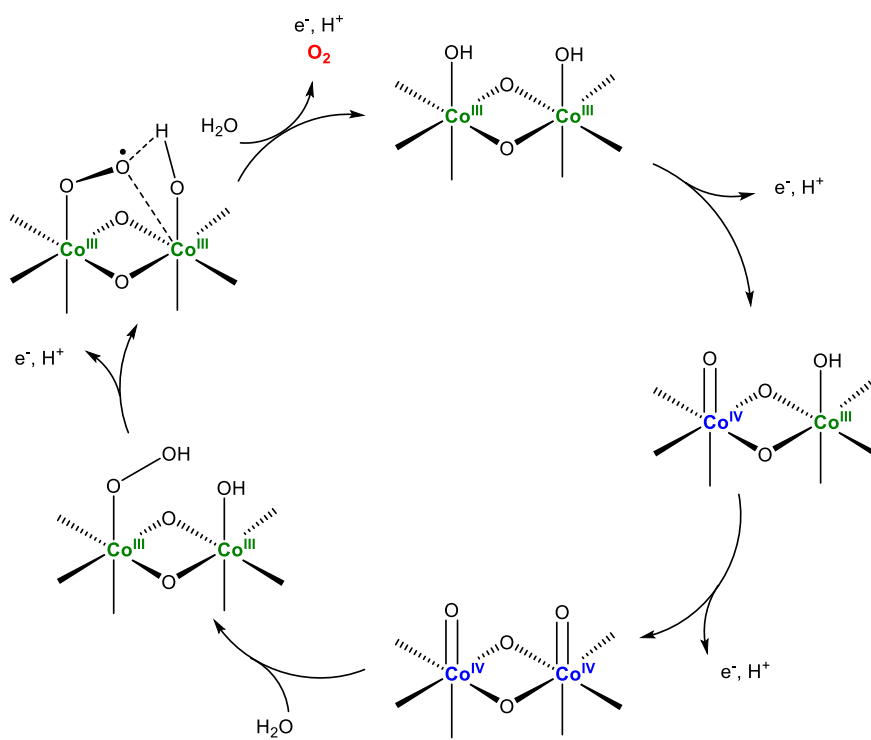


Figure 100. Electrocatalytic mechanism of water oxidation by cobalt oxide-based materials. Figure adapted with permission from ²⁵⁰. Copyright 2014 Nature Publishing Group.

Various strategies directed to the preparation of cobalt oxide-functionalized photoelectrodes have been evaluated in the literature. Notably, electrodeposition of cobalt oxide films directly on an electrode surface was found convenient, the very working electrode being used as a platform to grow the catalytic deposit to be further employed. Systematic analyses elucidated how the electrodeposition outcome would largely depend on the electrolyte composition, on the

electrochemical conditions chosen (applied potential or current density) and on the cobalt precursor. Indeed (*vide supra*) cobalt complexes tend to undergo decomposition in aqueous environment under anodic conditions. While detrimental towards molecular catalysis of the OER by cobalt complexes, it led to synthetic approaches in which molecular complexes have been intentionally decomposed to electrodeposit cobalt oxide. Examples involve controlled electrochemical decomposition of cobalt oximes or EDTA complexes, aside from simpler cobalt(II) salts as discussed in Section 4.1.5 (Figure 101).^{246,251–257}

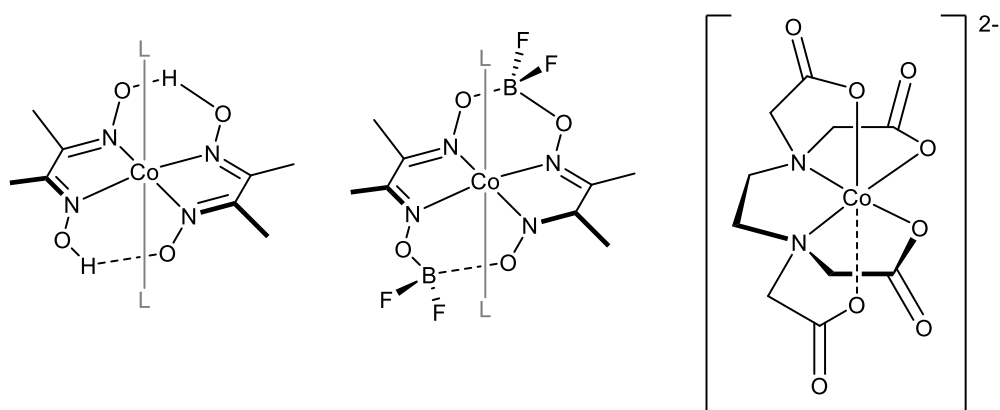


Figure 101. Structures of cobalt complexes used for deliberate electrodecomposition to nanostructured cobalt oxide materials.

However versatile, this approach proved poorly controllable in terms of nanoparticle morphology, composition and crystallinity. Oftentimes, the variegate composition of the cobalt oxide deposits led to a generic label (CoO_x), defying a controllable determination of the heterogeneous active sites.

Finer synthetic approaches are based on the solvothermal decomposition of cobalt molecular precursors in controlled reaction conditions. These methods can reproducibly afford nanostructured crystalline Co_3O_4 with a wide dimensional range and different shapes such as cubes, rods, and spheres. For these reasons, above cited literature reports tend to prefer solvothermal methods to obtain better characterized catalytic materials. Electrodeposition, on the other hand, is a more

convenient and usually more easily scalable method for preparing nanostructured cobalt oxide.

4.1.7 Use of photoactive dye-WOC dyads in operational systems

In the scope of applying hybrid WOC-chromophore dyads to water oxidation, the present work will be dedicated more extensively to DSPEC photoanodes based on such dyadic systems. For these reasons, a more detailed treatment will be hereafter provided about crucial parameters functional to description and benchmarking of photoelectrodes. Photocatalytic studies as those described in Chapter 5 will be instead treated as proof of reactivity of the dyads and as means for mechanistic investigation, functional to their application in devices as DSPEC's.

4.1.7.1 Efficiency parameters of photoelectrochemical cells

Screening of a photoelectrode relies on electrochemical methods in which its current density response is measured under irradiation. Intermittent (chopped) illumination current traces are often recorded to obtain a comparison, internal to each experiment, between the photocurrent and the “dark” current (in the absence of irradiation). Given the topic of the present section, the focus will be restricted to photoanodes and their operation mechanisms.

The ability of the dye to photoinject electrons in the SCO and thus their applicability in DSPEC's can be independently studied by performing photoelectrochemical experiments in the presence of sacrificial electron donors. These are usually amines, ascorbic acid (*vide supra*) or Br^- , this latter resembling in concept the cell scheme of DSSC's. Sacrificial electron donors are kinetically and thermodynamically easy to oxidize and undergo irreversible chemical processes. Therefore, sacrificial agents allow the study of electron injection dynamics in the absence of recombination.

Incidentally, a photoelectrochemical response is observable beyond the photocurrent onset potential, *i.e.*, the voltage at which photoinduced electron injection results in transport to the TCO and collection by the circuit. This latter is another benchmarking parameter to consider when describing such systems.

When a WOC is introduced, its mechanism in light-activated processes at a photoelectrode is expected not to differ from that observed in the dark. However, electrocatalytic features of the catalyst are not observable in the photoelectrochemical response, as more negative potential ranges are explored in these experiments. The current observed under irradiation is therefore related to the charge carriers being mobilized in the semiconductor film, rather than the molecular species interacting with it.

i) The key parameter to characterize a photoelectrode is its steady-state photocurrent density. It may be obtained from linear scan voltammetry (LSV) or chronoamperometry experiments. In both cases, the photocurrent should be evaluated as a function of the applied bias.

ii) The Faradaic efficiency of photoelectrodes is a key parameter to determine their efficiency and selectivity towards the desired catalytic reaction, as detailed in Chapter 1. It is often the most informative parameter, indirectly accounting for the efficiency of electron transfer management by the system and of the dark cycle. However, the usually encountered low photocurrent densities pose a prominent issue towards detection and quantification of reaction products. In the case of the OER, O₂ may be quantified by gas chromatography or dioxygen sensors, upon running preparative scale photoelectrolysis experiments. However, this time-demanding approach is prone to large errors due to the high detection limits of the above methods with respect to the activity of the photoanodes. Furthermore, the long electrolysis time required can impact on device chemical stability, thus preventing an accurate quantification. Usually, electrochemical strategies are preferred. The most commonly used is the two-plate generator-collector (G-C) method.^{258,259} Briefly, it is a bipotentiostatic method in which the photoanode is placed in the close vicinity of a second working electrode. Inert

spacers are employed to prevent direct contact between the electrodes and to maintain a thin layer of electrolyte between them (Figure 102). When the photoanode is operated, alleged O₂ generation occurs: therefore, it is denoted as generator (G) electrode. The collector (C) working electrode is instead poised at a negative potential, so to reduce O₂ upon its diffusion through the thin electrolyte layer. The role of the collector electrode is to detect the electroactive product released from the generator, thus acting as an amperometric sensor. The Faradaic efficiency of a photoanode may therefore be determined by integrating the charge passing through the G and C electrodes and applying Eq. 42:

$$FE = \frac{|Q_C|}{Q_G} \times \frac{1}{\eta_{coll}} \quad (\text{Eq. 42})$$

The collection efficiency, η_{coll} , is specific of the G-C setup geometry and must be independently determined *via* chronoamperometric experiments with generators displaying known Faradaic efficiency for the OER.

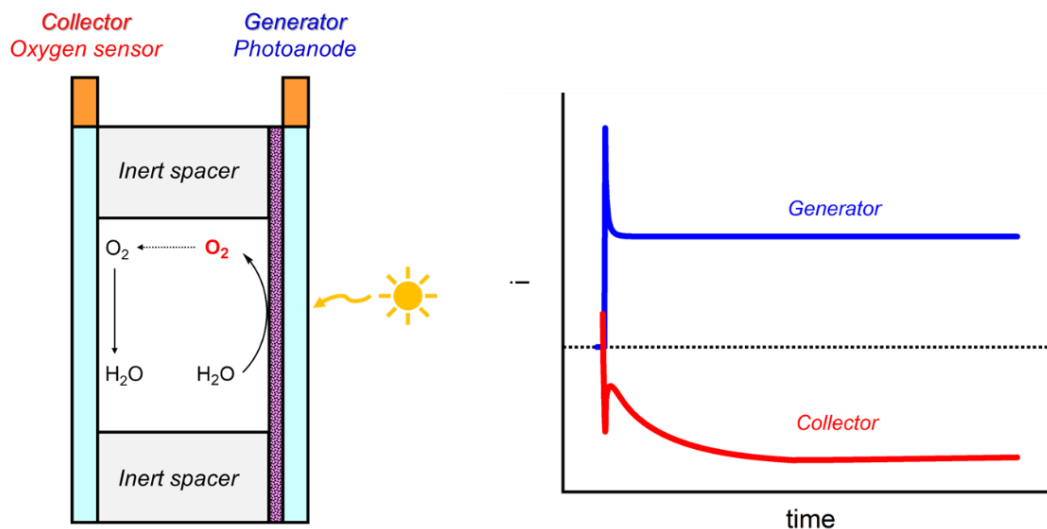


Figure 102. Left: schematic representation of a two-plate generator-collector setup used for trace oxygen detection. Right: simulated chronoamperograms associated with the current response of generator and collector electrodes. The traces are simulated as detailed in Appendix 1.

iii) The efficiency of incident light conversion into photocurrent by a photoelectrode is quantified by the incident photon-to-current conversion efficiency (IPCE). It is expressed as per Eq. 43:

$$IPCE (\%) = \frac{\Phi_e}{\Phi_{hv}} \times 100 \quad (\text{Eq. 43})$$

In Eq. 43, Φ_e and Φ_{hv} are the fluxes of electrons and incident photons, respectively. The term Φ_e is related to the measured photocurrent density. The photon flux, on the other hand, is related to the power of the incident light.^{219,220}

IPCE may be expressed to highlight its physico-chemical significance in microscopic terms by Eq. 44:

$$IPCE = LHE \times \varphi_{inj} \times \varphi_{coll} \quad (\text{Eq. 44})$$

The expression contains the terms φ_{inj} and φ_{coll} , the injection and collection yields, respectively. While φ_{inj} quantifies the fraction of excited dye molecules that inject electrons in the SCO, φ_{coll} is the fraction of injected electrons that are collected through the circuit and not lost upon charge recombination. The light harvesting efficiency (LHE), on the other hand, represents the portion of incident photons that are absorbed by the photoactive element of the electrode (*i.e.*, by the dye molecules in a dye-sensitized photoelectrode), and is expressed by Eq. 45:

$$LHE = 1 - 10^{-Absorbance} \quad (\text{Eq. 45})$$

Therefore, Eq. 44 highlights how the IPCE of a device might be limited by either of the key processes necessary to achieve a net photoinduced charge flow through the circuit, namely light absorption, charge injection, and charge transport. If the latter two processes had unit efficiency, the maximum IPCE would be limited by light absorption.

Eq. 43 may be reformulated in terms of the photocurrent density (J , in μAcm^{-2}) and of the irradiance (P , in Wm^{-2}) at each individual wavelength (λ , in nm), following Eq. 46:

$$IPCE \approx 1240 \times \frac{J_\lambda}{\lambda \times P_\lambda} \quad (\text{Eq. 46})$$

To obtain IPCE according to Eq. 46, the photoelectrochemical response must be examined using monochromatic light sources. The implication is that an IPCE spectrum may be reconstructed, as a function of the wavelength of the incident light. These plots are denoted as (photo)action spectra and represent how the device employs photons to produce the observed photocurrent response. Ideally, the photoaction spectrum should match or be relatable to the optical spectrum of the dye. It is also possible (and meaningful) to report an overall IPCE value by considering the photocurrent density under polychromatic illumination and the full emission spectrum of the light source (Eq. 47):

$$IPCE \approx 1240 \times J \times \left\{ \int_{\lambda_0}^{\lambda_1} \lambda P_\lambda d\lambda \right\}^{-1} \quad (\text{Eq. 47})$$

iv) Each photoelectrode is characterized by specific optoelectronic properties. To account for the utilization of *absorbed* incident photons by the photoelectrode, the absorbed photon-to-current conversion efficiency (APCE) is introduced, Eq. 48. It represents a parameter describing the internal quantum efficiency of the device.

$$APCE = \frac{IPCE}{LHE} = \varphi_{inj} \times \varphi_{coll} \quad (\text{Eq. 48})$$

5. Polyquinoid dye-cobalt oxide hybrids: novel rare metal-free dyads for photoelectrochemical Water Oxidation

5.1 Rationale

In the present chapter, the work involving cobalt oxide nanoparticles bound to a shell composed of a polyquinoid organic chromophore is reported. These hybrid materials have been proven as photoactive catalysts for the water oxidation reaction. The work is a collaborative effort involving several research groups:

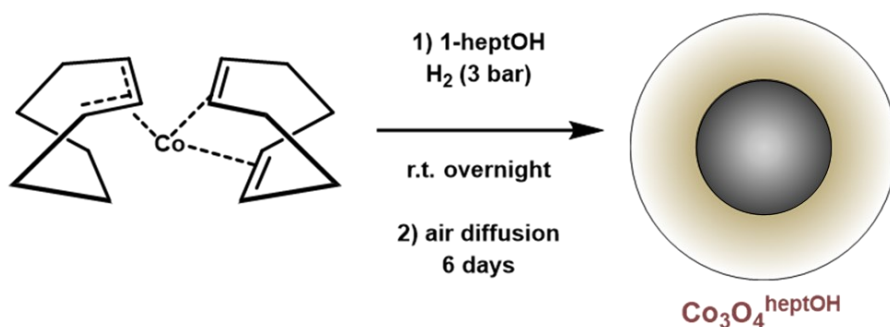
- Prof. Xavier Sala Román, Prof. Jordi Garcia-Antón Aviñó, Dr. Laia Francàs Forcada – *Department of Chemistry, Universitat Autònoma de Barcelona*. Synthesis of the hybrids, photocatalytic studies;
- Prof. Andrea Sartorel, Ruggero Bonetto, Dr. Giulia Alice Volpato – *Department of Chemical Sciences, Università degli Studi di Padova*. Photoelectrochemical studies;
- Prof. Pierluca Galloni, Dr. Federica Sabuzi, Mattia Forchetta – Department of Chemical Science and Technologies, *Università di Roma Tor Vergata*. Synthesis of the chromophores;
- Dr. Nuria Romero, Prof. Karine Philippot – *CNRS, Laboratoire de Chimie de Coordination, Université de Toulouse*. Synthesis of the hybrids, transmission electron microscopy (TEM) characterization, photocatalysis;
- Prof. Mirco Natali – *Department of Chemical, pharmaceutical and agricultural sciences, Università di Ferrara*. Photophysical characterizations of the hybrids.
- Dr. Marcos Gil Sepulcre and Dr. Olaf Rüdiger – *Max-Planck-Institut für Chemische Energiekonversion*

The research in which I was directly involved is founded upon the complementary expertise of the Nano and Molecular Catalysis group in Padova in dye-sensitized photoelectrochemical systems and of researchers in the SelOxCat group in metal and metal oxide nanoparticle synthesis. Synthesis and characterization of the

particles will be described briefly, followed by a discussion of the photocatalytic experiments and of their evaluation on photoelectrodes.

5.2 Synthesis and characterization of the hybrid particles

The synthesis of spherical cobalt oxide nanoparticles was performed *via* the organometallic approach. This peculiar synthetic route involves decomposition of an organometallic precursor under mild conditions (room temperature and 3 bar of H₂), to generate metal particles in the presence of a suitable organic ligand acting as a stabilizer.²⁴³ The synthetic outcome has typically a high reproducibility, and the particle size dispersity and shape are controllable. In principle, the organometallic approach affords well-defined nanoparticles that lend themselves to post-synthetic modifications and potentially fine-tuning of their properties for catalytic applications. In the specific case, cobalt oxide nanoparticles were synthesized through a two-step method (Scheme 13). The first stage involved decomposition of a cobalt organometallic compound, (cyclooctadienyl)(1,5-cyclooctadiene)cobalt(I) [Co(η^3 -C₈H₁₃)(η^4 -C₈H₁₂)], to generate Co particles in 1-heptanol (heptOH), acting both as solvent and stabilizer. The outcome is constituted by spherical particles with a diameter of *circa* 3 nm, stabilized by a heptOH shell (Co^{heptOH}). Subsequently, air diffusion in the suspension allowed for controlled oxidation of the particles to generate Co₃O₄^{heptOH}. TEM images of the particles before and after air diffusion are provided in Figure 103.



Scheme 13. Synthesis of Co₃O₄^{heptOH} following the organometallic approach.

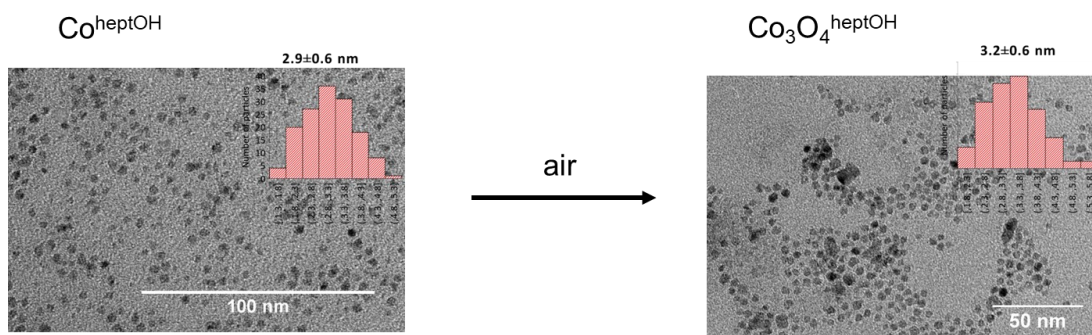


Figure 103. TEM images of $\text{Co}^{\text{heptOH}}$ (left) and $\text{Co}_3\text{O}_4^{\text{heptOH}}$ nanoparticles (right).

These particles had been previously studied as WOC in electrocatalytic conditions displaying promising onset overpotentials for the OER (0.29 V in 1 M NaOH and 0.77 V in pH 5.60 $\text{NaHCO}_3/\text{Na}_2\text{SiF}_6$ electrolyte). Subsequently, production of a photocatalytic dye-catalyst dyad was undertaken. Dyads of such kind incorporate in a single entity several chromophore units bound to a catalyst particle and are supposedly designed to provide a controllable catalyst:dye ratio and a fast electron transfer pathway (*vide supra*). $\text{Co}_3\text{O}_4^{\text{heptOH}}$ has been studied in photocatalytic dyads comprising ruthenium bipyridyl derivatives bound to the particles through phosphonate moieties in the ligand scaffold. These were applied for the OER in photocatalytic systems based on the use of $\text{S}_2\text{O}_8^{2-}$ as sacrificial electron acceptor, reaching a TON for O_2 evolution up to 82 with TOF 2.05 molmin^{-1} referred to $\text{Co}_3\text{O}_4^{\text{heptOH}}$ (2.53 TON and $0.063 \text{ molmin}^{-1}$ when referred to the RuPS).

In the current project, the dyad was constituted by choosing organic polyquinoid chromophores, denominated KuQuinones (KuQ), represented in Figure 104.

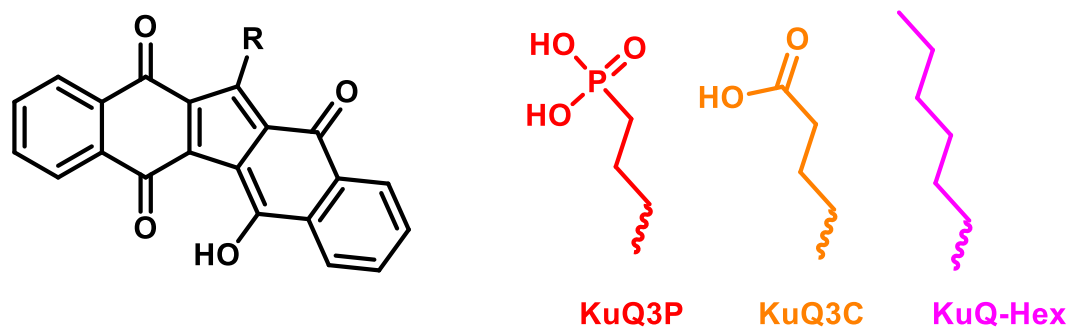
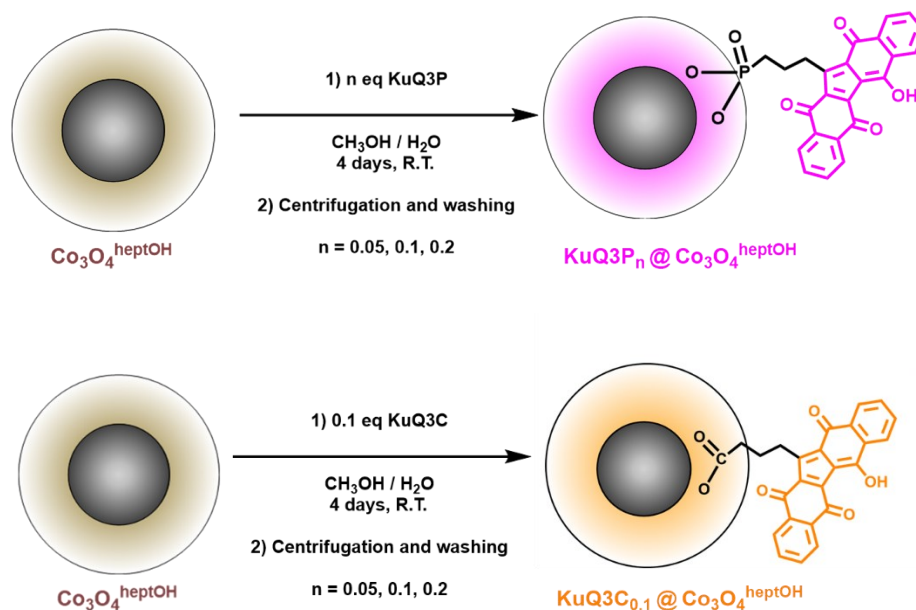


Figure 104. Structure of the KuQuinone core, with different side chains.

These were discovered and synthesized by the group of Prof. Pierluca Galloni (University of Rome Tor Vergata, Rome), and thoroughly studied in terms of their redox and optical properties.^{260–267} The KuQ dyes are well suited for application in the photoanode of a WS-DSPEC. Indeed, it was demonstrated that KuQ dyes can manage and partake in proton-coupled electron transfer (PCET) events, both in the ground and excited states. This highly valuable feature is beneficial in the scope of targeting multi-electron, multi-proton electrochemical reactions such as water oxidation. Indeed, the structural quinoid motif is found in natural photosynthetic systems, employing quinones as paramount electron transfer relays. KuQuinones exhibit absorption in the visible region (*vide infra*), their singlet excited state is highly oxidizing ($> 2 \text{ V vs NHE}$; 2.34 V vs RHE), and they can inject electrons from their reduced form ($E^0_{\text{KuQ}/\text{KuQ}^-} \approx 0.08 \text{ V vs NHE}$ at pH 5.8; 0.42 V vs RHE) in the conduction band of *meso*-SnO₂ ($E_c = 0.16 \text{ V vs NHE}$ at pH 5.8; 0.50 V vs RHE). In a previous joint report with NanoMolCat, KuQ dyes were employed to sensitize SnO₂ and produce water oxidizing photoanodes in conjunction with a ruthenium polyoxometalate catalyst (Ru₄POM, mentioned in Section 4.1.5), with a photocurrent density of $\sim 20 \mu\text{mAcm}^{-2}$ at 0.6 V vs Ag/AgCl and Faradaic efficiency for the OER up to 75%.²⁶⁶ Lastly, the dyes can bear side chains that do not impact on the chromophore core, while imparting different acid-base and solubility properties.

In this project, KuQ dyes with pendant phosphonate (KuQ3P) and carboxylate (KuQ3C) moieties were used, exploiting the side chains to anchor them on the surface of $\text{Co}_3\text{O}_4^{\text{heptOH}}$. Incidentally, carboxylate and phosphonate groups can indeed be used to anchor organic molecules on the surface of metal oxides, including SCO films. The hybrid particles will be denoted $\text{KuQ3P}_n@\text{Co}_3\text{O}_4^{\text{heptOH}}$ ($n = 0.05, 0.1, 0.2$, where n are the nominal equivalents of KuQ with respect to $\text{Co}_3\text{O}_4^{\text{heptOH}}$ used in the synthesis) and $\text{KuQ3C}_{0.1}@\text{Co}_3\text{O}_4^{\text{heptOH}}$.

The hybrid particles were synthesized by simply stirring KuQ3P or KuQ3C for 4 days in a $\text{CH}_3\text{OH}/\text{H}_2\text{O}$ mixture (Scheme 14) and were characterized by means of infrared spectroscopy, transmission electron microscopy (TEM) and high-resolution TEM (HR-TEM), and X-ray absorption spectroscopy (XAS, in the facilities of the ALBA synchrotron in Cerdanyola del Vallès, Barcelona, in collaboration with Dr. Marcos Gil Sepulcre and Dr. Olaf Rüdiger). The elemental composition of the particles was analyzed by optical emission inductively coupled plasma (ICP-OES) and ICP coupled to mass spectrometry (ICP-MS).



Scheme 14. Synthesis of $\text{KuQ3P}_n@\text{Co}_3\text{O}_4^{\text{heptOH}}$ (top) and $\text{KuQ3C}_{0.1}@\text{Co}_3\text{O}_4^{\text{heptOH}}$ (bottom) hybrid nanoparticles.

The TEM analysis of the particles highlighted a substantial modification of their environment. A modest diameter increase of the particles to *circa* 4 nm was observed, consistent with a negligible degree of particle aggregation. Furthermore, the particles were found surrounded by a gray matter of yet unspecified origin. By analyzing the particles *via* HR-TEM, it was found that the cobalt oxide nanoparticles had retained their crystallinity after KuQ binding. The gray matter surrounding the nanoparticles, when analyzed by HR-TEM and EDX (energy-dispersive X-ray spectroscopy), displayed punctiform features that were revealed to contain cobalt (Figure 105).

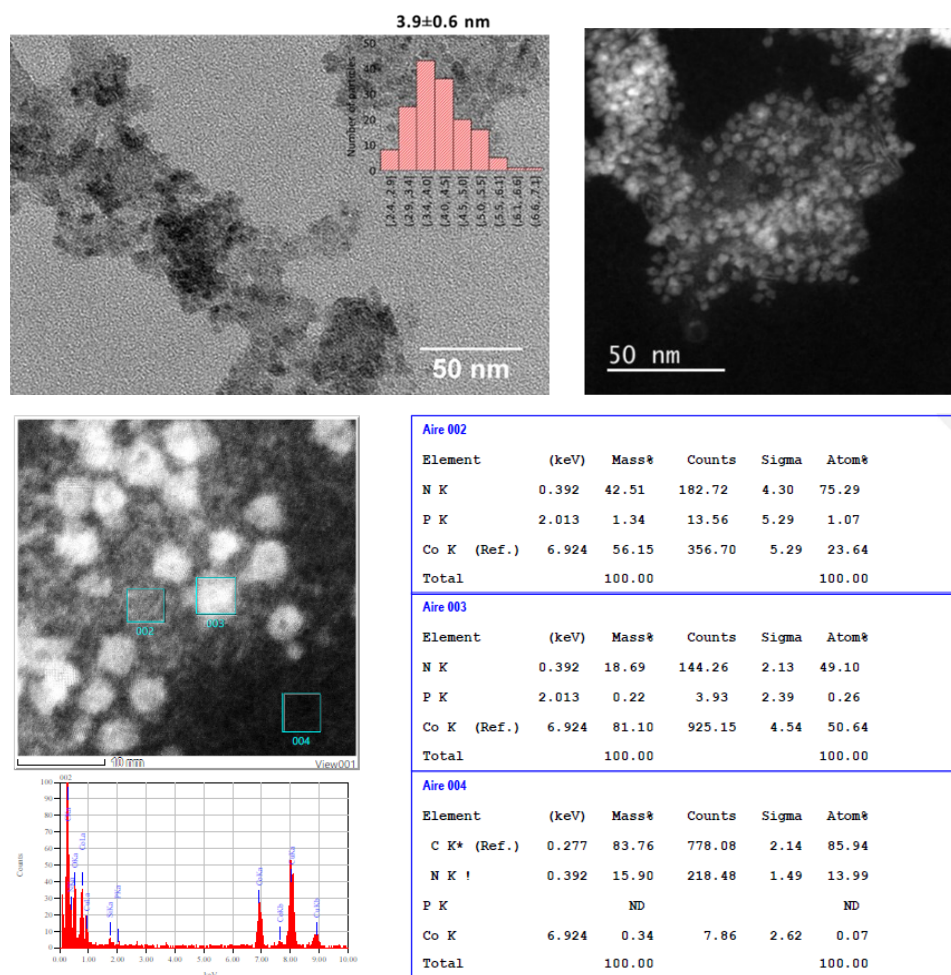


Figure 105. Top: TEM (left) and HR-TEM (right) images of $\text{KuQ3P}_{0.1}@\text{Co}_3\text{O}_4^{\text{heptOH}}$ hybrid nanoparticles. Bottom: EDX analysis results of different sites, highlighting the different composition of nanoparticles, grey matter, and grid (used as reference).

XAS analysis of the hybrids highlighted different XANES (X-ray absorption near-edge structure) and EXAFS (extended X-ray absorption fine structure) features with respect to the pristine $\text{Co}_3\text{O}_4^{\text{heptOH}}$ (Figure 106). This latter was instead found consistent with Co_3O_4 spinel-structure. In particular, the XANES of the hybrids is radically different in comparison with $\text{Co}(0)$, CoO , $\text{Co}(\text{OH})_2$, $\text{Al}_2\text{Co}^{\text{II}}\text{O}_4$, and Co_3O_4 . The decrease of intensity in the pre-edge indicates a more pronounced octahedral degree of the geometry of the otherwise tetrahedral Co^{II} sites. In the EXAFS, the Co-Co band characteristic of the spinel is lost while new species dominate the spectrum. Most probably, the sample is constituted by a mixture of a new species and of Co_3O_4 spinel. Preliminary attributions ascribe the observed features to the formation of Co single atoms upon KuQ binding, in particular the disappearance of the FT-EXAFS signals associated to Co-O and Co-Co interactions. The lack of closely interacting cobalt sites suggests the formation of single Co atoms, possibly in an octahedral coordination environment. However, a more detailed investigation is currently being carried out to further elucidate the nature of these atoms and their potential role in the operational mechanism of the hybrid dyads towards water oxidation.

Interestingly, attempts at producing a hybrid material upon treatment of $\text{Co}_3\text{O}_4^{\text{heptOH}}$ with KuQ-Hex (Hexyl KuQuinone, see Figure 104) proved successful, with features ascribable to Co atoms identified by HR-TEM and EDX. The possible chemical interaction between the cobalt oxide and the KuQ-Hex lacking an anchoring moiety might involve the oxygen (enolate) donor sites at the chromophore core, as detailed below. Regardless, the formation of Co atoms is related to the nature of the KuQ dye, independently on the chemical identity of its side chain. This is further supported by the absence of Co atoms in the analogous $\text{RuPS}@ \text{Co}_3\text{O}_4$ dyads. Further studies on the identity of the interaction between KuQ-Hex and cobalt oxide are currently ongoing. However, the strongly hydrophobic nature of the dye prevented suspension of the particles in water-based media for photocatalysis, while suspending the hybrids in organic solvents resulted in detachment of KuQ-Hex. For these reasons, the system was not investigated in catalytic conditions relevant to the OER.

The study reported insofar, albeit incomplete, highlights the more complicated nature of the hybrids. These do not simply involve a chemical bond of KuQ to $\text{Co}_3\text{O}_4^{\text{heptOH}}$, but are rather based on more complex interactions probably involving dye-dye interaction by π -stacking at a significant degree.

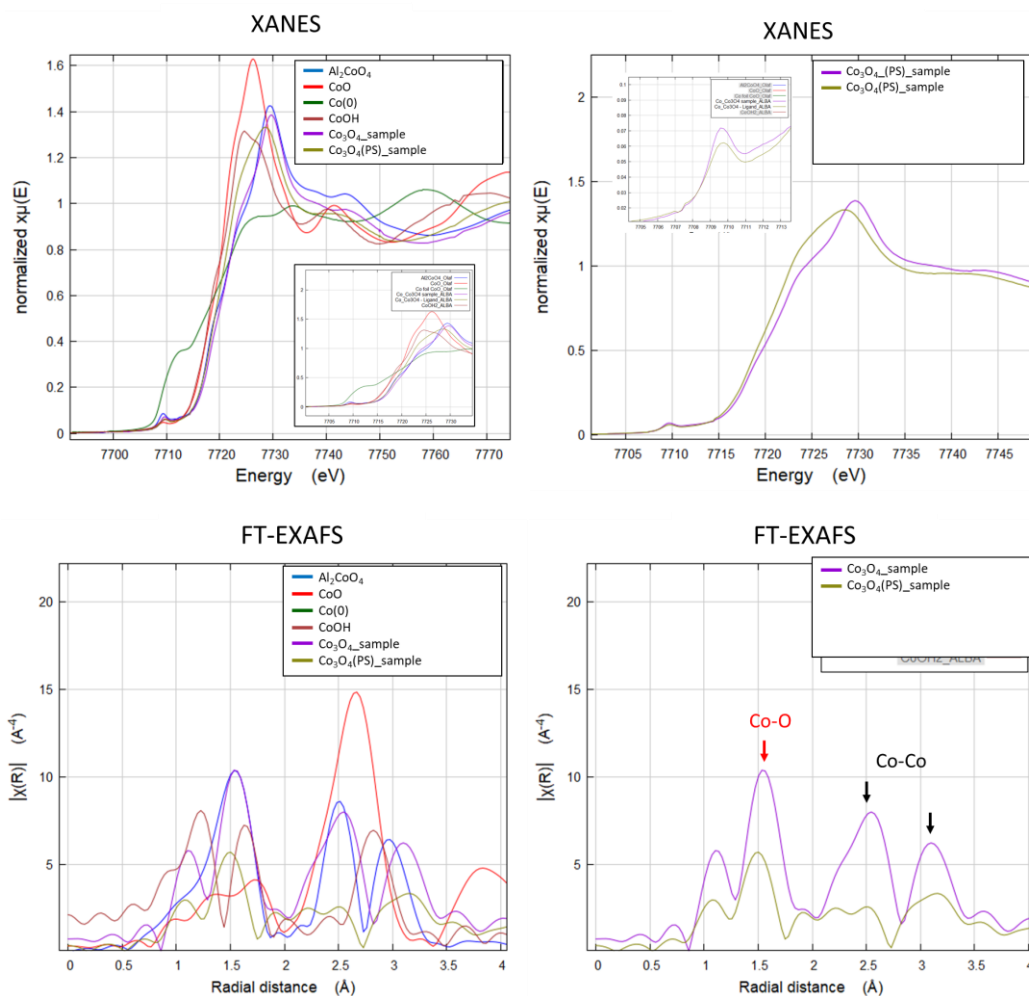


Figure 106. XANES (top) and EXAFS (bottom) of $\text{CuQ3P}_{0.1}@\text{Co}_3\text{O}_4^{\text{heptOH}}$ nanoparticles compared with pristine $\text{Co}_3\text{O}_4^{\text{heptOH}}$ and several cobalt-containing references compounds.

5.3 Photocatalytic experiments

The particles were then evaluated for the photocatalytic water oxidation reaction in aqueous electrolyte ($\text{NaHCO}_3/\text{Na}_2\text{SiF}_6$, pH 5.6), under simulated solar visible ($\lambda > 400 \text{ nm}$) light irradiation from a Xe short-arc lamp in the presence of 84 mM $\text{S}_2\text{O}_8^{2-}$ as a sacrificial electron acceptor, at the same concentration of cobalt oxide particles ($\sim 0.7 \text{ g/mL}$). Evolution of O_2 was followed *via* a Clark sensor inserted in a thermostated and sealed glass reactor (Figure 107).

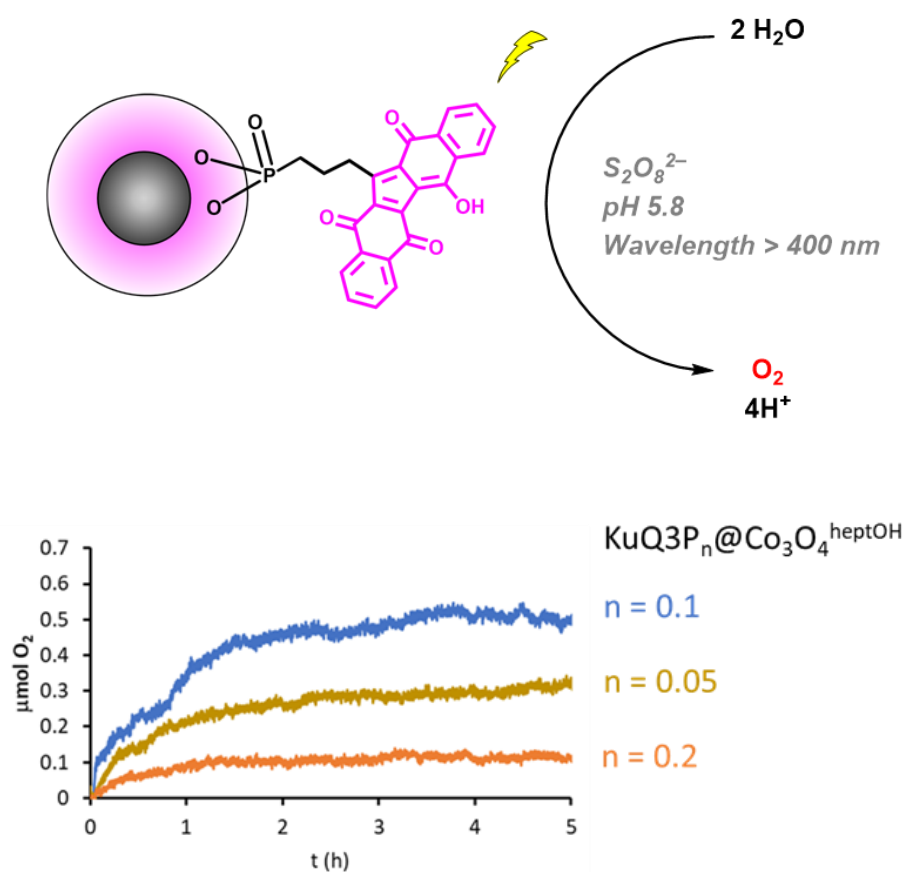


Figure 107. Top: photocatalytic oxygen evolution promoted by the $\text{KuQ3P}_n@ \text{Co}_3\text{O}_4^{\text{heptOH}}$ hybrid dyads. Bottom: oxygen evolution kinetics for $\text{KuQ3P}_n@ \text{Co}_3\text{O}_4^{\text{heptOH}}$.

The $\text{KuQ3P}_n@\text{Co}_3\text{O}_4^{\text{heptOH}}$ particles displayed activity with a trend depending on the dye : catalyst stoichiometric ratio. In particular, the activity (expressed as $\mu\text{mol O}_2$ evolved over 5 h of irradiation) followed a reproducible trend $\text{KuQ3P}_{0.1}@\text{Co}_3\text{O}_4^{\text{heptOH}} > \text{KuQ3P}_{0.5}@\text{Co}_3\text{O}_4^{\text{heptOH}} > \text{KuQ3P}_{0.2}@\text{Co}_3\text{O}_4^{\text{heptOH}}$, producing 0.5, 0.3 and 0.1 $\mu\text{mol O}_2$ after 5 h irradiation, respectively. The observed trend is coherent with the mutual influence of the molar amount of KuQ3P on the photoactivity of the system and on the availability of the cobalt oxide surface active sites upon dye binding. The KuQ3P equivalents in the hybrids impact on both parameters with an opposite trend, and the overall better performance of $\text{KuQ3P}_{0.1}@\text{Co}_3\text{O}_4^{\text{heptOH}}$ may therefore be justified on the basis of a balancing effect between the two. A similar observation was in fact reported in the case of the previously described $\text{RuP}@\text{CoOx}$ hybrids.²⁴³

The $\text{KuQ3C}_{0.1}@\text{Co}_3\text{O}_4^{\text{heptOH}}$, on the other hand, displayed a lower activity ($< 0.2 \mu\text{mol O}_2$ after 5 h), comparable with the cobalt oxide particles in the absence of KuQ. This is likely attributable to the lower stability of the carboxylate anchoring group with respect to the phosphonate, causing leaching of the dye. Furthermore, suspending unsensitized $\text{Co}_3\text{O}_4^{\text{heptOH}}$ in the presence of 0.1 equivalents of KuQ3P in the reaction solution did not afford an active system, again displaying the features of experiments conducted with $\text{Co}_3\text{O}_4^{\text{heptOH}}$ only.

As a parallel control experiment, the assembly of the hybrid dyad was attempted in the aqueous $\text{NaHCO}_3/\text{Na}_2\text{SiF}_6$ buffer in the absence of light and persulfate. By stirring a suspension of the $\text{Co}_3\text{O}_4^{\text{heptOH}}$ particles in the presence of 0.1 equivalents of KuQ3P, discoloring of the initially red dye liquid phase was observed after several hours. ICP analysis of the solid and liquid phases suggested that the phosphonate dye had quantitatively bound to the cobalt oxide particles, thus generating a hybrid dyad (see the Experimental Section of the present Chapter for details). Consistent observations were garnered by HR-TEM and XAS (data not shown). It was then concluded that the inability of the system produced by mixing the separately added components to display catalytic activity

could be attributed to a faster dye degradation preventing *in situ* formation of the hybrid in the reaction environment.

ICP analysis of the reaction mixtures after irradiation of suspensions of $\text{KuQ3P}_n@\text{Co}_3\text{O}_4^{\text{heptOH}}$ revealed the presence of phosphorus, deriving from the KuQ3P , only in the liquid solution. These findings suggested that deactivation of the photocatalytic system is related to the detachment of KuQ from $\text{Co}_3\text{O}_4^{\text{heptOH}}$. Given the colorless nature of the liquid phase, the simple decoordination of the deeply colored water-soluble KuQ3P was excluded. The hypothesis that the molecular structure of the KuQ could be altered during photolysis leading to loss of the anchoring chain was then considered. However, no species displaying the spectroscopic features of the KuQ chromophore could be recovered by solvent extraction of the liquid phase with dichloromethane. Therefore, we hypothesized that the transformation of the dye involves contextual loss of the side chain and disruption of the chromophore core.

Consistent examination of the particles after photocatalysis by TEM, HR-TEM, and XAS showed the disappearance of the features associated with the grey matter containing the single atoms, with a particle diameter increase to *circa* 5 nm. Briefly (Figure 108), the XANES of the starting $\text{Co}_3\text{O}_4^{\text{heptOH}}$ is partially recovered for the material after catalysis, with a shift of the edge and of the white line suggestive of a higher degree of oxidation of the cobalt centers, in particular of Co^{II} to Co^{III} . The FT-EXAFS displays signals indicative of the Co-Co distance recovered after catalysis; overall, the spectrum matches with $\text{Co}_3\text{O}_4^{\text{heptOH}}$ albeit with a shorter Co-Co distance, coherent with a higher fraction of Co^{III} ions. It is therefore possible to propose that, after photocatalysis, the alleged molecular, single-atom Co species are not observable.

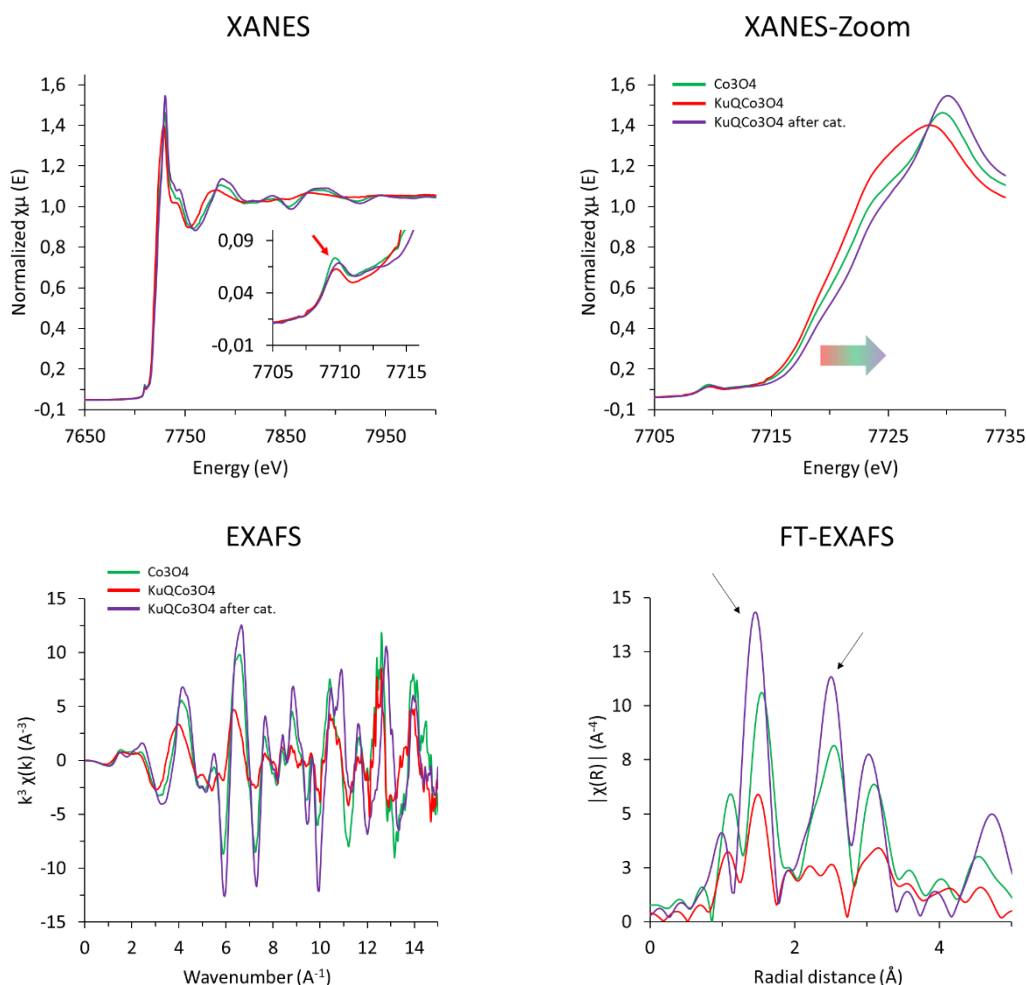


Figure 108. XANES (top) and EXAFS (bottom) of pristine KuQ3P_{0.1}@Co₃O₄^{heptOH} (red traces), Co₃O₄^{heptOH} (green traces) and KuQ3P_{0.1}@Co₃O₄^{heptOH} after photocatalysis (violet traces).

These considerations combined point to a chemical disruption of the hybrid dyads in the aggressive environment found in photocatalysis. Deactivation of the photocatalytic hybrid system could reasonably be ascribed to bleaching of the organic dye, usually regarded as the weak point of a dyad composed by inorganic, nanoparticulate and organic, molecular units. Dye decomposition would also account for decomposition of the single-atom species, in turn generated upon dye binding to Co₃O₄^{heptOH}. Further dye decomposition studies are being planned to

probe the hypothesis of a decomposition route based on the attack of KuQ by sulfate radicals ($\text{SO}_4^{\cdot -}$) formed upon cleavage of the persulfate peroxy bridge.

5.4 Photophysical studies on the hybrid particles

The photocatalytic reaction mechanism was further studied *via* fluorescence quenching experiments by Prof. Mirco Natali (University of Ferrara). Briefly, it was found that fluorescence of KuQ in the dyads is strongly quenched by $\text{Co}_3\text{O}_4^{\text{heptOH}}$, thus suggesting a fast quenching process from the cobalt oxide. This is consistent with previous findings indicating that the highly oxidizing excited state of KuQ dyes displays a high tendency to undergo reductive quenching (with concomitant oxidation of $\text{Co}_3\text{O}_4^{\text{heptOH}}$). The residual emission observed was ascribed to possible dye detachment, due to the same lifetime of the excited state of KuQ in the hybrid as in the free state (0.50 ns). The failure to observe any other emission lifetime suggests that ET from Co_3O_4 to KuQ^* is extremely fast (< 0.2 ns, the instrumental limit of the setup, corresponding to a quenching constant $k > 5 \cdot 10^9 \text{ s}^{-1}$). Conversely, neither ^1KuQ nor ^3KuQ quenching by persulfate was observed, thus supporting the role of ^1KuQ reductive quenching by the WOC. Thus, we proposed a mechanism for the photocatalytic cycle, in which catalysis is initiated by light absorption by the KuQ to produce the singlet excited state ^1KuQ , then involved in oxidation of the cobalt oxide catalyst (Figure 109).

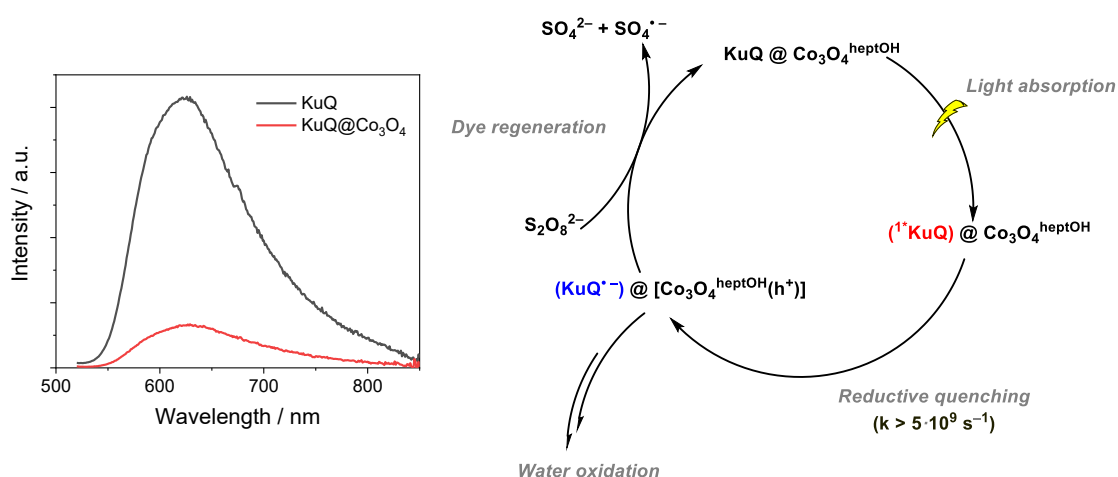


Figure 109. Left: emission quenching experiments registered for the free KuQ3P dye (black trace) and $\text{KuQ3P}_{0.2}@\text{Co}_3\text{O}_4^{\text{heptOH}}$ (red trace), registered in $\text{NaHCO}_3/\text{Na}_2\text{SiF}_6$ (pH 5.2) electrolyte. $\lambda_{\text{exc}} = 355 \text{ nm}$. Inner filter scattering effect is reasonably negligible.

Right: proposed photocatalytic cycle for the OER by the $\text{KuQ3P}_n@\text{Co}_3\text{O}_4^{\text{heptOH}}$.

Previous studies on electrodes produced by sensitizing SnO_2 with KuQ3C and adding a ruthenium polyoxometalate catalyst support our hypothesis that a reductive quenching mechanism could be active also on our photoanodes.

We then aimed at translating the proven reactivity of the dye-catalyst hybrids in photocatalysis to a SnO_2 semiconductor, developing a regenerative photoanode while getting rid of the persulfate electron acceptor.

5.5 $\text{KuQ3P}_n@\text{Co}_3\text{O}_4^{\text{heptOH}}$ on *meso*- SnO_2 : hybrid dyads for photoelectrochemical water oxidation

We then focused on producing the photoanodes based on the hybrid dyads. *Meso*- SnO_2 was chosen as the SCO due to its low conduction band edge, with an increased driving force for charge injection with respect to TiO_2 . Incidentally, however, it was reported that also recombination kinetics are much faster in SnO_2 sensitized films, thus counteracting the benefits provided by the greater driving force for injection.²⁶⁸ Nonetheless, optimized photoanodes based on sensitization

with KuQ3P and KuQ3C were obtained with *meso*-SnO₂ as the SCO.²⁶⁷ This was our substrate of choice also in the current project. SCO films were prepared by Dr. Giulia Alice Volpato (University of Padova) by blade-coating on FTO a paste of colloidal tin oxide, then thermally treated and sintered to produce mesoporous films with 2 μm thickness.²⁶⁹ Dropcasting of colloidal suspensions of the KuQ3X_n@Co₃O₄^{heptOH} particles in distilled THF afforded the photoelectrodes. In order to have a point of comparison between the hybrids, we decided to introduce an amount of particles to attain the same *nominal* dye loading, *i.e.* the same number of dye molecules in all cases (140 nmol_{dye}cm⁻²). The calculations were based on the formal molar weights of the hybrids and the nominal dye molar amount as per the ICP data. The electrodes were then tested in a three-electrode, one-compartment photoelectrochemical cell constituted by a silver/silver chloride (3 M NaCl) reference electrode (RE), a glassy carbon counter electrode (CE), and FTO/SnO₂/KuQ3X_n@Co₃O₄^{heptOH} as the working electrodes (WE). The incident light intensity was measured for each electrode with a silicon photodiode connected to a multimeter. A long-pass filter ($\lambda > 400$ nm) was employed to cut the UV radiation and avoid direct band excitation.

Initially, the photoelectrodes were tested by cyclic (CV) voltammetry in aqueous NaHCO₃/Na₂SiF₆ (pH 5.8) electrolyte. The materials displayed the electrochemical features of cobalt oxide-based electrocatalysts for the OER, specifically an electrocatalytic discharge on the forward scan, associated with water oxidation²⁴⁴ (with an onset potential of *circa* 0.8 V vs Ag/AgCl), and the reduction of the cobalt centres (as two ill-defined peaks at 0.63 ÷ 0.77 V vs Ag/AgCl) to restore the starting form of the oxide on the backwards scan (Figure 110).

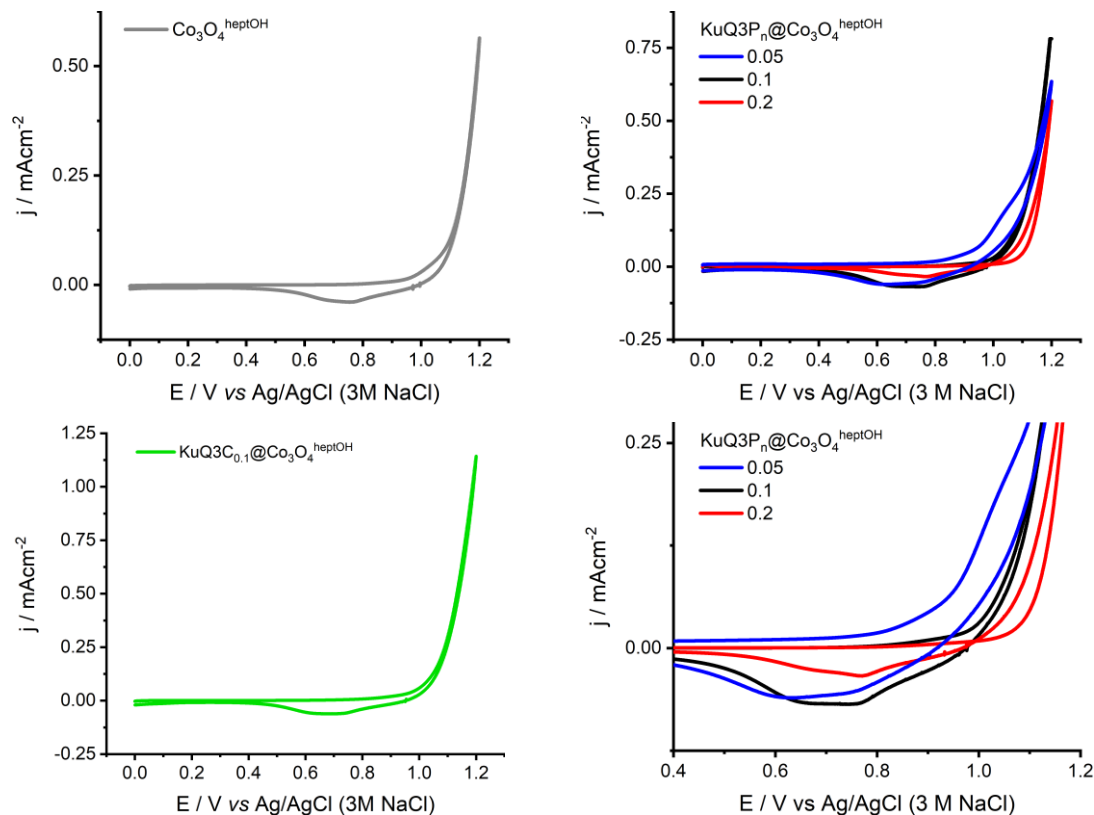


Figure 110. CV traces of $\text{Co}_3\text{O}_4^{\text{heptOH}}$ -based particles deposited on FTO/SnO₂ electrodes, registered in $\text{NaHCO}_3/\text{Na}_2\text{SiF}_6$ (pH 5.8) electrolyte, scan rate 0.020 Vs^{-1} . Top left (gray trace): $\text{Co}_3\text{O}_4^{\text{heptOH}}$; bottom left (green trace): $\text{KuQ3C}_{0.1}@ \text{Co}_3\text{O}_4^{\text{heptOH}}$; right: $\text{KuQ3P}_n@ \text{Co}_3\text{O}_4^{\text{heptOH}}$ ($n = 0.05$, black trace; 0.1 , blue trace; 0.2 , red trace). The inset (bottom right) focuses on the return scan.

Interestingly, the hybrid particles display anodic discharges which shift anodically as the amount of KuQ3P in the shell of $\text{Co}_3\text{O}_4^{\text{heptOH}}$ increases (Figure 109). Moreover, $\text{KuQ3P}_{0.05}@ \text{Co}_3\text{O}_4^{\text{heptOH}}$ exhibits a pre-wave peaking at $1.05 \text{ V vs Ag/AgCl}$ that is absent for $\text{KuQ3P}_{0.1+0.2}@ \text{Co}_3\text{O}_4^{\text{heptOH}}$. The voltammetric trace of $\text{KuQ3P}_{0.2}@ \text{Co}_3\text{O}_4^{\text{heptOH}}$, on the other hand, is characterized by reproducible curve crossing at $1.00 \text{ V vs Ag/AgCl}$, which is retained after the first cycle. The attribution of such features was not attempted, however likely residing in the surface modification of $\text{Co}_3\text{O}_4^{\text{heptOH}}$ upon KuQ3P binding.

The photoanodes were analyzed by open-circuit chronopotentiometry (OCCP) under irradiation (Figure 111). Incidentally, the electrodes were illuminated

through the back contact, to minimize the exciton travel length. In experiments under irradiation, the electrodes were illuminated by a Xe short-arc lamp, with a nominal irradiance of 1 Sun (100 mWcm^{-2}). OCCP was performed by measuring the open-circuit potential (V_{OC}) as a function of the irradiation time. Irradiation was sustained for 120 s, then the potential was recorded for 30 s in the dark. The substantial voltage drop under illumination ($173 \div 189 \text{ mV}$) and the slow recovery trace in the dark both indicate an effective mobilization of charge carriers in the SnO_2 film upon light absorption by the photoelectrode. Electrodes prepared with unsensitized $\text{Co}_3\text{O}_4^{\text{heptOH}}$ display a much lower voltage drop (82 mV) and a fast recovery trace, with V_{OC} rapidly reaching its pristine value in less than 30 s. Incidentally, the open circuit potential of the photoelectrode is dependent on the ratio between the rate of charge injection and charge recombination according to Eq. 49.^{219,220}

$$V_{OC} \propto \frac{k_B T}{e} \ln \left(\frac{\text{rate}_{\text{charge in}}}{\text{rate}_{\text{charge out}}} \right) \quad (\text{Eq. 49})$$

Where k_B is the Boltzmann constant ($1.380649 \cdot 10^{-23} \text{ JK}^{-1}$), T the temperature in Kelvin, e the elemental charge ($1.602 \cdot 10^{-19} \text{ C}$) and $\text{rate}_{\text{charge in}}$ and $\text{rate}_{\text{charge out}}$ the rates of charge injection and recombination, respectively.

The observed decrease of V_{OC} under illumination indicates a positive shift of the quasi-Fermi level of the electrons in SnO_2 , in turn corresponding to a greater relative rate of charge injection under illumination conditions when the dye is present.

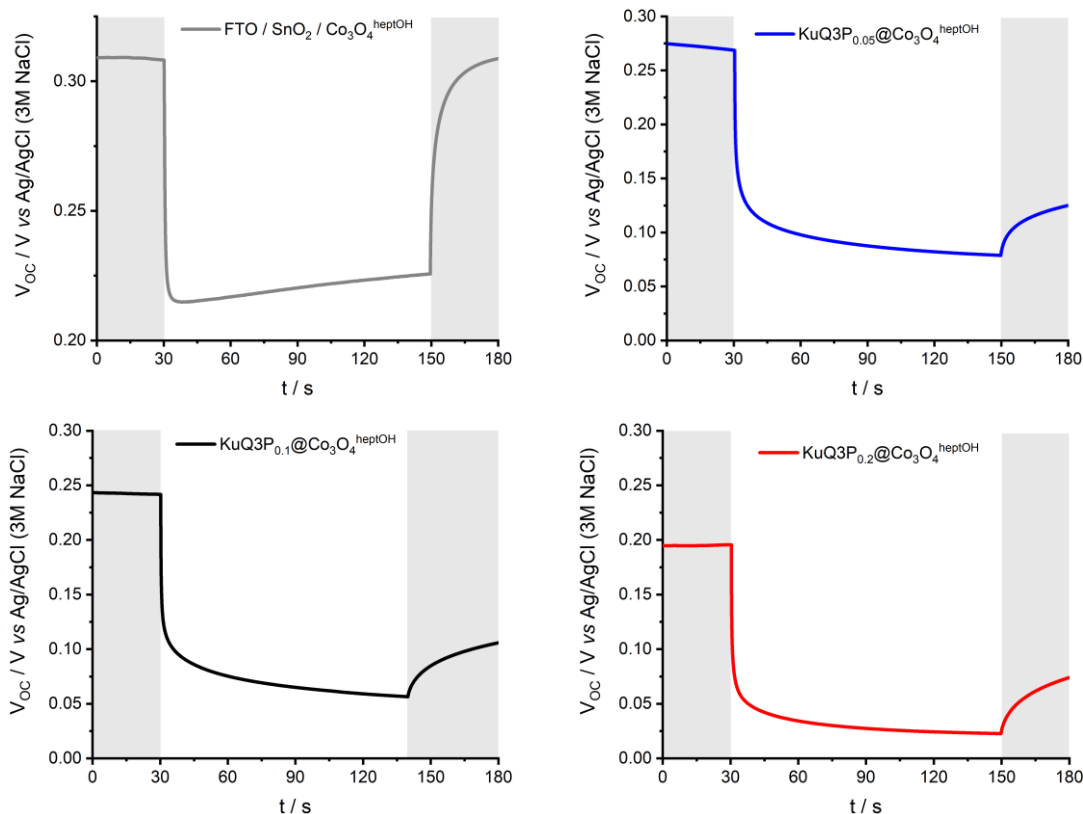


Figure 111. Open-circuit chronopotentiograms recorded in the dark (30 s), under illumination (120 s), and in the dark after illumination (30 s). Top left (gray trace): $\text{Co}_3\text{O}_4^{\text{heptOH}}$; top right (blue trace): $\text{KuQ3P}_{0.05}@\text{Co}_3\text{O}_4^{\text{heptOH}}$; bottom left (black trace): $\text{KuQ3P}_{0.1}@\text{Co}_3\text{O}_4^{\text{heptOH}}$; bottom right (red trace): $\text{KuQ3P}_{0.2}@\text{Co}_3\text{O}_4^{\text{heptOH}}$. Measurements were recorded in $\text{NaHCO}_3/\text{Na}_2\text{SiF}_6$ (pH 5.8) electrolyte.

The voltammetric profile was analyzed by comparing cyclic voltammograms under dark, intermittent and continuous illumination. In all cases but the latter, the return scan was acquired without illuminating the photoanode. The discussion herein provided will focus on $\text{KuQ3P}_{0.2}@\text{Co}_3\text{O}_4^{\text{heptOH}}$ as a representative of the hybrids (Figure 112). Under continuous illumination, a pseudo-diffusional couple is observed ($E_{p,a} = 0.35 \text{ V vs Ag/AgCl}$, $E_{p,c} = 0.21 \text{ V vs Ag/AgCl}$) that is completely absent in the dark trace. Moreover, in the forward trace under intermittent light the increase in photocurrent as the applied bias becomes more positive is associated to the progressive disappearance of recombination spikes past the anodic peak observed under continuous illumination. These observations are rationalized in

terms of mobilization of photoinjected charge carriers in SnO₂, displaying quasi-diffusional behaviour in the micrometer-thick semiconductor film. Indeed, the driving force for charge collection by the FTO contact increases with the applied bias after E_{p,a}, close in value to the conduction band edge of SnO₂ (~0.3 V vs Ag/AgCl).²⁶⁶

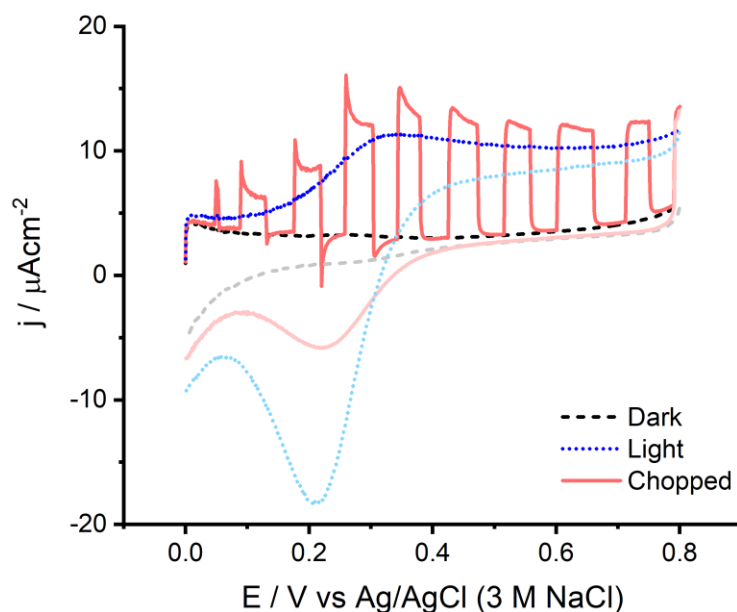


Figure 112. CV traces recorded for KuQ3P_{0.2}@Co₃O₄^{heptOH} in the dark (black, dashed trace) and under chopped (red, full trace) or continuous (blue, dotted trace), registered in NaHCO₃/Na₂SiF₆ (pH 5.8) electrolyte, scan rate 0.020 Vs⁻¹.

The electrodes were further studied by linear scan voltammetry (LSV) and chronoamperometry (CA) under intermittent illumination. LSV traces were recorded between 0.00 and 0.80 V vs Ag/AgCl, *i.e.*, in a less positive potential range than the one required for electrocatalytic OER by cobalt oxide (underpotential regime). The hybrids displayed higher photocurrent densities at every applied potential with respect to the unsensitized Co₃O₄^{heptOH} (Figure 113), suggesting the role of KuQ3P acting as the light harvester. Charge recombination, being a bias-dependent process, was not observable at potentials more positive than *circa* 0.3 V vs Ag/AgCl (conduction band edge of SnO₂, *vide supra*), as indicated by the disappearance of cathodic current spikes when interrupting the

irradiation. After an initial decay of the photocurrent, the segments recorded under illumination displayed nearly constant photocurrent densities of $10 \mu\text{Acm}^{-2}$. Incidentally, the initial photocurrent densities were higher for $\text{KuQ3P}_{0.1}@Co_3O_4^{\text{heptOH}}$ and $\text{KuQ3P}_{0.2}@Co_3O_4^{\text{heptOH}}$ (36 and $37 \mu\text{Acm}^{-2}$ at 0.2 V vs Ag/AgCl , respectively) than for $\text{KuQ3P}_{0.5}@Co_3O_4^{\text{heptOH}}$ ($16 \mu\text{Acm}^{-2}$ at 0.2 V vs Ag/AgCl).

A comparison with the photocatalytic reactions based on the maximum molar amount of evolved O_2 in photocatalytic experiments (*vide supra*) may be provided. However, given the intrinsic differences between photoanodes and colloidal photocatalytic reactions and the different criteria chosen to operate, caution is required. In particular, the photoelectrodes were prepared by keeping the nominal amount of KuQ dye constant, while the photocatalytic reactions were compared at the same mass concentration of colloidal catalyst. In the former case, photocurrent is proposed as a more operatively convenient indicator of the photoelectrochemical performance of the hybrid dyads. Notably, differences in the photocurrent trend ($\text{KuQ3P}_{0.2}@Co_3O_4^{\text{heptOH}} \approx \text{KuQ3P}_{0.1}@Co_3O_4^{\text{heptOH}} < \text{KuQ3P}_{0.05}@Co_3O_4^{\text{heptOH}}$) are observed in comparison with the hybrids studied in photocatalysis. The attribution of this observation is based on the higher number of electrons photoinjected in SnO_2 and therefore mobilized by $\text{KuQ3P}_{0.1}@Co_3O_4^{\text{heptOH}}$ and $\text{KuQ3P}_{0.2}@Co_3O_4^{\text{heptOH}}$, possessing a higher density of chromophore molecules in contact with the WOC particles than their poorer counterpart $\text{KuQ3P}_{0.05}@Co_3O_4^{\text{heptOH}}$.

to rest until its potential reached its original OCP value (~ 0.20 V vs Ag/AgCl) or by performing a 60 s CA in the dark at 0.00 V vs Ag/AgCl. Such finding indicates that the photocurrent decay is ascribable to a non-optimized managing of the mobilized charges upon light irradiation, rather than physical or chemical degradation of the device.

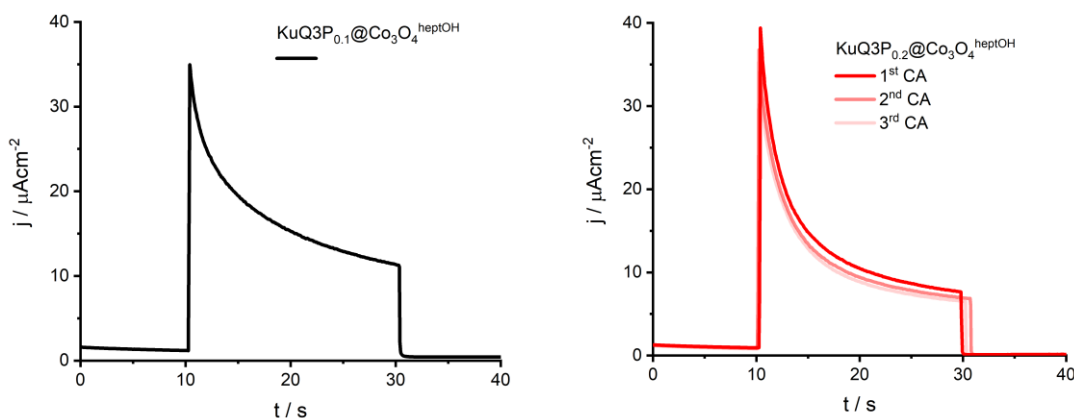


Figure 114. Chronoamperograms of $\text{KuQ3P}_{0.1}@Co_3O_4^{\text{heptOH}}$ (left, black trace) and $\text{KuQ3P}_{0.2}@Co_3O_4^{\text{heptOH}}$ (right, red traces), registered at 0.6 V vs Ag/AgCl in $\text{NaHCO}_3/\text{Na}_2\text{SiF}_6$ (pH 5.8) electrolyte.

Notably, $\text{KuQ3C}_{0.1}@Co_3O_4^{\text{heptOH}}$ also displays a modest photoelectrochemical activity, albeit its unremarkable performance in photocatalytic systems (Figure 115). The initial photocurrent densities at 0.6 V vs Ag/AgCl and their value after 20 s of illumination, 8 and $5 \mu\text{Acm}^{-2}$ respectively, are both much lower than for KuQ3P-based hybrids. The overall worse performance of $\text{KuQ3C}_{0.1}@Co_3O_4^{\text{heptOH}}$, displaying photocurrent densities only 50% greater than unsensitized $\text{Co}_3O_4^{\text{heptOH}}$, is attributable to a less stable dye-WOC interaction that impairs its usability, consistently with the photocatalytic trials.

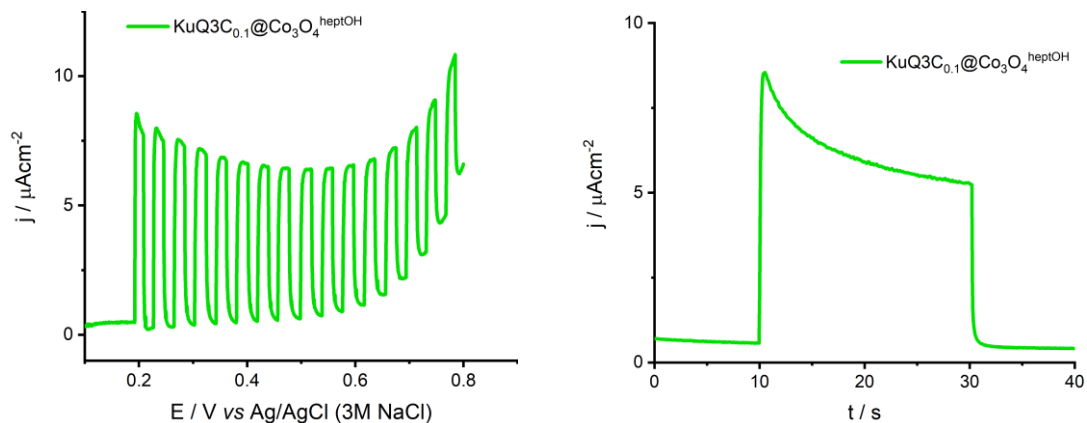


Figure 115. Left: LSV trace under chopped illumination of $\text{KuQ3C}_{0.1}@\text{Co}_3\text{O}_4^{\text{heptOH}}$, registered in $\text{NaHCO}_3/\text{Na}_2\text{SiF}_6$ (pH 5.8) electrolyte, scan rate 0.020 Vs^{-1} . Right: chronoamperogram of $\text{KuQ3P}_{0.1}@\text{Co}_3\text{O}_4^{\text{heptOH}}$ registered at 0.6 V vs Ag/AgCl in $\text{NaHCO}_3/\text{Na}_2\text{SiF}_6$ (pH 5.8) electrolyte.

5.6 Faradaic efficiency for the Oxygen Evolution Reaction

To assess whether the photocurrent response corresponded to oxygen evolution and to quantify the Faradaic efficiency (FE) of the supposed photoelectrocatalytic process, generator-collector chronoamperometric experiments were performed, the outcome of which is displayed in Figure 116. The setup used was the same described in previous reports by our group.^{239,266} Briefly, the collector electrode was an FTO slide poised at $-0.9 \text{ V vs Ag/AgCl}$, closely spaced from the photoanode to produce a thin layer of solution with a narrow length for the evolved O_2 to travel to reach the collector and be reduced. Further details are provided in the Experimental section of the present chapter. The FE of the process occurring at the generator was estimated upon integration of the charge passed at both electrodes during the experiment, after calibration of the amperometric sensor to determine its collection efficiency.

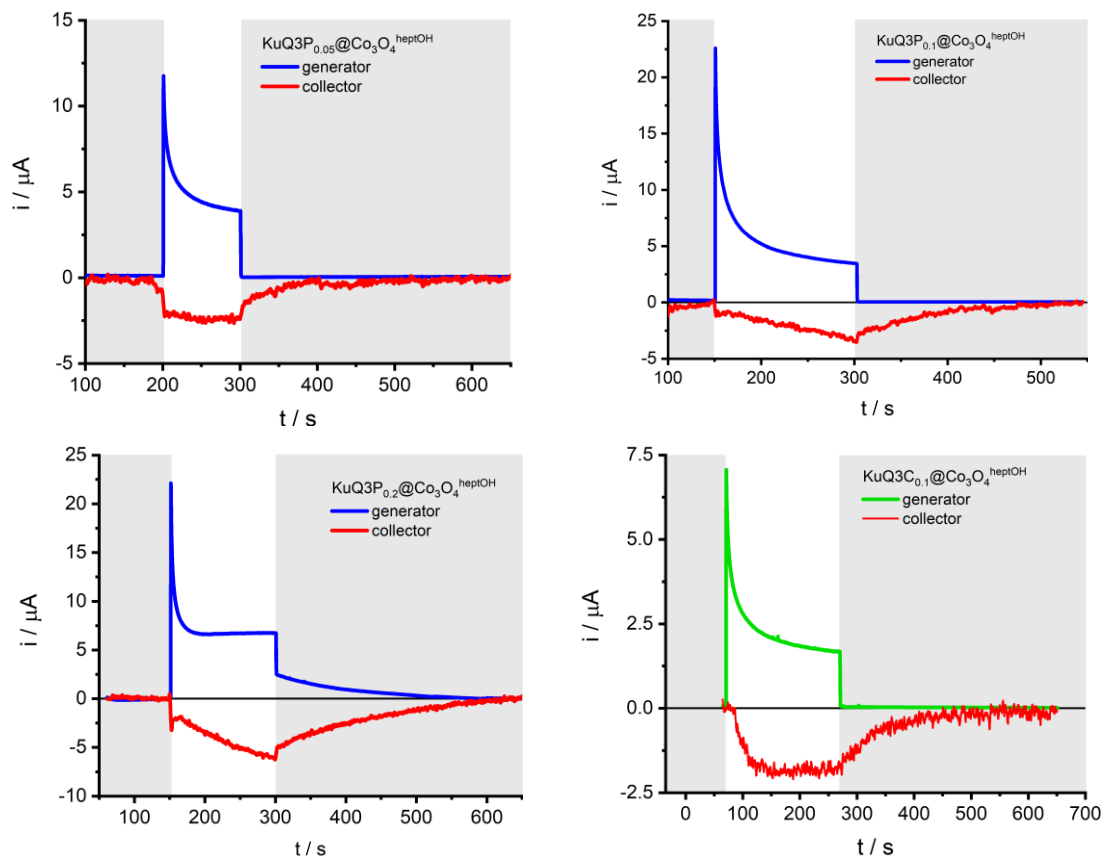


Figure 116. Chronoamperograms recorded in a two-plate generator-collector setup to detect evolved O_2 . Top left: $KuQ3P_{0.05}@Co_3O_4^{heptOH}$; top right: $KuQ3P_{0.1}@Co_3O_4^{heptOH}$; bottom left: $KuQ3P_{0.2}@Co_3O_4^{heptOH}$; bottom right: $KuQ3C_{0.1}@Co_3O_4^{heptOH}$. The generator was poised at 0.6 V vs Ag/AgCl, the collector was poised at -0.9 V vs Ag/AgCl, registered at 0.6 V vs Ag/AgCl in $NaHCO_3/Na_2SiF_6$ (pH 5.8) electrolyte.

The FE of the electrodes was determined to be close to 90% for almost all the hybrids except for $KuQ3P_{0.05}@Co_3O_4^{heptOH}$ (69%) (results are summarized in Table 8). Overall, the values observed are coherent with other DSPEC photoanodes containing organic dyes and cobalt oxide nanoparticles as the catalyst. Based on these results, the performance of the dyads may be compared based on photocurrent attained and FE values for the OER. Indeed, $KuQ3P_{0.1}@Co_3O_4^{heptOH}$ and $KuQ3P_{0.2}@Co_3O_4^{heptOH}$ display the best features among the series. The lower value observed for $KuQ3P_{0.05}@Co_3O_4^{heptOH}$ might be related to the non-catalytic pre-wave feature observed in the CV without

illumination. Notably, an 87% FE was determined for $\text{KuQ3C}_{0.1}@\text{Co}_3\text{O}_4^{\text{heptOH}}$ supports the potential applicability of this hybrid as photoactive dyad, albeit suffering from a less stable dye-chromophore interaction.

5.7 Photoelectrochemical response under monochromatic illumination

The response of the photoanodes was analyzed under monochromatic irradiation to positively ascribe the photocurrent to the presence of the KuQ3P chromophores. A 150 W Xe short-arc lamp was thus coupled to a monochromator and several chronoamperometries were recorded at 0.6 V vs Ag/AgCl, irradiating the electrode with wavelengths spaced by 10 nm. The photoaction spectrum of the electrodes was recorded in terms of the incident photon-to-current conversion efficiency (IPCE) as a function of the wavelength of the incident light. The power of the latter was independently measured with a photodiode.

From the shape of the photoaction spectrum, it is possible to discern information about the species imparting photoactivity to the electrode, *i.e.*, the dye (Figure 117). In the specific case, low IPCE values were determined (IPCE = 0.44% at 510 nm for $\text{KuQ3P}_{0.2}@\text{Co}_3\text{O}_4^{\text{heptOH}}$), but the IPCE spectra matched well with the optical spectrum of the KuQ dyes. The low values of IPCE are ascribable to the modest photocurrents and to the nature of the electron transfer events occurring through the photoactive ink deposit on SnO_2 . Specifically, inter-particle and therefore inter-chromophore interactions could play a detrimental role (*vide infra*). The observed values are consistent with the previously reported $\text{SnO}_2/\text{KuQ}/\text{Ru}_4(\text{POM})$ photoanodes, reaching IPCE up to 0.12%.²⁶⁶

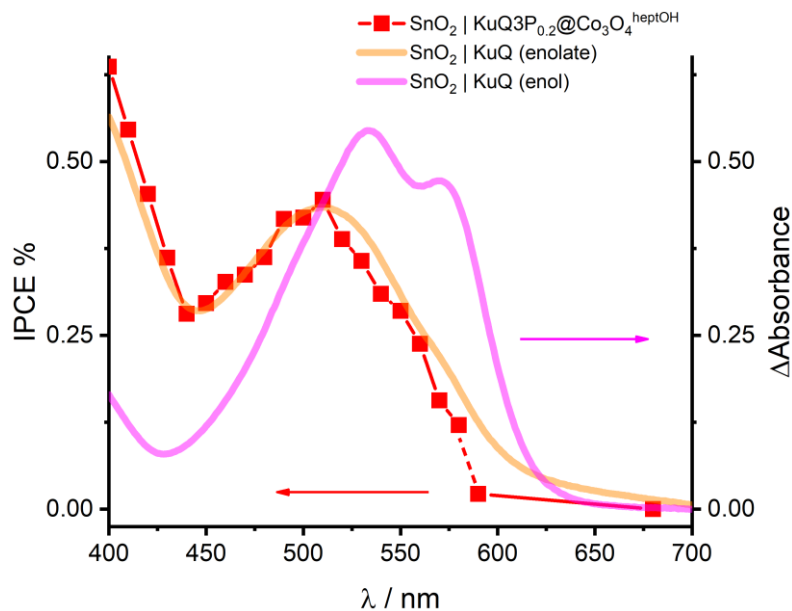


Figure 117. IPCE photoaction spectrum (red squares) for FTO/SnO₂/KuQ3P_{0.2}@Co₃O₄^{heptOH} photoanodes, superimposed to the absorption spectra of FTO/SnO₂/KuQ3C electrodes with the dye in the enolate (orange trace) and enol (magenta trace) forms. Chronoamperometries were registered at 0.6 V vs Ag/AgCl in NaHCO₃/Na₂SiF₆ (pH 5.8) electrolyte.

Additionally, the operational chemical state of the dye in the dyad could be determined indirectly from the photoaction spectrum: KuQ dyes can in fact partake in keto-enol tautomerism and enol-enolate equilibria at the level of the pentacyclic core depending on its protonation state, the enol and enolate forms displaying different optical spectra. Indeed, IPCE spectra support the KuQ3P chromophore in its enolate form in the dyads, as discussed below.

As a complementary experiment, the photoaction spectrum was recorded with monochromatic LED light sources, to provide a higher power of incident light especially in the low-energy spectral range, where the photocurrent response of the electrodes is minimum. The analysis was performed with four LED's, at 680, 590, 530, and 490 nm. The IPCE spectrum restricted to this region matched unequivocally with the optical absorption of KuQ dyes in their enolate form, further

supporting the hypothesis that the enolate state of KuQ3P is involved in the hybrid dyad formation; points at 680 and 590 nm are included in Figure 117.

5.8 Comparison with SnO₂/KuQ/Co₃O₄^{heptOH} photoanodes

A key comparison with the “unbound” system, *i.e.* a photoanode constituted by sensitized SnO₂ and unsensitized Co₃O₄^{heptOH} (FTO/SnO₂/KuQ3C/Co₃O₄^{heptOH}) is required to assess the advantages of the hybrid dyads. Indeed, such advantages have already been discussed in terms of performance of photocatalytic systems. However, the intrinsically different reaction symmetry of a photoelectrode calls for a dedicated investigation: the proximity between the dye and the catalyst should in principle allow for a functional photoelectrochemical device despite the lack of a direct chemical interaction between KuQ and the WOC. The use of KuQ3C for sensitizing SnO₂ was chosen because of the optimal binding and electronic communication between SnO₂ and KuQ3C over KuQ3P granted by the carboxylate linker, as was reported by Volpato *et al.*²⁶⁶ Photoanodes were prepared by soaking FTO/SnO₂ electrodes in a 0.11 mM KuQ3C solution in THF for 24 h. After soaking, SnO₂ displayed an orange colour, due to binding of KuQ3C in its enolate form generated upon deprotonation of the enol group by SnO₂. The films were subsequently treated with aqueous H₂SO₄ (pH 2) to convert the dye to its pink, enol form, and dried. The photoelectrodes were characterized by optical absorption spectroscopy. Dye loading was estimated to be (140 nmolcm⁻²) by spectroscopic analysis. The spectroscopic features of the dyes were identified both in the enolate, orange form (λ_{\max} 510 nm) and in the enol, pink state (λ_{\max} 533 nm, 570 nm), Figure 118. The two absorption maxima displayed by electrodes obtained after acidic treatment were red-shifted with respect to solutions of KuQ, with a worse-resolved character of the peaks. Both observations were attributed to dye aggregation on the SCO film. Indeed, KuQ-functionalized photoanodes rely on π -stacking of dye molecules constituting a locally hydrophobic layer^{266,267} that prevents spontaneous deprotonation of the dye molecules (pK_a 4.7)²⁶⁵ in the electrolyte solution.

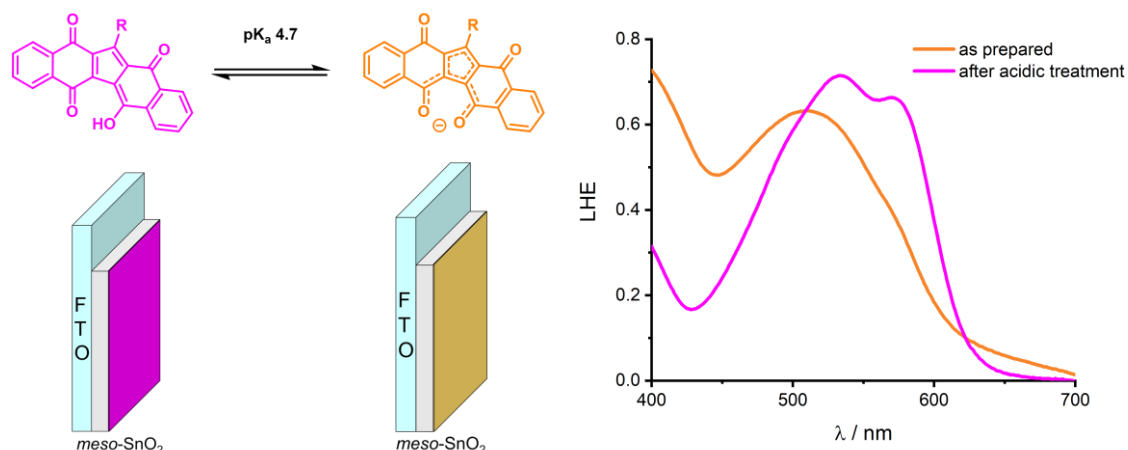


Figure 118. Left: acid-base equilibrium involving the enol (pink) and enolate (orange) forms of KuQ, occurring both in solution and on the electrodes. Right: electronic absorption spectra expressed as a function of LHE for FTO/SnO₂/KuQ3C electrodes containing the enolate (orange trace) and enol (pink trace) of the dye.

The photoanodes, displaying 70% LHE at 533 nm, were functionalized by dropcasting a 2.18 mg/mL suspension of Co₃O₄^{heptOH} in methanol, to attain a nominal dye : WOC 1:10 molar ratio and reproduce the composition of KuQ3P_{0.1}@Co₃O₄^{heptOH}.

The SnO₂/KuQ3C and SnO₂/KuQ3C/Co₃O₄^{heptOH} electrodes were tested in photoelectrochemical conditions, in pH 5.8 NaHCO₃/Na₂SiF₆ electrolyte (Figure 119). The LSV trace of the sensitized electrodes in the absence of cobalt oxide displays a photocurrent trend analogous to that measured by LSV for the hybrid systems, albeit with higher photocurrent densities. CA at 0.6 V vs Ag/AgCl gave rise to initial photocurrent densities of 80 μAcm⁻², again rapidly decaying to a lower value (20 μAcm⁻²). The higher photocurrents observed than in the case of the hybrid particles are indeed ascribed to the direct chemical linkage between SnO₂ and the chromophore. As previously ascertained, the SnO₂/KuQ anodes are not kinetically able to perform the 4-electron water oxidation reaction to O₂: therefore, the photocurrent observed is to be ascribed to other photoinduced chemical processes. Substantial self-degradation or detachment of the dye on the timescale of the CA is excluded, given the restored photocurrent trace obtainable

upon depolarization of the electrode. Another possibility, previously formulated and not explored herein, might rely on the ability of KuQ dyes to manage PCET events that could be exploited in the 2-electron oxidation of H₂O to hydrogen peroxide.

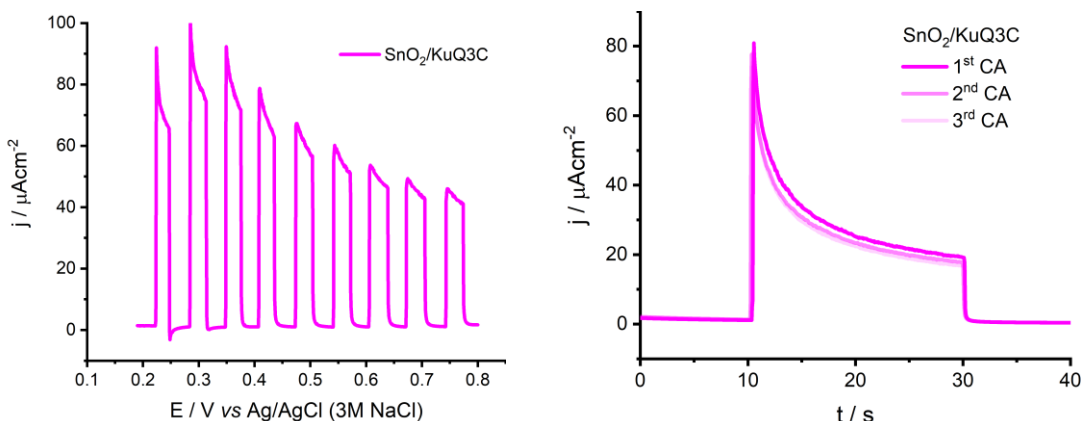


Figure 119. Left: LSV trace under chopped illumination of FTO/SnO₂/KuQ3C photoelectrodes, registered in NaHCO₃/Na₂SiF₆ (pH 5.8) electrolyte, scan rate 0.020 Vs⁻¹. Right: chronoamperogram of FTO/SnO₂/KuQ3C photoelectrodes registered at 0.6 V vs Ag/AgCl in NaHCO₃/Na₂SiF₆ (pH 5.8) electrolyte.

Regardless, the “unbound” photoanodes loaded with unsensitized Co₃O₄^{heptOH} displayed a markedly different photoelectrochemical behaviour. Incidentally, their preparation resulted in physically stable electrodes in the electrolyte solution, leaching of cobalt oxide particles being likely prevented by the hydrophobic 1-heptanol shell. The voltammetric profile and the CA traces registered under irradiation reproducibly exhibited a decrease in photocurrent densities upon introduction of Co₃O₄^{heptOH}. Specifically (Figure 120), the photocurrent densities observed at 0.2 V vs Ag/AgCl (34 μAcm⁻²) and 0.6 V vs Ag/AgCl (20 μAcm⁻²) were found significantly lower than in the case of the FTO/SnO₂/KuQ3C electrodes (95 and 60 μAcm⁻², respectively, see Figure 119).

Such observation may be rationalized upon invoking the high WOC loading on the photoelectrode. The presence of catalyst particles in fact introduces electron scavenging sites that may result, assuming the aforementioned reductive

quenching mechanism, in back electron transfer from $\text{KuQ}^{\cdot-}$ to the oxidized $\text{Co}_3\text{O}_4^{\text{heptOH}}$. The somewhat counterintuitive anti-catalytic effect of the presence of the catalyst on the photocurrent is therefore justified. The introduction of a catalyst able to selectively (*vide supra*) drive the kinetically demanding OER process may also contribute to the drop in photocurrent albeit through its productive mechanism. Not only electrons funnelled in the circuit travel through a more complicated ET chain, but also they are garnered upon the slow water oxidation reaction. As a corollary, Finke and co-workers reported that a further detrimental role might be played by “carbon impurities” introduced by either dye or WOC deposition on SnO_2 , this SCO being particularly affected by C-based recombination sites. However, this aspect was not experimentally investigated for the $\text{KuQ}/\text{Co}_3\text{O}_4^{\text{heptOH}}$ system.²⁷⁰

A notable result are the comparable photocurrents obtained for the “unbound” $\text{SnO}_2/\text{KuQ3C}/\text{Co}_3\text{O}_4^{\text{heptOH}}$ photoanodes with respect to the hybrid systems ($\text{SnO}_2/\text{KuQ3P}_n@\text{Co}_3\text{O}_4^{\text{heptOH}}$). Indeed, no distinct comparison between the systems may be provided at the present stage. To acquire evidence for the alleged beneficial direct chemical link between the dye and the WOC, the photogenerated charge management by the system was targeted. In fact, the Faradaic efficiency for the oxygen evolution reaction promoted by the $\text{SnO}_2/\text{KuQ3C}/\text{Co}_3\text{O}_4^{\text{heptOH}}$ photoanodes was determined as $< 50\%$ *via* generator-collector experiments. This result provides the underlying interpretation of the otherwise enigmatic photoelectrochemical response of the compared systems. The higher Faradaic efficiency observed for the $\text{KuQ3P}_n@\text{Co}_3\text{O}_4^{\text{heptOH}}$ suggests that the direct chemical interaction between the WOC particles and the dye shell surrounding their surface is the basis for a more efficient management of the electron transfer chain. This is especially relevant in the framework of a mechanism based on dye emission quenching by the WOC, in which the chemical link is suggested to constitute a preferential ET pathway.

related anthraquinone dye alizarin, albeit with smaller (five- or six-membered) metallacycles in this latter case. Incidentally, the chemical binding interaction was found to be rather weak, apolar organic solvents being able to easily dissolve the dye deposit. Regardless, the electrodes were subjected to acidic treatment without previous examination of the photoelectrochemical response of the KuQ enolate-functionalized SnO₂. Upon immersing the electrodes in aqueous H₂SO₄ (pH 2), they turned deep purple, displaying a broad spectral feature indicative of the enol form (λ_{max} 584 nm, LHE 90%; 540 nm, LHE 94%, Figure 121). The ill-defined vibronic structure of the dye is indicative of higher aggregation degree of KuQ-Hex with respect to KuQ3C.

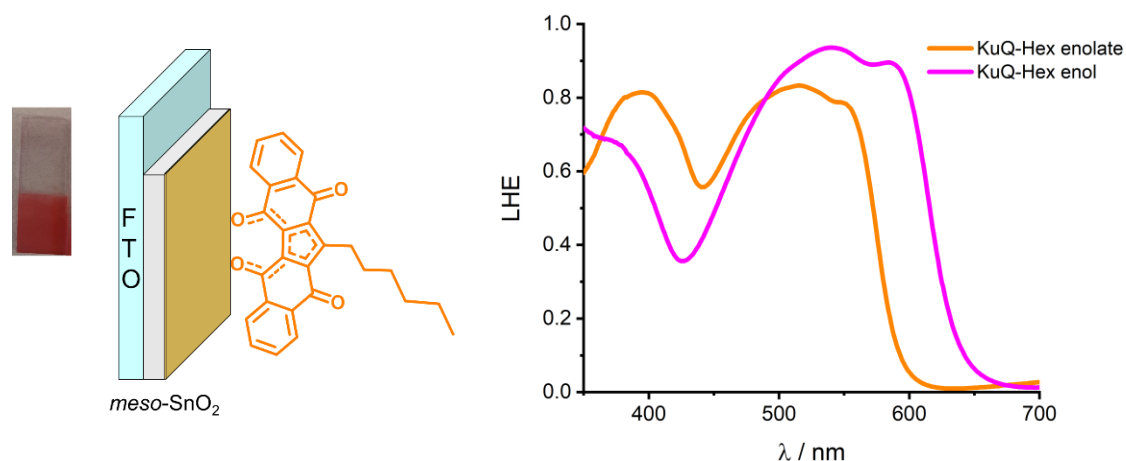


Figure 121. Left: picture of the FTO/SnO₂/KuQ-Hex photoelectrodes as obtained by soaking, displaying KuQ-Hex in its orange form (before treatment with H₂SO₄). The putative binding mode of the dye to SnO₂ is schematically shown. Right: electronic absorption spectra expressed as a function of LHE for FTO/SnO₂/KuQ-Hex electrodes containing the enolate (orange trace) and enol (pink trace) of the dye.

The electrodes were studied by LSV in a pH 5.8 0.1 M ascorbic acid/sodium ascorbate electrolyte, to probe the ability of KuQ-Hex to photoinject electrons in the conduction band of SnO₂ in the presence of a sacrificial agent (Figure 122). The voltammetric trace in ascorbate electrolyte exhibits square-shaped segments under irradiation, superimposed to the dark oxidation current of ascorbate at the

electrode. Indeed, photocurrent densities measured at 0.1 V vs Ag/AgCl in the presence of ascorbate ($130 \mu\text{Acm}^{-2}$) are 40% of those reported for KuQ3C.²⁶⁷ Similarly lower photocurrents were observed for SnO₂/KuQ-Hex photoanodes in NaHCO₃/Na₂SiF₆ (pH 5.8) electrolyte ($60 \mu\text{Acm}^{-2}$ at 0.2 V vs Ag/AgCl and $22 \mu\text{Acm}^{-2}$ at 0.6 V vs Ag/AgCl).

These much lower values are indicative of a lower injection efficiency by KuQ-Hex. The reasons underlying the lower ϕ_{inj} are likely related to:

- i) The higher aggregation of the dye molecules, providing more prominent thermal relaxation route for KuQ-Hex*.
- ii) The alleged lack of a direct chemical linkage between KuQ-Hex and SnO₂. Indeed, despite the possible binding of KuQ-Hex *via* its enolate groups, it is believed that the enol form would be less prone to form a chemical bond with the SCO.

In addition, the presence of a dye film characterized by substantial aggregation, especially relevant for planar aromatic dyes, can pose a further barrier for electron diffusion towards the TCO.

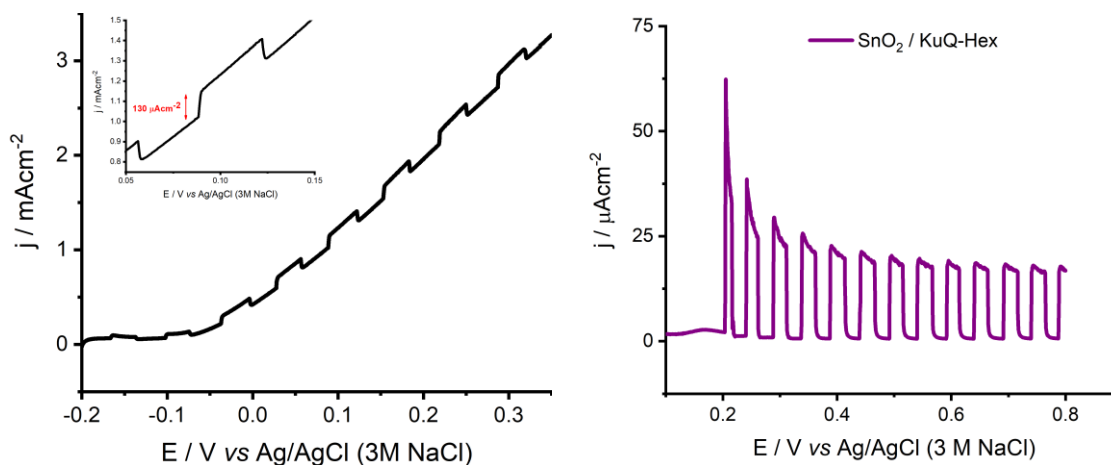


Figure 122. LSV traces of FTO/SnO₂/KuQ-Hex photoelectrodes registered in 0.1 M ascorbate (pH 5.8) electrolyte (left) and in NaHCO₃/Na₂SiF₆ (pH 5.8) electrolyte (right).

Scan rate 0.020 Vs^{-1} .

5.10 Further insights and future perspectives

The discussion so far highlights the potential application of the catalytic dyads herein described for the constitution of water-oxidizing photoanodes. The dyads, composed of an organic polyquinoid dye and a first-row transition metal oxide, represent a completely rare-metal free catalytic component able to act as catalysts for the water oxidation reaction both in photocatalytic colloidal systems and in the photoanodic unit of photoelectrochemical cells. Further studies will be undertaken to understand the nature of the dye- $\text{Co}_3\text{O}_4^{\text{heptOH}}$ interaction more in depth. Specifically, XAS and resonance Raman spectroscopy experiments are currently being performed on the pristine hybrid particles and on the photoanodes, to determine the changes in chemical environment upon binding of the dye and possibly the influence of deposition and photoelectrocatalysis on the photoanodes. A possible advancement could be represented by the use of the dyads in dual-chromophore systems exploiting the photophysical and PCET management features of the KuQ shell as mediator of the electron transfer chain events.

Entry	j @ 0.2 V vs Ag/AgCl (μAcm^{-2})	j_{initial} @ 0.6 V vs Ag/AgCl (μAcm^{-2})	$j_{20\text{s}}$ @ 0.6 V vs Ag/AgCl (μAcm^{-2})	FE_{O_2} (%)	IPCE (%) @ 510 nm
$\text{KuQ3P}_{0.05}@\text{Co}_3\text{O}_4^{\text{heptOH}}$	16	6	3	69	–
$\text{KuQ3P}_{0.1}@\text{Co}_3\text{O}_4^{\text{heptOH}}$	36	34	11	88	0.20
$\text{KuQ3P}_{0.2}@\text{Co}_3\text{O}_4^{\text{heptOH}}$	37	33	6	87	0.44
$\text{KuQ3C}_{0.1}@\text{Co}_3\text{O}_4^{\text{heptOH}}$	16	8	5	87	–
$\text{SnO}_2 / \text{KuQ3C} / \text{Co}_3\text{O}_4^{\text{heptOH}}$	32	28	8	47	–

Table 8. Photoelectrochemical performance of $\text{FTO}/\text{SnO}_2/\text{KuQ3X}_n@\text{Co}_3\text{O}_4^{\text{heptOH}}$ and $\text{FTO}/\text{SnO}_2/\text{KuQ3C}/\text{Co}_3\text{O}_4^{\text{heptOH}}$ photoanodes.

A first optimization strategy would involve chemically bridging the SCO and the catalyst by appropriately designing the side chains of KuQ. However, this task should take into account the intrinsic borders of the synthetic space of

KuQuinones derivatives, that would limit the achievable variations to the side chain.

A second possibility would rely on the peculiar photoredox properties of KuQ. Specifically, its highly oxidizing excited state might suggest that the reactivity of the relatively long-lived radical anion formed on the photoelectrode surface upon reductive quenching could be exploited further. A concept to be explored is the use of $\text{KuQ3P}_n@ \text{Co}_3\text{O}_4^{\text{heptOH}}$ hybrids in catalytic amounts, in conjunction with pre-sensitized SCO films. These dual-chromophore systems (Figure 123), representable as $\text{SCO/dye/KuQ3P}_n@ \text{Co}_3\text{O}_4^{\text{heptOH}}$, should be designed by appropriate choice of organic dyes. These latter should in principle be predominantly reducing in their excited state and be chemically linked to the SCO directly, so to perform photoinjection by oxidative quenching. Therefore, the radical cation form of the dye would annihilate with $\text{KuQ}^{\cdot -}$ generated by the fast reductive quenching of $^1\text{KuQ3P}$ bound to the surface of $\text{Co}_3\text{O}_4^{\text{heptOH}}$. This dye-dye junction is expected to minimize charge recombination by means of a preferential ET chain guided by chemical bonds.

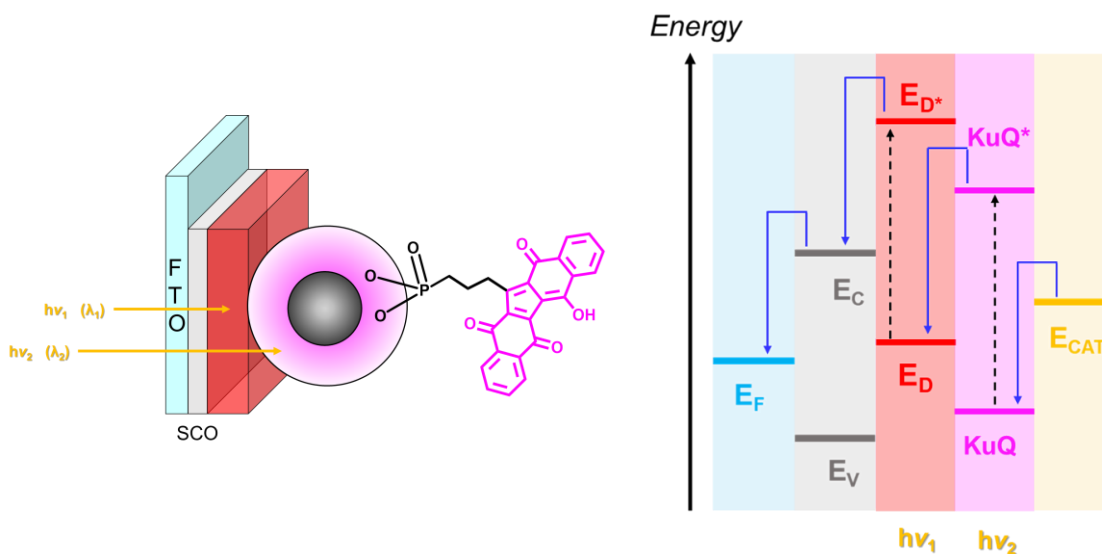


Figure 123. Left: schematic view of a dual-chromophore photoanode featuring a dye-sensitized SCO film and the $\text{KuQ3P}_n@ \text{Co}_3\text{O}_4^{\text{heptOH}}$ hybrids ($\text{SCO/dye/KuQ3P}_n@ \text{Co}_3\text{O}_4^{\text{heptOH}}$). Right: schematic energy levels of the component involved in such systems.

Preliminary attempts to study electrodes based on such concept of a dye-dye junction were undertaken by dropcasting catalytic amounts of $\text{KuQ3P}_{0.1}@\text{Co}_3\text{O}_4^{\text{heptOH}}$ and $\text{KuQ3P}_{0.2}@\text{Co}_3\text{O}_4^{\text{heptOH}}$ on $\text{SnO}_2/\text{KuQ3C}$ photoanodes. Indeed, higher photocurrent densities were observed with respect to $\text{SnO}_2/\text{KuQ3P}_n@\text{Co}_3\text{O}_4^{\text{heptOH}}$. CA registered at 0.6 V vs Ag/AgCl displayed initial photocurrent densities of $90 \div 100 \mu\text{Acm}^{-2}$, decaying to $20 \div 25 \mu\text{Acm}^{-2}$ over 20 s of illumination (Figur 123). However, operating the photoanodes resulted in a lowered photocurrent upon repeated studies, as may be appreciated by examining the voltammetric profile of these photoanodes under intermittent illumination. Over the course of the photoelectrode testing, a systematic gradual decrease in the attained photocurrents was observed, as per previous reports (Doctoral Thesis of Dr. Giulia Alice Volpato). By examining the electrodes after testing, a drastic colour change was observed. Indeed, the originally pink SnO_2 films displayed an orange colour (Figure 124), suggestive of KuQ3C deprotonation upon photoelectrochemical stress. This transformation was not observed for $\text{SnO}_2/\text{KuQ3C}$ photoanodes. It is therefore proposed that the presence of $\text{KuQ3P}_n@\text{Co}_3\text{O}_4^{\text{heptOH}}$ hybrids as WOC-based photoactive units induces a local disruption of the dye-sensitized KuQ3C film upon O_2 evolution. Enhanced access by the electrolyte, and therefore deprotonation of the KuQ3C film, has been suggested to allow for a change in its aggregation state. The locally more hydrophilic environment is proposed at the basis of dye desorption from SnO_2 , given the low hydrolytic stability of the carboxylate linker at the operational pH (see Table 7).

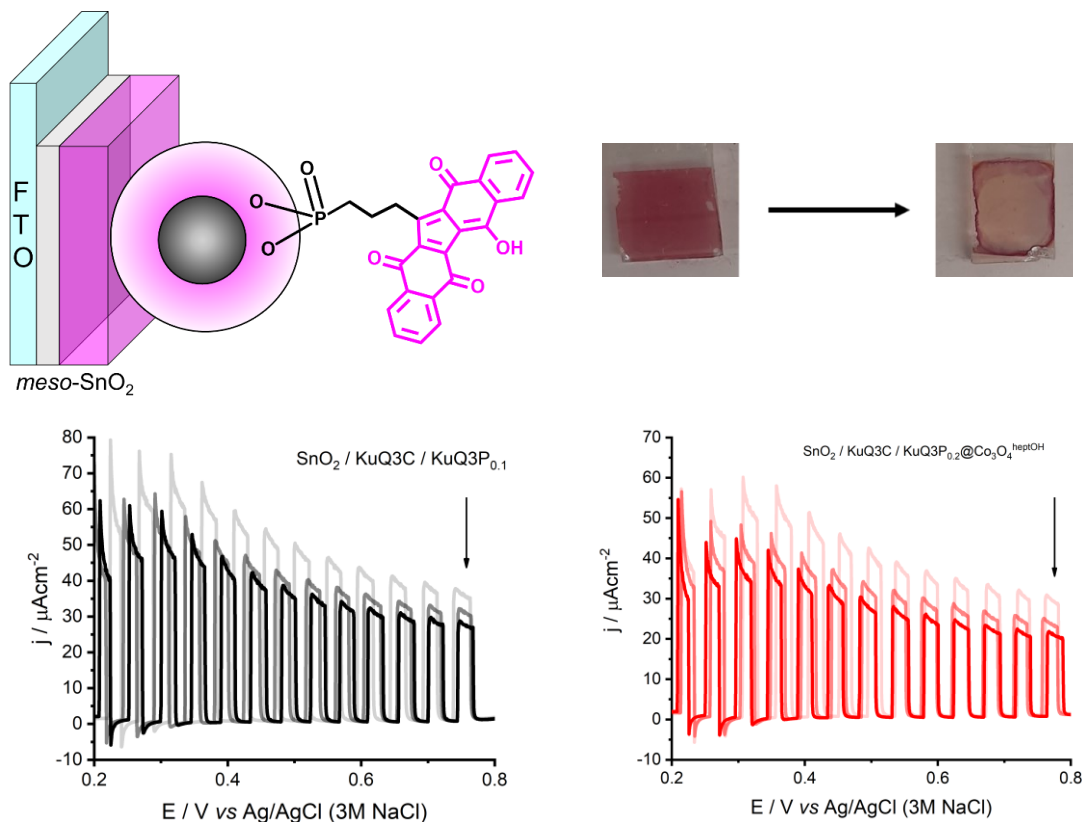


Figure 124. Top left: schematic view of $\text{SnO}_2/\text{KuQ3C}/\text{KuQ3P}_n@\text{Co}_3\text{O}_4^{\text{heptOH}}$ photoanodes preliminarily studied. Top right: image of the photoanodes before and after photoelectrochemical testing. Bottom: LSV traces of $\text{SCO}/\text{dye}/\text{KuQ3P}_n@\text{Co}_3\text{O}_4^{\text{heptOH}}$, where $n = 0.1$ (left, black traces) and 0.2 (right, red traces), registered in $\text{NaHCO}_3/\text{Na}_2\text{SiF}_6$ (pH 5.8) electrolyte, scan rate 0.020 V s^{-1} .

While these crude results are encouraging with regards to a possible use of the hybrid dyads as a photocatalytic ink on dye-sensitized films, the optimization of the dye-KuQ couples should be specifically tackled. Paramount design points would be the chemical stability of the dye sensitizing the SCO, its energy levels in relationship with those of the KuQ3P dye on the cobalt oxide shell and the role of dye-dye chemical interactions.

5.11 Experimental section

5.11.1 Materials and methods

Solid samples were accurately weighed by means of a MX5 Mettler Toledo Microbalance. All spectrophotometric analyses were performed by means of a Cary 60 Agilent spectrophotometer.

Unless otherwise noted, tetrahydrofuran (THF) was distilled under Ar atmosphere over Na/benzophenone to remove water and radical stabilizers and used within 24 h from withdrawal.

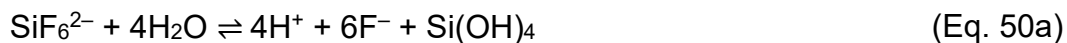
ICP-OES and IPC-MS analyses were performed by the Chemical Analysis Service of the Autonomous University of Barcelona.

Details of the synthetic procedures of the KuQ dyes and hybrid materials, emission quenching experiments, TEM and HR-TEM characterization, and XAS measurements, performed by Prof. Mirco Natali, Prof. Federica Sabuzi, Dr. Mattia Forchetta, Dr. Nuria Romero, Dr. Olaf Rüdiger and Dr. Marcos Gil Sepulcre, were omitted from the present Thesis.

5.11.2 Electrolyte solutions preparation

NaHCO₃/Na₂SiF₆ buffer solutions were prepared by mixing 0.512 g of NaHCO₃ and 0.705 g of Na₂SiF₆ in 95 mL of mQ water. The solution was left to stir overnight. After the specified time, the obtained suspension was filtered over cellulose wool to remove silica precipitates, then the pH was measured and, if required, adjusted with 1 M NaOH. Finally, the solution was brought to volume in a volumetric flask (100.00 mL).

For the sake of clarity, the reactions leading to buffer preparation are reported below (Equations 50a-c):



Ascorbate electrolyte was prepared by dissolving sodium ascorbate (1.98 g) and bringing to 100.00 mL with mQ water, then acidified by concentrated sulfuric acid to reach pH 5.80.

5.11.3 FTO/SnO₂ electrodes preparation

The FTO/SnO₂ electrodes were prepared by Dr. G. A. Volpato as previously reported by our group.²⁶⁶ Briefly, a SnO₂ colloidal paste (10 nm sized NPs), containing acetic acid as peptizing agent and a polyethylene glycol-based copolymer (CARBOWAX™) both as thickening agent and porogen material, was deposited onto clean FTO substrates by blade-coating. After deposition, the substrates were sintered and annealed following a slow temperature ramp to allow for slow water evaporation and avoid cracking of the films: 25 → 70 °C, 1.5 °C/min; 70 °C, 40 min; 70 → 450 °C, 13 °C/min; 450 °C, 20 min; 450 → 500 °C, 5 °C/min; 500 °C, 30 min. The mesoporous (pore diameter 10 ÷ 40 nm) SnO₂ films displayed 2.5 μm thickness.

5.11.4 Photoanodes preparation

5.11.4.1 Hybrid-based photoanodes

KuQ3X_n@Co₃O₄^{heptOH} particles were suspended upon sonication (10 min) in freshly distilled THF to reach *circa* 1.7 mg/mL concentration. Subsequently, aliquots of the colloidal suspension were deposited by dropcasting on the FTO/SnO₂ electrodes. In between depositions, the substrates were dried with a gentle stream of air. Deposition was carefully restricted to the SnO₂ film.

To provide a meaningful comparison between the hybrids, the photoanodes were prepared in order to attain a 140 nmol_{dye}cm⁻² nominal molar amount of KuQ. By knowing the molar mass of the hybrids (MW_{NP}) (independently determined by ICP and summarized in Table 9), the internal molar equivalents of KuQ dye in the hybrids (n), the specific mass of hybrids (\tilde{m}) to be deposited on the FTO/SnO₂ electrodes could be calculated by Eq. 51:

$$\tilde{m}(\mu\text{g}_{NP}/\text{cm}^2) = \frac{140 \text{ nmol}_{dye}/\text{cm}^2}{n(\text{mol}_{dye}/\text{mol}_{NP})} \cdot MW_{NP}(\text{g}/\text{mol}) \cdot 10^{-3}(\text{ng}/\text{mg}) \quad (\text{Eq. 51})$$

By imposing the mass concentration of the colloidal suspension (C_{coll}) and the geometric area of the SnO₂ film (A), the total volume of colloidal suspension of hybrid particles to be deposited (v_d) was calculated (Eq. 52):

$$v_d(\mu\text{L}) = A(\text{cm}^2) \cdot \frac{\tilde{m}(\mu\text{g}_{NP}/\text{cm}^2)}{c_{coll}(\text{mg}/\text{mL})} \quad (\text{Eq. 52})$$

Particles	MW (gmol ⁻¹)
Co ₃ O ₄ ^{heptOH}	564.28
KuQ3P _{0.05} @Co ₃ O ₄ ^{heptOH}	491.08
KuQ3P _{0.1} @Co ₃ O ₄ ^{heptOH}	505.11
KuQ3P _{0.2} @Co ₃ O ₄ ^{heptOH}	535.73
KuQ3C _{0.1} @Co ₃ O ₄ ^{heptOH}	505.11

Table 9. Molecular weights of the Co₃O₄^{heptOH}-based particles.

5.11.4.2 Dye-sensitized FTO/SnO₂ electrodes preparation

FTO/SnO₂/KuQ3C

Sensitization with KuQ3C was performed based on the method already reported by our group.²⁶⁶ FTO/SnO₂ electrodes were sensitized with KuQ3C by soaking for 24 h in a 0.11 mM solution of KuQ3C in THF. 2.0 mL of solution were used for each electrode. Given the long dyeing time, the solvent was not distilled prior to use. After soaking, the electrodes were recovered, rinsed with fresh THF, dried with a gentle stream of N₂. The electrodes were then immersed in aqueous H₂SO₄ (pH 2.0): upon immersion, the orange SnO₂ film turned pink, due to protonation of the enolate form of the dye to the enol. This treatment greatly improves the stability of the film in aqueous solution (see ²⁶⁶ and Paragraph 5.10). After acidic treatment, the electrodes were rinsed with mQ water and dried with a gentle stream of air. The electrodes were characterized by UV/Vis absorption spectrophotometry before and after acidic treatment.

In order to quantify the amount of dye deposited on the electrodes (dye loading), the THF solutions were analyzed by UV/Vis absorption spectrophotometry with a 1.0 mm optical path quartz cuvette. An aliquot of the starting THF solution was kept for reference. Prior to spectrophotometric analysis, all KuQ3C solutions were acidified with 25 μ L of p-toluenesulfonic acid to quantitatively convert KuQ3C into its enol form and diluted (1:10). Quantification was based on the absorbance at 563 nm ($\epsilon_{563} = 1.5 \cdot 10^4 \text{ M}^{-1}\text{cm}^{-1}$), using the Beer-Lambert law.

FTO/SnO₂/KuQ3C/Co₃O₄^{heptOH}

After dyeing, the electrodes were functionalized with Co₃O₄^{heptOH} by dropcasting a 1.50 mg/mL suspension of cobalt oxide in methanol to reach a 1 : 10 KuQ3C : Co₃O₄^{heptOH} molar ratio. After deposition, photoanodes were dried under a gentle stream of air.

FTO/SnO₂/KuQ-Hex

Photoelectrodes functionalized with KuQ-Hex were prepared either by dropcasting a 1.1 mM solution of the dye in CH₂Cl₂ or by soaking the FTO/SnO₂ electrodes in the same solution for 5 h. Upon treatment with the initially pink solution, the dye deposit on SnO₂ films immediately turned bright orange. The electrodes were then soaked in aqueous H₂SO₄ (pH 2.0), inducing an immediate colour change of the film to purple.

5.11.5 Photocatalysis

Photocatalytic reactions were performed in $\text{NaHCO}_3/\text{Na}_2\text{SiF}_6$ pH 5.60 buffer. The reaction mixture contained 1.0 mg/mL $\text{Co}_3\text{O}_4^{\text{heptOH}}$ particles and 84 mM $\text{Na}_2\text{S}_2\text{O}_8$. The particles and the persulfate were suspended and dissolved, respectively, in separate portions of the buffer and mixed in a thermostated glass reactor (Figure 125) prior to reaction. The temperature was kept at 25.0 °C by means of a water jacket controlled by a Huber thermostat. The reactor was sealed with a rubber septum. Oxygen evolution was analyzed with a gas-phase Clark-type amperometric oxygen sensor (Unisense Ox-N needle microsensor) connected to a Unisense UniAmp ammeter. The probe needle of the Clark sensor was used to pierce the rubber septum and placed in the headspace of the photoreactor. The reaction mixture was degassed by sparging the liquid and gas phases with Ar gas for 20 minutes each. After degassing, the rubber septum was protected with Parafilm M film and silicone grease.

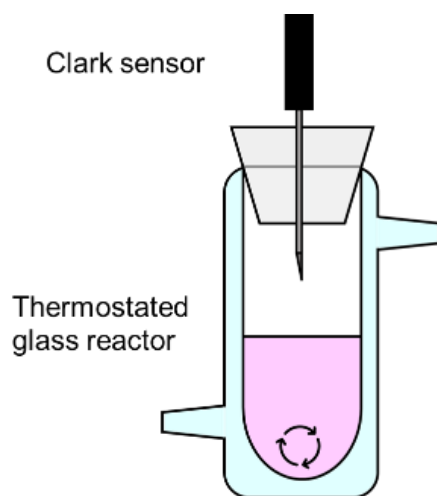


Figure 125. Schematic representation of the thermostated glass photoreactor (assembled). The Clark sensor inserted in the headspace is displayed.

The reactor was irradiated with an Abet Technologies LS150 150 W Xe lamp equipped with a 400 nm SP400LP Abet Technologies long-pass optical filter mounted on a Thorlabs SM1L03 holder. The distance between the light source and the photoreactor was set to reach a nominal incident power of 100 mWcm^{-2} . A Thorlabs FDS100 Si photodiode (0.13 cm^2 detector area, responding to wavelengths in the range $350 \div 1100 \text{ nm}$) connected to a digital multimeter was used to measure the incident light intensity.

The Clark sensor was calibrated after each photocatalytic reaction by degassing the reaction mixture and the reactor headspace with Ar and by performing subsequent additions of known volumes of O_2 with a gastight Hamilton syringe. A pseudo-calibration curve was constructed by plotting the steady-state differential signal of the Clark sensor after each gas addition as a function of the O_2 volume and, by means of the ideal gas law, of the molar amount of O_2 (Figure 126).

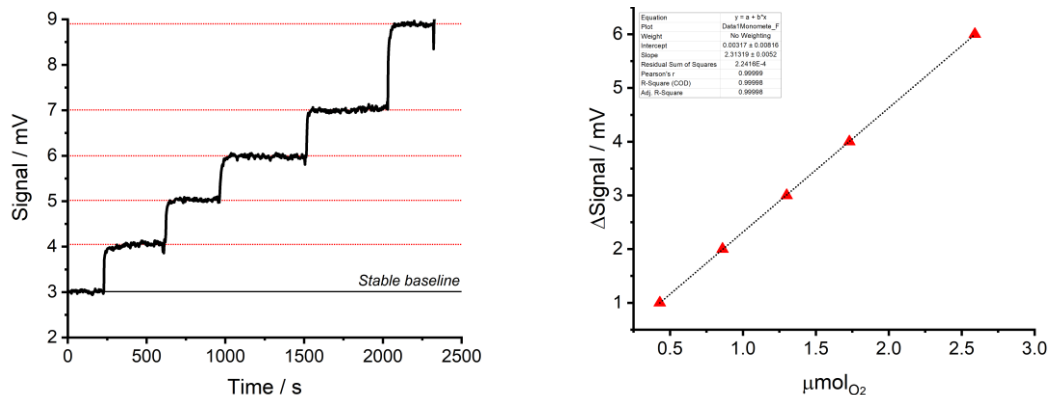


Figure 126. Left: response of the Clark sensor upon additions of known volumes of O_2 . Right: pseudo-calibration curve of the Clark sensor.

At the end of the photocatalytic reactions, the liquid phase was recovered and centrifuged. The supernatant was filtered over Celite. The residue was washed with mQ water (x 3), with methanol (x 3) and with diethyl ether (x 3), and finally left to dry to be further analyzed (by ICP, TEM, HR-TEM, XAS. The experiments were either upscaled or performed multiple times to produce sufficient amounts

of material for analysis). The results of the IPC analyses are summarized in Table 10.

The photoreactor and the stirrer bar were thoroughly cleaned by sonicating with *aqua regia* for 10 minutes, followed by thorough rinsing with deionized water, and finally sonicated with deionized water (10 minutes) and mQ water (5 minutes).

	Before cat.			After cat.		
	%Co	%P	eq KuQ3X	%Co	%P	Liquid analysis (mgL ⁻¹)
Co ₃ O ₄ ^{heptOH} NPs	31	0				
KuQ3P _{0.05} Co ₃ O ₄ ^{heptOH} NPs	36	0.26	0.04	46	0.04	[Co] = 24 [P] = 4.6
KuQ3P _{0.1} Co ₃ O ₄ ^{heptOH} NPs	35	0.52	0.08	43	0.17	[Co] = 21 [P] = 4.7
KuQ3P _{0.2} Co ₃ O ₄ ^{heptOH} NPs	33	1.02	0.18	41	0.16	[Co] = 13 [P] = 4.4
KuQ3C _{0.1} Co ₃ O ₄ ^{heptOH} NPs	35	0	–	–	–	–
0.1 eq KuQ3P+Co ₃ O ₄ ^{heptOH} NPs	9.3	0.39	–	28	0.09	–

Table 10. ICP analysis data relative to the hybrid particles before and after photocatalysis.

5.11.6 Photoelectrochemical experiments

Experiments were performed in a glass single compartment cell (Figure 127) by using either NaHCO₃/Na₂SiF₆ pH 5.80 or 0.1 M ascorbate (pH 5.80) electrolytes. The single compartment glass cell was fitted with a PFTE holder. The working electrodes were FTO/SnO₂ electrodes, the reference electrode was an Ag/AgCl (3 M NaCl) (BASi), the auxiliary electrode was a glassy carbon disk electrode (ø 3 mm, BASi). The working electrode was connected *via* an alligator clip soldered to a thin copper wire. The contacts were protected with a layer of Parafilm M to prevent contact with the electrolyte solution. The experiments were performed by means of a PalmSens4 potentiostat-galvanostat-impedance analyzer controlled with PSTrace 5.9 software.

Photoelectrodes were irradiated from the side of the back contact with an Abet Technologies LS150 150 W Xe lamp equipped with a 400 nm SP400LP Abet Technologies long-pass optical filter mounted on a Thorlabs SM1L03 holder. A Thorlabs FDS100 Si photodiode connected to a digital multimeter was used to measure the incident light intensity, set to 100 mWcm^{-2} for each electrode. In chopped-light experiments, irradiation was manually interrupted by interposing a piece of black cardboard between the light source and the photoelectrochemical cell.

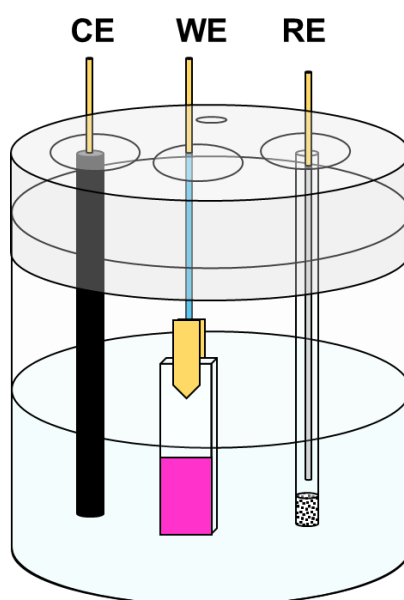


Figure 127. Schematic view of the one-compartment photoelectrochemical cell used for testing the photoelectrodes.

5.11.7 Determination of the Faradaic efficiency for O_2 evolution

The generator-collector method previously described by our group was used to quantify evolved O_2 .^{239,266} Briefly, the photoanode, used as oxygen generator, was interfaced to a FTO electrode used as oxygen sensor (collector). Collector electrodes were cleaned by 10 min sonication in KOH saturated in $i\text{PrOH}$, 10 min sonication in $i\text{PrOH}$, and thermally treated at $500 \text{ }^\circ\text{C}$ for 30 min. The inert spacer between collector and generator electrodes was constituted by an H-shaped

mask made with three layers of unstretched Parafilm M, with openings left to allow for electrolyte exchange between the bulk and the thin layer of solution between the electrodes (Figure 102). Connections were made *via* copper tape posed on the edge of each electrode. The contacts, the alligator clips, and all parts not intended to come into contact with the electrolyte solution were isolated by wrapping them with Parafilm M.

Once the contacts had been prepared and the Parafilm mask was laid between the electrodes, these were clamped together by means of a custom-made PEEK frame held together by four PTFE nuts (realized by Lorenzo Dainese, technician in the Department of Chemical Sciences of the University of Padova). The setup is reproduced in Figure 128.

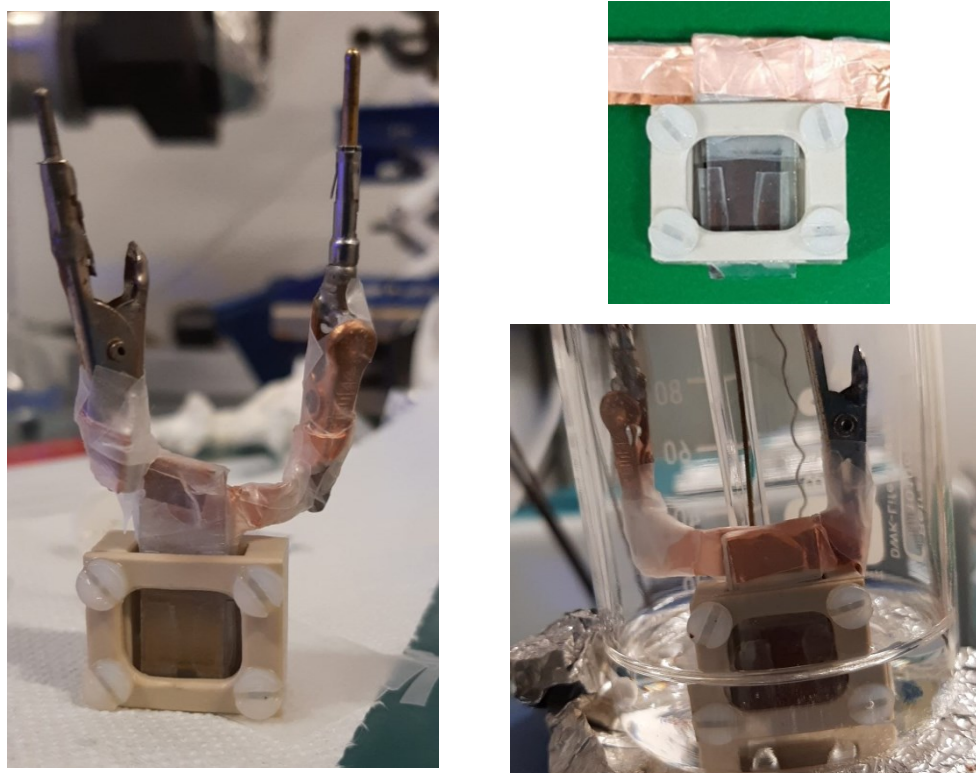


Figure 128. Pictures displaying of the setup used for two-plate generator-collector experiments. The top right figure displays the H-shaped mask between the electrodes clamped together in the PEEK frame.

The experiments were run in a four-electrode setup controlled by a Metrohm Autolab PGSTAT302N bipotentiostat. The two working electrodes were the generator and collector electrodes, while an Ag/AgCl (3 M NaCl) (BASi) and a platinum wire were used as reference and auxiliary electrodes, respectively. The single compartment glass cell was fitted with a PTFE holder. The photoanodes were illuminated with 100 mWcm^2 simulated solar light from a LOT-Quantum Design solar simulator, equipped with an AM 1.5 G filter and an Andover Corp. 400fh90-50s 400 nm long-pass optical filter to cut the contribution of UV light.

The electrolyte solution ($\text{NaHCO}_3/\text{Na}_2\text{SiF}_6$ pH 5.80) was introduced by means of a syringe after placing the electrodes in the cell, and thoroughly degassed with N_2 for 20 minutes before each measurement. During measurements, the electrolyte solution was kept under a blanket of N_2 provided by a gentle stream of the gas above the solution.

Chronoamperometries were performed by poisoning the generator electrode at 0.6 V vs Ag/AgCl and the collector electrode at -0.9 V vs Ag/AgCl. This latter value was chosen as sufficiently negative to provide extensive oxygen reduction on FTO.²⁶⁶ The experiments were constituted by a 100 s dark phase to ensure stabilization of the collector baseline current, followed by a 150 s illumination phase. Finally, after interrupting the illumination phase, chronoamperograms were recorded to ensure complete consumption of the evolved O_2 , indicated by a decay to the baseline signal of the collector current (usually 200 s were required). Determination of the Faradaic efficiency for O_2 evolution was performed by integrating the generator photocurrent during the illumination phase and the collector current during the illumination phase and the subsequent dark recovery phase.

The collection efficiency of the setup was independently determined *via* calibration of the cell.²⁶⁶ The equipment, the electrolyte, and the degassing procedures were the same as those used for the experiments on photoanodes. The cell was calibrated by employing a FTO generator interfaced with a FTO collector poised at -0.9 V vs Ag/AgCl. The double-step chronoamperometric

experiments were composed by a first phase (60 s), in which the generator was poised at 0.6 V vs Ag/AgCl, followed by a second phase (120 s) in which the generator potential was stepped to a higher value so to access electrocatalytic oxygen evolution by the FTO generator. Oxygen evolution was induced to an increasing degree by varying the generator potential during this second oxygen-evolving phase from 1.40 V vs Ag/AgCl to 1.90 V vs Ag/AgCl in a series of experiments. Incidentally, this chronoamperometric method was intended as a viable strategy to produce variable generator charges, and therefore to vary the amount of O₂ evolved in the thin layer between the working electrodes, in the same time interval. A second method could have relied on working at a single oxygen-evolving generator potential at variable times. Finally, the generator potential was brought back to 0.6 V vs Ag/AgCl to measure the recovery trace until complete exhaustion of the evolved O₂ by the collector (240 s). The outcome of the calibration experiments is reported in Figure 129.

This procedure has been previously reported and provides a calibration setup as close as possible to the photoelectrocatalytic regime. Conceptually, the second potential step is intended as a simulation of the irradiation phase during photoelectrochemical experiments.

Integration of the generator (during the second phase) and collector (during the second and third phases) current traces provided the charges Q_{gen} and Q_{coll} used to construct the calibration curve (Figure 129, bottom) under the assumption of unit Faradaic efficiency for the OER by the FTO generator. The slope of the calibration curve was used as the collection efficiency of the cell ($\eta_{\text{coll}} = 76\%$).

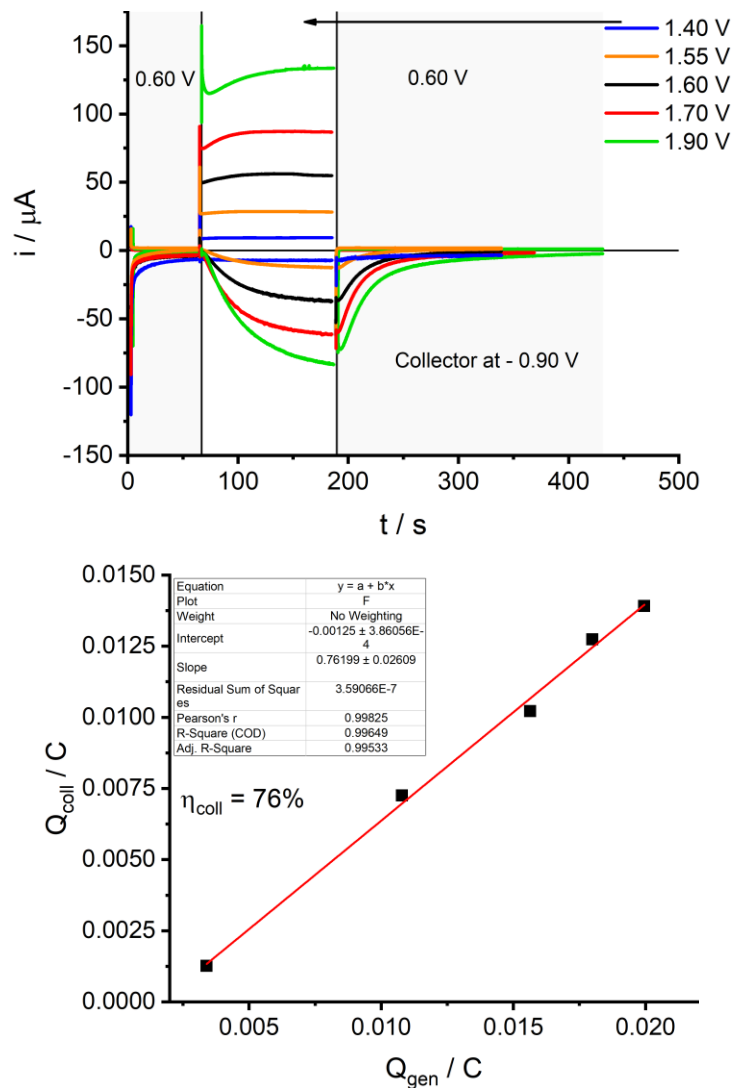


Figure 129. Calibration of the generato-collector setup with FTO generator and FTO collector (poised at -0.9 V vs Ag/AgCl), registered in $\text{NaHCO}_3/\text{Na}_2\text{SiF}_6$ ($\text{pH } 5.8$) electrolyte. Top: chronoamperograms; bottom: calibration curve obtained upon integration of the generator and collector current traces, displaying the collection efficiency.

5.11.8 Incident photon-to-current conversion efficiency (IPCE) determination

Experiments were performed by employing a custom-made PTFE one-compartment cell equipped with two diametrically opposed quartz windows, in between of which photoanodes (used as the working electrodes) were located. Cell design allowed for fitting on common holders compatible with optical benches. The electric contact was achieved by means of a PTFE clamp internally lined with copper foil and containing a copper cylinder (\varnothing 1 mm), fitted through a rubber septum to allow for height regulation (Figure 130).

A PalmSens4 potentiostat was used to control the cell. The auxiliary electrode (glassy carbon disk, \varnothing 3 mm, BASi) and the reference electrode (Ag/AgCl, 3 M NaCl, BASi) were inserted through a separate port and located adjacent to the working electrode. The electrolyte solution ($\text{NaHCO}_3/\text{Na}_2\text{SiF}_6$ pH 5.80) was introduced by means of a syringe after inserting and connecting the electrodes.

The setup used for the IPCE determination in full photoaction spectral measurements was courtesy of Prof. Jordi Hernando (Autonomous University of Barcelona) and is depicted in Figure 130. The light source was a 150 W Xe short-arc lamp powered by an Applied Photophysics 04-122 Power Controlled Lamp Supply and mounted in an Applied Photophysics lamp housing. The light beam was collimated by means of optical lenses of an Applied Photophysics Laser Kinetic Spectrometer. Monochromatic irradiation was obtained with an Applied Photophysics 05-109 pbp SpectraKinetic Monochromator controlled *via* custom-made software. Inlet and outlet slit openings of 5 mm were selected to maximize the irradiance output and obtain a better signal-to-noise ratio in photoelectrochemical experiments. The photoelectrochemical cell was placed in front of the monochromator, by illuminating the photoanode from the side of the back contact.

Chronoamperometries were recorded at 0.6 V vs Ag/AgCl. A 10 s dark phase was followed by 30 s of illumination and, finally, by another 10 s dark phase. Steady-

state photocurrent densities were measured from the difference between the stabilized photocurrent at the end of the 30 s illumination phase and the stabilized dark current in the last dark phase of the experiment (Figure 130).

The incident light irradiance was measured with a Thorlabs S120VC photodiode connected to a Thorlabs PM100A power meter (responsive in the range 200 ÷ 1100 nm, detector area 0.94 cm²).

When using LED as monochromatic light sources, the cell was fitted to a Thorlabs MB3060U/M optical bench by means of Thorlabs BA1S/M mounting base. Irradiation was performed using Thorlabs M680L4, M590L4, M530L4, M490L4, M430L4, M405L4 LED sources (λ_{em} = 680 nm, 590 nm, 530 nm, 490 nm, 430 nm, 405 nm, respectively), equipped with Thorlabs FB680-10, FB590-10, FB530-10, FB490-10, FB430-10, FB405-10 band-pass optical filters to achieve a FWHM of 10 nm, and with a Thorlabs SM1U25-A collimator.

The light was collimated to fully illuminate the optical quartz window of the photoelectrochemical cell. The output power of the LED's was regulated by connecting the light sources to a Thorlabs LEDD1B driver. The power was selected to provide photocurrents in the range of those obtained with the Xe lamp-monochromator system. The setup is displayed in Figure 131. The irradiance was measured, as in the case of the Xe lamp source, with a Thorlabs S120VC photodiode connected to a Thorlabs PM100A power meter.

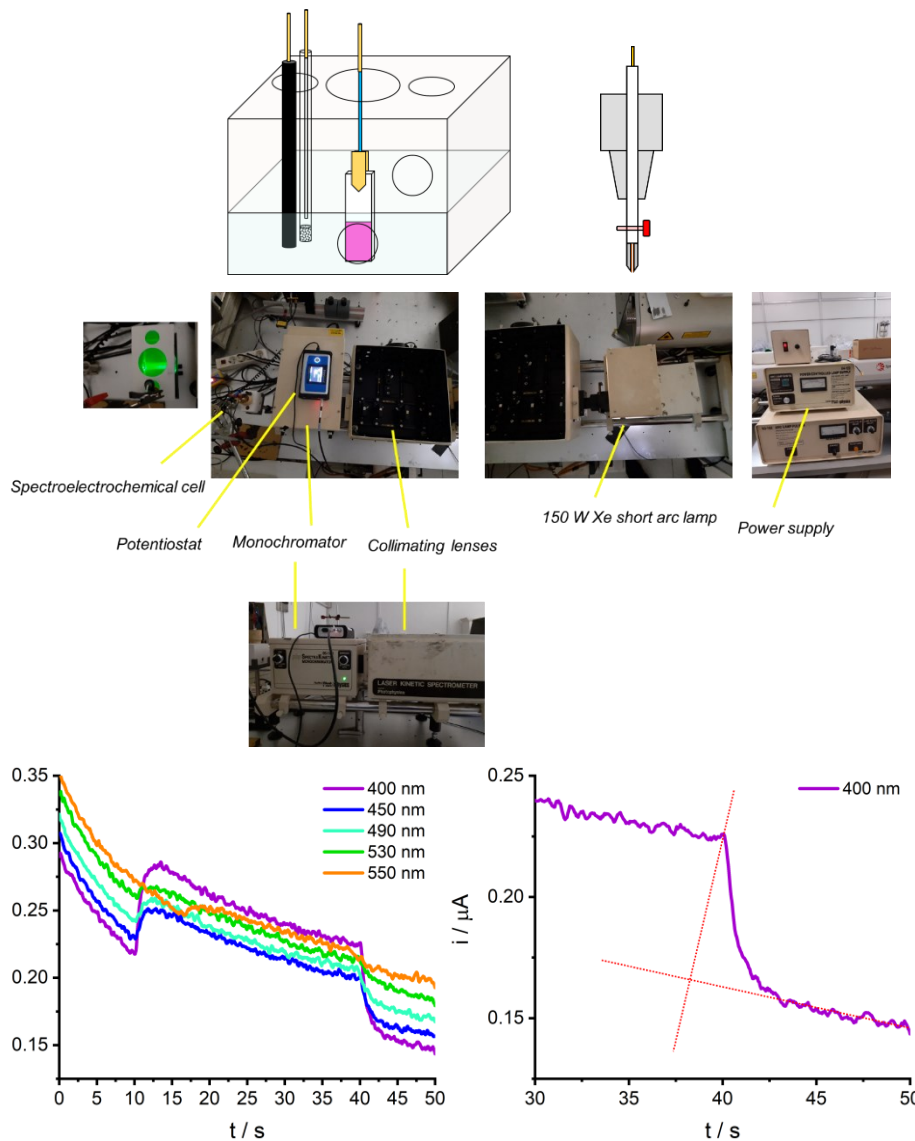


Figure 130. Top: Schematic view of the custom-made cell used for registering the IPCE photoaction spectra. Middle: photophysical setup used in the study with the Xe lamp source. Bottom: chronoamperograms recorded at 0.6 V vs Ag/AgCl recorded under monochromatic irradiation. Photocurrent determination procedure is displayed.

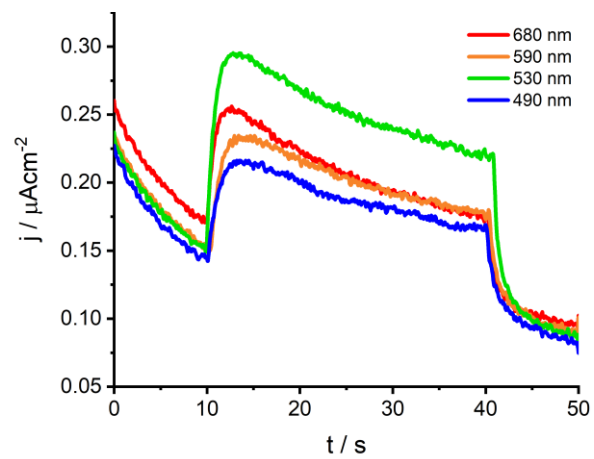
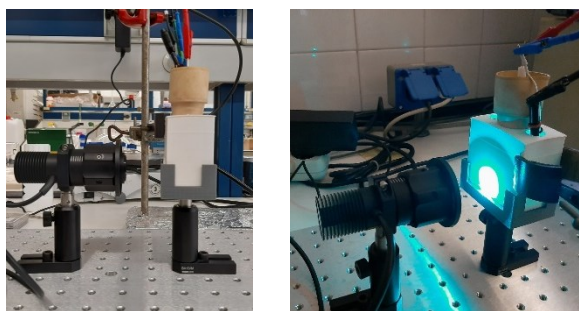


Figure 131. Top: setup used for registering the IPCE photoaction spectrum with LED sources. Bottom: chronoamperograms recorded at different wavelengths with LED sources.

SECTION 3.

Emerging (photo)electrochemical strategies for organic reactivity

Disclaimer:

This section contains material previously published in scientific journals, in the form of articles of which I was an author. Reproduction of the of graphic material from the publications in the present Thesis was authorized by the Editors.

*
**

“Photoelectrochemical C-H activation through a quinacridone dye enabling proton-coupled electron transfer” Y. Yang, G. A. Volpato, E. Rossin, N. Peruffo, F. Tumbarello, C. Nicoletti, R. Bonetto, L. Paoloni, P. Umari, E. Colusso, L. Dell’Amico, S. Berardi, E. Collini, S. Caramori, S. Agnoli, A. Sartorel
ChemSusChem **2022**, <https://doi.org/10.1002/cssc.202201980>.

Copyright Wiley 2022

“Basicity as a Thermodynamic Descriptor of Carbanions Reactivity with Carbon Dioxide: Application to the Carboxylation of α,β -Unsaturated Ketones” Franceschi, P.; Nicoletti, C.; Bonetto, R.; Bonchio, M.; Natali, M.; Dell’Amico, L.; Sartorel, A. *Front. Chem.* **2021**, *9*, 783993.

6. Emerging (photo)electrochemical strategies for organic reactivity

As a part of the research carried out during my Ph.D., I have been involved in other projects developed in our group at the University of Padova. These projects deal with an alternative, innovative vision of artificial photosynthesis, and with exploiting the redox routines in synthetic organic chemistry. Paragraph 6.1 reports a reductive activation of α,β -unsaturated carbonyls to promote carbon dioxide fixation; Paragraph 6.2 reports the photoelectrochemical activation of C–H bonds with electrodes sensitized with a quinacridone organic dye. Specifically, I have provided supervision to students in laboratory activities and method development in the two projects that are herein briefly described, contributed to data analysis and interpretation, participated to scientific discussions and contributed to writing the manuscripts.

6.1 Electrochemical carboxylation of α,β -unsaturated ketones

A promising strategy in the utilization of carbon dioxide alongside its catalytic reduction is its fixation into organic compounds, to access sustainable production of fine chemicals. Specifically, electrocarboxylation relies on the addition of CO_2 to organic compounds promoted by electrochemistry.

Conceptually, electrocarboxylation may occur by generation of the radical anion of carbon dioxide, $\text{CO}_2^{\cdot-}$; however, the high overpotentials generally required when working with carbon-based electrodes (*vide supra*) make it an unpreferred route. Conversely, electrocarboxylation may be performed upon electrogeneration of a nucleophilic species *via* reduction of an organic molecule. The reduced form of the molecule may in turn perform addition of CO_2 , thus constituting the first step towards generation of a carboxylic acid derivative. Deeply investigated classes of molecules are organic halides, undergoing dissociative electron transfer when reduced at an electrode with production of a

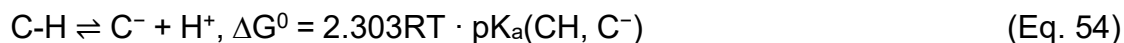
carbon-based radical, that can be further reduced to a carbanion, in turn able to attack CO₂. Other molecules capable of undergoing electrocarboxylation are characterized by olefinic (C=C) or imine (C=N) bonds.

Our group approached this subject by investigating the reaction mechanism of the electrocarboxylation of α,β -unsaturated ketones, specifically chalcone and flavone. Briefly, a thermodynamic study corroborated by computational analysis provided the basis to predict:

- i) The possibility for a specific reduced form of a substrate to undergo carboxylation (e.g., either radical anion or dianion derived from reduction of a C=C bond).
- ii) The preferred site undergoing carboxylation, in the case of chemically non-equivalent carbon sites of the C=C bond.

In cyclic voltammetries along a cathodic scan, chalcone and flavone undergo two stepwise one-electron reductions to the radical anion and to the dianion. The CV of flavone as a representative case is reported in Figure 132, where the two quasi-reversible waves are observed at -2.1 and -2.4 V vs Fc⁺/Fc, respectively. In the presence of carbon dioxide, significant changes are observed at the second wave and, consistently, controlled potential electrolysis at the potential of the second wave afforded the carboxylated products in β -position with good Faradaic yields (44 and 55% for chalcone and flavone, respectively, isolated as the methyl esters, Figure 132). Conversely, electrolysis at the first wave gave the products in traces (*circa* 2% yield).

These results were rationalized on the basis of a thermochemical cycle and of DFT calculations on 50 organic compounds containing C–H bonds, that support a linear correlation between the Gibbs free energy of the carboxylation step of the carbanion C⁻ (Eq. 53) and the basicity of the involved carbanion, expressed as the pK_a value of the C–H/C⁻ couple (Eq. 54). This analysis identified a threshold value of the pK_a of 36 (in acetonitrile), above which the carboxylation of the carbanion is exergonic, Figure 132.

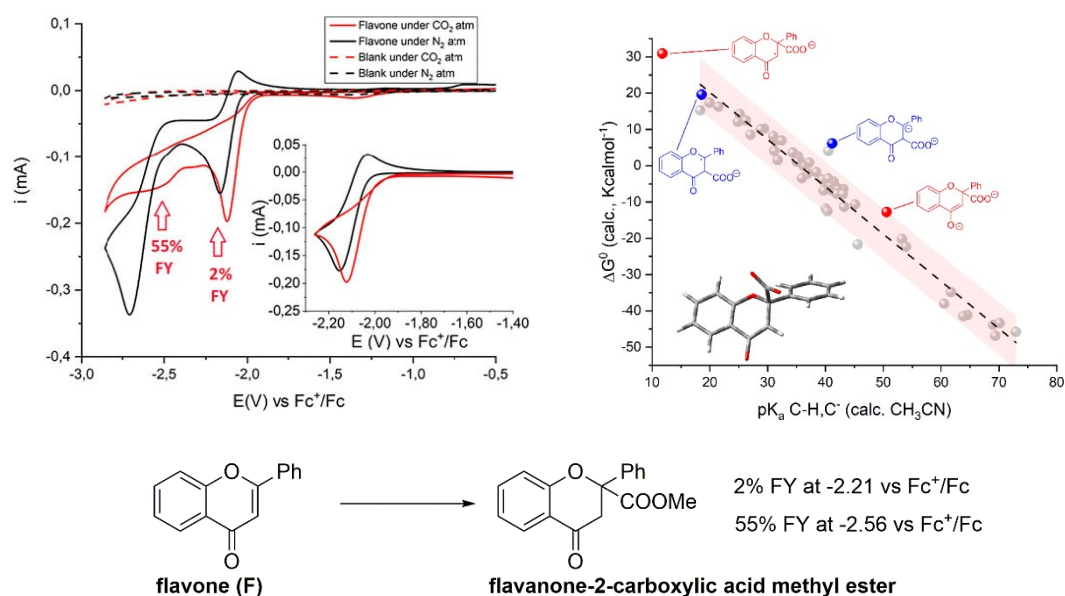


Application of this model to the carboxylation of α,β -unsaturated carbonyls supported the experimental electrochemical outcome and the reactivity towards CO_2 of the dianions in β -position, since calculated ΔG^0 of carboxylation was -12.8 and $-20.0 \text{ Kcalmol}^{-1}$ for flavone and chalcone, respectively, associated with pK_a values for the conjugate acids of 50.6 and 51.8, respectively. Consistently, an endergonic carboxylation was predicted for the carboxylation in α -position, or starting from the singly reduced radical anions of flavone and chalcone (Figure 132). The predictive reactivity model was also applied to other case studies previously reported in the literature.

The study “Basicity as a Thermodynamic Descriptor of Carbanions Reactivity with Carbon Dioxide: Application to the Carboxylation of α,β -Unsaturated Ketones” was published in 2021 in *Frontiers in Chemistry*.

6.1.1 Contribution to the work

My contribution was mainly devoted to the optimization of electrochemical protocols for cyclic voltammetry and controlled potential electrolysis, together with Pietro Franceschi and Catia Nicoletti. In particular, two protocols for constant potential electrolysis were devised, that are described in the Experimental Section.



1. CPE, 20 mM F in CH₃CN (0.1 M TBAPF₆), CO₂
2. MeOH, H₂SO₄, 1 h MW heating (80°C)

Figure 132. Top left: CV of 5 mM Flavone in ACN with 0.1 M tetrabutylammonium hexafluorophosphate supporting electrolyte under N₂ (black traces) and CO₂ (red traces). The inset shows the scan conducted in a narrow potential range and limited to the first reduction process. Top right: Plot of calculated standard free energy of carboxylation (ΔG_0^1) vs calculated pK_a of the C–H/C[−] couples. Red dots indicate flavone derivatives upon carboxylation in the β position; blue dots indicate flavone derivatives upon carboxylation in the α position. The carboxylation product in β starting from flavone radical anion is unstable during the calculation and explodes releasing CO₂: in this case, the ΔG^0 value is extrapolated by the linear correlations among 50 organic substrates. Inset: optimized geometry of the carboxylated product in β starting from flavone dianion. The light grey dots indicate the 50 organic molecules used to construct the model. Bottom: electrochemical carboxylation of flavone and formation of flavanone-2-carboxylic acid methyl ester (from carboxylation in β -position to the carbonyl group) after esterification of the electrolysis solution.

6.2 Photoelectrochemical C–H activation by SnO₂ electrodes dye-sensitized with Quinacridone

6.2.1 Introduction

The design principles of dye-sensitized photoelectrochemical cells (DSPEC's) have reached a sophisticated level of detail over the last decades. In terms of performance, promising results in fuel-forming devices are accompanied by a widespread use of dye-sensitized solar cells (DSSC's) in photovoltaics. DSSC's are currently being evaluated for use in domestic and industrial (e.g., in greenhouses) context.

A limiting factor for water splitting DSPEC's is the non-trivial architecture of the photoanodes for photoelectrochemical water oxidation. Specifically, three-components photoelectrodes constituted by a semiconductive oxide (SCO), a dye, and a WOC require efficient design of each component and of their mutual interaction at the molecular and the nanoscale levels (see Chapter 5), that is not always repaid in terms of efficient photoelectrocatalysis. Therefore, researchers are currently being prompted towards investigating simpler photoanodic reactions, that do not suffer the thermodynamic and kinetic limitations of the 4-electron 4-proton water oxidation. In the context of simplifying the DSPEC design while contextually enhancing its performance, photoelectrochemical oxidation of organic substrates to value-added chemicals is currently being targeted. These reactions are kinetically more facile, usually undergoing radical mechanisms, and may be driven by photoelectrodes sensitized with suitable dyes without the need of a metal catalyst. A major advantage would be constituted by the access to novel synthetic strategies in a scalable setup, compatible with flow chemistry.

A class of oxidation reactions that are suitable for studying in such systems is alcohol oxidation. It is usually performed in the presence of an aminoxyl radical as a catalyst. Indeed, our group reported preliminary evidence of SnO₂-based photoanodes sensitized with KuQ3C promoting benzyl alcohol oxidation.

More recently, the photoelectrochemical approach has been directed towards C–H bond activation, a most relevant goal for organic synthesis. This process involves hydrogen atom abstraction from a reactive C–H site in an organic substrate; the reports were limited by the direct irradiation of semiconductors such as BiVO₄, WO₃, Fe₂O₃, while to the best of our knowledge no reports were dealing with dye-sensitized photoanodes for C–H activation.

6.2.2 Quinacridone-sensitized SnO₂ photoanodes

Our contribution involves SnO₂ photoanodes sensitized with the quinacridone (QNC) dye. QNC is an acridone chromophore with extended absorption in the visible region and high chemical stability. Its planar structure and the presence of two NH groups per molecule confer QNC a high insolubility; in its aggregate forms, generated by both π - π interactions and hydrogen bonds, QNC behaves as an organic semiconductor. QNC derivatives, functionalized at the nitrogen sites with alkyl groups, have been applied in sensing, optoelectronics, photoelectrochemical cells and photocatalytic systems. Introducing bulky groups at the nitrogen sites of QNC in fact counteracts the planarity of dye molecules and disrupts the network of hydrogen bonds, thus improving dye solubility. QNC insolubility is a major obstacle to its use on photoelectrodes. For this reason, authors using QNC in optoelectronic applications have exploited its thermal stability by sublimating the dye and depositing it onto surfaces.

The use of QNC in mediating C–H activation would rely on its possibility to manage PCET events, with generation of N-centered radicals (N[•]) upon oxidation (Figure 133). The N-centered radicals are in fact capable of hydrogen atom abstraction (HAT) from suitable organic substrates, thus leading to their oxidation. In a QNC-sensitized SCO photoanode, the N[•] radicals would be generated upon light absorption and charge injection by QNC into the SCO.

We studied the ability of QNC to manage PCET in aqueous environment. Then, we approached the preparation of photoanodes by sublimating QNC under

vacuum onto FTO/SnO₂ electrodes. These were studied by photoelectrochemistry in acetonitrile, demonstrating their ability to promote C–H activation in xanthene and γ -terpinene substrates at the preparative level. A thermodynamic cycle to determine the activity of QNC dye in C–H activation *via* HAT was established. This was based on the difference between the bond dissociation free energy (BDFE) of the N–H group of QNC (80.5 kcalmol⁻¹) and that of the organic substrates targeted for the reaction. Coherently, the ratio between the photocurrent density in the presence of the organic substrates and the one observed in their absence was used as a reactivity indicator (J_{sub}/J_0 , see Figure 133).

Finally, our mechanistic proposal was based on reaction of the C-centered radical, generated upon HAT from the substrate to QNC, with O₂, eventually acting as an oxidizing agent to conclude the oxidative aromatization of the substrate (a representative scheme is provided in Figure 133, focusing on γ -terpinene). To probe this hypothesis, an experiment conducted under N₂ atmosphere revealed no production of aromatized product starting from γ -terpinene.

The study “Photoelectrochemical C–H activation through a quinacridone dye enabling proton-coupled electron transfer” was published in 2022 in *ChemSusChem*.

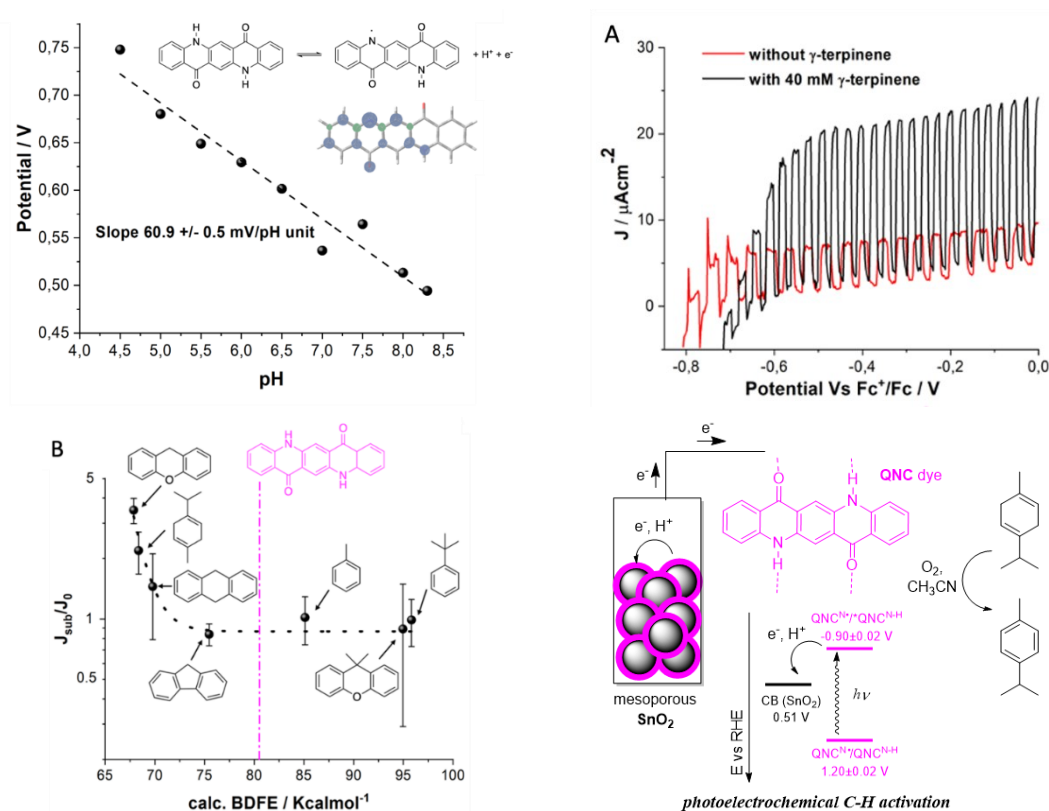
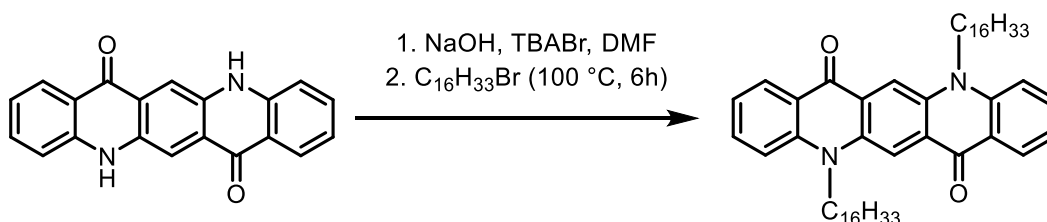


Figure 133. Top left: Pourbaix diagram of the one electron oxidation process; inset shows the redox reaction involving the QNC^{N•}/QNC^{NH} couple, and the optimized geometry and spin density analysis of QNC^{N•}. Top right: LSV traces under chopped irradiation of FTO/SnO₂/QNC photoelectrodes in ACN with 0.1 M tetrabutylammonium hexafluorophosphate, in the absence (red trace) and in the presence (black trace) of 40 mM γ -terpinene. Scan rate: 0.020 Vs⁻¹. Bottom left: Photoelectrochemical C–H activation through a quinacridone dye (QNC)-sensitized SnO₂ mesoporous semiconductor. Bottom right: plot of the J_{sub}/J_0 observed for FTO/SnO₂/QNC electrodes at 0 V vs Fc⁺/Fc in the presence of 40 mM organic substrate, depending on the BDFE of the C–H bond.

6.2.3 Contribution to the work

My initial contribution to this research was the investigation of N-functionalized QNC derivatives and the optimization of photoelectrochemical synthesis. The focus was indeed directed towards the experimental demonstration of the necessity for NH groups in order to attain the desired photoelectrochemical reactivity. QNC was therefore functionalized at the N sites with C₁₆ alkyl chains by Catia Nicoletti, following the synthetic route in Scheme 15, bottom. Briefly, the dye was allowed to react in DMF with NaOH acting as a base towards the NH sites. Deprotonation of these latter produced the nucleophilic anionic form of QNC (indicated by a blue colour) that could react with excess 1-bromohexadecane *via* nucleophilic substitution. Finally, the reaction crude was precipitated by addition of water and purified by column chromatography to isolate the desired compound as an orange powder in 60% yield.



Scheme 15. Synthesis of QNC-C₁₆.

QNC-C₁₆, soluble in organic solvents, was deposited by dropcasting a 0.76 mM CH₂Cl₂ solution onto SnO₂ anodes pre-heated at 40 °C. Deposition was performed by fully covering the SnO₂ film with the dye solution followed by letting the solvent quickly and uniformly evaporate. After dyeing, the electrodes were dried under a gentle stream of N₂ and soaked in ACN for 10 minutes, followed by drying under N₂. The absorption spectrum of the resulting pink electrodes is reported in Figure 134, displaying maxima at 505 nm and 550 nm. Incidentally, N-substitution does not impact substantially on the optical properties of QNC.

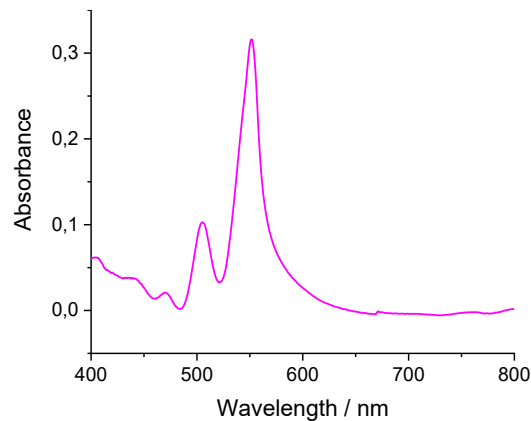


Figure 134. Electronic absorption spectrum of FTO/SnO₂/ QNC-C₁₆.

The photoelectrodes were tested by CV under intermittent irradiation (Figure 135), in acetonitrile with 0.1 M tetrabutylammonium hexafluorophosphate as supporting electrolyte. Increasing concentrations of xanthene and γ -terpinene (10 mM, 20 mM, 40 mM), were used. As expected for QNC-C₁₆, no appreciable photocurrent increase could be observed upon addition of the organic substrates. Indeed, J_{sub}/J_0 was found to remain in the range 1 \div 1.3 independently on substrate concentration. Table 11 provides J_{sub}/J_0 for γ -terpinene. These findings thus support the need for the NH/N^{*} reactivity for C–H activation.

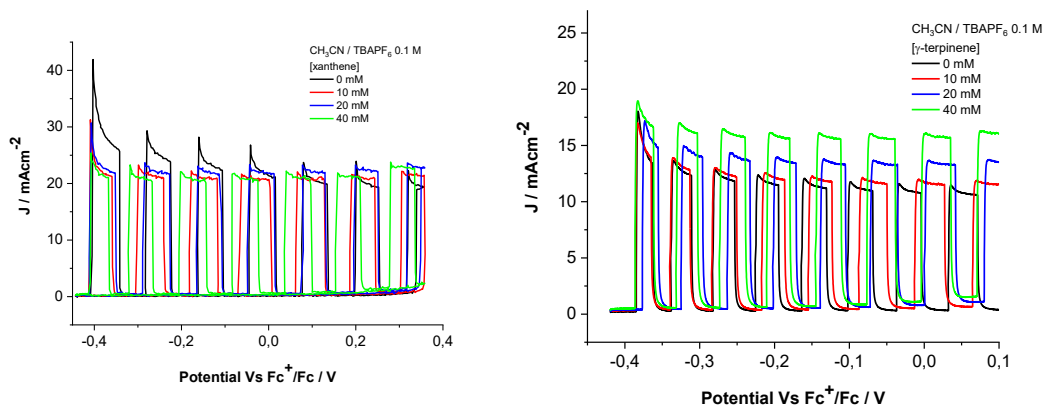


Figure 135. LSV traces under chopped irradiation of FTO/SnO₂/QNC-C₁₆ photoelectrodes in acetonitrile with 0.1 M tetrabutylammonium hexafluorophosphate, as a function of [xanthene] (left) and [γ -terpinene] (right). Scan rate: 0.020 Vs⁻¹.

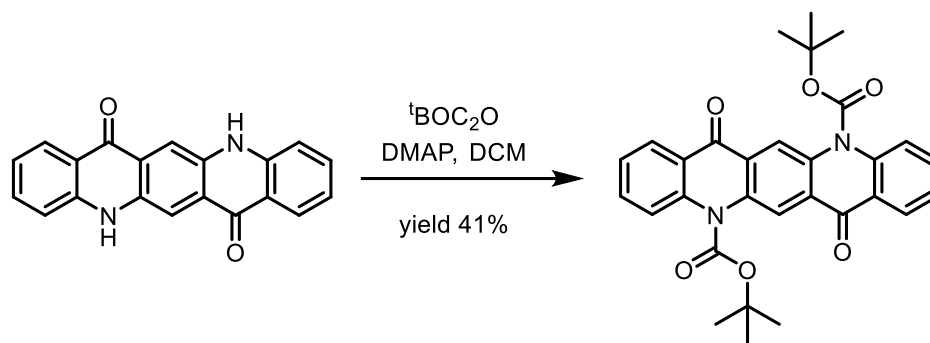
[γ -terpinene]	J_{sub}/J_0	
	0.15 V vs Fc ⁺ /Fc	0.30 V vs Fc ⁺ /Fc
0	1	1
10 mM	1.04	1.05
20 mM	1.17	1.19
40 mM	1.37	1.27

Table 11. J_{sub}/J_0 values for FTO/SnO₂/QNC-C₁₆ photoelectrodes as a function of [γ -terpinene] at two different potential values.

6.2.4 Further developments

An optimization strategy for improving the ease of photoelectrode preparation was also pursued. Despite the satisfactory results, the vacuum sublimation method was indeed a limiting factor. QNC photoanodes preparation was then approached by more easily manageable solution methods. For this purpose, the latent pigment approach was applied. Briefly, it is a chemical strategy first reported by Zambounis *et al.* in 1997.²⁷¹ It involves reversible protection of the N-sites of an otherwise insoluble dye with *tert*-butoxycarbonyl (BOC) groups. The presence of bulky groups compromising the planarity and H-bond formation capacity of the chromophores indeed confers solubility to the protected molecules. These groups may then be cleaved either chemically (by treating with acid or base) or thermally. Thermal treatment induces decomposition of BOC to isobutene and carbon dioxide, to restore the original QNC chromophore.

The protected ^{BOC}QNC was synthesized by following the procedure reported by Sytnyk *et al.* (Scheme 16)²⁷², consisting in the reaction between QNC and di-*tert*-butylcarbonate (^tBOC₂O) in the presence of 4-dimethylaminopyridine (DMAP) in CH₂Cl₂. The product was isolated as a bright yellow powder with a strong green fluorescence in organic solution, after purification *via* column chromatography. Incidentally, the yellow colour is indicative of lack of aggregation of QNC derivatives, both in solution and in the solid state.



Scheme 16. Synthesis of ^{BOC}QNC.

SnO₂ photoanodes were prepared by dropcasting a 1 mM solution of ^{BOC}QNC in CH₂Cl₂, then dried under a stream of N₂. The yellow-coloured electrodes were then subjected to a thermal treatment (200 °C, 2 minutes), inducing a colour change to pink (Figure 136).

Preliminary testing of the photoanodes prepared *via* the latent pigment approach have provided encouraging results, comparable with those obtained with electrodes prepared *via* vacuum sublimation of QNC ($J_{\text{sub}}/J_0 \approx 3$ in the presence of 40 mM xanthene).

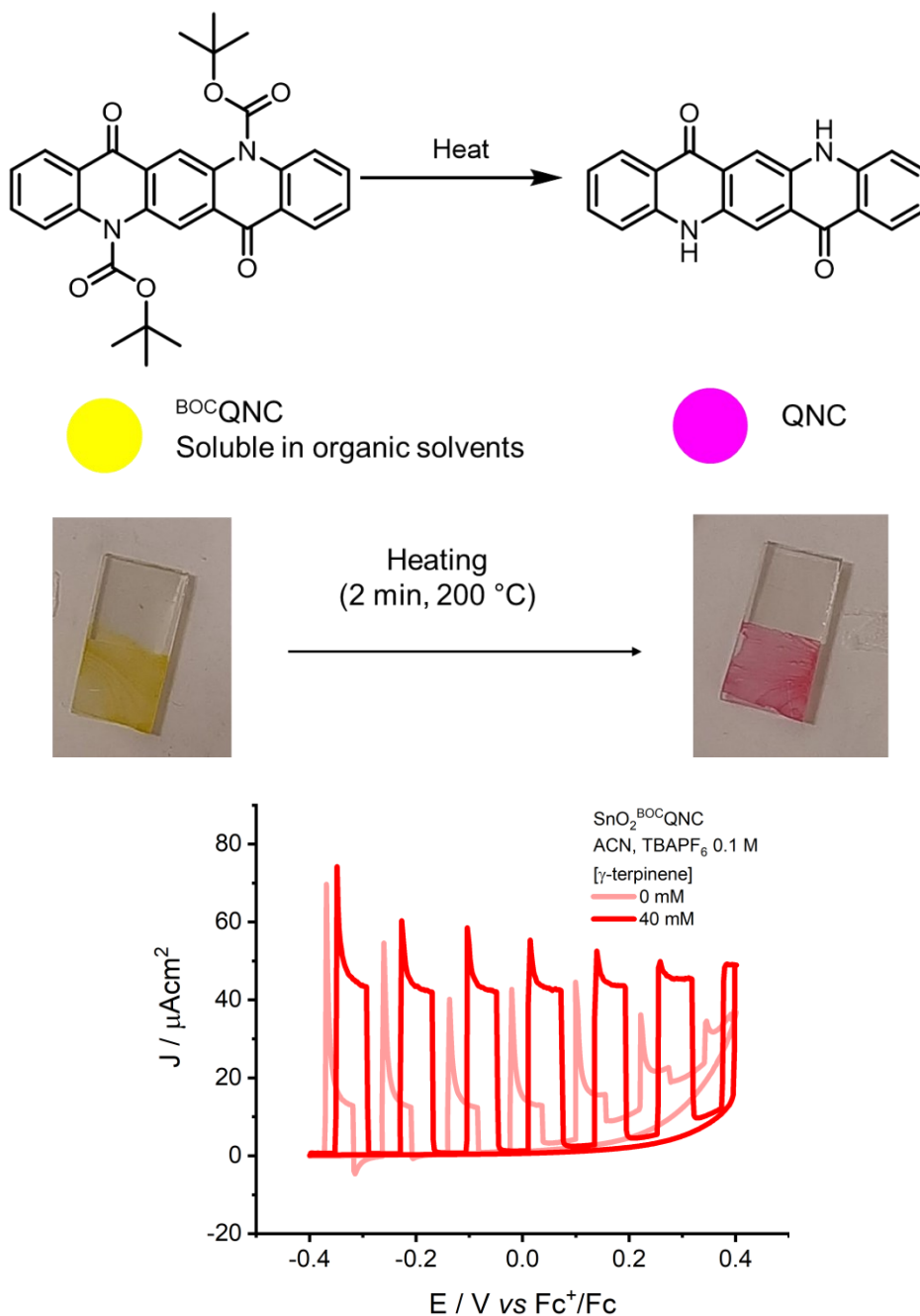


Figure 136. Top: schematic synthesis of QNC-sensitized photoanodes upon deposition and thermal treatment of ^{BOC}QNC. Bottom: LSV trace of FTO/SnO₂/QNC electrodes prepared starting from ^{BOC}QNC in the presence of γ -terpinene.

6.3 Experimental Section

6.3.1 Electrochemical carboxylation of α,β -unsaturated ketones

Procedure 1

The gas-tight two-compartment, six-neck electrochemical cell already reported (see Chapters 2 and 3) was used. 25 mL of a 0.1 M solution in CH₃CN of 0.1 M tetrabutylammonium hexafluorophosphate as supporting electrolyte, containing 20 mM substrate, were loaded in the working (cathodic) compartment. The anodic compartment contained 10 mL of CH₃CN solution of 0.1 M tetrabutylammonium hexafluorophosphate containing 10 eq (200 mM) triethylamine. The working electrode was a glassy carbon rod (SIGRADUR, HTW; geometric area *circa* 1.5 cm²), fitted in the cathodic compartment together with the reference electrode (Ag/AgCl, 3 M NaCl). The reference electrode was separated from the solution *via* the already described custom-made salt bridge (see Chapter 3). The auxiliary electrode was a platinum coiled wire, inserted in the anodic compartment.

Both compartments were degassed with CO₂ for 20 minutes, then the electrolysis experiment was started. An atmosphere of CO₂ was kept above the solutions throughout the electrolysis. The electrolysis was run in potentiostatic mode, at the potential of the second voltammetric peak.

Procedure 2

The use of single-compartment electrochemical cells was studied to simplify the system in the scope of an overall more sustainable setup requiring no noble metal anode nor a toxic sacrificial agent. To allow for compatibility of the anodic process with the target reaction in a single compartment, an aluminium sacrificial anode was used. Sacrificial anodes, usually made of Al or Mg, are often used in carboxylation reactions, given the very negative potentials required for the metal ions (Al³⁺, in this case, or Mg²⁺) deposition at the cathode. Furthermore,

carboxylate product formation can benefit from the presence of Al^{3+} ions, as they may stabilize carboxylates *via* salt formation.

Two single-compartment cells were designed and produced in collaboration with Mauro Meneghetti (glassblower at the Department of Chemical Sciences of the University of Padova), and are represented in Figure 137. The first was equipped with four ACE glass screw joints that were used to accommodate the electrodes and allow for degassing of the internal solution. Sealing of the cell was achieved by fitting the electrodes with suitable O-rings and using a gas-tight GC rubber septum as the self-sealing inlet port for degassing and injecting reactants.

The second cell was constructed following a similar design, albeit with a smaller volume (to allow for working with *circa* 25 mL of electrolyte solution). Furthermore, the four-neck cell was equipped with Schlenk-type side arm fitted with a ground glass stopcock, which allowed introduction of CO_2 gas upon insertion of a PTFE tube through the side arm. This latter could eventually be sealed after degassing, without the need for piercing the central rubber septum.

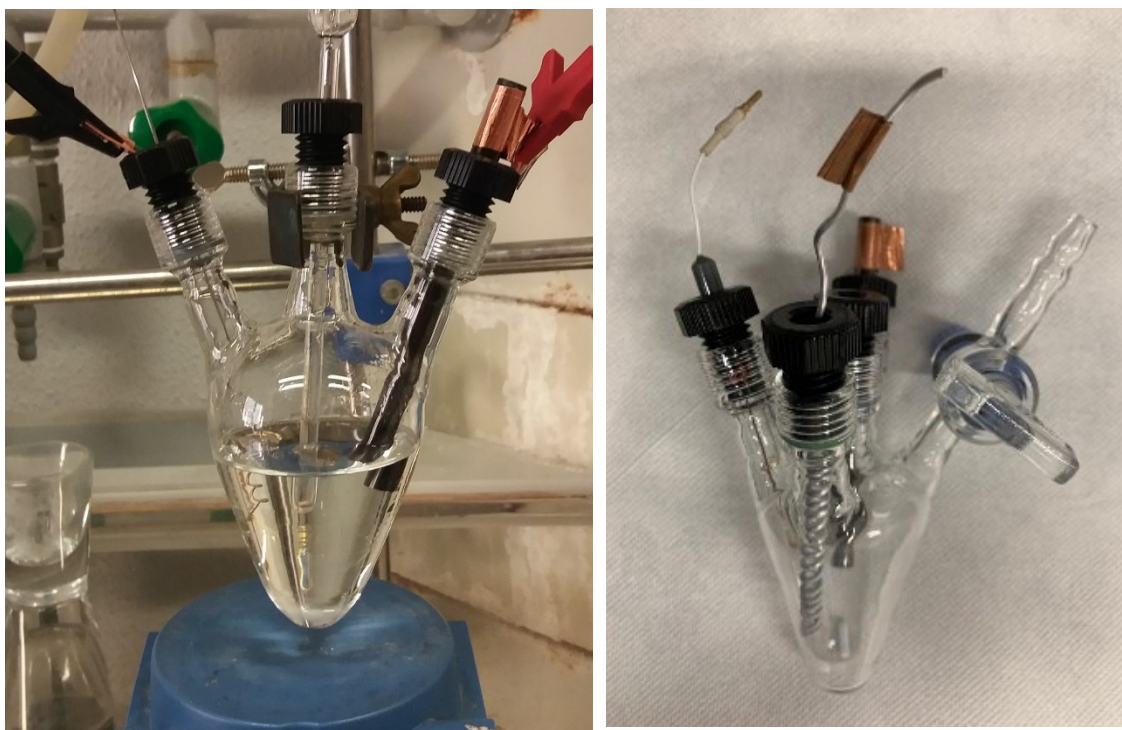


Figure 137. Single-compartment electrochemical cells using for electrosynthetic protocols with Al sacrificial anode.

The solution in the cell was constituted by 0.1 M tetrabutylammonium hexafluorophosphate or 0.1 M tetrabutylammonium chloride in CH₃CN. 2 equivalents (40 mM) of N,N-dicyclohexylmethylamine (Cy₂NCH₃) were introduced in the electrolytic solution directly in the cell. The electrodes were:

- i) A glassy carbon rod as working electrode (*circa* 1.5 cm² geometric area)
- ii) An Ag/AgCl (3 M NaCl) *via* salt bridge reference electrode
- iii) An aluminium coiled wire as the auxiliary electrode (sacrificial anode). The metal was activated by immersion in 2 M HCl until vigorous hydrogen evolution was observed, in order to remove the surface oxide layer. After activation, the wire was rinsed with deionized water and acetonitrile, then inserted in the electrolysis cell.

After assembling the electrochemical cell and degassing the solution for 20 minutes, the electrolysis was run in potentiostatic mode, at the potential of the second voltammetric peak.

6.3.2 Photoelectrochemical C–H activation by SnO₂ electrodes dye-sensitized with Quinacridone

Photoelectrochemical measurements

The experimental setup was the same as described in Chapter 5. A gold electrode (\varnothing 1.6 mm, BASi) was used as the CE, while potentials, registered vs Ag/AgCl (3 M NaCl) were referenced towards the Fc⁺/Fc couple.

Synthesis of ^{BOC}QNC

312 mg (1 mmol) of QNC were suspended in 50 mL of CH₂Cl₂, to which ^tBOC₂O (1.059 g, 4.8 mmol) and DMAP (254 mg, 2.1 mmol) were added. The reaction mixture was left to stir at room temperature for 48 h. After the specified time, the reaction mixture displayed a feeble green fluorescence. The mixture was brought to dryness by rotary evaporation and treated with a minimal quantity of ethyl acetate. ^{BOC}QNC was purified twice by column chromatography on silica gel:

- 1) eluent gradient starting from pentane/ethyl acetate (80:20), to pure ethyl acetate;
- 2) eluent gradient starting from hexane/dichloromethane (80:20), to pure dichloromethane.

The product was obtained as a yellow powder (210 mg, yield 41%).

The compound was highly soluble in many organic solvents, including dichloromethane, ethanol and acetonitrile. The compound was found to be quite sensitive to temperature and acid, undergoing partial decomposition on silica gel. For this reason, CDCl₃ was treated with basic aluminium oxide before registering the ¹H-NMR spectrum of the compound (Figure 138).

¹H-NMR (300 MHz, CDCl₃): δ 8.78 (s, 2H), δ 8.47–8.43 (dd, 2H), δ 7.90–7.71 (m, 4H), δ 7.46–7.38 (td, 4H), δ 1.79 (s, 18H). Impurities of water and dichloromethane were observed.

Elemental analysis: calculated for $C_{30}H_{28}N_2O_6$ C: 70.30% H: 5.51% N: 5.47%.
Found C: 70.09% H: 5.44% N: 5.04%.

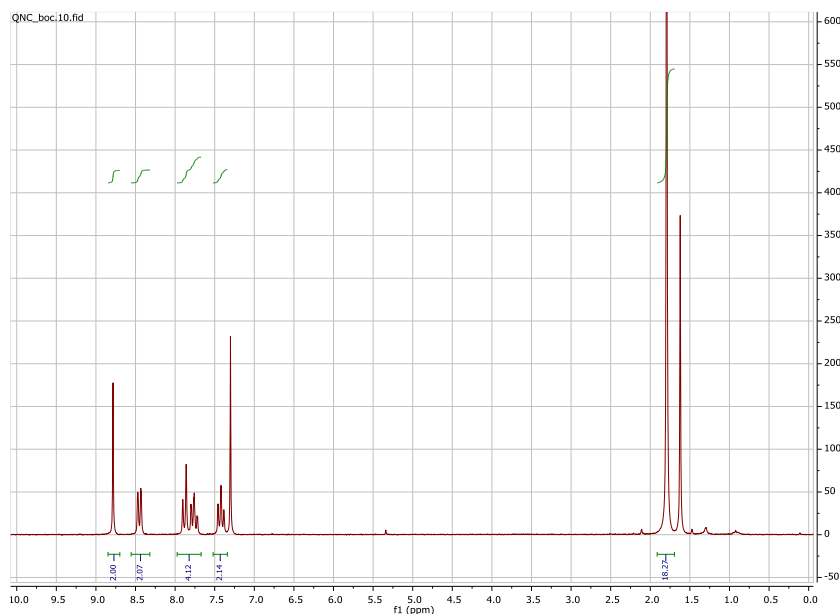


Figure 138. $^1\text{H-NMR}$ spectrum of BOCQNC .

Electrochemical cell design

Some work was dedicated to the design of a two-compartment glass gas-tight electrochemical cell suited for studying photoelectrochemical preparative reactions. A first cell (Figure 139) was designed together with Dr. Giulia Alice Volpato (University of Padova) and realized by glassblower Mauro Meneghetti. The cell was similar in structure to the one already described in Chapters 2 and 3, requiring similar degassing procedures. Briefly, it was constituted by two compartments separated by a porous glass frit. The working electrode compartment was equipped with four ACE glass screw joints and a ground glass opening. This latter was added to house photoanodes, connected *via* alligator clips to a copper wire contact, that could be lowered inside the electrochemical cell. The copper wire contact was passed through a rubber septum, in turn granting a gas-tight seal. The ACE glass screw joints were either used to insert the reference electrode or sealed with rubber disk septa, as described in Chapters

2 and 3. The auxiliary electrode compartment was instead equipped with two ACE glass screw joints, to allow insertion of the auxiliary electrode in a sealed environment. This cell was the one eventually used to run preparative photoelectrolysis experiments in this project.



Figure 139. Two-compartment photoelectrochemical cell used to study QNC-based photoanodes in gas-tight conditions.

A second cell was designed to have a simpler design and a wider optical window for working with photoelectrodes. It was realized by Mauro Meneghetti and tested for operativity, despite not being eventually used in the project. Briefly, it was constituted by a cylindrical body composed by two compartments separated by a sintered glass frit. The working electrode compartment (internal volume *circa* 50 mL) was fitted with two necks, one bearing a ground glass joint to locate the reference electrode and one equipped with a GL 14 screw joint. This latter was closed by a plastic screw cap with a hole in the middle. A silicone disk was interposed between the cap and the glass joint to provide a gas-tight seal.

The working electrode was inserted in the cell by connecting it to a copper contact *via* an alligator clip soldered to a copper wire. The copper wire was in turn used

to pierce the silicone disk, thus allowing for introduction of the working electrode into the cell. Similarly, degassing of the working compartment and injection of liquid reagents could be performed by piercing the silicone septum. To prevent air leakage, the holes pierced through the silicone seal were protected with UHU Patafix.

The reference electrode was located in a custom-made salt bridge (constructed by Mauro Meneghetti) fitted with a porous glass frit to grant electrolytic contact between the solution in the working electrode compartment and the inner solution in the salt bridge. The reference electrode was lowered into the salt bridge through an ACE glass screw joint, so to allow for a gas-tight sealed environment. The salt bridge was equipped with a ground glass joint that could fit into the inlet of the working electrode compartment. Silicone grease was used to seal the ground glass joint.

The auxiliary electrode compartment was equipped with one neck with a ground glass joint. The auxiliary electrode (usually a Pt grid) was fitted through a rubber septum that could seal the compartment. Schematic and *operando* representations of the cell are provided in Figure 140.

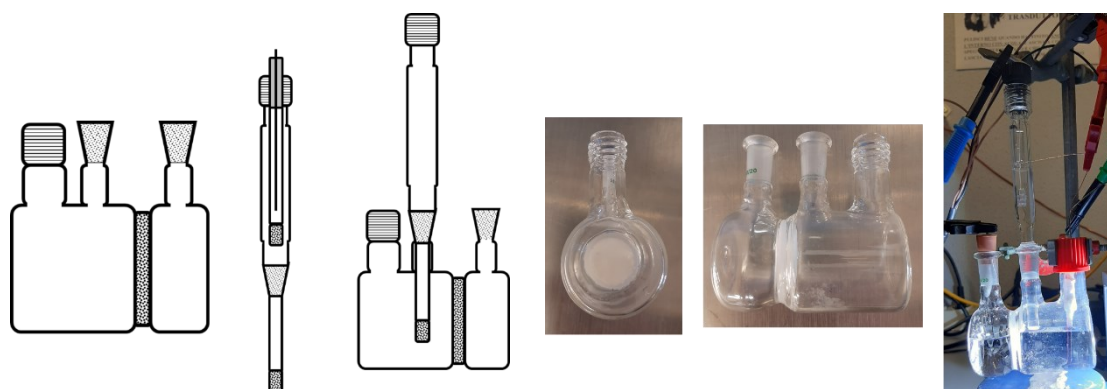


Figure 140. Schematic (left) and *operando* (right) representations of the photoelectrochemical cell designed to work in gas-tight conditions.

7. Bibliography

- (1) Nishiyama, H.; Yamada, T.; Nakabayashi, M.; Maehara, Y.; Yamaguchi, M.; Kuromiya, Y.; Nagatsuma, Y.; Tokudome, H.; Akiyama, S.; Watanabe, T.; Narushima, R.; Okunaka, S.; Shibata, N.; Takata, T.; Hisatomi, T.; Domen, K. *Nature* **2021**, 598 (7880), 304.
- (2) Zhou, P.; Navid, I. A.; Ma, Y.; Xiao, Y.; Wang, P.; Ye, Z.; Zhou, B.; Sun, K.; Mi, Z. *Nature* **2023**, 613 (7942), 66.
- (3) Pescarmona, P. P. *Current Opinion in Green and Sustainable Chemistry* **2021**, 29:100457.
- (4) Senboku, H.; Katayama, A. *Current Opinion in Green and Sustainable Chemistry* **2017**, 3, 50.
- (5) Leung, C. F.; Ho, P. Y. *Catalysts* **2019**, 9 (9), 760.
- (6) Tanaka, K.; Ooyama, D. *Coordination Chemistry Review* **2002**, 226, 211.
- (7) Bonin, J.; Maurin, A.; Robert, M. *Coordination Chemistry Reviews* **2017**, 334, 184.
- (8) Elgrishi, N.; Chambers, M. B.; Fontecave, M. *Chemical Science* **2015**, 6 (4), 2522.
- (9) Francke, R.; Schille, B.; Roemelt, M. *Chemical Reviews* **2018**, 4631.
- (10) Savéant, J.-M. *Chemical Reviews* **2008**, 108 (7), 2348.
- (11) Lee, K. J.; Elgrishi, N.; Kandemir, B.; Dempsey, J. L. *Nature Reviews Chemistry* **2017**, 1, 0039.
- (12) Rountree, E. S.; McCarthy, B. D.; Eisenhart, T. T.; Dempsey, J. L. *Inorganic Chemistry* **2014**, 53 (19), 9983.
- (13) Lu, X.; Ahsaine, H. A.; Dereli, B.; Garcia-Esparza, A. T.; Reinhard, M.; Shinagawa, T.; Li, D.; Adil, K.; Tchallala, M. R.; Kroll, T.; Eddaoudi, M.; Sokaras, D.; Cavallo, L.; Takanabe, K. *ACS Catalysis* **2021**, 11, 6499.
- (14) Rosser, T. E.; Windle, C. D.; Reisner, E. *Angewandte Chemie - International Edition* **2016**, 55 (26), 7388.
- (15) Limoges, B.; Savéant, J. M. *Journal of Electroanalytical Chemistry* **2004**, 562 (1), 43.
- (16) Limoges, B.; Savéant, J. M.; Yazidi, D. *Journal of the American Chemical Society* **2003**, 125 (30), 9192.
- (17) Shen, J.; Kortlever, R.; Kas, R.; Birdja, Y. Y.; Diaz-Morales, O.; Kwon, Y.; Ledezma-Yanez, I.; Schouten, K. J. P.; Mul, G.; Koper, M. T. M. *Nature Communications* **2015**, 6, 8817.
- (18) Balapanuru, J.; Chiu, G.; Su, C.; Zhou, N.; Hai, Z.; Xu, Q. H.; Loh, K. P. *ACS Applied Materials and Interfaces* **2015**, 7 (1), 880.
- (19) Rosser, T. E.; Reisner, E. *ACS Catalysis* **2017**, 7 (5), 3131.
- (20) Louis, M. E.; Fenton, T. G.; Rondeau, J.; Jin, T.; Li, G. *Comments on Inorganic Chemistry*. 2016, 36, 38–60.
- (21) Li, F.; Fan, K.; Wang, L.; Daniel, Q.; Duan, L.; Sun, L. *ACS Catalysis* **2015**, 5 (6), 3786.
- (22) Costentin, C.; Savéant, J. M. *Current Opinion in Electrochemistry* **2019**, 58.
- (23) Costentin, C.; Robert, M.; Savéant, J. M. *Current Opinion in Electrochemistry* **2017**, 2 (1), 26.

- (24) Costentin, C.; Robert, M.; Savéant, J. M. *Current Opinion in Electrochemistry* **2017**, 26.
- (25) Torbensen, K.; Boudy, B.; Joulié, D.; von Wolff, N.; Robert, M. *Current Opinion in Electrochemistry* **2020**, 49
- (26) Lim, R. J.; Xie, M.; Sk, M. A.; Lee, J. M.; Fisher, A.; Wang, X.; Lim, K. H.. *Catalysis Today* **2014**, 233, 169.
- (27) Torbensen, K.; Han, C.; Boudy, B.; von Wolff, N.; Bertail, C.; Braun, W.; Robert, M. *Chemistry - A European Journal* **2020**, 26 (14), 3034.
- (28) Jiang, C.; Nichols, A. W.; Walzer, J. F.; Machan, C. W. *Inorganic Chemistry* **2020**, 59 (3), 1883.
- (29) Ren, S.; Joulié, D.; Salvatore, D.; Torbensen, K.; Wang, M.; Robert, M.; Berlinguette, C. P. *Science* **2019**, 365 (6451), 367.
- (30) Bhugun, I.; Lexa, D.; Savéant, J.-M. *Journal of the American Chemical Society* **1994**, 116 (11), 5015.
- (31) Costentin, C.; Drouet, S.; Passard, G.; Robert, M.; Savéant, J. M. *Journal of the American Chemical Society* **2013**, 135 (24), 9023.
- (32) Costentin, C.; Drouet, S. *Journal of the American Chemical Society* **2017**, 134, 11235.
- (33) Costentin, C.; Drouet, S.; Robert, M.; Savéant, J. M. *Journal of the American Chemical Society* **2012**, 134 (27), 11235.
- (34) Costentin, C.; Robert, M.; Savéant, J. M.; Tatin, A. *Proceedings of the National Academy of Sciences USA* **2015**, 112 (22), 6882.
- (35) Costentin, C.; Robert, M.; Savéant, J. M. *Accounts of Chemical Research* **2015**, 48 (12), 2996.
- (36) Sanchis-Gual, R.; Seijas-Da Silva, A.; Coronado-Puchau, M.; Otero, T. F.; Abellán, G.; Coronado, E. *Electrochimica Acta* **2021**, 388, 138613.
- (37) de Groot, M. T.; Merx, M.; Wonders, A. H.; Koper, M. T. M. *Journal of the American Chemical Society* **2005**, 127 (20), 7579.
- (38) Costentin, C.; Savéant, J. M. *Journal of the American Chemical Society* **2017**, 139 (24), 8245.
- (39) Costentin, C.; Savéant, J.M. *Elements of Molecular and Biomolecular Electrochemistry* **2019**, Wiley.
- (40) Saveant, J. M.; Su, K. B. *Journal of Electroanalytical Chemistry and Interfacial Electrochemistry* **1984**, 171, 1-2, 341.
- (41) Costentin, C.; Robert, M.; Savéant, J. M. *Chemical Society Reviews* **2013**, 42 (6), 2423.
- (42) Martin, D. J.; McCarthy, B. D.; Rountree, E. S.; Dempsey, J. L. *Dalton Transactions* **2016**, 4524, 9970.
- (43) Costentin, C.; Savéant, J.-M. *ChemElectroChem* **2014**, 1 (7), 1226.
- (44) Bhugun, I.; Savéant, J.-M. *Journal of Electroanalytical Chemistry* **1996**, 408, 5.
- (45) Bhugun, I.; Savéant, J.-M. *Journal of Electroanalytical Chemistry* **1995**, 395, 127.
- (46) Ribelli, T. G.; Fantin, M.; Daran, J. C.; Augustine, K. F.; Poli, R.; Matyjaszewski, K. *Journal of the American Chemical Society* **2018**, 140 (4), 1525.

- (47) Stubbert, B. D.; Peters, J. C.; Gray, H. B. *Journal of the American Chemical Society* **2011**, *133* (45), 18070.
- (48) McCrory, C. C. L.; Uyeda, C.; Peters, J. C. *Journal of the American Chemical Society* **2012**, *134* (6), 3164.
- (49) Fantin, M.; Isse, A. A.; Matyjaszewski, K.; Gennaro, A. *Macromolecules* **2017**, *50* (7), 2696.
- (50) Lee, K. J.; McCarthy, B. D.; Dempsey, J. L. *Chemical Society Reviews* **2019**, 2927.
- (51) Martin, D. J.; McCarthy, B. D.; Donley, C. L.; Dempsey, J. L. *Chemical Communications* **2015**, *51* (25), 5290.
- (52) Artero, V.; Fontecave, M. *Chemical Society Reviews* **2013**, *42* (6), 2338.
- (53) Ghachtouli, S. el; Guillot, R.; Brisset, F.; Aukauloo, A. *ChemSusChem* **2013**, *6* (12), 2226.
- (54) Anxolabéhère-Mallart, E.; Costentin, C.; Fournier, M.; Robert, M. *Journal of Physical Chemistry C* **2014**, *118* (25), 13377.
- (55) Anxolabéhère-Mallart, E.; Costentin, C.; Fournier, M.; Nowak, S.; Robert, M.; Savéant, J. M. *Journal of the American Chemical Society* **2012**, *134* (14), 6104.
- (56) Britz, D.; Strutwolf, J. *Digital Simulation in Electrochemistry Fourth Edition*. Springer International Publishing Switzerland, **2016**. (First edition published in 1981).
- (57) Gosser, D. K.; Vch, J. *Cyclic Voltammetry Simulation and Analysis of Reaction Mechanisms*. VCH, New York, N. Y., **1993**.
- (58) Cometto, C.; Chen, L.; Lo, P. K.; Guo, Z.; Lau, K. C.; Anxolabéhère-Mallart, E.; Fave, C.; Lau, T. C.; Robert, M. *ACS Catalysis* **2018**, *8* (4), 3411.
- (59) Sconyers, D. J.; Blakemore, J. D. *Chemical Communications* **2017**, *53* (53), 7286.
- (60) Kaeffer, N.; Morozan, A.; Fize, J.; Martinez, E.; Guetaz, L.; Artero, V. *ACS Catalysis* **2016**, *6* (6), 3727.
- (61) Kaim, W.; Fiedler, J. *Chemical Society Reviews* **2009**, *38* (12), 3373.
- (62) Lozeman, J. J. A.; Führer, P.; Olthuis, W.; Odijk, M. *Analyst*, **2020**, *145*, 2482.
- (65) Lever, A. B. P.; Tse, Y.; Manivannan, V.; Seymour, P.; Strelets, V.; Persaud, L. S. *Inorganic Chemistry* **1996**, *35* (3), 725–734
- (66) Rahman, M. H.; Ryan, M. D.; Vazquez-Lima, H.; Alemayehu, A.; Ghosh, A. *Inorganic Chemistry* **2020**, *59* (5), 3232.
- (67) Rosser, T. E.; Reisner, E. *ACS Catalysis* **2017**, *7* (5), 3131.
- (68) Ke, X.; Kumar, R.; Sankar, M.; Kadish, K. M. *Inorganic Chemistry* **2018**, *57* (3), 1490.
- (69) Fernández, S.; Dubed Bandomo, G. C.; Lloret-Fillol, J. "Recent Advances in Electrocatalytic CO₂ Reduction with Molecular Complexes." In *Advances in Inorganic Chemistry*; Academic Press Inc., **2022**, *79*, 297.
- (70) Boutin, E.; Merakeb, L.; Ma, B.; Boudy, B.; Wang, M.; Bonin, J.; Anxolabéhère-Mallart, E.; Robert, M. *Chemical Society Reviews* **2020**, 5772
- (71) Tignor, S. E.; Kuo, H. Y.; Lee, T. S.; Scholes, G. D.; Bocarsly, A. B. *Organometallics* **2019**, *38* (6), 1292.

- (72) Roy, S. S.; Talukdar, K.; Jurss, J. W. *ChemSusChem* **2021**, *14* (2), 662.
- (73) Ngo, K. T.; Mckinnon, M.; Mahanti, B.; Narayanan, R.; Grills, D. C.; Ertem, M. Z.; Rochford, J. *Journal of the American Chemical Society* **2017**, *139* (7), 2604.
- (74) Blaszczak, V.; McKinnon, M.; Suntrup, L.; Aminudin, N. A.; Reed, B.; Groysman, S.; Ertem, M. Z.; Grills, D. C.; Rochford, J. *Inorganic Chemistry* **2022**, *61* (40), 15784.
- (75) Sampson, M. D.; Nguyen, A. D.; Grice, K. A.; Moore, C. E.; Rheingold, A. L.; Kubiak, C. P. *Journal of the American Chemical Society* **2014**, *136* (14), 5460.
- (76) Abu-Omar, M. M. *Dalton Transactions*. **2011**, 3435.
- (77) Gonell, S.; Assaf, E. A.; Lloret-Fillol, J.; Miller, A. J. M. *ACS Catalysis* **2021**, *11* (24), 15212.
- (78) Franco, F.; Rettenmaier, C.; Jeon, H. S.; Roldan Cuenya, B. *Chemical Society Reviews* **2020**, 6884.
- (79) Bonetto, R.; Crisanti, F.; Sartorel, A. *ACS Omega* **2020**, 21309.
- (80) Fernández, S.; Franco, F.; Casadevall, C.; Martin-Diaconescu, V.; Luis, J. M.; Lloret-Fillol, J. A *Journal of the American Chemical Society* **2020**, *142* (1), 120.
- (81) Beley, M.; Collin, J. P.; Ruppert, R.; Sauvage, J. P. *Journal of the Chemical Society - Series Chemical Communications* **1984**, *19*, 1315.
- (82) Dutta, A.; Lense, S.; Hou, J.; Engelhard, M. H.; Roberts, J. A. S.; Shaw, W. J. *Journal of the American Chemical Society* **2013**, *135* (49), 18490.
- (83) Fujihira, M.; Hirata, Y.; Suga, K. *Journal of Electroanalytical Chemistry and Interfacial Electrochemistry* **1990**, 292, 199.
- (84) Lam, K.-M.; Wong, K.-Y.; Yangb, S.-M.; Che, C.-M. *Journal of the Chemical Society, Dalton Transactions* **1995**, 1103.
- (85) Ma, L.; Hu, W.; Mei, B.; Liu, H.; Yuan, B.; Zang, J.; Chen, T.; Zou, L.; Zou, Z.; Yang, B.; Yu, Y.; Ma, J.; Jiang, Z.; Wen, K.; Yang, H. *ACS Catalysis* **2020**, *10* (8), 4534.
- (86) Angamuthu, R.; Byers, P.; Lutz, M.; Spek, A. L.; Bouwman, E. *Science* **2010**, *327* (5963), 313.
- (87) Parkin, A.; Seravalli, J.; Vincent, K. A.; Ragsdale, S. W.; Armstrong, F. A. *Journal of the American Chemical Society* **2007**, *129* (34), 10328.
- (88) Wang, V. C. C.; Ragsdale, S. W.; Armstrong, F. A. **2013**, *14* (14), 1845.
- (89) Svetlitchnyi, V.; Peschel, C.; Acker, G.; Meyer, O. *Journal of Bacteriology* **2001**, *183* (17), 5134.
- (90) Shin, W.; Lee, S. H.; Shin, J. W.; Lee, S. P.; Kim, Y. *Journal of the American Chemical Society* **2003**, *125* (48), 14688.
- (91) Azcarate, I.; Costentin, C.; Robert, M.; Savéant, J. M. *Journal of the American Chemical Society* **2016**, *138* (51), 16639.
- (92) Grodkowski, J.; Neta, P.; Fujita, E.; Mahammed, A.; Simkhovich, L.; Gross, Z. *Journal of Physical Chemistry A* **2002**, *106* (18), 4772.
- (93) Chen, L.; Guo, Z.; Wei, X. G.; Gallenkamp, C.; Bonin, J.; Anxolabéhère-Mallart, E.; Lau, K. C.; Lau, T. C.; Robert, M. *Journal of the American Chemical Society* **2015**, *137* (34), 10918.

- (94) Loipersberger, M.; Cabral, D. G. A.; Chu, D. B. K.; Head-Gordon, M. *Journal of the American Chemical Society* **2021**, *143* (2), 744.
- (95) Cometto, C.; Chen, L.; Mendoza, D.; Lassalle-Kaiser, B.; Lau, T. C.; Robert, M. *ChemSusChem* **2019**, *12* (19), 4500.
- (96) Cometto, C.; Kuriki, R.; Chen, L.; Maeda, K.; Lau, T. C.; Ishitani, O.; Robert, M. *Journal of the American Chemical Society* **2018**, *140* (24), 7437.
- (97) Guo, Z.; Cheng, S.; Cometto, C.; Anxolabéhère-Mallart, E.; Ng, S. M.; Ko, C. C.; Liu, G.; Chen, L.; Robert, M.; Lau, T. C. *Journal of the American Chemical Society* **2016**, *138* (30), 9413.
- (98) Rickmeyer, K.; Niederegger, L.; Keilwerth, M.; Hess, C. R. *ACS Catalysis* **2022**, *12* (5), 3046.
- (99) Zee, D. Z.; Nippe, M.; King, A. E.; Chang, C. J.; Long, J. R. *Inorganic Chemistry* **2020**, *59* (7), 5206.
- (100) Pun, S. N.; Chung, W. H.; Lam, K. M.; Guo, P.; Chan, P. H.; Wong, K. Y.; Che, C. M.; Chen, T. Y.; Peng, S. M. *Journal of the Chemical Society, Dalton Transactions* **2002**, *4*, 575.
- (101) Nichols, A. W.; Chatterjee, S.; Sabat, M.; MacHan, C. W. *Inorganic Chemistry* **2018**, *57* (4), 2111.
- (102) Taheri, A.; Berben, L. A. *Inorganic Chemistry* **2016**, *55* (2), 378.
- (103) Diego Rail, M.; Berben, L. A. *Journal of the American Chemical Society* **2011**, *133* (46), 18577.
- (104) Loewen, N. D.; Neelakantan, T. v.; Berben, L. A. *Accounts of Chemical Research* **2017**, *50* (9), 2362.
- (105) Choi, J.; Benedetti, T. M.; Jalili, R.; Walker, A.; Wallace, G. G.; Officer, D. L. *Chemistry - A European Journal* **2016**, *22* (40), 14158.
- (106) Abdinejad, M.; Tang, K.; Dao, C.; Saedy, S.; Burdyny, T. *Journal of Materials Chemistry A* **2022**, *10*(14), 7626.
- (107) Amanullah, S.; Saha, P.; Dey, A. *Journal of the American Chemical Society* **2021**, *143* (34), 13579.
- (108) Costentin, C.; Robert, M.; Savéant, J. M. *Accounts of Chemical Research* **2015**, *48* (12), 2996.
- (109) Azcarate, I.; Costentin, C.; Robert, M.; Savéant, J. M. *Journal of Physical Chemistry C* **2016**, *120* (51), 28951.
- (110) Zhang, Y. Q.; Chen, J. Y.; Siegbahn, P. E. M.; Liao, R. Z. *ACS Catalysis* **2020**, *10* (11), 6332.
- (111) Bonin, J.; Chaussemier, M.; Robert, M.; Routier, M. *ChemCatChem* **2014**, *6*(11), 3200.
- (112) Aresta, M.; Dibenedetto, A.; Quaranta, E. "CO₂ Coordination to Metal Centres: Modes of Bonding and Reactivity." In *Reaction Mechanisms in Carbon Dioxide Conversion*; Springer Berlin Heidelberg, **2016**; pp 35–69.
- (113) Mondal, B.; Ye, S. *Coordination Chemistry Reviews* **2020**, *405*, 213115.
- (114) Mondal, B.; Rana, A.; Sen, P.; Dey, A. *Journal of the American Chemical Society* **2015**, *137* (35), 11214.
- (115) Pugliese, E.; Gotico, P.; Wehrung, I.; Boitrel, B.; Quaranta, A.; Ha-Thi, M. H.; Pino, T.; Sircoglou, M.; Leibl, W.; Halime, Z.; Aukauloo, A. *Angewandte Chemie - International Edition* **2022**, *61* (14).

- (116) Croisy, A.; Lexa, D.; Momenteau, M.; Saveant, J.-M. *Organometallics* **1985**, *4* (9), 1574.
- (117) Matsu-Ura, M.; Tani, F.; Naruta, Y. *Journal of the American Chemical Society* **2002**, *124* (9), 1941.
- (118) Costentin, C.; Savéant, J. M. *Current Opinion in Electrochemistry* **2017**, 104.
- (119) Costentin, C.; Drouet, S.; Passard, G.; Robert, M.; Savéant, J. M. *Journal of the American Chemical Society* **2013**, *135* (24), 9023.
- (120) Bhugun, I.; Lexa, D.; Savéant, J.-M. *Journal of Physical Chemistry* **1996**, *100*(51), 19981.
- (121) Zhang, Y.; MacIntosh, A. D.; Wong, J. L.; Bielinski, E. A.; Williard, P. G.; Mercado, B. Q.; Hazari, N.; Bernskoetter, W. H. *Chemical Sciences* **2015**, *6* (7), 4291.
- (122) Sampson, M. D.; Kubiak, C. P. *Journal of the American Chemical Society* **2016**, *138* (4), 1386.
- (123) Isse, A. A.; Gennaro, A.; Vianello, E.; Floriani, C. *Journal of Molecular Catalysis* **1991**, *70* (2), 197.
- (124) Rao, H.; Schmidt, L. C.; Bonin, J.; Robert, M. *Nature* **2017**, *548* (7665), 74.
- (125) Rao, H.; Lim, C. H.; Bonin, J.; Miyake, G. M.; Robert, M. *Journal of the American Chemical Society* **2018**, *140* (51), 17830.
- (126) Margarit, C. G.; Asimow, N. G.; Costentin, C.; Nocera, D. G. *ACS Energy Letters* **2020**, *5* (1), 72.
- (127) Connor, G. P.; Mayer, K. J.; Tribble, C. S.; McNamara, W. R. *Inorganic Chemistry* **2014**, *53* (11), 5408.
- (128) Cavell, A. C.; Hartley, C. L.; Liu, D.; Tribble, C. S.; McNamara, W. R. *Inorganic Chemistry* **2015**, *54* (7), 3325.
- (129) Hartley, C. L.; Dirisio, R. J.; Chang, T. Y.; Zhang, W.; McNamara, W. R. *Polyhedron* **2016**, *114*, 133.
- (130) Benhamou, L.; Lachkar, M.; Mandon, D.; Welter, R. *Dalton Transactions* **2008**, *48*, 6996.
- (131) Saveant, J.-M. *Angewandte Chemie International Edition* **2019**, *58*, 2125.
- (132) Costentin, C.; Drouet, S.; Robert, M.; Savéant, J. M. *Science* **2012**, *338* (6103), 90.
- (133) Costentin, C.; Passard, G.; Robert, M.; Savéant, J. M. *Journal of the American Chemical Society* **2014**, *136* (33), 11821.
- (134) Costentin, C.; Robert, M.; Savéant, J. M.; Tatin, A. *Proceedings of the National Academy of Sciences USA* **2015**, *112*(22), 6882.
- (135) Gotico, P.; Boitrel, B.; Guillot, R.; Sircoglou, M.; Quaranta, A.; Halime, Z.; Leibl, W.; Aukauloo, A. *Angewandte Chemie* **2019**, *131* (14), 4552.
- (136) Sen, P.; Mondal, B.; Saha, D.; Rana, A.; Dey, A. *Dalton Transactions* **2019**, *48* (18), 5965.
- (137) Nichols, E. M.; Derrick, J. S.; Nistanaki, S. K.; Smith, P. T.; Chang, C. J. *Chemical Sciences* **2018**, *9* (11), 2952.
- (138) Khadhraoui, A.; Gotico, P.; Boitrel, B.; Leibl, W.; Halime, Z.; Aukauloo, A. *Chemical Communications* **2018**, *54* (82), 11630.

- (139) Margarit, C. G.; Schnedermann, C.; Asimow, N. G.; Nocera, D. G. *Organometallics* **2019**, *38*(6), 1219.
- (140) Luca, O. R.; Crabtree, R. H. *Chemical Society Reviews* **2013**, *42* (4), 1440.
- (141) Lacy, D. C.; McCrory, C. C. L.; Peters, J. C. *Inorganic Chemistry* **2014**, *53* (10), 4980.
- (142) Ghosh, S.; Rahaman, A.; Holt, K. B.; Nordlander, E.; Richmond, M. G.; Kabir, S. E.; Hogarth, G. *Polyhedron* **2016**, *116*, 127.
- (143) Guillard L, R.; Kadish, K. M. *Chemical Reviews* **1988** *88*, 1121.
- (144) Fang, Y.; Gorbunova, Y. G.; Chen, P.; Jiang, X.; Manowong, M.; Sinelshchikova, A. A.; Enakieva, Y. Y.; Martynov, A. G.; Tsvadze, A. Y.; Bessmertnykh-Lemeune, A.; Stern, C.; Guillard, R.; Kadish, K. M. *Inorganic Chemistry* **2015**, *54* (7), 3501.
- (145) Will, S.; Lex, J.; Vogel, E.; Adamian, V. A.; van Caemelbecke, E.; Kadish, K. M. *Inorganic Chemistry* **1996**, *35* (19), 5577.
- (146) Kadish, K. M.; Sazou, L. D.; Liu, Y. M.; Saoiabi, L. A.; Ferhat, M.; Guillard, R. *Inorganic Chemistry* **1988**, *27* (7), 1198.
- (147) Maher, A. G.; Liu, M.; Nocera, D. G. *Inorganic Chemistry* **2019**, *58* (12), 7958.
- (148) Solis, B. H.; Maher, A. G.; Dogutan, D. K.; Nocera, D. G.; Hammes-Schiffer, S. *Proceedings of the National Academy of Sciences USA* **2016**, *113* (3), 485.
- (149) Solis, B. H.; Maher, A. G.; Honda, T.; Powers, D. C.; Nocera, D. G.; Hammes-Schiffer, S. *ACS Catalysis* **2014**, *4* (12), 4516.
- (150) Pellegrin, Y.; Odobel, F. *Comptes Rendus Chimie* **2017**, 283.
- (151) Rao, H.; Bonin, J.; Robert, M. *ChemSusChem* **2017**, *10* (22), 4447.
- (152) Puntoriero, F.; Arrigo, A.; Santoro, A.; Ganga, G. Ia; Tuyèras, F.; Campagna, S.; Dupeyre, G.; Lainé, P. P. *Inorganic Chemistry* **2019**, *58* (9), 5807.
- (153) Yamazaki, Y.; Takeda, H.; Ishitani, O. Photocatalytic Reduction of CO₂ Using Metal Complexes. *Journal of Photochemistry and Photobiology C: Photochemistry Reviews* **2015**, *25*, 106.
- (154) Takeda, H.; Ohashi, K.; Sekine, A.; Ishitani, O. *Journal of the American Chemical Society* **2016**, *138* (13), 4354.
- (155) Takeda, H.; Cometto, C.; Ishitani, O.; Robert, M. *ACS Catal* **2017**, *7* (1), 70.
- (156) Kientz, M.; Lowe, G.; McCarthy, B. G.; Miyake, G. M.; Bonin, J.; Robert, M. *ChemPhotoChem* **2022**, *6* (7) e20220000.
- (157) Guo, Z.; Yu, F.; Yang, Y.; Leung, C.-F.; Ng, S.-M.; Ko, C.-C.; Cometto, C.; Lau, T.-C.; Robert, M. *ChemSusChem* **2017**, *10* (20), 4009.
- (158) Rao, H.; Bonin, J.; Robert, M. *Journal of Physical Chemistry C* **2018**, *122* (25), 13834.
- (159) Yuan, H.; Cheng, B.; Lei, J.; Jiang, L.; Han, Z. *Nature Communications* **2021**, *12* (1).
- (160) White, D. W.; Eskilsen, D.; Lee, S. K.; Ragsdale, S. W.; Dyer, R. B. *Journal of Physical Chemistry Letters* **2022**, *13* (24), 5553.
- (161) Takeda, H.; Koike, K.; Inoue, H.; Ishitani, O. *Journal of the American Chemical Society* **2008**, *130* (6), 2023.

- (162) Genoni, A.; Chiridon, D. N.; Boniolo, M.; Sartorel, A.; Bernhard, S.; Bonchio, M. *ACS Catalysis* **2017**, *7* (1), 154.
- (163) Yuan, H.; Du, J.; Ming, M.; Chen, Y.; Jiang, L.; Han, Z. Combination of Organic Dye and Iron for CO₂ Reduction with Pentanuclear Fe₂Na₃Purpurin Photocatalysts. *J Am Chem Soc* **2022**, *144* (10), 4305–4309.
- (164) Sartorel, A.; Bonchio, M.; Campagna, S.; Scandola, F. *Chemical Society Reviews* **2013**, *42* (6), 2262.
- (166) Geiger, D. K.; Pavlak, E. J.; Kass, L. T. *Journal of Chemical Education* **1961**, *68*(4), 337.
- (167) Cozzi, P. G. *Chemical Society Reviews* **2004**, *33* (7), 410.
- (168) Ueda, T.; Inazuma, N.; Komatsu, D.; Yasuzawa, H.; Onda, A.; Guo, S. X.; Bond, A. M. *Dalton Transactions* **2013**, *42* (31), 11146.
- (171) Gerloch, M.; Lewis, J.; Mabbs, F. E.; Richards, A. *Journal of the Chemical Society A: Inorganic, Physical, Theoretical* **1968**, 112.
- (172) Toniolo, D.; Scopelliti, R.; Zivkovic, I.; Mazzanti, M. *Journal of the American Chemical Society* **2020**, *142* (16), 7301.
- (173) Ortiz, B.; Park, S.-M. *Bulletin of the Korean Chemical Society* **2000**, *21* (4), 405.
- (174) Carrfi, B.; Costes, J.-P.; Tommasino, J.-B.; de Montauzon, D.; Soulet, F.; Fabre, P.-L. *Polyhedron* **1993**, *12*(6), 641.
- (175) Ranchet, D.; Tommasino, J. B.; Vittori, O.; Fabre, P. L. *Journal of Solution Chemistry* **1998**, *27* (11), 979.
- (176) Costes, J.-P.; Tommasino, J.-B.; Carré, B.; Soulet, F.; Fabre, P.-L. *Polyhedron* **2003**, *14* (6), 771.
- (177) Kadish, K. M.; Larson, G.; Lexa, D.; Momenteaulb, M. *Journal of the American Chemical Society* **1975**, *97* (2), 282.
- (178) McCarthy, B. D.; Martin, D. J.; Rountree, E. S.; Ullman, A. C.; Dempsey, J. L. *Inorganic Chemistry* **2014**, *53* (16), 8350.
- (179) Bonetto, R.; Altieri, R.; Tagliapietra, M.; Barbon, A.; Bonchio, M.; Robert, M.; Sartorel, A. *ChemSusChem* **2020**, *13* (16), 4111.
- (180) Citek, C.; Oyala, P. H.; Peters, J. C. *Journal of the American Chemical Society* **2019**, *141* (38), 15211.
- (181) Bhugun, I.; Lexa, D.; Savéant, J. M. *Journal of the American Chemical Society* **1996**, *118* (7), 1769.
- (182) Ahmed Isse, A.; Cennaro, A.; Vianello, E. *Electrochimica Acta* **1997**, *13-14*, 2065.
- (183) Cometto, C.; Chen, L.; Mendoza, D.; Lassalle-Kaiser, B.; Lau, T. C.; Robert, M. *ChemSusChem* **2019**, *12* (19), 4500.
- (184) Gallo, E.; Solar, E.; de Angelis, S.; Floriani, C.; Re, N.; Chiesi-Villa, A.; Rizzoli, C. *Journal of the American Chemical Society* **1993**, *115*, 9850.
- (185) de Angelis, S.; Solari, E.; Gallo, E.; Floriani, C.; Chiesi-Villa, A.; Rizzoli, C. *Inorganic Chemistry* **1996**, *35*, 5995.

- (186) Gallo, E.; Solari, E.; Re, N.; Floriani, C.; Chiesi-Villa, A.; Rizzoli, C.; Floriani, C. *Angewandte Chemie International Edition English* **1996**, 35 (17), 1981.
- (187) Corazza, F.; Floriani, C.; Zehnder, M. *Journal of the Chemical Society, Dalton Transactions* **1987**, 709.
- (188) Gallo, E.; Solari, E.; Re, N.; Floriani, C.; Chiesi-Villa, A.; Rizzoli, C. *Journal of the American Chemical Society* **1997**, 119 (22), 5144.
- (189) Andrez, J.; Guidal, V.; Scopelliti, R.; Pécaut, J.; Gambarelli, S.; Mazzanti, M. *Journal of the American Chemical Society* **2017**, 139 (25), 8628.
- (190) Lam, Y. C.; Nielsen, R. J.; Gray, H. B.; Goddard, W. A. *ACS Catalysis* **2015**, 5 (4), 2521.
- (191) Jameei Moghaddam, N.; Gil-Sepulcre, M.; Wang, J. W.; Benet-Buchholz, J.; Gimbert-Suriñach, C.; Llobet, A. *Inorganic Chemistry* **2022**, 61 (42), 16639.
- (192) Rennie, B. E.; Eleftheriades, R. G.; Morris, R. H. *Journal of the American Chemical Society* **2020**, 142 (41), 17607.
- (193) McCarthy, P. J.; Hovey, R. J.; Ueno, K.; Martell, A. E. *Journal of the American Chemical Society* **1955**, 77 (20), 5820.
- (194) Biswas, A.; Drew, M. G. B.; Ghosh, A. *Polyhedron* **2010**, 29 (3), 1029.
- (195) Costes, J.-P.; Cros, G.; Darbieu', M.-H.; Laurent, J.-P. *Inorganica Chimica Acta* **1982**, 60, 111.
- (196) Guieu, S.; Cardona, F.; Rocha, J.; Silva, A. M. S. *New Journal of Chemistry* **2014**, 38 (11), 5411.
- (197) Cisterna, J.; Artigas, V.; Fuentealba, M.; Hamon, P.; Manzur, C.; Hamon, J. R.; Carrillo, D. *Inorganics (Basel)* **2018**, 6 (1) 5.
- (198) Concepcion, J. J.; House, R. L.; Papanikolas, J. M.; Meyer, T. J. *Proceedings of the National Academy of Sciences USA* **2012**, 109 (39), 15560.
- (199) Gust, D.; Moore, T. A.; Moore, A. L. *Accounts of Chemical Research* **2009**, 42 (12), 1890.
- (200) Tachibana, Y.; Vayssieres, L.; Durrant, J. R. *Nature Photonics* **2012**, 6, 511.
- (201) Andreiadis, E. S.; Chavarot-Kerlidou, M.; Fontecave, M.; Artero, V. *Photochemistry Photobiology* **2011**, 87 (5), 946.
- (202) Alibabaei, L.; Brennaman, M. K.; Norris, M. R.; Kalanyan, B.; Song, W.; Losego, M. D.; Concepcion, J. J.; Binstead, R. A.; Parsons, G. N.; Meyer, T. J. *Proceedings of the National Academy of Sciences USA* **2013**, 110 (50), 20008.
- (203) Xu, P.; Huang, T.; Huang, J.; Yan, Y.; Mallouk, T. E. *Proceedings of the National Academy of Sciences USA* **2018**, 115 (27), 6946.
- (204) Ding, X.; Gao, Y.; Ye, L.; Zhang, L.; Sun, L. *ChemSusChem* **2015**, 8 (23), 3992.
- (205) Xu, P.; Huang, T.; Huang, J.; Yan, Y.; Mallouk, T. E. *Proceedings of the National Academy of Sciences USA* **2018**, 115 (27), 6946.
- (206) Peter, L. M.; Upul Wijayantha, K. G. *ChemPhysChem* **2014**, 15, 1983.
- (207) Xu, P.; Mallouk, T. E. *Journal of Physical Chemistry C* **2019**, 123 (1), 299.
- (208) Swierk, J. R.; Mallouk, T. E. *Chemical Society Reviews* **2013**, 42 (6), 2357.

- (210) Xu, P.; McCool, N. S.; Mallouk, T. E. *Nano Today* **2017**, *14*, 42.
- (211) Xu, P.; Gray, C. L.; Xiao, L.; Mallouk, T. E. *Journal of the American Chemical Society* **2018**, *140* (37), 11647.
- (212) Youngblood, W. J.; Anna Lee, S. H.; Maeda, K.; Mallouk, T. E. *Accounts of Chemical Research* **2009**, *42* (12), 1966.
- (213) McCool, N. S.; Swierk, J. R.; Nemes, C. T.; Schmuttenmaer, C. A.; Mallouk, T. E. *Journal of Physical Chemistry Letters* **2016**, *7* (15), 2930.
- (214) Swierk, J. R.; McCool, N. S.; Nemes, C. T.; Mallouk, T. E.; Schmuttenmaer, C. A. *Journal of Physical Chemistry C* **2016**, *120* (11), 5940.
- (215) Swierk, J. R.; McCool, N. S.; Saunders, T. P.; Barber, G. D.; Mallouk, T. E. *Journal of the American Chemical Society* **2014**, *136* (31), 10974.
- (216) Yao, L.; Rahmanudin, A.; Guijarro, N.; Sivula, K. *Advanced Energy Materials* **2018**, *8*, 1802585.
- (217) Sytnyk, M.; Głowacki, E. D.; Yakunin, S.; Voss, G.; Schöffberger, W.; Kriegner, D.; Stangl, J.; Trotta, R.; Gollner, C.; Tollabimazraehno, S.; Romanazzi, G.; Bozkurt, Z.; Havlicek, M.; Sariciftci, N. S.; Heiss, W. *Journal of the American Chemical Society* **2014**, *136* (47), 16522.
- (218) Kirner, J. T.; Finke, R. G. *Journal of Materials Chemistry A* **2017**, *5* (37), 19560.
- (219) Kirner, J. T.; Finke, R. G. *ACS Applied Materials and Interfaces* **2017**, *9* (33), 27625.
- (220) Kirner, J. T.; Stracke, J. J.; Gregg, B. A.; Finke, R. G. *ACS Applied Materials and Interfaces* **2014**, *6* (16), 13367.
- (221) Manfredi, N.; Boldrini, C. L.; Abboto, A. *ChemElectroChem* **2018**, *5* (17), 2395.
- (222) Materna, K. L.; Crabtree, R. H.; Brudvig, G. W. *Chemical Society Reviews* **2017**, *46*, 6099.
- (223) Troiano, J. L.; Crabtree, R. H.; Brudvig, G. W. *ACS Applied Materials and Interfaces* **2022**, *14* (5), 6582.
- (224) Zhu, Y.; Wang, D.; Huang, Q.; Du, J.; Sun, L.; Li, F.; Meyer, T. J. *Nature Communications* **2020**, *11* (1).
- (225) di Iorio, Y.; Rodríguez, H. B.; San Román, E.; Grela, M. A. *Journal of Physical Chemistry C* **2010**, *114* (26), 11515.
- (226) di Iorio, Y.; Parra, R.; Szaciłowski, K.; Grela, M. A. *New Journal of Chemistry* **2013**, *37* (4), 969.
- (227) Soria, F. A.; Daldossi, C.; di Valentin, C. *Mater Today Energy* **2022**, *28*, 101085.
- (228) Fisher, K. J.; Materna, K. L.; Mercado, B. Q.; Crabtree, R. H.; Brudvig, G. W. *ACS Catalysis* **2017**, *7* (5), 3384.
- (229) Moore, G. F.; Blakemore, J. D.; Milot, R. L.; Hull, J. F.; Song, H. E.; Cai, L.; Schmuttenmaer, C. A.; Crabtree, R. H.; Brudvig, G. W. *Energy & Environmental Science* **2011**, *4* (7), 2389.
- (230) Dau, H.; Limberg, C.; Reier, T.; Risch, M.; Roggan, S.; Strasser, P. *ChemCatChem* **2010**, *2*, 724.
- (231) Hettler, D. G. H.; Reek, J. N. H. *Angewandte Chemie - International Edition* **2012**, *51*, 9740.

- (232) Chen, Z.; Concepcion, J. J.; Jurss, J. W.; Meyer, T. J. *Journal of the American Chemical Society* **2009**, *131* (43), 15580.
- (233) Matheu, R.; Garrido-Barros, P.; Gil-Sepulcre, M.; Ertem, M. Z.; Sala, X.; Gimbert-Suriñach, C.; Lobet, A. *Nature Reviews Chemistry*, **2019**, *3*, 331.
- (234) Kaveevivitchai, N.; Chitta, R.; Zong, R.; el Ojaimi, M.; Thummel, R. P. A Molecular Light-Driven Water Oxidation Catalyst. *J Am Chem Soc* **2012**, *134* (26), 10721–10724.
- (235) Volpe, A.; Tubaro, C.; Natali, M.; Sartorel, A.; Brudvig, G. W.; Bonchio, M. *Inorganic Chemistry* **2019**, *58* (24), 16537.
- (236) Rigodanza, F.; Marino, N.; Bonetto, A.; Marcomini, A.; Bonchio, M.; Natali, M.; Sartorel, A. *ChemPhysChem* **2021**, *22* (12), 1208.
- (237) Swierk, J. R.; McCool, N. S.; Saunders, T. P.; Barber, G. D.; Strayer, M. E.; Vargas-Barbosa, N. M.; Mallouk, T. E. *Journal of Physical Chemistry C* **2014**, *118* (30), 17046.
- (238) Bonchio, M.; Syrgiannis, Z.; Burian, M.; Marino, N.; Pizzolato, E.; Dirian, K.; Rigodanza, F.; Volpato, G. A.; la Ganga, G.; Demitri, N.; Berardi, S.; Amenitsch, H.; Guldi, D. M.; Caramori, S.; Bignozzi, C. A.; Sartorel, A.; Prato, M.. *Nature Chemistry* **2019**, *11* (2), 146.
- (239) Gobatto, T.; Rigodanza, F.; Benazzi, E.; Costa, P.; Garrido, M.; Sartorel, A.; Prato, M.; Bonchio, M. *Journal of the American Chemical Society* **2022**, *144* (31), 14021.
- (240) Morris, N. D.; Suzuki, M.; Mallouk, T. E. *Journal of Physical Chemistry A* **2004**, *108* (42), 9115.
- (241) Youngblood, J. W.; Lee, S. H. A.; Kobayashi, Y.; Hernandez-Pagan, E. A.; Hoertz, P. G.; Moore, T. A.; Moore, A. L.; Gust, D.; Mallouk, T. E. *Journal of the American Chemical Society* **2009**, *131* (3), 926.
- (242) Sherman, B. D.; Pillai, S.; Kodis, G.; Bergkamp, J.; Mallouk, T. E.; Gust, D.; Moore, T. A.; Moore, A. L. *Canadian Journal of Chemistry* **2011**, *89* (2), 152.
- (243) de Tovar, J.; Romero, N.; Denisov, S. A.; Bofill, R.; Gimbert-Suriñach, C.; Ciuculescu-Pradines, D.; Drouet, S.; Lobet, A.; Lecante, P.; Colliere, V.; Freixa, Z.; McClenaghan, N.; Amiens, C.; García-Antón, J.; Philippot, K.; Sala, X. *Materials Today Energy* **2018**, *9*, 506.
- (244) Chou, N. H.; Ross, P. N.; Bell, A. T.; Tilley, T. D. *ChemSusChem* **2011**, *4* (11), 1566.
- (245) Deng, X.; Tüysüz, H. Cobalt-Oxide-Based Materials as Water Oxidation Catalyst: Recent Progress and Challenges. *ACS Catalysis* **2014**, *4*(10), 3701.
- (246) Risch, M.; Klingan, K.; Ringleb, F.; Chernev, P.; Zaharieva, I.; Fischer, A.; Dau, H. *ChemSusChem* **2012**, *5* (3), 542.
- (247) Chen, Z.; Duan, Z.; Wang, Z.; Liu, X.; Gu, L.; Zhang, F.; Dupuis, M.; Li, C. *ChemCatChem* **2017**, *9* (19), 3641.
- (248) Jiao, F.; Frei, H. *Energy and Environmental Science* **2010**, *3*, 1018.
- (249) Reith, L.; Triana, C. A.; Pazoki, F.; Amiri, M.; Nyman, M.; Patzke, G. R. *Journal of the American Chemical Society* **2021**, *143* (37), 15022.
- (250) Zhang, M.; de Respinis, M.; Frei, H. *Nature Chemistry* **2014**, *6* (4), 362.
- (251) Sprague-Klein, E. A.; He, X.; Mara, M. W.; Reinhart, B. J.; Lee, S.; Utschig, L. M.; Mulfort, K. L.; Chen, L. X.; Tiede, D. M. *ACS Energy Letters* **2022**, *7* (9), 3129.

- (252) Han, A.; Wu, H.; Sun, Z.; Jia, H.; Du, P. *Physical Chemistry Chemical Physics* **2013**, *15* (30), 12534.
- (253) Nguyen, A. I.; Ziegler, M. S.; Oña-Burgos, P.; Sturzbecher-Hohne, M.; Kim, W.; Bellone, D. E.; Tilley, T. D. *Journal of the American Chemical Society* **2015**, *137* (40), 12865.
- (254) Kwapien, K.; Piccinin, S.; Fabris, S. *Journal of Physical Chemistry Letters* **2013**, *4* (24), 4223.
- (255) Han, A.; Wu, H.; Sun, Z.; Jia, H.; Yan, Z.; Ma, H.; Liu, X.; Du, P. *ACS Applied Materials and Interfaces* **2014**, *6* (14), 10929.
- (256) Haase, F. T.; Bergmann, A.; Jones, T. E.; Timoshenko, J.; Herzog, A.; Jeon, H. S.; Rettenmaier, C.; Cuenya, B. R. *Nature Energy* **2022**, *7* (8), 765–773.
- (257) Mohammadi, M. R.; Loos, S.; Chernev, P.; Pasquini, C.; Zaharieva, I.; González-Flores, D.; Kubella, P.; Klingan, K.; Smith, R. D. L.; Dau, H. *ACS Catalysis* **2020**, *10* (14), 7990.
- (258) Swierk, J. R.; Méndez-Hernández, D. D.; McCool, N. S.; Liddell, P.; Terazono, Y.; Pahk, I.; Tomlin, J. J.; Oster, N. v.; Moore, T. A.; Moore, A. L.; Gust, D.; Mallouk, T. E. *Proceedings of the National Academy of Sciences* **2015**, *112* (6), 1681.
- (259) Sherman, B. D.; Sheridan, M. v.; Dares, C. J.; Meyer, T. J. *Analytical Chemistry* **2016**, *88* (14), 7076.
- (260) Forchetta, M.; Conte, V.; Fiorani, G.; Galloni, P.; Sabuzi, F. *Organics* **2021**, *2* (2), 107.
- (261) Valentini, F.; Sabuzi, F.; Conte, V.; Nemykin, V. N.; Galloni, P. *Journal of Organic Chemistry* **2021**, *86* (8), 5680.
- (262) Bonomo, M.; Sabuzi, F.; di Carlo, A.; Conte, V.; Dini, D.; Galloni, P. *New Journal of Chemistry* **2017**, *41* (7), 2769.
- (263) Sabuzi, F.; Armuzza, V.; Conte, V.; Floris, B.; Venanzi, M.; Galloni, P.; Gatto, E. *Journal of Materials Chemistry C* **2016**, *4* (3), 622.
- (264) Coletti, A.; Lentini, S.; Conte, V.; Floris, B.; Bortolini, O.; Sforza, F.; Grepioni, F.; Galloni, P. *Journal of Organic Chemistry* **2012**, *77* (16), 6873.
- (265) Sabuzi, F.; Lentini, S.; Sforza, F.; Pezzola, S.; Fratelli, S.; Bortolini, O.; Floris, B.; Conte, V.; Galloni, P. *Journal of Organic Chemistry* **2017**, *82* (19), 10129.
- (266) Volpato, G. A.; Marasi, M.; Gobbato, T.; Valentini, F.; Sabuzi, F.; Gagliardi, V.; Bonetto, A.; Marcomini, A.; Berardi, S.; Conte, V.; Bonchio, M.; Caramori, S.; Galloni, P.; Sartorel, A. *Chemical Communications* **2020**, *56* (15), 2248.
- (267) Volpato, G. A.; Colusso, E.; Paoloni, L.; Forchetta, M.; Sgarbossa, F.; Cristino, V.; Lunardon, M.; Berardi, S.; Caramori, S.; Agnoli, S.; Sabuzi, F.; Umari, P.; Martucci, A.; Galloni, P.; Sartorel, A. *Photochemical and Photobiological Sciences* **2021**, *20* (10), 1243.
- (268) Swierk, J. R.; Regan, K. P.; Jiang, J.; Brudvig, G. W.; Schmuttenmaer, C. A. *ACS Energy Letters* **2016**, *1* (3), 603.
- (269) Jewell, C. F.; Subramanian, A.; Nam, C.-Y.; Finke, R. G. *ACS Applied Materials and Interfaces* **2022**, *14*, 25326.
- (270) Zambounis, J. S.; Hao, Z.; Iqbal, A. *Nature* **1997**, *388*, 6638, 131

- (271) Sytnyk, M.; Głowacki, E. D.; Yakunin, S.; Voss, G.; Schöfberger, W.; Kriegner, D.; Stangl, J.; Trotta, R.; Gollner, C.; Tollabimazraehno, S.; Romanazzi, G.; Bozkurt, Z.; Havlicek, M.; Sariciftci, N. S.; Heiss, W. *Journal of the American Chemical Society* **2014**, *136* (47), 16522.

Ringraziamenti – Acknowledgements

Un sentito ringraziamento va al mio Supervisore, Prof. Andrea Sartorel, per avermi accompagnato durante questi tre anni di Dottorato, come guida attenta e lasciandomi sempre la più grande libertà di pensare e di tentare.

Ringrazio i miei colleghi del laboratorio, per aver condiviso con me tutti i momenti del lavoro durante questi anni.

Ad Elena e Catia va il mio più grande in bocca al lupo per gli anni di Dottorato che ancora dovranno venire. Grazie per esservi prese cura di me quando da solo non ci sarei riuscito.

Ringrazio Thomas per la sua amicizia, fuori e dentro il laboratorio. Tante sfide ci aspettano ancora, ma con lo spirito giusto ne verremo fuori più forti di prima.

Grazie Paolo, per la sincerità e l'onestà che ti rendono un uomo speciale.

Grazie Giulia e Claudio. Anche se ora non lavoriamo più insieme, io continuo a seguire i vostri passi nel laboratorio. I vostri scritti rimangono sempre una mappa per navigare i mari della scienza.

Grazie Francesco, Simone, Leonardo, Jiaying, Alessio, Tommaso, Angelo, Sara, Ricardo, Marina, Giorgia, Gianpaolo, Ilaria, Giulia, Martina, Pietro, Valeria, Jintao!

Grazie a tutti gli amici e alle amiche di Mestre, di Padova e di ovunque.

I would like to acknowledge Prof. Juilen Warnan and Dr. Niklas von Wolff for their attentive review of the present Thesis and their kind words.

Ringrazio il Ministero dell'Università e della Ricerca e il Dipartimento di Scienze Chimiche, grazie ai quali la mia borsa a tema di ricerca libero è stata finanziata nell'ambito del progetto NExuS.

I wish to thank Prof. Xavier Sala for his supervision during my visiting stay in the Autonomous University of Barcelona, who granted me one of the best periods in my professional life.

Un sentito ringraziamento va al Dr. Loris Calore, per il supporto nelle analisi elementari presso il Dipartimento di Scienze Chimiche dell'Università di Padova.

Grazie a Stefano Mercanzin e a Mauro Meneghetti, insieme ai quali più di un orgoglio del nostro laboratorio è stato creato e che ogni giorno si dimostrano indispensabili, non soltanto per il lavoro.

Ringrazio il Prof. Abdirisak Ahmed Isse e il Prof. Christian Durante per il loro corso di Elettrochimica e le utili discussioni in merito a problemi di ricerca.

Thank you, Jordi, Nuria, Laia, Alvaro and Gerard. It was amazing working with you. Thank you, Laura! I wish you the best of luck for everything.

I wish to thank also Prof. Jordi Hernando for his generous help in the lab, and Dr. Ignasi Villarroya Antillac, Dr. Sandra Izquierdo Salado, and Mònica Pujalte Comas of the Analytical Service in the U.A.B. Also, I would like to acknowledge

the help from the Technical Service of the Department of Physics at the U.A.B. when we were most in need.

I would like to sincerely thank Prof. Marc Robert from the University of Paris, together with Dr. Cédric Tard and Prof. Costentin, for providing guidance and education in the field of Electrochemistry.

Thank you to the amazing people I met in Paris during CVIS2022. Jerome, you'll probably be my last teaching lab mate, at least for a long time. It was super!

Thank you Zewen, for sharing life and friendship so far from home.

Thank you to the S.A.F. and Frozensand, for contributing to my health during some of the hardest months.

A special thank you is reserved to Mark J. Ferrari, for giving me the strongest motivation throughout the last years (unbeknownst to him – or maybe he'll know by now).

Thanks also to C. Bajakian, M. Land, P. McConnell, G. Sanger, B. Moriarty and R. Gilbert, I would have loved to meet you in person.

Grazie Maria, Gaetano, Luigi e Federica per avermi sempre accolto come una seconda famiglia. Vi voglio bene. E grazie Poldo per la tua amicizia.

Per concludere, vorrei ringraziare la mia famiglia. Durante questi anni, nonostante tutte le difficoltà, mi avete dato ogni conforto e supporto, senza mai chiedere nulla in cambio e senza mai farmi sentire solo, nemmeno mentre ero lontano. Un bel pezzo di questa Tesi è dedicato a voi.

Cara Luana, leggerai di te per ultima, per cui scusami per la pazienza che ti ho fatto portare. Grazie per avermi accompagnato in questo percorso. Le parole forse mi mancano, ma sappi che in ogni lettera battuta in questa Tesi c'è un ringraziamento per te, che mi hai dato la forza di fare e di diventare ciò che non avrei potuto mai da solo. Ora tocca a te!